

Dissertation in Astronomy
submitted to the
Combined Faculties of the Natural Sciences and Mathematics
of the Ruperto-Carola-University of Heidelberg, Germany,
for the degree of
Doctor of Natural Sciences

Put forward by
Dipl.Phys. *Gabriele Cologna*
born in: Trento, Italy
Oral examination: 11.05.2016

**TeV observations of hard spectrum
active galactic nuclei
with HESS-I and HESS-II**

Gabriele Cologna

Landessternwarte, Zentrum für Astronomie (ZAH) of Heidelberg University

**Referees: Prof. Dr. Stefan J. Wagner
Priv.-Doz. Dr. Konrad Bernlöhr**

Zusammenfassung

In meiner Dissertation präsentiere ich die Ergebnisse der Analyse dreier γ -strahlenden Punktquellen, die in sehr hohen Energien mit dem High Energy Stereoscopic system (H.E.S.S.) beobachtet worden sind: die zwei bekannte Blazare 1ES 0229+200 und Mrk 501, und HESS J1745-290. Die Natur der letzten Quelle ist unklar, obwohl sie wahrscheinlich mit Sgr A*, dem schwarzen Loch im Zentrum der Galaxie, verbunden ist. Ich benutze Multiwellenlänge Beobachtungen, um die physikalischen Eigenschaften der Quellen und des Umgebungsmediums einzuschätzen, sowohl durch Spektral- und Variabilitätsstudien, als auch durch den Vergleich mit Modellen und Vorhersagen aus der Literatur. Außerdem präsentiere ich systematische Vergleiche der Energien der γ -Strahlen, wie sie für die verschiedenen Sub-Arrays des H.E.S.S. Systems rekonstruiert werden.

Ich suche nach korrelierter Variabilität in simultanen Beobachtungen in Röntgen und sehr-hohen Energien, um zu verstehen, ob die γ -Strahlung von HESS J1745-290 aus dem schwarzen Loch entsteht, was dann ein aktiver Galaxien Kern wäre, oder nicht. Die Korrelation der Flussvariabilität in verschiedenen Energiebändern für 1ES 0229+200 unterstützt das Synchrotron-Self-Compton Emissionsmodell für diese Quelle. Das verbesserte Spektrum des IC Peaks hilft bei der Einschränkung der Stärke des intergalaktischen magnetischen Feldes. Das harte intrinsische Spektrum von Mrk 501 zeigt eine Abhängigkeit vom Flussniveau. Das Spektrum kann genutzt werden, um die Intensität des extragalaktischen Hintergrundlichtes im mittel-Infrarot einzuschränken. Multiwellenlänge Beobachtungen weisen auf die Anwesenheit zweier Emissionszonen oder Mechanismen hin, um die Breitband Emission der Quelle zu erklären.

Abstract

In my PhD thesis, I present the results of the analysis of three point-like γ -ray emitters observed at very high energies with the High Energy Stereoscopic System (H.E.S.S.): the two well known blazars 1ES 0229+200 and Mrk 501, and HESS J1745-290. The nature of the latter source is unclear, although it is likely linked to Sgr A*, the black hole at the center of the Galaxy. I make use of multiwavelength observations in order to assess the physical properties of the three sources and of the ambient medium, both via spectral and variability studies and by comparison with models and predictions found in the literature. I also present systematic comparisons of the γ -ray energies as reconstructed for different sub-arrays of the H.E.S.S. system.

I search for correlated variability in simultaneous x-ray and very high energy observations of Sgr A* in order to understand whether or not the γ -ray emission of HESS J1745-290 originates from the black hole, making it an active galactic nucleus. The correlation of the flux variability in different energy bands for 1ES 0229+200 supports the interpretation of a synchrotron self Compton emission model for this source. The refined spectrum of the inverse Compton peak helps constraining the strength of the intergalactic magnetic field. The hard intrinsic spectrum of Mrk 501 shows a dependency on the flux state. The spectrum can be used to constrain the extragalactic background light intensity in the mid-infrared for the redshift of the source. Multiwavelength observations suggest the presence of at least two emission zones or mechanisms in order to explain the broadband emission.

*“The first principles of the universe are atoms and empty space;
everything else is merely thought to exist.”*

Democritus

CONTENTS

INTRODUCTION	13
1 ACTIVE GALACTIC NUCLEI	19
1.1 BLAZARS	22
2 ACCELERATION, RADIATION AND ABSORPTION PROCESSES	25
2.1 PARTICLE ACCELERATION	25
2.1.1 SECOND ORDER FERMI MECHANISM (STOCHASTIC SHOCK ACCELERATION)	25
2.1.2 FIRST ORDER FERMI MECHANISM (DIFFUSIVE SHOCK ACCELERATION)	27
2.1.3 MAGNETIC RECONNECTION	29
2.1.4 EXTRAGALACTIC ACCELERATORS	29
2.2 RADIATIVE PROCESSES	31
2.2.1 SYNCHROTRON EMISSION	31
2.2.2 INVERSE COMPTON EMISSION	33
2.2.3 SYNCHROTRON SELF COMPTON AND EXTERNAL COMPTON EMISSION	35
2.2.4 BREMSSTRAHLUNG (FREE-FREE EMISSION)	36
2.2.5 PAIR PRODUCTION	37
2.2.6 ELECTRON-POSITRON ANNIHILATION	37
2.3 HADRONIC INTERACTIONS AND γ -RAY PRODUCTION	37
2.4 VHE ASTRONOMY	38
2.4.1 AIR SHOWERS	38
2.4.1.1 Electromagnetic showers	39
2.4.1.2 Hadronic showers	40
2.4.2 CHERENKOV EMISSION	41

2.4.3	EXTRAGALACTIC BACKGROUND LIGHT (EBL)	43
2.4.4	INTERGALACTIC MAGNETIC FIELD (IGMF)	46
3	THE H.E.S.S. EXPERIMENT	51
3.1	THE H.E.S.S. TELESCOPE SYSTEM	52
3.1.1	LOCATION	52
3.1.2	THE ARRAY	53
3.1.3	MOUNT AND DRIVE SYSTEM	55
3.1.4	MIRRORS	55
3.1.5	CAMERAS	57
3.1.6	TRIGGER SYSTEM	58
3.2	AUTOMATED TELESCOPE FOR OPTICAL MONITORING (ATOM)	60
4	DATA COLLECTION AND ANALYSIS	63
4.1	OBSERVATION METHODS	63
4.2	SHOWER IMAGING	64
4.3	HILLAS RECONSTRUCTION	64
4.3.1	ENERGY RECONSTRUCTION	68
4.3.2	γ -HADRON SEPARATION	68
4.4	MODEL RECONSTRUCTION	70
4.4.1	γ -HADRON SEPARATION	71
4.4.2	COMPARISON MODEL VS. HILLAS RECONSTRUCTION	74
4.5	SIGNAL EXTRACTION	77
4.6	SYSTEM ACCEPTANCE	78
4.7	BACKGROUND EVALUATION	80
4.7.1	REFLECTED REGION BACKGROUND MODEL	80
4.7.2	RING BACKGROUND MODEL	82
4.8	SPECTRAL ANALYSIS	82
4.9	LIGHTCURVE DETERMINATION	84
4.10	MORPHOLOGICAL ANALYSIS	85
4.11	<i>ParisAnalysis</i> SOFTWARE	85
5	GALACTIC CENTER	87
5.1	CHANDRA 3 Ms VISIONARY PROJECT	88
5.2	H.E.S.S. OBSERVATIONS AND ANALYSIS	89
5.3	SPECTRAL ANALYSIS	89
5.4	TEMPORAL ANALYSIS	89
5.5	CONCLUSIONS	95

6	1ES 0229+200	97
6.1	1ES 0229+200: THE SOURCE	97
6.2	VHE OBSERVATIONS WITH H.E.S.S.	99
6.3	OBSERVATIONS OUTSIDE THE VHE BAND	100
6.3.1	HIGH ENERGIES	100
6.3.2	X-RAYS	101
6.3.3	OPTICAL	103
6.4	H.E.S.S. DATA REDUCTION	105
6.5	H.E.S.S. SPECTRAL ANALYSIS	107
6.6	SPECTRAL ANALYSIS WITH EBL ABSORPTION	118
6.7	TEMPORAL ANALYSIS	120
6.8	INTERGALACTIC MAGNETIC FIELD (IGMF) DETERMINATION	123
6.8.1	EFFECTS OF THE VHE VARIABILITY	123
6.8.2	LIMITS FROM THE REVISED <i>Fermi</i> SPECTRUM	124
6.8.3	COMMENTS ON PLASMA EXCITATION THEORIES	125
6.9	CONCLUSIONS	126
7	MRK 501	129
7.1	SOURCE DESCRIPTION	129
7.2	VHE OBSERVATIONS WITH H.E.S.S.	131
7.3	OBSERVATIONS AT LOWER ENERGIES	132
7.3.1	X-RAYS	132
7.3.2	OPTICAL	133
7.4	H.E.S.S. DATA REDUCTION	134
7.5	SPECTRAL ANALYSIS	136
7.5.1	OBSERVED SPECTRA	136
7.5.1.1	Cumulative dataset	136
7.5.1.2	Yearly datasets	139
7.5.1.3	Daily datasets	144
7.5.1.4	2006 dataset: comparison of H.E.S.S. and MAGIC spectra	154
7.5.2	INTRINSIC SPECTRA	156
7.6	EBL DETERMINATION	162
7.7	TEMPORAL ANALYSIS	165
7.8	LORENTZ INVARIANCE VIOLATION (LIV) STUDIES	170
7.9	POSITION FIT	172
7.10	MONO AND STEREO ANALYSIS WITH CT5	174
7.10.1	MONO AND STEREO SPECTRA	176

7.10.2	MONO AND STEREO SPECTRA WITH EBL ABSORPTION	180
7.11	LIGHTCURVE COMPARISON	181
7.12	CONCLUSIONS	186
8	SYSTEMATIC STUDIES: HESS-I vs HESS-II COMPARISON	189
8.1	COMPARISON WITH ORIGINAL DATA CALIBRATION AND CUTS	189
8.1.1	MRK 501	190
8.1.2	CRAB NEBULA	194
8.1.3	PKS 2155-304	197
8.1.4	SUMMARY	197
8.2	COMPARISON WITH UPDATED DATA CALIBRATION AND OPTIMIZED CUTS	198
8.2.1	MRK 501	199
8.2.2	CRAB NEBULA	202
8.2.3	PKS 2155-304	202
8.2.4	SUMMARY OF THE UPDATED ANALYSIS	207
8.3	EFFECTS OF THE CUTS	209
8.4	TEST WITH INDEPENDENT SOFTWARE AND DATA CALIBRATION	210
8.5	CONCLUSIONS	212
	SUMMARY AND OUTLOOK	215
	BIBLIOGRAPHY	217

INTRODUCTION

“The results of the present observations are most easily explained by the assumption that the radiation with very high penetrating power enters the atmosphere from above; even in its lower layers, this radiation produces part of the ionization observed in close vessels... Since there was neither a decrease at night or during a solar eclipse, the Sun can hardly be considered as the source.”

Victor Hess

In 1912, Victor Hess discovered the cosmic rays (CR). He carried out measurements of the ionization levels in the air during balloon flights up to 5300 m of altitude, showing a four-fold increase with respect to ground level. With further measurements at night and during a solar eclipse, he not only demonstrated that the CR must enter the atmosphere from above, but he also excluded the Sun as their source. Victor Hess won the Nobel prize in 1936 for this discovery.

Initially, the nature of CR was not clear. Robert Millikan believed they were γ -rays produced in interstellar space and that the ionization was due to electrons that had been Compton scattered in the atmosphere. In the following years, evidence collected that CR were in fact charged particles, and for the large majority positively charged. In 1927, Jacob Clay found that the CR intensity changed with latitude, which indicated that CR are deflected by the earth magnetic field. In 1933-34, three independent measurements from Thomas Johnson, from Luis Alvarez and Arthur Compton and from Bruno Rossi found confirmation of the “east-west effect”: the CR intensity is greater from the west, which proves that most particles are positively charged.

CR are composed for the 89% by protons, 9% α particles, 1% heavier nuclei and 1% electrons. A very small fraction consists of antimatter particles, like positrons and antiprotons. The CR spectrum (Fig. 1) extends for 12 orders of magnitude in energy ($\sim 10^9 < E/\text{eV} < 10^{21}$) and 34 in flux ($10^{-28} < F/(\text{m}^{-2}\text{sr}^{-1}\text{s}^{-1}\text{GeV}^{-1}) < 10^4$). This corresponds to 10^4 particles/m²/s at 1 GeV and to 1 particle/km²/century at 100 EeV (10^{20} eV). CR with energies above 10^{18} eV are called ultra high energy cosmic rays (UHECR). Among them, in 1991, a particle¹ with energy of 3.2×10^{20} eV (ca. 50 J) was measured for the first time.

¹This particle is known as the Oh-my-God particle, expressing the surprise of the astrophysicists for its enormous

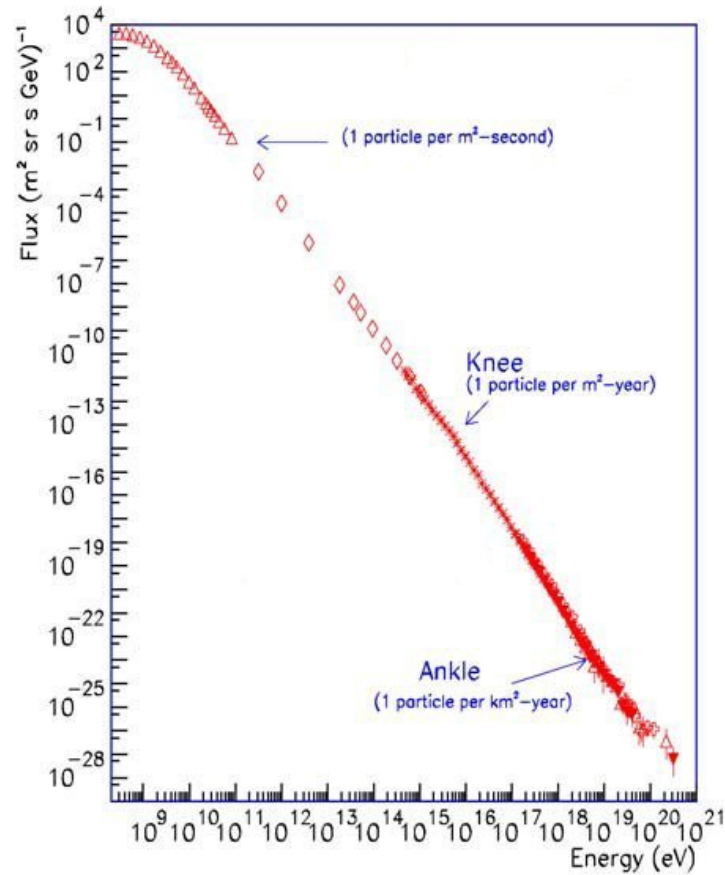


Figure 1: Spectrum of the cosmic rays. Two features are clearly visible at $\sim 5 \times 10^{15}$ eV (knee) at $\sim 10^{19}$ eV (ankle). It is generally believed that CR below the knee have Galactic origin, while those above the ankle are produced outside the Milky Way.

The CR spectrum is described by a power-law shape with index ~ 2.7 over almost the whole energy range. It peaks and flattens significantly below 1 GeV. This behaviour is explained by the interaction with the solar wind, that acts as a barrier for the low energy CR. Two other main features are present in the spectrum: the knee at $\sim 5 \times 10^{15}$ eV, where the spectrum steepens, and the ankle, at $\sim 10^{19}$ eV, where it hardens again. A further steepening at $\sim 10^{17}$ eV characterizes the second knee (Fig. 2). CR are isotropized by the intervening magnetic fields between the source and the Earth, so that it has not been possible yet to link any of them to a discrete emission region. As a consequence, both their composition and spectrum are isotropic, as well.

It is generally believed that CR below the knee are produced in supernova remnants in the Galaxy, while those above the ankle are produced outside the Milky Way, likely in active galactic nuclei. The knee would therefore reflect the maximal energy that can be obtained in Galactic accelerators. However, it must be taken into account that the steepening could partly depend on the fact that more energetic particles cannot be confined in the Galaxy by the Galactic magnetic

energy: a single particle with an energy equivalent to the kinetic energy of a 100 g mass travelling at 80 km/h!

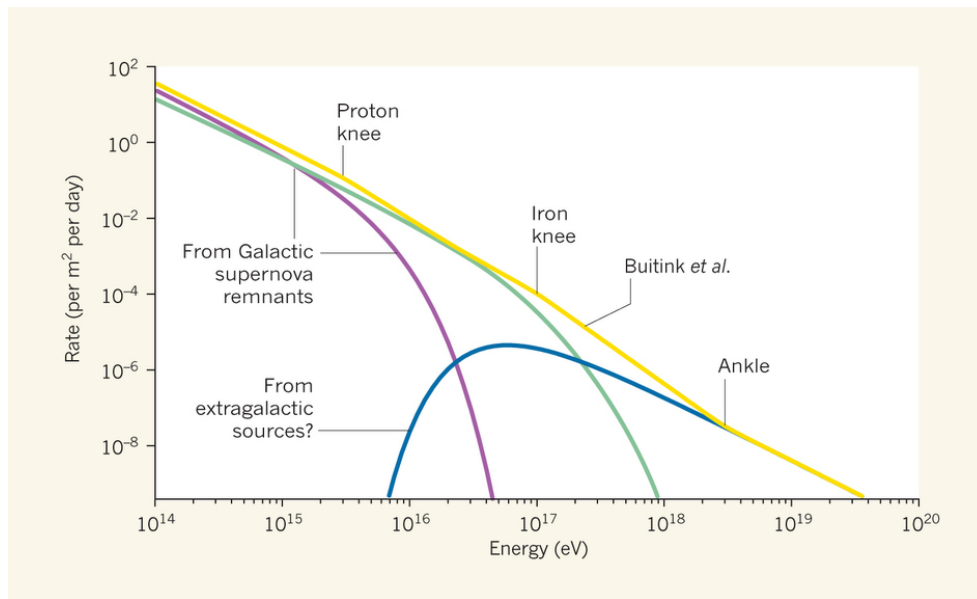


Figure 2: Zoom-in of the cosmic ray spectrum. The knees and the ankle are clearly visible. The components of the spectrum are also indicated (from Taylor 2016).

field, and therefore escape into extragalactic space. The two knees are likely linked to the composition of CR: protons below the first knee, and iron nuclei below the second knee (Fig. 2). If the particles above the ankle have extragalactic origin, then a cut-off in the spectrum is expected above 10^{20} eV (Greisen-Zatsepin-Kuzmin limit, GZK limit). At these energies, protons interact with the photons of the cosmic microwave background (CMB) creating pions ($p + \gamma_{CMB} \rightarrow p + \pi^0$ and $p + \gamma_{CMB} \rightarrow n + \pi^+$) until their energy falls below the pion production threshold. Protons with energies greater than this threshold traveling over distances larger than 50 Mpc (163 Mly) should lose all their energy and never be observed on Earth (GZK horizon).

With the discovery of CR, Victor Hess opened a new branch of astronomy. Scientists have been looking for accelerators powerful enough to explain the humongous energies reached by CR and for the acceleration mechanisms able to reproduce the incredibly stable power-law spectrum over so many orders of magnitude. However, energetic particles lose their energy through radiative processes, and through interactions with other particles or photons. They are the source of non-thermal radiation that spans the whole electromagnetic spectrum from radio wavelengths up to high energy (HE, $100 \text{ MeV} < E < 100 \text{ GeV}$) and very high energy (VHE, $E > 100 \text{ GeV}$) γ -ray photons. They signed the theoretical birth of γ -ray astronomy².

As I mentioned earlier, it is believed that CR with energies above 10^{19} eV have extragalactic origin and possibly are produced in AGN. However, most AGN peak at high energies in the MeV range, probably too low to be able to accelerate particles to such extreme energies. In order to

²Observations must await the 1960s and the 1970s, with the launch of the first dedicated satellites and the installation of the first ground based telescope for VHE observations.

have efficient accelerators, emitters with intrinsic hard luminous spectra are preferred. These are the kind of sources that have been chosen here.

In this thesis, I present the data reduction and the analysis of point-like γ -ray emitters observed at VHE with the High Energy Stereoscopic System (H.E.S.S.). Three sources have been taken into consideration, specifically, HESS J1745-290 and two well known blazars, 1ES 0229+200 and Mrk 501. The nature of the first source is unclear. The compact γ -ray emission towards the Galactic Center is probably linked to the central black hole Sgr A* (making it an active galactic nucleus), although it has never been possible to conclusively demonstrate it. Albeit obviously not a powerful extragalactic source, HESS J1745-290 has a hard spectrum, and its emission reaches at least up to 40 TeV. Would the association with Sgr A* be correct, this source would be a low luminosity AGN. From an observational point of view, this issue is overcome thanks to its proximity.

I make use of multiwavelength observations in order to assess the physical properties of the sources and of the ambient medium both via variability studies and by comparison with models and predictions found in the literature. I also present systematic comparisons of the γ -ray energies as reconstructed for different sub-arrays of the H.E.S.S. system.

In chapter 1 and 2, I introduce the basic observational and theoretical concepts on which this thesis is based. I describe the active galactic nuclei phenomenology, as well as the particle acceleration mechanisms, and the radiation and absorption processes of VHE photons.

In chapter 3, I describe the H.E.S.S. experiment and the telescope array. In chapter 4, I present the methods used for the analysis of the VHE data.

The results from the 2012 VHE and x-ray multiwavelength campaign on Sgr A* with H.E.S.S. and *Chandra* are reported in chapter 5. No significant flare was simultaneously covered by both instruments and no definitive conclusion can be drawn about the nature of the TeV source HESS J1745-290.

In chapter 6, I present the long term monitoring of the blazar 1ES 0229+200. The source shows variability at VHE, as well as in the x-ray band. The correlation of the variability supports a synchrotron self Compton emission model. Together with a refined spectrum in the GeV band, it helps constraining the strength of the intergalactic magnetic field.

Chapter 7 is based on the analysis of the flaring state of the blazar Mrk 501. The hard intrinsic spectrum shows a dependency on the flux state. It can be used to constrain the extragalactic background light intensity in the mid-infrared at the redshift of the source. Multiwavelength observations hint towards the necessity of at least two emission zones or mechanisms to explain the broadband emission.

In chapter 8, I present a systematic comparison of the photon energy as it is reconstructed for different H.E.S.S. subarrays. Three sources are used (Mrk 501, Crab Nebula and PKS 2155-304), which cover three complementary energy and Zenith angle bands, in order to look for possible dependencies. I find a systematic energy bias, which is not linked on either properties.

In the last chapter, I summarize the work, with an outlook on possible future studies.

Some of the results contained in this work have been presented at the *International Cosmic Ray Conference (ICRC) 2015* and published in the respective proceedings:

- **Cologna G.**, Mohamed M., Wagner S. J., Wierzcholska A. and Romoli C. for the H.E.S.S. Collaboration and Kurtanidze O., *Long term lightcurve of the BL Lac object 1ES 0229+200 at TeV energies*, 2015, ArXiv e-prints [arXiv:1509.04470]
- **Cologna G.**, Chakraborty N., Mohamed M., Rieger F., Romoli C., Taylor A., Wagner S. J., Wierzcholska A. and Jacholkowska A. for the H.E.S.S. Collaboration and Kurtanidze O., *Spectral characteristics of Mrk 501 during the 2012 and 2014 flaring states*, 2015, ArXiv e-prints [arXiv:1509.04458]
- Chakraborty N., **Cologna G.**, Kastendieck M. A., Rieger F., Romoli C., Wagner S. J., Jacholkowska A. and Taylor A. for the H.E.S.S. Collaboration, *Rapid variability at very high energies in Mrk 501*, 2015, ArXiv e-prints [arXiv:1509.04893]

CHAPTER 1

ACTIVE GALACTIC NUCLEI

All types of galaxies are believed to host a super massive black hole (SMBH, $M > 10^6 M_{\odot}$)¹ at their center. In a small percentage of the cases, enough matter accretes onto the black hole, leading to emission of energy through various mechanisms. In this case, the SMBH is called active galactic nucleus, or in short AGN. Several types of AGNei exist, hosted in both elliptical and spiral galaxies and they are categorized based on their emission properties. One common characteristic of these sources is their bright luminosity, which is at least comparable to (if not completely dominant over) the luminosity of the host galaxy. Depending on the AGN class, the emission can cover the entirety of the electromagnetic spectrum, from radio up to VHE γ -rays. The main AGN classes are the following (from Carroll & Ostlie 1996):

- *Seyfert I* (Sy I) galaxies: they are very luminous sources, which show a power-law continuum that often outshines the stellar emission of the galaxy. In addition, their spectra show a thermal component with broad (1000-5000 km/s) and narrow (500 km/s) emission lines of allowed and forbidden transitions. The line width is attributed to Doppler broadening and is always much larger than the emission line width of the stellar component of the host galaxy. The x-ray component is often variable, while the radio emission is very weak. The host galaxy is normally a spiral galaxy;
- *Seyfert II* (Sy II) galaxies: the continuum is weaker than for Sy I, as well as the x-ray emission, which is probably absorbed by material on the line of sight to the observer. They also show only narrow lines of both allowed and forbidden transitions;
- *Radio galaxies*: they are (giant or supergiant) elliptical galaxies extremely bright at radio frequencies. Similarly to Seyfert galaxies, they have very bright and star-like nuclei in the optical. There are two classes analogous to Sy I and Sy II: broad-line radio galaxies (BLRGs) and narrow-line radio galaxies (NLRGs). Radio galaxies show giant structures

¹ $M_{\odot} = 1.988 \times 10^{30}$ kg is the solar mass.

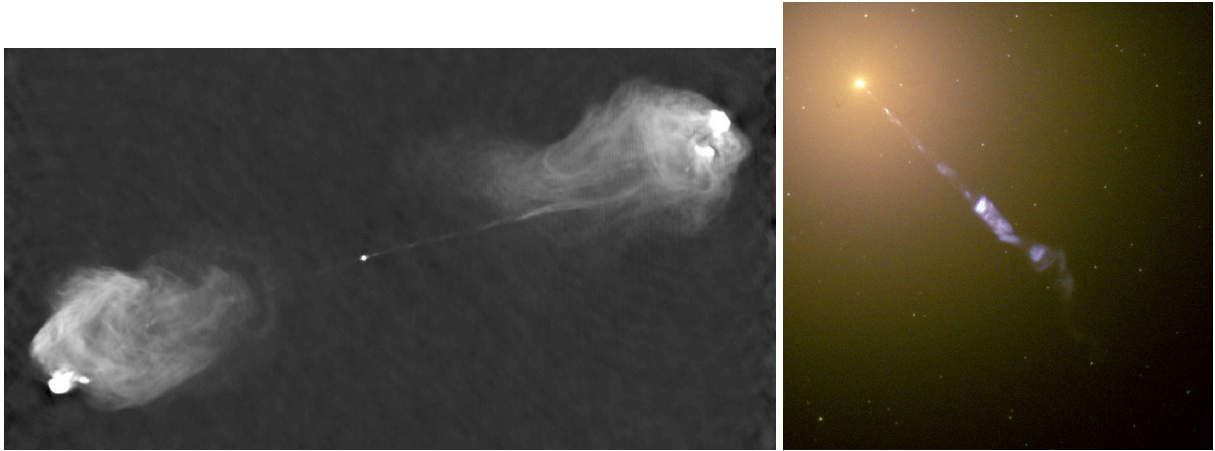


Figure 1.1: Examples of two radio galaxies. *Left:* VLA radio image of Cygnus A showing the radio lobes and the jet extending from the galaxy core to the right lobe (from Perley et al. 1984). *Right:* HST optical image of M 87 and its jet. Several knots are visible (from APOD 2015)

on the kpc scale called lobes, often connected to the central core through collimated jets (Fig. 1.1). Based on their morphology, they are divided in Fanaroff-Riley I and II classes (FR I, FR II). The former have lower radio luminosities, their jet is collimated only up to the periphery of the host galaxy and have a strong flaring in the lobes. The latter are more luminous in radio, with highly collimated jets up to the lobes and pronounced hotspots at their termination points in the lobes;

- *Quasars:* the name stands for quasi-stellar radio sources and reflects the fact that they appear in optical images as overwhelmingly bright star-like objects ($L \sim 10^{45} - 10^{49}$ erg/s). They are also called radio-loud quasi-stellar objects (QSOs) in contrast to radio-quiet QSOs. Their spectra are similar to those of Sy I galaxies, with bright broad and narrow emission lines and power-law continua. They show an excess of ultraviolet light with respect to the emission of stars with similar colors at smaller wavelengths. Their radio emission can reach up to 60% of linear polarization;
- *Blazars:* their emission is strongly and swiftly variable. They have strongly linearly polarized (30-40%) non-thermal power-law continua which cover the complete electromagnetic spectrum. Most reside in elliptical galaxies. They are historically divided in two classes, BL Lac objects (from the name of the prototype BL Lacertae) and flat spectrum radio quasars (FSRQs, also known as optically violent variables, OVVVs). The difference is based on the emission lines: very faint and narrow for BL Lac objects, strong and broad for FSRQs.

This broad range of characteristics seems to be due almost exclusively to observational effects, specifically to the angle under which an AGN is seen. The unified model was introduced by Urry & Padovani (1995). It is based on the idea that the sources are not physically different, and all share the same building blocks (Fig. 1.2):

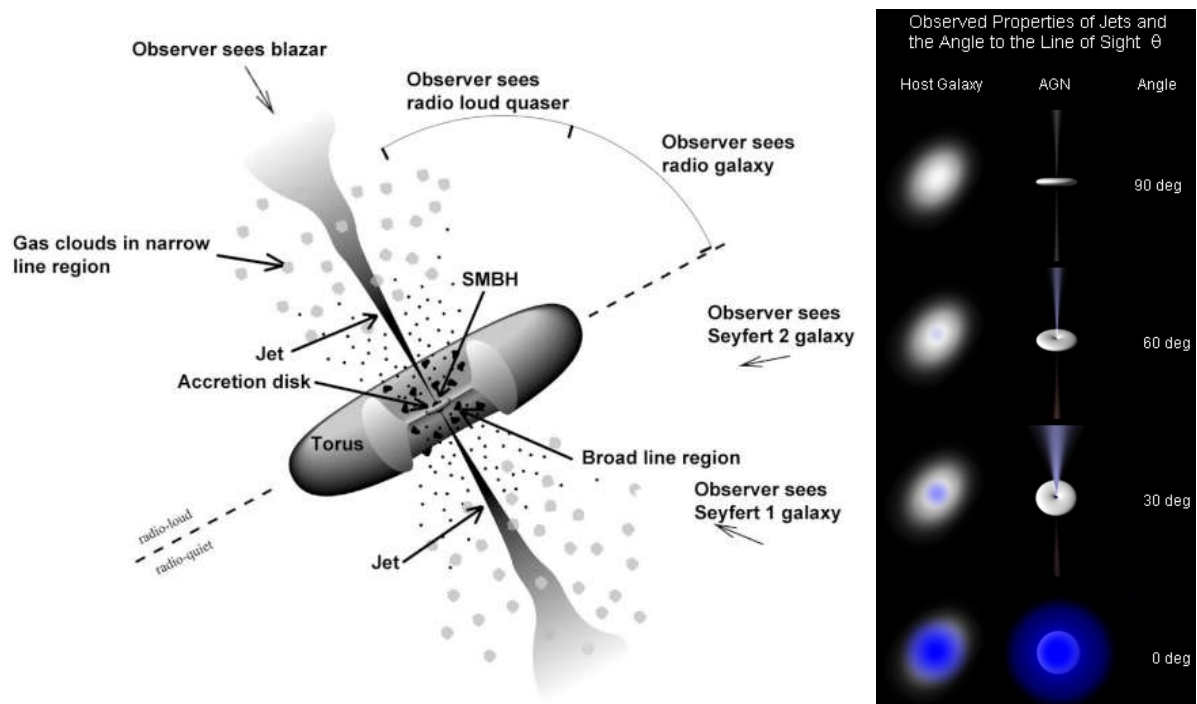


Figure 1.2: *Left:* Sketch of the AGN unification model, adapted from Urry & Padovani (1995). The various components of the AGN are indicated, together with the AGN type as function of the viewing angle. *Right:* effect of the viewing angle. From top to bottom: edge on, radio galaxy and Sy II galaxy; intermediate angle, quasar and Sy I galaxy; face on, blazar (from Wikipedia 2016).

- a SMBH at the center of the galaxy;
- a very hot accretion disk that surrounds the black hole. It is responsible for the excess of thermal emission at optical-UV frequencies that often appears in the so called “blue bump” over the non-thermal continuum;
- twin jets ejected in opposite direction perpendicular to the rotational plane of the black hole and of the accretion disk;
- a broad line region (BLR) in close proximity to the SMBH and the accretion disk;
- a thick warm dusty torus on the same plane of the SMBH and the accretion disk delimiting the BLR;
- a narrow line region (NLR) further away from the central region. The smaller line width compared to the BRL only derives by the different orbits of the clouds, since the width is caused by Doppler broadening.

This model can explain most of the features and characteristics of the AGN zoo. In this picture, AGNei which show only narrow lines, like Sy II and NLRG, are seen almost edge on (viewing angle $\theta_v \sim 90^\circ$). The dusty torus blocks the line of sight to the BLR and absorbs most of the x-ray emission. At smaller viewing angles, the torus is no more on the line of sight, so that

both the accretion disk and the BLR can be seen (Sy I and BLRG). The absence of the jets in Seyfert galaxies can be explained with an inefficient accretion process or with lack of material to be accreted. The different morphological appearances of FR I and II galaxies is probably due to the jets being subsonic and supersonic in the two cases, respectively. This can be linked to the properties of the inter stellar medium (ISM) in the host galaxies, in the first place its density. In radio-loud AGNei, often only the jet facing the observer is visible, while the counter jet is much dimmer or totally invisible. Since the velocities in play are relativistic, the emission is collimated in a very narrow cone and boosted in the direction of motion. For this reason, the luminosity of the primary jet is enhanced, while the luminosity of the counter jet appears much reduced. The presence of jets and polarized emission hints towards an efficient accretion process, which leads to the creation of the jet itself, strongly magnetized, in which synchrotron emission takes place. The more the viewing angle becomes small approaching the axis of the jet, the more the sources become luminous and variable. This is the case of quasars. Blazars are seen almost face on, under small viewing angles ($\theta_v \sim 0^\circ$) and directly into the jet. The emission is dominated by relativistic particles, and its polarization and high variability are explained by Doppler boosting of the synchrotron and other non-thermal radiations.

The present work will focus on the analysis of the TeV emission from blazars. For this reason, they will be described in greater detail in the following.

1.1 BLAZARS

Blazars are the most extreme class of AGNei. Their spectra span over 18 magnitudes in frequency, covering the whole electromagnetic spectrum from radio up to VHE γ -rays. At present, they constitute the bulk of the extragalactic TeV detections² with 56 sources, 5 of which are FS-RQs³, the others being BL Lac objects. Only 4 other objects belong to the radio galaxy class⁴ and 2 are starburst galaxies⁵.

A typical characteristic of blazars is their variability at all wavelengths on various timescales that range from years down to minutes even at the highest energies, as it has been shown, for instance, for the BL Lac objects PKS 2155-304 (Fig. 1.3 *left*, Aharonian et al. 2007b, 2009a) and Mrk 501 (Albert et al. 2007).

The spectral energy distribution (SED) of blazars is typically characterized by two broad non-thermal components (also called peaks or “bumps” because of their shape), which peak between the infrared (IR) and the x-ray and between GeV and TeV energies, respectively. The SED of PKS 2155-304 from Aharonian et al. (2009a) is shown in the right plot of Fig. 1.3 as an example. The emission is generally thought to be synchrotron radiation from ultrarelativistic

²For an up-to-date list, please visit <http://tevcat.uchicago.edu/>.

³3C 279, 4C +21.35, PKS 1441+25, PKS 1510-089 and S4 0954+65

⁴Cen A, M 87, NGC 1275 and PKS 0625-35

⁵Starburst galaxies do not belong to the AGN class. They are normal galaxies that undergo a phase of very intense star formation, often associated with the interaction or the merger with a nearby galaxy. Their TeV emission is linked to the high supernova rates and densities. At TeV energies, only M 82 and NGC 253 have been detected.

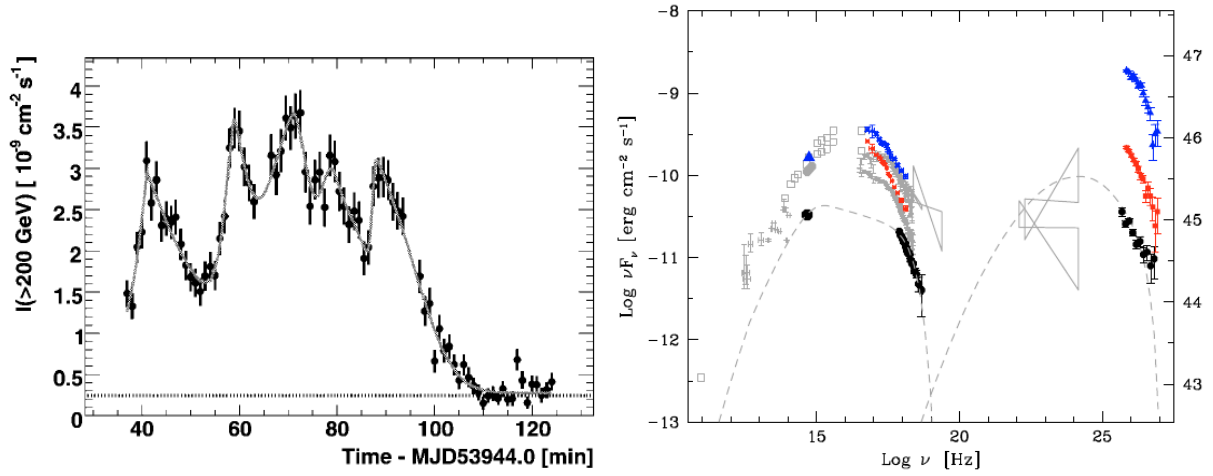


Figure 1.3: *Left:* PKS 2155-304 lightcurve in the first hours of July 28, 2006. The data are binned in 1 minute intervals (from Aharonian et al. 2007b). *Right:* simultaneous optical/x-ray/gamma-ray SED of PKS 2155-304 during the night of July 29-30, 2006 (red and blue symbols, from Aharonian et al. 2009a).

electrons, and inverse Compton (IC) of a target photon field off these electrons for the two bumps respectively. The photon field(s) can be either the produced synchrotron photons (synchrotron-self-Compton, SSC) or external photon fields such as thermal photons from stars, dust or the accretion disk (external Compton, EC).

Blazars are divided into subcategories as a function of the peak frequency of the synchrotron component:

- *low synchrotron peaked* (LSP) blazars: the low energy component peaks in the IR, at frequencies $\nu_{peak} < 10^{14}$ Hz. The x-ray emission belongs to the high energy component. All FSRQs belong to this class, together with some BL Lac objects;
- *intermediate synchrotron peaked* (ISP) blazars: the low energy component peaks at frequencies $10^{14} < \nu_{peak} < 10^{15}$ Hz, between IR and UV. The x-ray emission belongs either to the low energy component or is inbetween the two components. All ISP are BL Lac objects;
- *high synchrotron peaked* (HSP) blazars: the low energy component peaks at frequencies $\nu_{peak} > 10^{15}$ Hz. In some cases, the maximum of the emission is in the x-rays, which always belong to the low energy component. All HSP are BL Lac objects.

Similarly, BL Lac objects are also ordered as a function of the peak frequency: *low, intermediate and high frequency peaked* BL Lac objects (LBL, IBL and HBL).

Fossati et al. (1998) first identified a blazar sequence while comparing the luminosities of the two emission components as function of ν_{peak} . They discovered that the total emitted power is inversely proportional to ν_{peak} , so that FSRQs and LBLs are more luminous than HBLs (Fig. 1.4). In addition, the “Compton dominance” parameter (which is the ratio of the peak fluxes of the high energy component to the low energy component) shows that FSRQs and LBL are compton

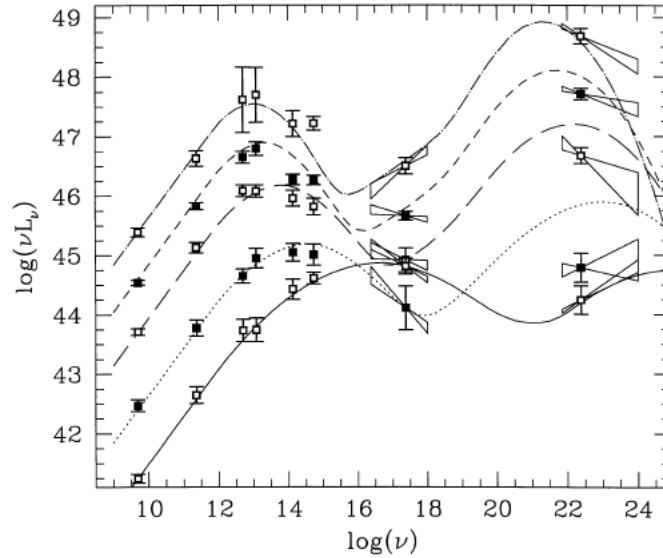


Figure 1.4: Blazar sequence as described by Fossati et al. (1998). With increasing peak frequency of the low energy component, the total luminosity decreases and the sources pass from synchrotron dominated to IC dominated.

dominated, while HBL are synchrotron dominated. This is true in general, although it is not always valid during flaring states, as shown by PKS 2155-304 in 2006 (Fig. 1.3, *right*). The blazar sequence goes monotonically from FSRQs to LBL to HBL.

The decreasing Compton dominance indicates that the primary cooling mechanism is IC for small ν_{peak} values and synchrotron for high ν_{peak} values. This can in principle be linked to the availability in the jet of photons that can be upscattered. In the case of FSRQs, the AGN is located in an ambient rich of external photon fields, as it is shown by the detection of strong emission lines in their spectra. These fields can provide a large number of photons that can be upscattered off the energetic electrons in the jet, which are cooled very efficiently in the process. The EC model seems therefore appropriate to describe these sources. According to this interpretation, the nuclei of IBL and HBL reside in an ambient poorer of external photon fields, and their emission is described by an SSC model. The difference of luminosity also derives from the denser circumnuclear environment of the LSPs, which leads to higher accretion rates and more powerful jets. This picture could even delineate an evolutionary sequence from FSRQs to HBLs governed by the gradual depletion of the circumnuclear environment (Böttcher & Dermer 2002).

CHAPTER 2

ACCELERATION, RADIATION AND ABSORPTION PROCESSES

The existence of cosmic rays (CR) with energies that can exceed 10^{20} eV rises the question about what acceleration processes are able to produce such energies. The emission of photons up to very high energies is then explained by radiative processes and particle interactions. The mechanisms involved will be briefly described in this chapter, as well as the CR and γ -ray interaction in the atmosphere and the source of opacity for γ -rays in space.

2.1 PARTICLE ACCELERATION

In an astrophysical environment, static electric fields cannot be maintained, because every electric field is immediately neutralized by opposite charges moving towards it. Particle acceleration can therefore take place only with non-stationary electric fields or with magnetic fields. The latter will be discussed in the following.

2.1.1 SECOND ORDER FERMI MECHANISM (STOCHASTIC SHOCK ACCELERATION)

In 1949, Enrico Fermi proposed an acceleration mechanism in which particles gain energy being reflected by magnetic mirrors associated with irregularities in the Galactic magnetic field (Fermi 1949). These mirrors move randomly with respect to the direction of the particle, which will interact with them in a series of head-on and following collision. If the magnetic field is entangled in a cloud of mass much larger than the particle mass (so that the collision is elastic) and of

velocity V , in the cloud rest frame the energy and three-momentum of the particle are

$$E' = \gamma_V(E + Vp) \quad p' = \gamma_V\left(p + \frac{VE}{c^2}\right) \quad \text{with} \quad \gamma_V = \left(1 - \frac{V^2}{c^2}\right)^{-1/2} \quad (2.1)$$

After interaction, the particle will have the same energy (elastic collision) and inverted impulse ($p' \cos \theta = p'_x \rightarrow -p'_x$). Back in the observer frame, the particle energy is

$$E'' = \gamma_V(E' + Vp' \cos \theta), \quad (2.2)$$

which becomes

$$E'' = \gamma_V^2 E \left[1 + \frac{2V_V \cos \theta}{c^2} + \left(\frac{V}{c}\right)^2 \right]. \quad (2.3)$$

Expanding $\gamma_V^2 \approx 1 + (V/c)^2$ one obtains the energy gain and energy loss for head-on and following collisions respectively

$$\Delta E = 2E \left[\frac{V_V \cos \theta}{c^2} + \left(\frac{V}{c}\right)^2 \right] \quad \text{and} \quad \Delta E = -2E \left[\frac{V_V \cos \theta}{c^2} - \left(\frac{V}{c}\right)^2 \right]. \quad (2.4)$$

Averaging over all angles and taking into account the head-on collision are more frequent (the probability is proportional to the relative velocity of particle and cloud) one obtains the net average gain

$$\left\langle \frac{\Delta E}{E} \right\rangle = \frac{8}{3} \left(\frac{V}{c}\right)^2. \quad (2.5)$$

For an average time between collision $t = 2L/c$ (with L the mean free path), the average rate of energy increase is

$$\frac{dE}{dt} = \frac{4}{3} \frac{V^2}{cL} E = \alpha E. \quad (2.6)$$

From the diffusion equation for particle acceleration, ignoring the diffusion and the source terms, one can find that the solution for $N(E)$ in equilibrium is

$$N(E) \propto E^{-1-(\alpha\tau)^{-1}}, \quad (2.7)$$

where τ is the characteristic time for which the particle remains in the acceleration region. Here, the power-law spectrum typical of the CR is reproduced. However, there is in principle no reason why the exponent should be the same as for the CR spectrum and that it should be the same everywhere.

This acceleration mechanism is not efficient, therefore considering it as the main source of energy leads to problems. The energy gain is of second order only $(V/c)^2$ and the mean free path of CR is known to be on the parsec scale. This means that the particle undergoes a only few collisions per year, and since the velocities of the clouds in the Galaxy are much smaller than the speed of light ($V/c \lesssim 10^{-4}$), the energy gain is very small and slow. A more efficient method is

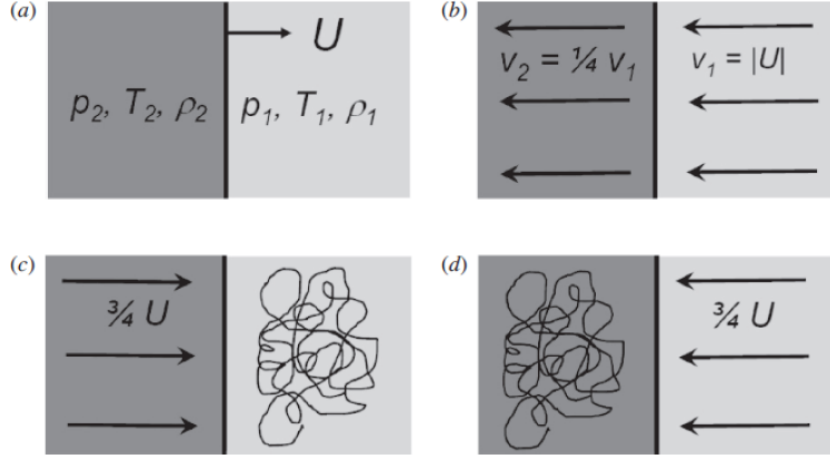


Figure 2.1: Sketch of the first order Fermi mechanism. (a) observer rest frame; (b) shock rest frame; (c) and (d) upstream and downstream rest frames, respectively.

then needed.

2.1.2 FIRST ORDER FERMI MECHANISM (DIFFUSIVE SHOCK ACCELERATION)

The second order Fermi mechanism was revised in the 1970s by several authors (e.g. Bell 1978; Blandford & Ostriker 1978) with the addition of strong shocks, which propagate in the interstellar medium with supersonic (but not relativistic) velocity much larger than the speed of sound in the medium ($U \gg c_s$)¹. The gas upstream (region 2) and downstream (region 1) the shock is formed by isotropized energetic particles and contains a turbulent and irregular magnetic field. The particles barely notice the shock, since their gyroradius is much larger than the shock thickness. The gas in the two regions can be described using the conservation of matter, momentum, and enthalpy:

$$\rho_1 v_1 = \rho_2 v_2 \quad (2.8a)$$

$$p_1 + \rho_1 v_1^2 = p_2 + \rho_2 v_2^2 \quad (2.8b)$$

$$\frac{\gamma}{\gamma - 1} \frac{p_1}{\rho_1} + \frac{v_1^2}{2} = \frac{\gamma}{\gamma - 1} \frac{p_2}{\rho_2} + \frac{v_2^2}{2}, \quad (2.8c)$$

where ρ is the density, v the particle velocity and γ the ratio of the specific heats. In the limit of strong shock, it follows

$$\frac{\rho_2}{\rho_1} = \frac{v_1}{v_2} \approx \frac{\gamma + 1}{\gamma - 1}. \quad (2.9)$$

For a fully ionized gas $\gamma = 5/3$ and hence $\rho_2/\rho_1 = 4$. In the reference frame at rest with the shock, the downstream region moves towards the shock with velocity $v_1 = U$, while the upstream region moves away from the shock with velocity $v_2 = v_1/4 = U/4$. In both the upstream and down-

¹This can easily be the case for supernova explosions, where the shock velocity is of the order of 10^4 km/s and the sound speed of the interstellar gas is of 10 km/s

stream reference frames, the isotropized gas sees the particles of the other region approaching with velocity $v_1 - v_2 = 3U/4$ (Fig. 2.1).

A particle in the downstream region can cross the shock and enter the upstream region. Here it is isotropized by the irregularities behind the shock, gaining energy in the head-on collision. If the particle returns then in the downstream region, it will be isotropized again and will gain energy again through head-on collision. For one crossing one has ($\gamma_v \approx 1$ if the shock is not relativistic)

$$E' = E + p_x \Delta v \quad \Rightarrow p_x = \frac{E}{c} \cos \theta \quad \frac{\Delta E}{E} = \frac{\Delta v}{c} \cos \theta. \quad (2.10)$$

Averaging on all possible angles of incidence of the cosmic rays approaching the shock and considering a round trip (two crossings)

$$\left\langle \frac{\Delta E}{E} \right\rangle = \frac{4}{3} \left(\frac{\Delta v}{c} \right) \quad \Rightarrow \quad \Delta v = v_1 - v_2 = \frac{3}{4} U \quad \left\langle \frac{\Delta E}{E} \right\rangle = \frac{U}{c}. \quad (2.11)$$

Here the energy gain is a first order process, since it goes linearly with the shock velocity U . For this reason it is called first order Fermi mechanism.

Let's consider now an energy increase per collision proportional to the initial energy $E = E_0 \beta$ and a probability P that the particle remains in the accelerating region after one collision. After k collisions $N = N_0 P^k$ and $E = E_0 \beta^k$. One can rewrite the two equations as

$$\frac{\ln(N/N_0)}{\ln(E/E_0)} = \frac{\ln P}{\ln \beta} \quad \Rightarrow \quad \frac{N}{N_0} = \left(\frac{E}{E_0} \right)^{\ln P / \ln \beta}. \quad (2.12)$$

Obviously, a fraction of the particles will undergo other collisions and further increase their energies. The differential increase will be

$$dN(E) \propto E^{-1 + \ln P / \ln \beta} dE. \quad (2.13)$$

The value of β can be derived from eq. 2.11, while the value of P is estimated to be

$$\beta = \frac{E}{E_0} = 1 + \frac{4}{3} \frac{\Delta v}{c} \quad P = 1 - \frac{4v_2}{c}, \quad (2.14)$$

respectively. Taking the logarithms of P and β and expanding them in series, it follows from eq. 2.9 that

$$\frac{\ln P}{\ln \beta} = \frac{\ln \left(1 - \frac{4v_2}{c} \right)}{\ln \left(1 + \frac{4\Delta v}{3c} \right)} = \frac{-\frac{4v_2}{c}}{\frac{4\Delta v}{3c}} = \frac{-U}{\frac{U}{c}} = -1. \quad (2.15)$$

Substituting into eq. 2.13 one has

$$dN(E) \propto E^{-2} dE. \quad (2.16)$$

Here, the power-law form is recovered, and the value of the index is similar to the 2.7 of the CR spectrum.

This method explains in a simple way but with excellent physical reasons why power-law energy spectra with equal index can be found in different astrophysical environments. The only requirements are a strong shock, some relativistic particles and a magnetic field. Particle acceleration up to the knee of the CR spectrum at $\sim 10^{15}$ eV can be explained by Galactic accelerators like supernovae. CR at higher energies are probably of extragalactic origin and need more powerful accelerators or other mechanisms.

2.1.3 MAGNETIC RECONNECTION

Magnetic reconnection is another kind of first order Fermi mechanism. Here the turbulence is brought not by a shock, but by the reconnection of magnetic field lines originally frozen-in in the plasma. In an infinitely conductive plasma, the particles are confined in circular orbits around magnetic field lines and will not be able to diffuse across them and mix. In the same way, the magnetic field lines will remain separate since they cannot penetrate the plasma. If plasmas carrying oppositely directed magnetic field lines are brought together, and the resistivity of the plasma is not null, a strong current sheet is established. The plasma can then diffuse and magnetic reconnection occurs, efficiently accelerating the particles.

It can be shown that the spectrum emitted via magnetic reconnection has a power-law form and that the spectral index has the same form as in eq. 2.13. Rewriting eq. 2.15 one has

$$\frac{\ln P}{\ln \beta} = -\frac{3v_2}{\Delta v} = -\frac{3}{\rho_2/\rho_1 - 1} \quad \Rightarrow \quad dN(E) \propto E^{-(1+\frac{3}{r-1})} dE, \quad (2.17)$$

where $r = \rho_2/\rho_1$ is the compression ratio. While assuming a monoatomic gas one finds $r = 4$, there are not enough constraints to derive its value for the magnetic reconnection. However, one expects a much denser output medium than the input one, so that $r \gg 1$ and the index tends to 1.

2.1.4 EXTRAGALACTIC ACCELERATORS

In chapter. 1 the main components of an AGN have been presented. The components responsible for the energy transfer from the material surrounding the black hole to the high energy particle populations are the accretion disk and the jets.

From the short time variability of the AGN emission, it follows that the central engine must be a compact object not larger than a few light days. In order to explain the AGN luminosity, a process much more efficient than nuclear reaction in transforming matter into energy must be involved. Accretion onto the central black hole can provide such high efficiencies. For accretion onto a maximally rotating SMBH, the mass to energy conversion is roughly 40%.

In order to fall onto the black hole, the accreting matter must lose angular momentum, so it collects in a flat accretion disk that rotates around the black hole. The disk is keplerian, therefore the gas moves faster in the inner than in the outer orbits. This leads to interactions between particles on different orbits and to friction-like effects that heat up the gas, transforming it into plasma. The disk emits then strong thermal radiation in UV and x-ray, originating the excess emission often seen as the “blue bump” in AGN spectra. At this point, pre-existing magnetic fields become frozen in the plasma and start to co-rotate with the disc, twisting around the rotational axis. Two jets are formed in opposite directions. Disk material can enter the jets and be accelerated to very high energies. The power extracted from the accreting material is estimated to be

$$\mathcal{L} \sim B_{disk}^2 R_{disk}^2 \sqrt{\frac{GM}{R_{disk}}} \sim 2 \times 10^{46} \left(\frac{B_{disk}}{10^3 \text{G}} \frac{M}{10^9 M_{\odot}} \right)^2 \text{erg/s} \quad (2.18)$$

with an efficiency around 12%. In other models, the power can be extracted from the rotational energy of the black hole, slowing it down, with an efficiency of around 9%. Possibly both mechanisms contribute to the total jet power.

The radiation in the rest frame of the emitting region is isotropic. However, it is known from measurements of superluminal motion in the jets that the velocities in play are relativistic. The energy of the emission is therefore Doppler boosted by a factor

$$\delta = \frac{E}{E_{iso}} = \frac{1}{\gamma(1 - \beta \cos \theta)} \quad (2.19)$$

and beamed in a cone of half-opening angle $\theta = 1/\gamma$. The observed energy flux is boosted by a factor δ^3 , while the timescale of the intrinsic variability is instead shortened of a factor $1/\delta$.

While the low energy component of the blazar emission is well established to be synchrotron radiation (sec. 2.2.1) from electrons, the high energy component can be described by hadronic or leptonic models, depending on whether or not protons can be accelerated to sufficiently high energies to reach the threshold for $p + \gamma \rightarrow \pi$ production. In the first case, the high energy component is dominated by cascades initiated by pion and pair production (sec. 2.2.5) from $p\gamma$ interactions, as well as synchrotron radiation from protons, π^{\pm} , and μ^{\pm} (*hadronic* models). In the latter case, it is dominated by the emission from ultra-relativistic electrons and/or pairs (*leptonic* models). For a review of emission models, as well as acceleration processes in the jets, see e.g. Böttcher (2007, 2012) and references therein.

Leptonic models explain the high energy emission via Compton upscatter of photons off ultrarelativistic electrons. If the photons field is the one produced by the electrons through synchrotron radiation, the process is called synchrotron-self-Compton (SSC), if it is an external one, external Compton (EC, sec. 2.2.3). In order to explain the rapid variability, small emission regions are needed. In many cases, the compactness would prevent the γ -rays to escape from it, so that Doppler boosting is required. However, it is difficult to explain variability on the minutes time scale even with large Doppler factors, because causality requires a size of the emitting region that might be smaller than the Schwarzschild radius of the central SMBH. For this reason it has been suggested that the γ -ray emission region could be only a small spine of ultrarelativistic

plasma within a larger, slower-moving jet (jet -or minijet- in a jet models). Especially during flares, the particle population cannot be considered stationary, and the time evolution of the energetics due to cooling must be taken into account. The simplest leptonic models consider that the whole emission comes from a single zone (*single-zone leptonic* model).

Hadronic models require magnetic fields on the order of several tens of Gauss in order to confine the protons inside the emission region, whereas $B \lesssim 1$ G for leptonic models. Electromagnetic cascades initiated by π^0 and π^\pm decay generate featureless γ -ray spectra, while those initiated by proton-synchrotron and μ^\pm -synchrotron photons produce a double-bumped γ -ray spectrum. These emissions are responsible for the high energy component of the SED, whereas the low energy component is still dominated by e^\pm -synchrotron emission.

Usually, leptonic single zone SSC models fit well the SED of IBLs and HBLs, while the use of EC emission is better suited for FSRQs and LBL. However, in some cases an EC or hadronic contribution to the SSC emission helps describing the blazar emission with more physical parameter values.

2.2 RADIATIVE PROCESSES

Photons more energetic than a few keV (~ 10) are no more of thermal origin. In order to emit such photons, thermal black-body radiation would require temperatures greater than a few tens of millions degree, which are practically impossible to reach outside massive stars. Instead, non-thermal processes involving highly energetic particles come in play. In the following, the most significant processes will be briefly described. A more detailed treatment can be found in, e.g., Heitler (1954); Blumenthal & Gould (1970); Rybicki & Lightman (1979); Longair (1981); Pohl (2002).

2.2.1 SYNCHROTRON EMISSION

Charged particles moving in a magnetic field feel an acceleration perpendicular to the field and will therefore radiate. For low energy particles, this process is known as cyclotron radiation. Relativistic particles, instead, undergo a more complex process called synchrotron radiation. The energy losses for an isotropic electron population, averaging over the angles, are given by

$$-\left(\frac{dE}{dt}\right)_{sync} = P_{sync} = \frac{4}{3}\sigma_T c \beta^2 \gamma^2 U_B \quad (2.20)$$

where σ_T is the Thomson cross section, c the speed of light, $\beta = v/c$, γ the particle Lorentz factor and $U_B = B^2/8\pi$ is the magnetic energy density. The emission is directly proportional to β^2 and γ^2 . Due to the relativistic motion of the particles, the emission is beamed in a cone with opening

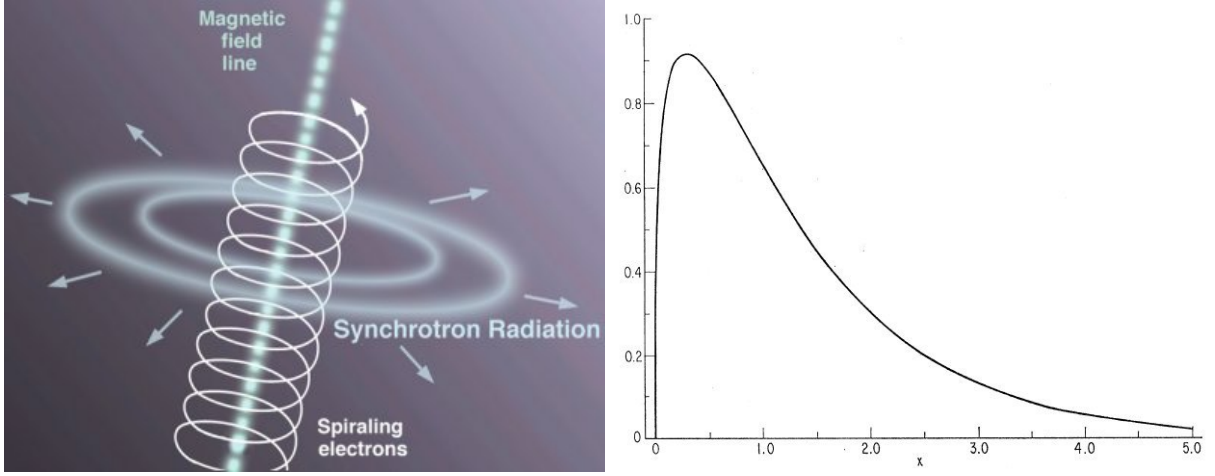


Figure 2.2: *Left:* sketch of the synchrotron process. *Right:* synchrotron emission from a single electron as a function of $x = \nu/\nu_c$ (from Blumenthal & Gould 1970).

angle $1/\gamma$. For a single electron, the spectral energy distribution is

$$I(\nu) = 1.8 \frac{\sqrt{3}e^3 B_{\perp}}{mc^2} \left(\frac{\nu}{\nu_c}\right)^{1/3} \exp\left(-\frac{\nu}{\nu_c}\right) \quad (2.21)$$

where B_{\perp} is the normal component of the magnetic field and

$$\nu_c = \frac{3eB_{\perp}}{4\pi mc} \gamma^2 \simeq 16 \left(\frac{B}{mG}\right) \left(\frac{E}{\text{GeV}}\right)^2 \text{GHz} \quad (2.22)$$

is the characteristic synchrotron frequency. The peak of the emission is at $\nu_{max} = 0.29\nu_c$ (Fig. 2.2). For the more realistic scenario of a power-law electron distribution of the form $N(E)dE \propto E^{-p}dE$, one will obtain a synchrotron spectrum with the same shape

$$I(\nu) \propto B^{s+1} \nu^{-s} \quad (2.23a)$$

$$\text{with the spectral index } s = \frac{p-1}{2}. \quad (2.23b)$$

The differential photon index will be $\Gamma = s + 1 = (p + 1)/2$. The total spectrum is given from the superposition of the emission of electron at different energies (Fig. 2.3).

The measurement of the synchrotron spectral index allows one to derive the energy spectrum of the underlying electron distribution. The cooling time for synchrotron radiation is given by

$$\tau = \left(\frac{dE}{dt} \cdot \frac{1}{E}\right)^{-1} = \frac{3mc}{4\sigma_T U_B \gamma} = \frac{3}{\sigma_T} \sqrt{\frac{3\pi emc}{B^3}} \nu^{-1/2}. \quad (2.24)$$

In the frequency dependent notation, the cooling time only depends on the emitted energy and not

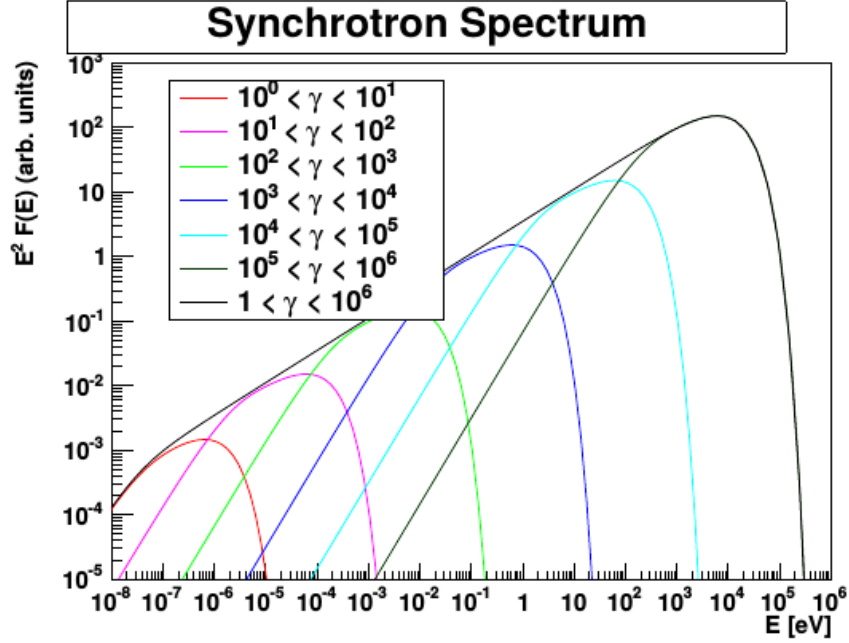


Figure 2.3: Synchrotron spectrum emitted by a power-law electron population. The contribution of electrons at different energies is visible (from De Naurois 2012).

on the electron energy. It is an “universal” measurement, provided that electrons exist energetic enough to emit at the given frequency. At high energies the cooling time is much shorter than at low energies, where the emission is a superposition of young and old electrons.

The synchrotron emission is also linearly polarized, theoretically up to 75%. The electric vector of the polarized emission lies perpendicular to the projection of the magnetic field onto the plane of the sky. The polarization is given by

$$\Pi = \frac{p + 1}{p + \frac{7}{3}}. \quad (2.25)$$

2.2.2 INVERSE COMPTON EMISSION

In the Compton scattering, a high energy photon up-scatters a low energy electron. If the photon energy in the electron rest frame is smaller than the electron rest mass mc^2 , the scattering is elastic and the photon energy remains almost unchanged (Thomson limit). If the energy is comparable to (or higher than) mc^2 , the scattering will be inelastic and a significant part of the energy will be transferred to the electron (Klein-Nishina limit). The energy transfer is given by

$$\epsilon_f = \frac{\epsilon_i}{1 + \frac{\epsilon_i}{mc^2}(1 - \cos \theta)} \quad (2.26)$$

where ϵ_i and ϵ_f are the initial and final photon energies. In the Thomson limit $\epsilon_i \ll mc^2$ and $\epsilon_f \approx \epsilon_i$.

The full relativistic treatment for the differential cross section of unpolarized radiation is given by the Klein-Nishina formula

$$\frac{d\sigma}{d\cos\theta} = \frac{3}{4}\sigma_T \frac{\epsilon_f^2}{\epsilon_i^2} \left(\frac{\epsilon_i}{\epsilon_f} + \frac{\epsilon_f}{\epsilon_i} - \sin^2\theta \right). \quad (2.27)$$

In the low energy limit, it reduces to the classical expression of the Thomson cross section ($\sigma_{KN} \approx \sigma_T$). In the ultrarelativistic limit ($\epsilon_i \gg mc^2$), one has

$$\sigma_{KN} = \frac{3}{8}\sigma_T \frac{1}{x} \left(\ln 2x + \frac{1}{2} \right) \quad \text{with } x = \frac{\epsilon_i}{mc^2}. \quad (2.28)$$

The quantum effects diminish the cross section with increasing photon energy.

The Inverse Compton (IC) radiation is the same process in opposite direction: a relativistic electron up-scatters a low energy photon. In the electron rest frame, the photon has energy $\sim \gamma\epsilon$. The Thomson limit holds for

$$4\gamma_e\epsilon < mc^2 \quad (2.29)$$

and the photon energy after the scatter will still be $\gamma\epsilon$. The transformation back in the observer rest frame gives another factor γ . The maximal scattered photon energy occurs for head-on collisions and is

$$\epsilon_{f,T} = 4\gamma_e^2\epsilon_i, \quad (2.30)$$

while the average energy from scatter on an isotropic photon field with mean energy ϵ_0 is

$$\bar{\epsilon}_T = \frac{4}{3}\gamma_e^2\epsilon_0. \quad (2.31)$$

In the Klein-Nishina limit, the photon energy after scatter is mc^2 in the electron rest frame. Back in the observer rest-frame one has

$$\epsilon_{f,KN} = \gamma_e mc^2 \quad (2.32)$$

which is independent from the initial photon energy. The electron loses most of its energy in a single interaction. The IC radiation is very efficient in the Thomson limit, allowing for enormous increase of energy. Cosmic microwave background (CMB) photons ($\epsilon \sim 6 \times 10^{-4}$ eV) can easily be up-scattered to an energy of 1 TeV by a 10 TeV electron ($\gamma = 2 \times 10^7$). In the Klein-Nishina limit, the radiation is less efficient, resulting in a steepening of the spectral energy distribution, and is a longer cooling time for the high energy electrons.

The electron emitted power in an isotropic photon field of energy density U_{ph} is

$$-\left(\frac{dE}{dt}\right)_{IC} = P_{IC} = \frac{3}{4}\sigma_T c \beta^2 \gamma^2 U_{ph}. \quad (2.33)$$

This equation has the same form as eq. 2.20. If synchrotron and IC radiation are emitted by the

same population of electrons, then the following relation is valid

$$\frac{P_{sync}}{P_{IC}} = \frac{U_B}{U_{ph}}. \quad (2.34)$$

This is a general result that holds for arbitrary electron energies, as long as the Thomson limit is fulfilled.

For a power-law electron distribution $N(E)/dE = KE^{-p}$, the radiated energy is

$$I(E) = \frac{2}{3}\sigma_T c U_{ph} K E^{-s} (mc^2)^s \quad (2.35a)$$

$$\text{with the spectral index } s = \frac{p-1}{2}. \quad (2.35b)$$

The energy dependence is the same as for the synchrotron emission (eq. 2.23a), the two spectra have the same shape. In the Thomson limit one has

$$\frac{dN}{dt dV d\epsilon_f} \propto \sigma_T c K n_{ph} \epsilon_f^{-s-1}. \quad (2.36)$$

Similarly as for the synchrotron case, the cooling time for IC radiation in the Thomson limit is

$$\tau_T = \left(\frac{dE}{dt} \cdot \frac{1}{E} \right)^{-1} = \frac{3mc}{4\sigma_T U_{ph} \gamma}. \quad (2.37)$$

In the Klein-Nishina regime, the cooling is almost independent from the energy and actually slowly increases with it

$$\tau_{KN} = \frac{2mc}{\sigma_T U_{ph}} \ln \left(2\gamma + \frac{1}{2} \right). \quad (2.38)$$

2.2.3 SYNCHROTRON SELF COMPTON AND EXTERNAL COMPTON EMISSION

In a very high energy emitting source, electrons naturally undergo cooling via both synchrotron and IC. If the photon field for the IC scatter is the synchrotron radiation itself, the process is called synchrotron self Compton (SSC) emission. From eq. 2.20 and 2.33 it follows

$$-\left(\frac{dE}{dt} \right)_{IC} = -\left(\frac{dE}{dt} \right)_{sync} \times \frac{U_{ph-sync}}{U_B} \propto -\left(\frac{dE}{dt} \right)_{sync}^2 \times \frac{1}{U_B}. \quad (2.39)$$

Hence, in the Thomson limit, the total luminosities of the two components have a square relation. It also follows from eq. 2.31 and 2.32 that the peaks of the two distributions will differ of a factor γ_{max}^2 and $m_e c^2 \gamma_{max}$ in the Thomson and Klein-Nishina limits, respectively.

If the IC emission involves other photon populations different from the synchrotron radiation, the process is called external Compton (EC). In this case, the ratio between the luminosities

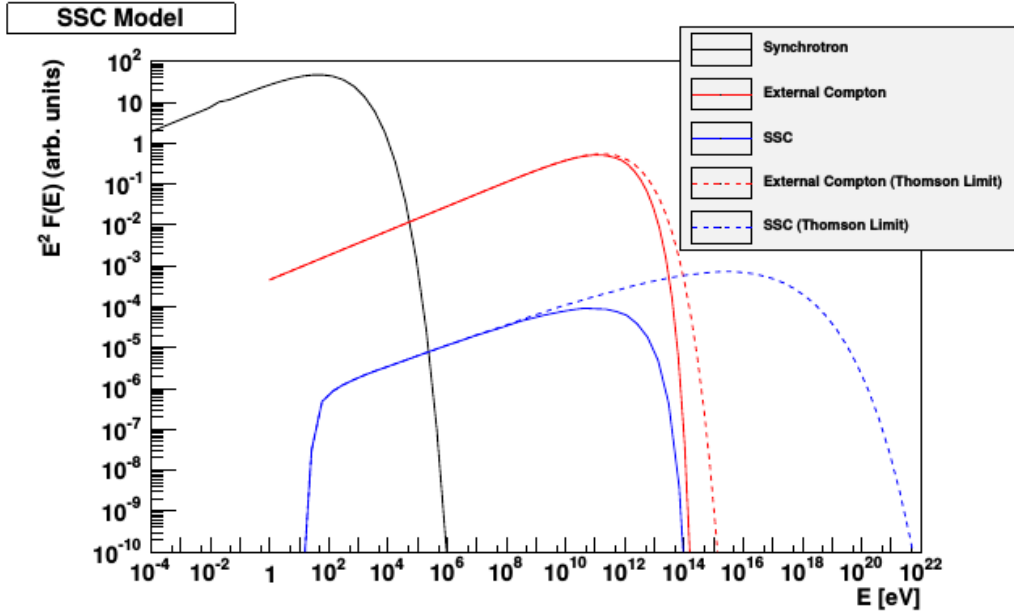


Figure 2.4: SSC (blue) and EC (red) emission using the Thomson approximation (dashed curve) and the full Klein-Nishina treatment (solid curves). From De Naurois (2012).

is linear, given by eq. 2.34. In the case of AGN, external photon fields can be accretion disk photons, jet synchrotron emission reflected off clouds in the circumnuclear material, infrared emission from a dust torus around the central engine, or even CMB photons.

Examples of SSC and EC spectra are shown in Fig. 2.4 for both Thomson approximation (dashed curve) and full Klein-Nishina treatment (solid curves).

2.2.4 BREMSSTRAHLUNG (FREE-FREE EMISSION)

The Bremsstrahlung (also called free-free emission) is due to the acceleration of a charged particle in the Coulomb field of another particle, usually a nucleus. The emission is zero for two particles of the same kind (e.g. electron-electron or proton-proton) because the dipole moment is proportional to the center of mass, which is a constant of the motion. Particles of different nature must be therefore involved. The total energy loss rate from the full quantum relativistic treatment is

$$-\left(\frac{dE}{dt}\right)_{br} = \frac{Z(Z+1.3)e^6 N_i}{8\pi^2 \epsilon_0^3 m^2 c^4 h} \left[\ln\left(\frac{183}{Z^{1/3}}\right) + \frac{1}{8} \right] \times E \quad (2.40)$$

where Z is the atomic number of the nucleus, N_i the space density of the nuclei in the laboratory frame and ϵ_0 the electric constant. The energy density spectrum is almost independent from the frequency up to $h\nu = (\gamma - 1)mc^2$, which corresponds to the electron transferring all its kinetic energy in a single collision. The differential photon spectrum is

$$I(\nu) d\nu = P(\nu) h\nu N_i d\nu \implies P(\nu) \propto 1/\nu \quad (2.41)$$

Being the energy spectrum flat, this implies that very energetic electrons deposit half of their energy in one or two high energy photons.

A radiation length over which the electron loses a fraction $1/e$ of its energy is defined as

$$\xi_{br} = \frac{716 M_A}{Z(Z + 1.3)[\ln(183Z^{-1/3}) + 1/8]} [g cm^{-2}], \quad (2.42)$$

with M_A the nucleus atomic weight. A critical energy E_c is defined as the energy for which bremsstrahlung losses equal ionization losses. In the air, $\xi_{br} = 36.7 g cm^{-2}$ and $E_c = 83 MeV$.

2.2.5 PAIR PRODUCTION

Pair production is the creation of an electron-positron pair from the interaction of one photon with another particle. One-photon pair production cannot happen because of momentum conservation. In outer space, usually two photons are involved ($\gamma\gamma$ absorption). The total energy of the photons must be larger than the energy threshold for this process, $2m_e c^2$, twice the rest mass of the electron. In astrophysics, pair production of very high energy γ -ray photons on CMB photons reduces the size of the observable Universe as the energies increases.

In the atmosphere, pair production usually involves a high energy photons ($E > 2m_e c^2$) and an ambient nucleus. A radiation length is defined as

$$\xi_{pair} = \frac{M_A}{N_0 \sigma_{pair}} [g cm^{-2}], \quad (2.43)$$

with M_A the nucleus atomic weight, N_0 the Avogadro's number and σ_{pair} the pair production cross section. The radiation lengths for pair production and for bremsstrahlung of ultrarelativistic electrons are similar ($\xi_{pair} \approx \frac{9}{7} \xi_{br}$). This reflects the similarity of the two processes according to quantum electrodynamics.

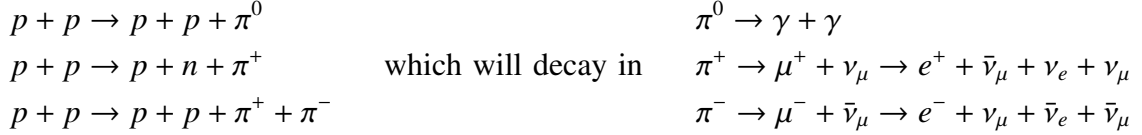
2.2.6 ELECTRON-POSITRON ANNIHILATION

The electron-positron annihilation is the opposite process than pair production. In this case an electron and a positron will interact to produce two photons. Here, no energy threshold must be satisfied and the produced photons will have an energy of at least mc^2 . For this reason, electron-positron annihilation will always take place in Klein-Nishina regime.

2.3 HADRONIC INTERACTIONS AND γ -RAY PRODUCTION

The radiative processes described above are usually dominated by the emission of low mass leptons. This is due to the fact that the emitted power is inversely proportional to the square of the particle mass. γ -ray emission from hadronic high mass particles normally occurs via decay

of unstable particles generated in hadronic interactions. These interactions are usually inelastic scattering of protons with nuclei and produce mesons (π^0, π^+, π^-, K), nucleons (p, n), hyperions ($\Delta, \Lambda, \Sigma, \Xi$) and fragments of the target nucleus. The most common process is the creation of pions:



Neutrinos hence provide the signature of hadronic interactions. Due to neutrino oscillations, the original ratio of the flavors is canceled. The fluxes of neutrinos on Earth are identical for the three flavors.

The production of neutral pions is extremely important for very high energy γ -ray production. A kinetic energy threshold of 280 MeV is necessary for the π^0 production ($m_{\pi^0} = 135$ MeV). The pion takes on average a fraction $\kappa \sim 0.17$ of the kinetic energy. It decays almost instantly ($\tau \sim 8 \times 10^{-17}$ s) in two photons with energy (in the pion rest frame)

$$E_\gamma = \frac{1}{2}m_\pi c^2 = 67.5 \text{ MeV}. \quad (2.44)$$

Below this energy, the hadronic contribution to the γ -ray emission is practically zero. At high energies, the γ -ray spectrum closely follows the shape of the parent proton spectrum. The mean photon energy is $\sim E_p/10$.

2.4 VHE ASTRONOMY

Any electromagnetic radiation more energetic than a few eV is completely absorbed by the atmosphere. Satellite or balloon experiments are therefore required for observations above these energies. Starting at a few tens of GeV, the γ -ray photon flux is so low that an increasing detection area is required in order to detect a significant number of events in a reasonable amount of time. Currently, it is not feasible to send into space satellites with collection areas larger than a few square meters. For this reason, observations at VHE must rely on ground based telescopes and exploit other detection techniques. In this section, the processes that allow for ground based observations of γ -ray sources are described. Opacity and absorption of VHE radiation in space are discussed as well.

2.4.1 AIR SHOWERS

A VHE particle entering the atmosphere will interact with the atmospheric nuclei and will produce secondary particles via electromagnetic, strong and weak interactions. Depending on the

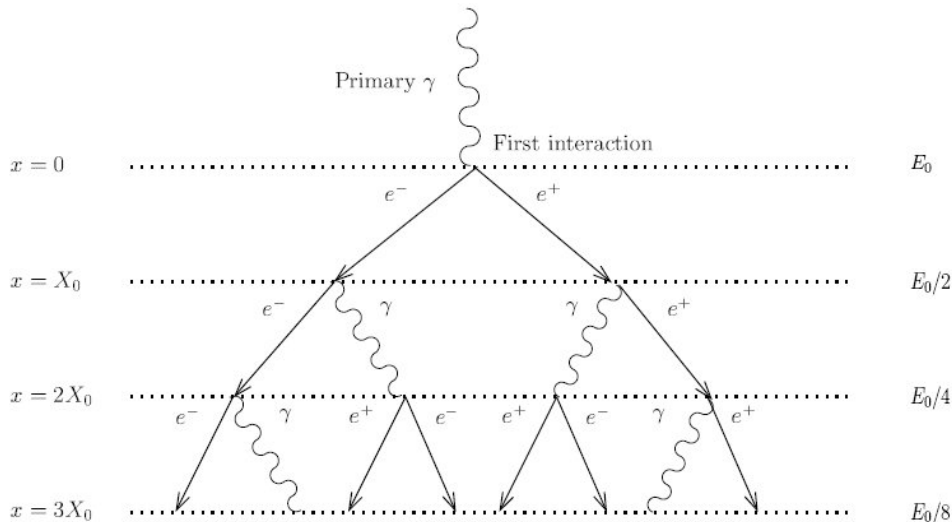


Figure 2.5: Schematic shower development as in the simple model by Heitler (1954). Only Bremsstrahlung and pair production are considered, with equal radiation length and equipartition of the energy between the particles.

nature of the primary particle, either electromagnetic or hadronic showers will generate. The former are created by γ -ray photons, electrons, positrons or high energy neutrinos, the latter from cosmic rays (CR - protons, α -particles and heavier nuclei) and constitute almost the totality of the events. Electromagnetic showers are only a minor fraction, around 0.2%.

The simplest shower development is obtained for electromagnetic events. Here, the main processes involved are: Bremsstrahlung and pair production in the Coulomb field of the atmospheric nuclei, e^\pm Coulomb multiple scattering, and e^\pm energy losses via ionization and atomic excitation. Energy losses are dominant below the critical energy $E_c = 83$ MeV (in the air) and lead to a rapid suppression of the shower. The only particles involved are photons and e^\pm .

2.4.1.1 ELECTROMAGNETIC SHOWERS

The first and easiest model for the development of electromagnetic showers was proposed by Heitler (1954): for simplicity, it is assumed that every particle loses half of its energy at every interaction and that the radiation lengths of bremsstrahlung and pair production are exactly the same ($\xi = \xi_{pair} = \xi_{br}$). The distance for which a particle loses half of its energy is $R = \xi \ln 2$. The model is depicted in Fig. 2.5.

In the case of a γ -ray photon² of energy E_0 , an e^\pm pair is created at the first interaction, each particle with energy $E_0/2$. After the same distance $R = \xi \ln 2$, the e^+ and e^- will produce a γ -ray each via bremsstrahlung, with energy $E_0/4$. At this point, two photons and two particles are left, all with energy $E_0/4$. Everyone of them will undergo the same interactions again and again, the

²For e^\pm the development is the same, only the first interaction is bremsstrahlung and take place slightly higher in the atmosphere.

number N of photons and particle will increase exponentially ($N(n) = 2^n$ after n interactions, with energy $E_n = E_0/2^n$) and a shower will generate. On average, the shower consists of $2/3$ e^\pm and $1/3$ photons. When the critical energy E_c is reached, ionization losses will become predominant and the shower will die out. The maximum shower depth is therefore given for $E_{n_{max}} = E_c$

$$E_{n_{max}} = \frac{E_0}{2^{n_{max}}} \equiv E_c \quad \implies \quad N(n_{max}) = 2^{n_{max}} = \frac{E_0}{E_c} \quad \implies \quad n_{max} = \frac{\ln(E_0/E_c)}{\ln 2}. \quad (2.45)$$

Hence, the number of particles in the shower is proportional to energy E_0 of the primary γ -ray and the depth of the maximum is proportional to its logarithm. For a 1 TeV photon, $n_{max} = 13.6$, the typical height of the first interaction ~ 25 km, the maximal depth ~ 8 km and the electromagnetic shower evolves in $\sim 50\mu\text{s}$.

2.4.1.2 HADRONIC SHOWERS

Hadronic interaction in the atmosphere are more complex than electromagnetic interactions. The proton or nucleus are most likely completely destroyed and generate several different particles. The largest fraction are mesons like pions (π^\pm , π_0), but also kaons (K), nucleons (p , n) and hyperions (Δ , Λ , Σ and Ξ), together with nuclear fragments. They lead to different shower components:

- hadronic component (nuclear fragments, nucleons, π^\pm , K mesons) that has an increased probability of new interactions with the atmospheric nuclei before the decay thanks to the relatively long lifetime of the particles ($\tau_{\pi^\pm} = 2.6 \times 10^{-8}$ s);
- electromagnetic component (mostly from $\pi_0 \rightarrow \gamma\gamma$ decay) that will develop in the same way described in the previous section;
- muonic component (from decay of charged mesons π^\pm and K^\pm) that loses energy mostly through ionization losses. Since most muons are created with high energy, they can reach the ground without decaying. For this reason, they are called the hard component of the cosmic rays;
- atmospheric neutrinos (from decay of charged mesons and muons π^\pm , K^\pm and μ^\pm).

Hadronic showers (Fig. 2.6) are characterized by a different energy distribution among the particles than in the electromagnetic showers. They also are ignited deeper in the atmosphere due to a larger radiation length of the hadrons (85 g cm^{-2} vs. 36.7 g cm^{-2}). The involvement of the strong interaction leads to a higher transverse momentum transferred to the generated particles. This has as a consequence that hadronic shower have a much larger lateral development and are more irregular (due to the several sub-showers components) than electromagnetic showers. In addition, a consistent part of the initial energy is lost in the creation of new particles like muons, other mesons, and secondary hadrons.

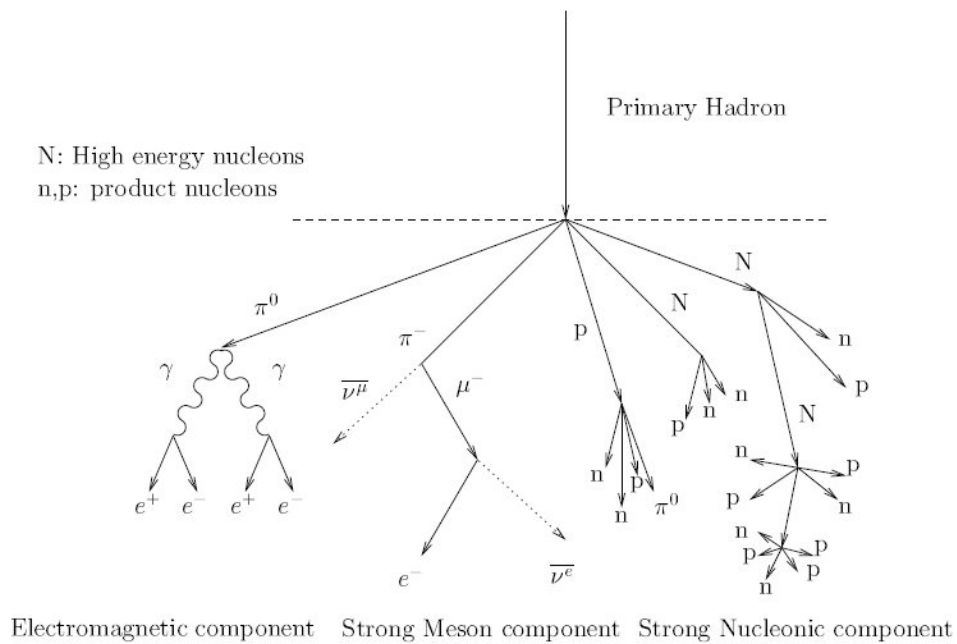


Figure 2.6: Schematic representation of the different interactions occurring in a hadronic shower.

2.4.2 CHERENKOV EMISSION

When relativistic particles move through a medium with a velocity greater than the phase velocity of light in said medium (so that $v > c/n$, with n the refractive index of the material), they emit Cherenkov radiation. This is the case for the particles generated in the electromagnetic and hadronic showers. The light is emitted along the path of the particle and propagates in a direction normal to a cone with opening angle Θ_C , so that

$$\cos \Theta_C = \frac{1}{\beta n} \approx \frac{1}{n} \quad \left(\text{for } \beta = \frac{v}{c} \approx 1 \right). \quad (2.46)$$

In the air, typical opening angle values are $\sim 1^\circ$ - 2° . Since $\cos \Theta_C < 1$, it must be $\beta > 1/n$ and an energy threshold follows

$$E_{min} = \gamma_{min} mc^2 = \frac{mc^2}{\sqrt{1 - n^{-2}}}. \quad (2.47)$$

Cherenkov emission is therefore dominated by low-mass particles. The spectrum is continuous and the loss rate per unit of path length is

$$\frac{dE(\omega)}{dx} = \frac{\omega e^2}{4\pi\epsilon_0 c^3} \left(1 - \frac{c^2}{n^2 v^2} \right) \quad (2.48)$$

The emission peaks in the UV region, but below 300 nm it is almost completely absorbed by the atmosphere. Above this wavelength, the average transmission is around 75%.

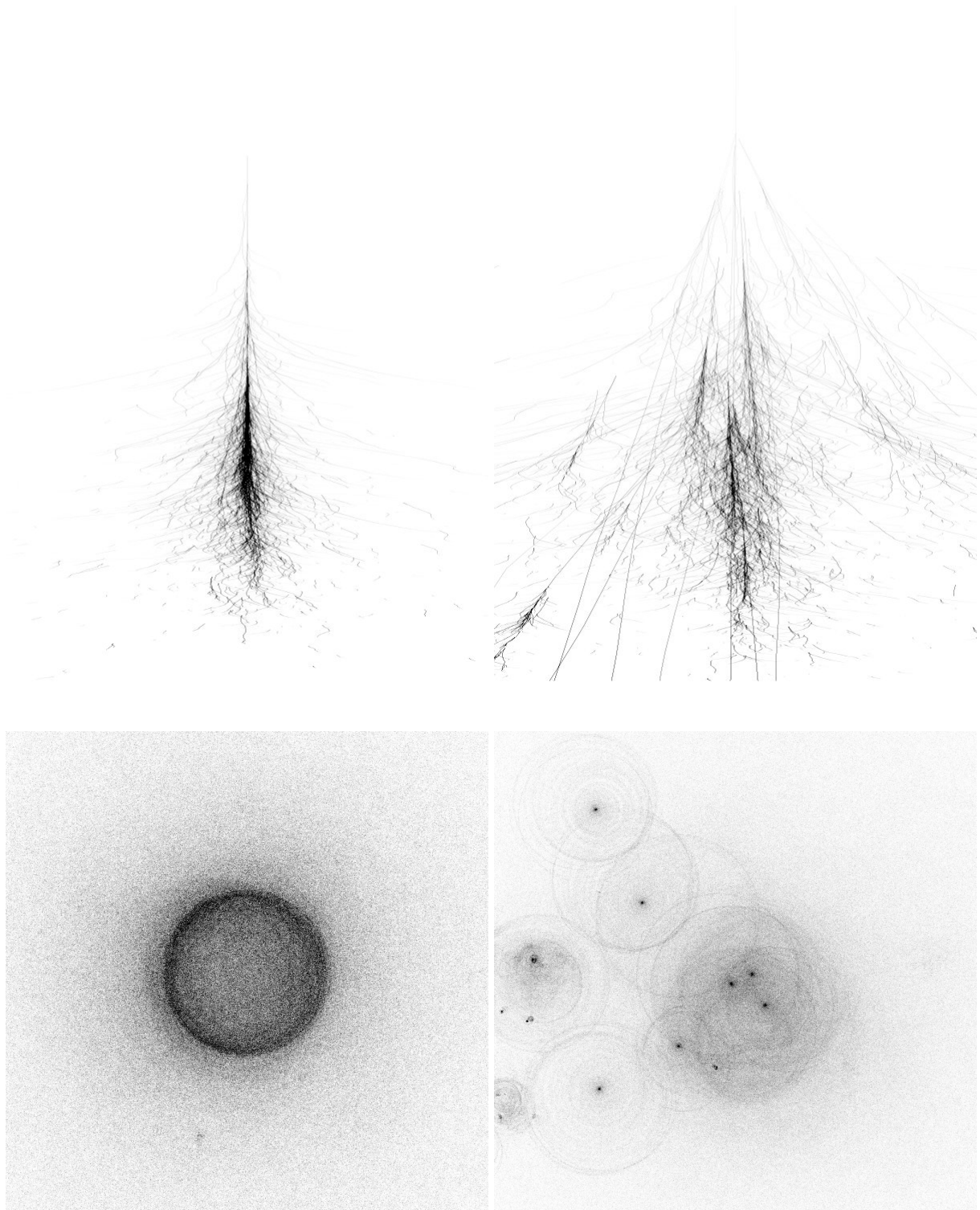


Figure 2.7: Longitudinal and lateral shower development of a 300 GeV photon (*left*) and of a 1 TeV proton (*right*). The energies are different to obtain the same amount of emitted Cherenkov light in the two cases. The figures on the top panels have an extension of 600 m in width and 27 km in height, while those in the bottom panels cover an area of $800 \times 800 \text{ m}^2$ (Bernlöhr 2000).

The radius of the Cherenkov light cone on the ground depends on the altitude of the emission. For electromagnetic showers the light is focused in a ring-shaped homogeneous distribution with a maximum radius of about ~ 150 m around the shower axis (Fig. 2.7, *left*). The intensity of the light decreases towards the axis and only low altitude emission contributes.

In the right panels of Fig. 2.7 the more irregular development of the hadronic showers can be seen. The Cherenkov light is more spread and is clustered around several sub-showers.

2.4.3 EXTRAGALACTIC BACKGROUND LIGHT (EBL)

The space is filled with a diffuse extragalactic background radiation that spans all the electromagnetic spectrum from radio to gamma-ray energies. It is an unavoidable source of opacity for the propagation of high energy CR and γ -rays. The largest flux component is the CMB, the thermal blackbody radiation that originated from the primeval plasma. It has been well characterized in all its aspects (spectrum, spatial distribution, photon density evolution) thanks to its flux dominance over the foreground emission of the Galaxy at the same wavelengths. Because of its large number density, every photon more energetic than 100 TeV will be absorbed after a very short mean free path.

From the point of view of γ -ray astronomy, two other components are of primary importance: the cosmic far-infrared background (CIRB) and the extragalactic background light (EBL) from UV to the near infrared. The former is light emitted by dust, the latter is direct stellar emission. Due to intense foreground radiation at these wavelengths, the characterization of the two component is very difficult. In addition, the time evolution of their number densities cannot be determined with a simple scaling relation as for the CMB, because these radiations are progressively generated by galaxies and AGN, especially for $z < 1$. Lower limits can be obtained from galaxy counts. Direct measurements usually provide upper limits. Upper limits can be derived also from observations of VHE extragalactic sources (e.g. Aharonian et al. 2006c, 2007a; Mazin & Raue 2007; Abdo et al. 2010; H.E.S.S. Collaboration et al. 2013; Biteau & Williams 2015). In order to estimate the correct EBL and CIRB intensities, modeling of galaxy evolution is required. Several authors used different empirical approaches to the modeling in order to predict the overall shape of the spectral energy distribution of the background radiation in the local Universe and its evolution over time. These can be divided in four groups:

- forward evolution, in which cosmological initial conditions are set and the galaxy are let evolved using semi-analytical models of galaxy formation (e.g. Primack et al. 2005; Gilmore et al. 2012);
- backward evolution, in which the existing galaxy populations are extrapolated backwards in time (e.g. Stecker et al. 2006; Franceschini et al. 2008);
- inferring the evolution of the galaxy populations over a range of redshifts, in which quantities derived from observations (e.g. the star formation rate density) are used (e.g. Finke et al. 2010; Kneiske & Dole 2010);

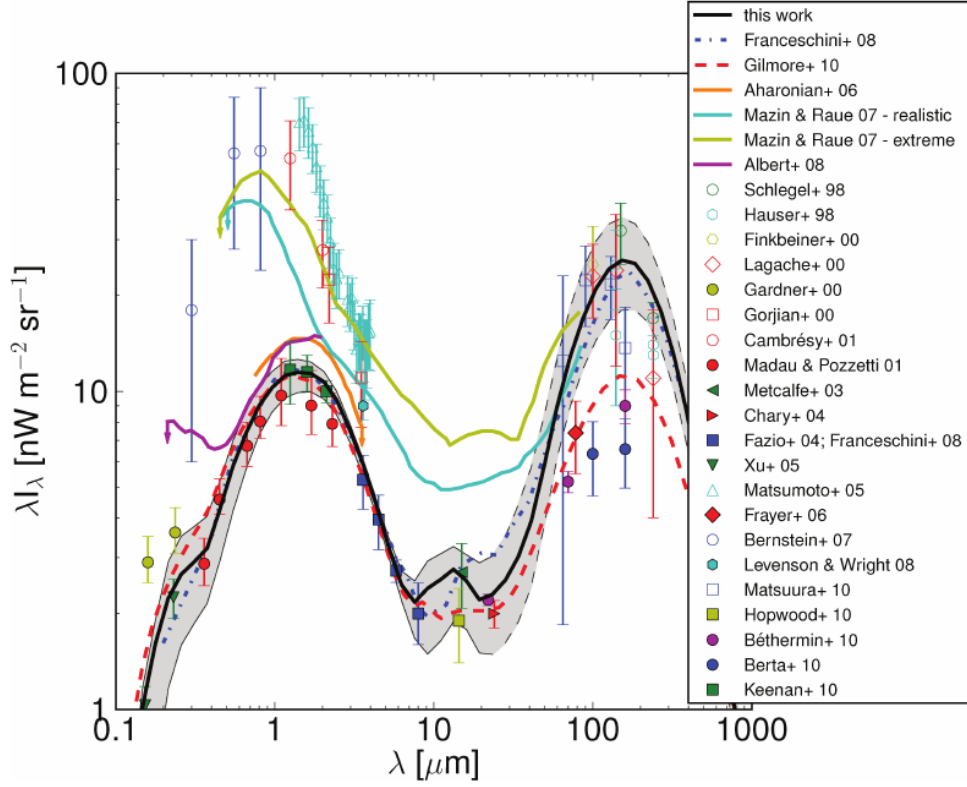


Figure 2.8: CIRB and EBL spectra for the models of Domínguez et al. (2011, black solid line), Franceschini et al. (2008, blue dot-dashed line) and Gilmore et al. (2010, red dashed line). The gray band represents the uncertainties of the first model. The filled symbols are lower limits from galaxy counts, the open symbols are direct measurements. The colored solid lines are upper limits from γ -ray observations of TeV blazars. The plot is taken from Domínguez et al. (2011), where more details on the several datasets can be found.

- direct observation of the evolution of the galaxy populations over the redshift range which contributes significantly to CIRB and EBL (e.g. Domínguez et al. 2011).

In Fig. 2.8 a comparison of three EBL models is shown, together with lower limits from galaxy counts and upper limits from direct measurements and from observations of γ -ray blazars. One can see that the models can sometimes differ significantly. In Fig. 2.9 the evolution of the EBL number density as function of the redshift is shown. The density is smaller at low redshift due to the expansion of the Universe. In Fig. 2.10 the effect of the use of different assumptions in the galaxy evolution models is shown.

Once the evolution of the EBL spectrum and number density has been derived, it is then possible to calculate the optical depth for the γ -ray photons as function of energy and redshift (Fig. 2.11). The peak of the pair production cross section between a TeV source photon of energy E_γ and an EBL photon of energy ϵ is at $E_\gamma \epsilon \approx (2m_e c^2)^2$ (H.E.S.S. Collaboration et al. 2013).

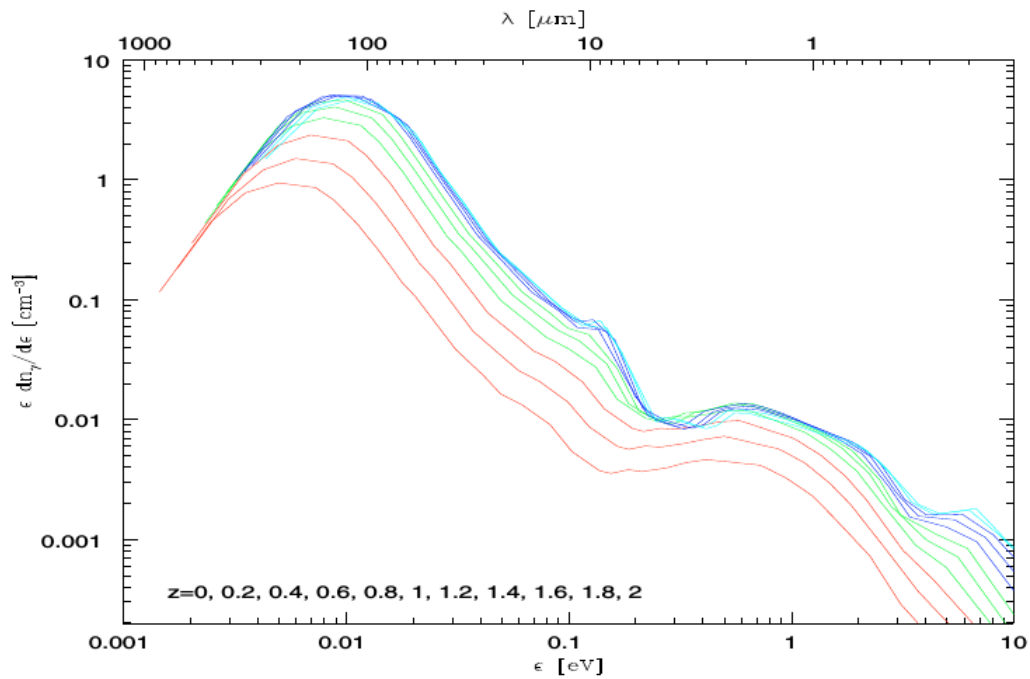


Figure 2.9: Number density of EBL photons as function of their energies for different redshift values: red correspond to $z = 0, 0.2, 0.4$; green to $z = 0.6, 0.8, 1.0$; blue to $z = 1.2, 1.4, 1.6$; cyan to $z = 1.8, 2.0$. From Franceschini et al. (2008)

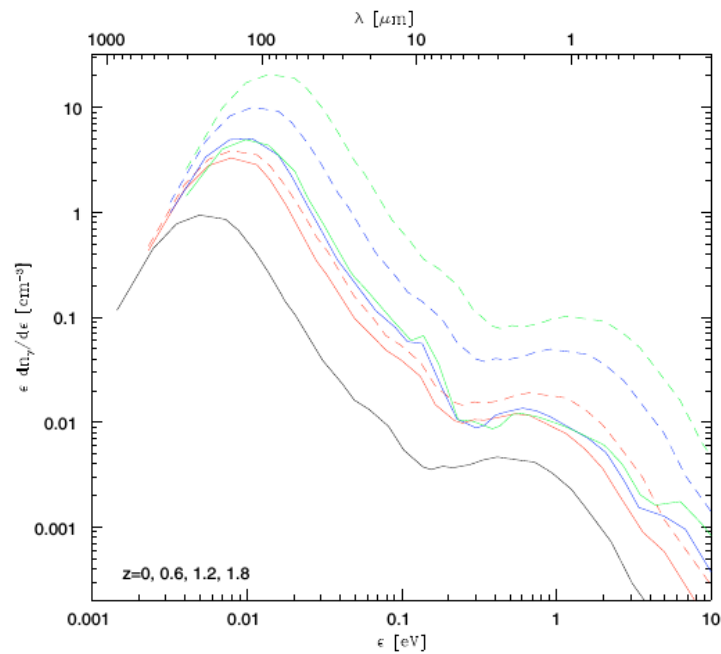


Figure 2.10: Same as in Fig. 2.9 for redshift $z = 0, 0.6, 1.2, 1.8$ (black, red, blue and green lines). The solid lines are obtained with galaxy evolutionary models and are compared with those corresponding to the case of a non-evolving population (dashed lines). From Franceschini et al. (2008)

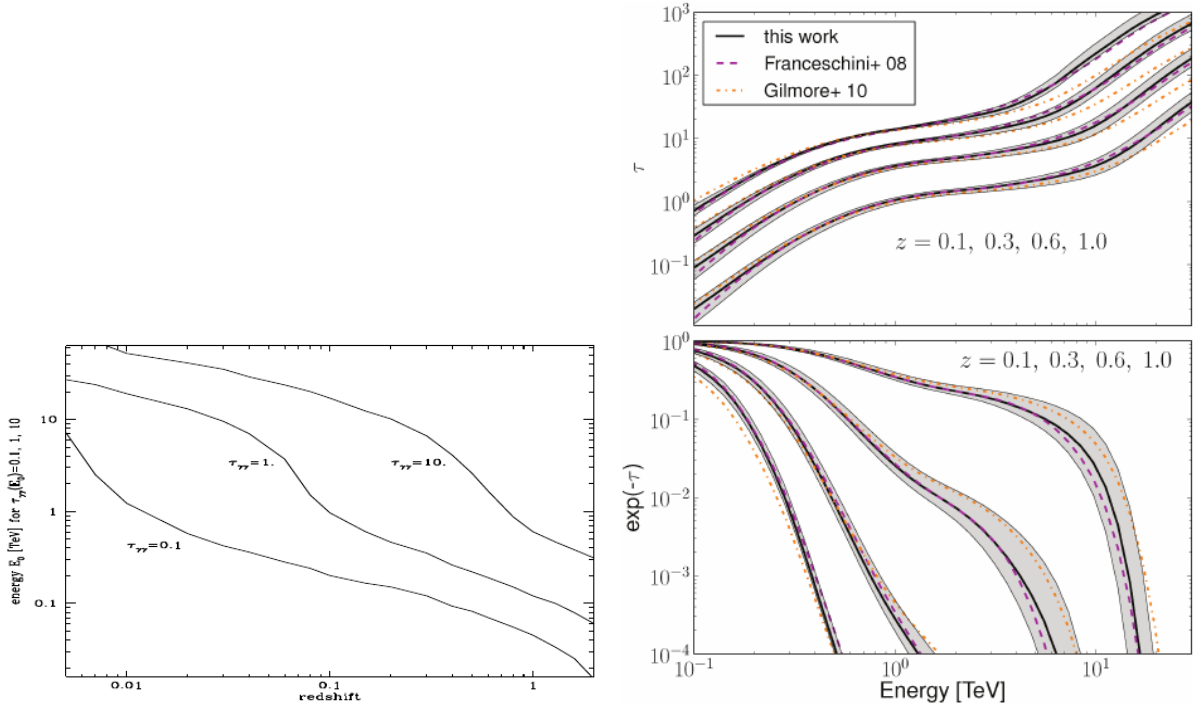


Figure 2.11: *Left:* γ -ray photon energies for which the optical depth $\tau_{\gamma\gamma} = 0.1, 1$ and 10 as function of the redshift (from Franceschini et al. 2008). *Right-top:* optical depth as function of the energy for the models of Domínguez et al. (2011, black solid line), Franceschini et al. (2008, violet dashed line) and Gilmore et al. (2010, orange dotted line) for $z = 0.1, 0.3, 0.6, 1.0$ (from bottom to top). *Right-bottom:* flux attenuation for the same redshift values (here from right to left) and same EBL models. The grey areas in both plots are the propagated model uncertainty from Fig. 2.8. From Domínguez et al. (2011).

From this, one can derive the wavelength of optimal interaction:

$$\lambda_{EBL} = 1.187 \times E [TeV] \times (1 + z')^2 \mu m \quad (2.49)$$

where $z' < z$, z is the redshift of the source and the factor $(1 + z')^2$ takes into account the fact that the interaction can take place at any point in the space between the source and the observer.

2.4.4 INTERGALACTIC MAGNETIC FIELD (IGMF)

Magnetic fields are present everywhere in the Universe. Their strengths range several orders of magnitude: from 10^{15} G of the most extreme magnetars to few μ G of the galaxies. Magnetic fields of the order of μ G are found ubiquitously also in galaxy clusters and superclusters, in regions between clusters and in cluster halos. They characterize the large scale structures of the Universe. It is generally believed that the μ G magnetic fields are the results of amplification of weak pre-existent “seed” fields. The nature of such seed fields is unknown. Two large groups of models exist. For one group, the fields are generated by motion of the plasma in galaxies and proto-galaxies. For the other group, the seeds fields might be of cosmological origin, from the early epochs of the expansion of the Universe (e.g. Neronov & Semikoz 2009; Neronov

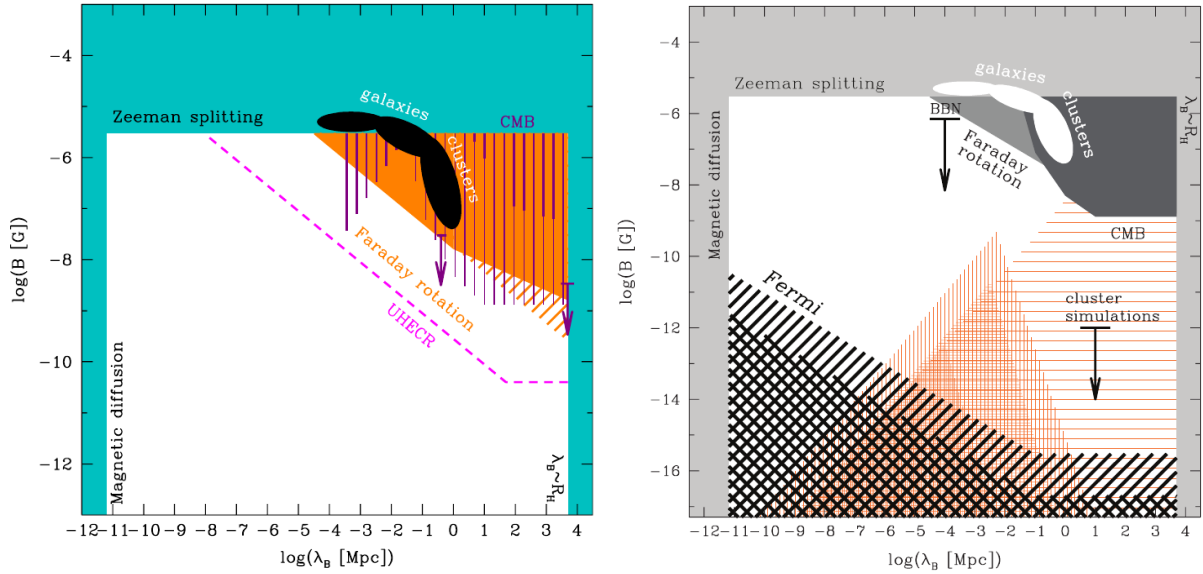


Figure 2.12: *Left:* observational limits on the IGMF from Neronov & Semikoz (2009). The cyan region shows the upper limit on B_{IGMF} imposed by the Zeeman splitting measurement, the lower bound on the correlation length imposed by the magnetic diffusion and the upper bound on correlation length given by the Hubble radius. The orange region shows the limit from Faraday rotation measurements. The magenta line shows the limit that can be imposed by observations of deflections of ultra high energy cosmic rays. The violet vertical-hatched regions and the arrows at $\lambda_B = 0.5$ Mpc and $\lambda_B \sim R_H$ (Hubble radius) show the limits imposed on cosmologically produced fields by the CMB observations. The black ellipses show the ranges of measured magnetic fields in galaxies and galaxy clusters. *Right:* gray regions and white ellipses are the same as before. Upper limits from Big Bang nucleosynthesis (BBN) and cluster simulations are also shown. The black hatched region shows the lower bound on the IGMF obtained from combined GeV and TeV observations. Orange hatched regions show the allowed ranges of B_{IGMF} and λ_B for magnetic fields generated at the epoch of inflation (horizontal hatching), the electroweak phase transition (dense vertical hatching), QCD phase transition (medium vertical hatching), and epoch of recombination (light vertical hatching). From Neronov & Vovk (2010)

& Vovk 2010 and references therein). In this last case, very weak intergalactic magnetic fields (IGMFs) should exist in the large scale voids. However, up to now no measurement could be done and only upper limits could be derived with different observation techniques. The upper limits on the IGMF strength B_{IGMF} as function of the coherence length λ_B have been summarized by Neronov & Semikoz (2009) and are shown in Fig. 2.12. Lower limits on the IGMF in voids can in principle be obtained from combined observations of extragalactic sources at GeV and TeV energies. In the following, a brief description of the method and the processes involved will be given. For more details, see e.g. Neronov & Semikoz (2009).

Due to the presence of EBL, γ -ray photons with energies $E_{\gamma 0} \gtrsim 1$ TeV cannot propagate over cosmological distances because they are absorbed via pair production. The mean free path (which depends on the EBL model assumed) is $\lambda_{\gamma\gamma} \approx 80 (10 \text{ TeV}/E_{\gamma 0}) \text{ Mpc}$. The generated e^\pm pairs will then emit secondary cascade radiation via IC on CMB photons. For an

e^\pm energy $E_e \simeq E_{\gamma 0}/2$ it follows from eq. 2.31 that the re-emitted radiation will have energies of $E_\gamma \approx 88 (E_{\gamma 0}/10 \text{ TeV})^2 \text{ GeV}$ (for $\epsilon_{CMB} = 6 \times 10^{-4} \text{ eV}$). The pairs will cool over distances $\lambda_e = 10^{23} (10 \text{ TeV}/E_e) \text{ cm}$, a factor 10^3 smaller than $\lambda_{\gamma\gamma}$. The power removed from the primary TeV γ -ray beam is therefore transferred to the cascade emission at GeV energies.

In the presence of magnetic fields, the charged particles will be deflected from their original path and their IC emission will spread around the original source (Fig. 2.13, *left*). The deflection angle θ_{dfl} will depend on the particle energy, as well as on the magnetic field strength and on its coherence length λ_B . Given R_L the Larmor radius, one has

$$\theta_{dfl} \simeq \frac{\lambda_e}{R_L} \simeq 3 \times 10^{-4} \left(\frac{B_{IGMF}}{10^{-16} \text{ G}} \right) \left(\frac{10 \text{ TeV}}{E_e} \right)^2 \quad \text{for} \quad \lambda_B \gg \lambda_e \quad (2.50)$$

$$\theta_{dfl} \simeq \frac{\sqrt{\lambda_e \lambda_B}}{R_L} \simeq 5 \times 10^{-5} \left(\frac{B_{IGMF}}{10^{-16} \text{ G}} \right) \left(\frac{10 \text{ TeV}}{E_e} \right)^{3/2} \left(\frac{\lambda_B}{1 \text{ kpc}} \right)^{1/2} \quad \text{for} \quad \lambda_B \ll \lambda_e \quad (2.51)$$

From these equations it follows that for a given B_{IGMF} , if E_e is large enough, e^\pm will not be deflected and all the secondary emission will reach the observer (Fig. 2.13, *right-top*). In the opposite case, if the energy is too low, the particles will be isotropized and the secondary flux will be reduced by a factor $\Omega_c/4\pi$ (being $\Omega_c \simeq \pi\theta_c^2$ the solid angle where the primary radiation is collimated, Fig. 2.13, *right-bottom*). In the intermediate case the reprocessed emission is beamed at different angles at different energies (Fig. 2.13, *right-middle*).

The effect of the coherence length λ_B on the derivation of lower limits is depicted in the right plot of Fig. 2.12. For $\lambda_B \gtrsim 1 \text{ Mpc}$, the lower bound on the IGMF does not depend on the IGMF coherence length because the IC cooling distance of electrons and positrons is much shorter. Instead, if $\lambda_B \lesssim 1 \text{ Mpc}$, the IC cooling distance becomes larger than the region with a correlated magnetic field. In this case, during their cooling the pairs pass through regions with different magnetic field orientations, so that the deflection angle scales proportionally to the square root of λ_B . The magnetic field must be stronger in order to deviate the particles trajectories by a given angle θ_{dfl} .

In order to be able to detect secondary emission from a point-like source like a blazar, the IC scattered photon must fall inside the PSF of the instrument. The following relation (from Fig. 2.14) must be satisfied

$$\theta = \frac{\lambda_{\gamma\gamma}(E_\gamma)\theta_{dfl}(E_e)}{d} < \theta_{PSF} \quad (2.52)$$

Since reprocessing involves emission from an ensemble of charged particles that are spread over an extended volume by the action of the magnetic field, energy dependent time delays are of the order of the light travel time of the excess distance that the re-emitted photons must cover with respect to the line of sight to the source, because of the finite e^\pm velocity $v_e < c$. In addition, the delay will depend also on the magnetic field strength. It can be analytically estimated to be

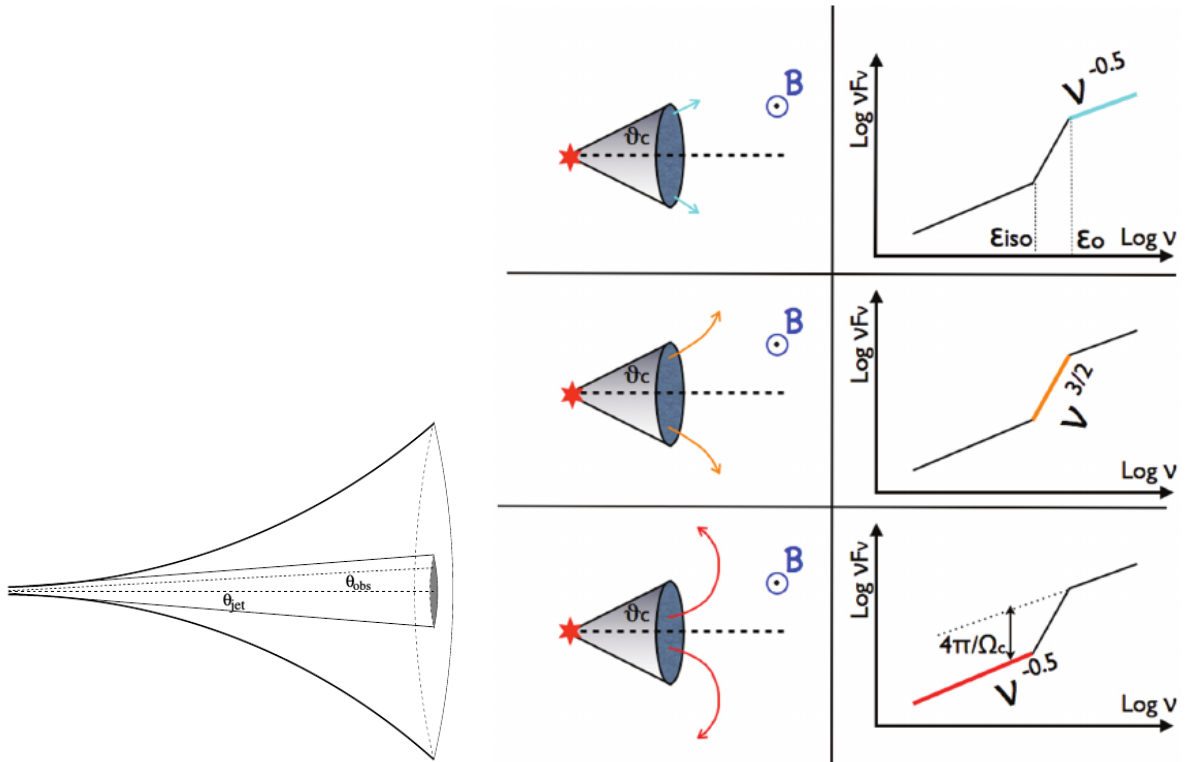


Figure 2.13: *Left:* Schematic representation of the effect of IGMF on the cascade development. The original conical jet emission is also shown. The inner shaded region represents the region filled by the intrinsic TeV emission (from Taylor et al. 2011). *Right:* Schematic representation of the reprocessing of the absorbed TeV radiation. The source illuminates the regions inside a cone with semi-aperture θ_c (equal to θ_{jet} in the left plot). For a given B_{IGMF} , e^\pm (arrows) with very high energy cool without changing their direction (*top*) and the reprocessed GeV IC emission is beamed within the same angle θ_c . Particles of progressively lower energy are deflected and spread their emission over larger angles (*middle*) up to the point where they are completely isotropized (*bottom*). From Tavecchio et al. (2010).

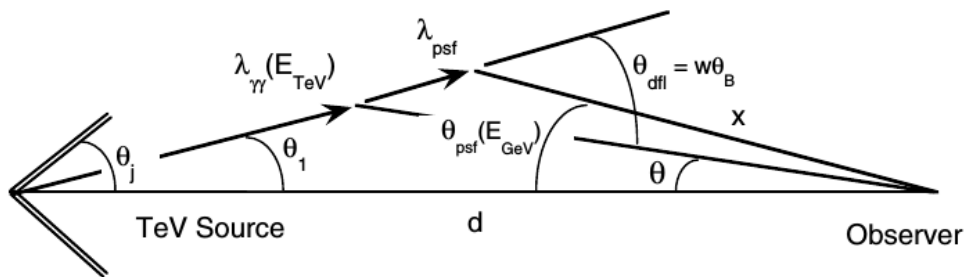


Figure 2.14: Schematic representation of the geometry of the process. A TeV photon is emitted at angle $\theta_1 < \theta_j$ to the line of sight and interacts with an EBL photon creating an e^\pm pair after a distance $\lambda_{\gamma\gamma}$ (here $\theta_j = \theta_{jet} = \theta_c$ of Fig. 2.13). The particle is deflected by the IGMF of an angle θ_{dfl} and scatters a CMB photon to GeV energies. The reprocessed photon is observed as a source photon if it is detected at an angular distance from the source $\theta < \theta_{PSF}$ (from Dermer et al. 2011).

(Dermer et al. 2011, see also Fig. 2 in both Taylor et al. 2011 and Arlen et al. 2014):

$$\Delta t \sim 2 \times 10^6 \lambda_{100} \left(\frac{B w}{10^{-15} \text{ G}} \right)^2 \left(\frac{10 \text{ GeV}}{E} \right)^2 \text{ yr} \quad (2.53)$$

with $\lambda_{100} = \lambda_{\gamma\gamma}/(100 \text{ Mpc})$ and w depending on the ratio between λ_e and λ_B , similar to the last factor in eq. 2.51. This holds true as long as the Compton cooling time is of the order of the gyroradius. If it is too fast, re-emission is almost immediate and time delay negligible. If it is too slow, this and not the magnetic field determines the time delay. The observed reprocessed emission corresponds therefore to the time-averaged original VHE emission and no variability is expected to be seen. Constrains on the IGMF hence rely on the assumption of a steady VHE flux on time scales of these delays. Is the VHE flux variable, average values can be used as long as the variability is shorter than the reprocessing time delay.

Lower limits on the strength of the IGMF can be derived from GeV and TeV observations making assumptions on the source intrinsic spectrum. Using an EBL model one can estimate the amount of energy flux that has been absorbed and reprocessed. Comparing the GeV observations with the expected total contribution of intrinsic and reprocessed fluxes for different IGMF strengths, one can determine the minimum magnetic field value that does not violate the observations. These lower limits obviously depend on the assumptions on the EBL model, on the intrinsic spectrum, on the livetime of the source engine, on the coherence length of the magnetic field and on the accuracy of the reprocessing model. The limits on B_{IGMF} as function of λ_B shown in Fig. 2.12 are therefore model dependent. Several authors (e.g. Neronov & Vovk 2010; Tavecchio et al. 2010, 2011; Ahlers 2011; Dermer et al. 2011; Dolag et al. 2011; Huan et al. 2011; Taylor et al. 2011; Takahashi et al. 2012; Vovk et al. 2012; Arlen et al. 2014; H. E. S. S. Collaboration et al. 2014) derived lower limits in the range $10^{-18} - 10^{-14} \text{ G}$.

CHAPTER 3

THE H.E.S.S. EXPERIMENT

Ground based observations of γ -ray sources rely on the Imaging Atmospheric Cherenkov (IAC) technique. This technique takes advantage of the same atmosphere that absorbs the γ -ray radiation (sec. 2.4.1). Imaging Atmospheric Cherenkov Telescopes (IACTs) have a very large collection area of the order of $10^5 - 10^6 \text{ m}^2$. They are able to record the Cherenkov light emitted in the air showers (sec. 2.4.1) initiated by the interaction of the primary particles in the atmosphere. IACTs are currently the most sensitive instruments for VHE γ -ray astronomy in the energy range above 50-100 GeV.

The first IACT was constructed by the Whipple collaboration (Cawley et al. 1990). It was a single tessellated reflector of 10 m diameter with an energy threshold of ~ 350 GeV. It operated from 1968 until its de-commissioning in 2013. The first detection of a VHE source was obtained with this telescope in 1989, when the Crab Nebula was discovered above 0.7 TeV (Weekes et al. 1989).

With the second generation of IACTs like HEGRA (Daum et al. 1997) or CAT (Barrau et al. 1998), significant improvements in the sensitivity were achieved through the use of arrays of telescopes that permitted the stereoscopic imaging of the air showers. Multiple views of the same shower provide a more accurate measurement of the shower parameters and allow for a better reconstruction of the primary particle compared to a single telescope. Requiring trigger coincidence for multiple telescopes, stereoscopy has also the advantage of reducing random triggers from the night sky background (NSB), as well as from muons and hadrons. This allows the telescope to operate with a lower energy threshold and a higher sensitivity.

The stereoscopic approach was then adopted in all third generation instruments: H.E.S.S. (Hinton & the HESS Collaboration 2004), VERITAS (Weekes et al. 2002), CANGAROO-III (Kubo et al. 2004), MAGIC¹ (Lorenz & The MAGIC Collaboration 2004). Compared to the pre-

¹After a first phase with a single 17 m telescope, a second one was installed a few years later. The stereo operation increased the sensitivity of the observatory by a factor of about 3 (<https://magic.mpp.mpg.de/>).



Figure 3.1: *Left:* satellite view of the H.E.S.S. site. The disposition of the four small telescopes in a square with the diagonals aligned in the North-South and East-West directions is visible. At the center, the big fifth telescope is being built. *Right:* map of Namibia. The red symbol marks the position of the H.E.S.S. site, about 110 km South-West from the capital Windhoek. The Tropic of Capricorn passes just a few km South. Credits: Imagery ©2016 GeoEye, Map data ©2016 Google.

vious generation, the new systems have a significantly lower energy threshold of about 100 GeV and higher sensitivity, provided by the use of larger mirror areas and improved electronics.

3.1 THE H.E.S.S. TELESCOPE SYSTEM

The High Energy Stereoscopic System (H.E.S.S.) is an array of five IACTs. It was named after Victor Hess, who received the Nobel Prize in Physics in 1936 for the discovery of the cosmic radiation in 1912.

3.1.1 LOCATION

H.E.S.S. is located in Namibia on the Kohmas Highlands. The site is about 110 km south-west of the capital Windhoek at $23^{\circ}16'18''$ S, $16^{\circ}30'00''$ E, 1800 m above sea level (Fig. 3.1). The location was chosen mainly for three reasons: its proximity to the Gamsberg area, its altitude, and its position in the southern hemisphere near the Tropic of Capricorn.

The Gamsberg area is well known for its excellent conditions for astronomical observations (Wiedner 1998): 57% of the ~ 1700 dark moonless hours have no clouds, 64% a cloud coverage less than 25% above 30° altitude. The relative humidity is below 90% for 94% of the time.

The importance of the southern location is due to one of the main goals of the H.E.S.S.



Figure 3.2: Aerial view of the full HESS-II array. In front of every telescope is a camera shelter, where the camera is parked during time of non operation. At the bottom of the image is building with the control rooms and the mechanic's and electrical workshops. Image credit: Christian Föhr.

experiment, i.e. the survey of the Galactic Plane. The Galactic Center culminates at Zenith during the southern autumn and winter, when the best observational conditions are met, with the longest nights and the driest and most stable atmosphere.

The altitude of the site is in the optimal range for the detection of the Cherenkov light emitted in the air showers, near their maximum.

3.1.2 THE ARRAY

H.E.S.S. consists of four identical small telescopes placed at the corners of a square of 120 m side length, whose diagonals are aligned in the north-south and west-east direction (Fig. 3.1, *left*). A fifth big telescope is placed at its center (Fig. 3.2). The distance was chosen in order to maximize the collection area, while requiring that at least two telescope are able to observe the same air shower, allowing for a good stereoscopic view of each event. For an easier identification, the telescopes are named as Cherenkov Telescope (CT) 1 to 5, the last one being the one at the center.

The H.E.S.S. experiment consists of two phases, marked by the presence of CT 5. To dis-



Figure 3.3: Close up of one of the CT 1-4 telescopes (*top*) and of CT 5 (*bottom*).

tinguish the two periods, a new nomenclature has been introduced: H.E.S.S. phase I (HESS-I) before 2012 and H.E.S.S. phase II (HESS-II) afterwards. HESS-I started in summer 2002, when the first of the small telescopes became operational. The construction of the fourth telescope was completed in December 2003, and the full CT 1-4 array has been functional since January 2004. HESS-II begun with the inauguration of CT 5 in September 2012 during the ten years anniversary of H.E.S.S. . The whole CT 1-5 system constitutes the world first hybrid system of IACTs.

Observations can be carried out using different telescope combinations: a Stereo mode involving any subsets of CT 1-4 with or without CT 5 and a Mono mode using CT 5 only. Mono and CT 1-4 stereo observations can be carried out simultaneously on different sources.

The stereoscopic technique of the HESS-I system provides a good angular resolution of 0.1° per photon and a good background rejection. This allows for a low energy threshold of ~ 100 GeV at Zenith and a 1% Crab flux sensitivity. The Mono system reaches lower energies around ~ 20 - 50 GeV at Zenith thanks to the significantly larger mirror area, but has a poorer angular resolution and background rejection capabilities, due to the lack of stereoscopy. The observations with the Stereo-Hybrid system exploit the advantages of both subsystems. This results in a lower energy threshold and in an improved sensitivity in the low energy domain up to ~ 1 TeV thanks to the larger collecting area and in a better background rejection from the stereoscopic view.

3.1.3 MOUNT AND DRIVE SYSTEM

All five telescopes have an alt-azimuth mount installed on a circular base frame which rotates around a vertical axis. A dish for the support of the mirrors is attached to the elevation axis. Both are realized as steel space frames.

CT 1-4 (Fig. 3.3, *top*) have hexagonal dishes with a flat-to-flat width of 12 m ($\varnothing = 13$ m) and a focal length $f = 15$ m ($f/d = 1.2$). The circular rail has a diameter of 13.6 m. The movements in both azimuth and elevation are achieved through friction drives that can reach an angular velocity of $100^\circ/\text{min}$. It allows a repointing between any two positions in the sky in less than 2 minutes. The position is controlled by shaft encoders with a digital step size of $10''$ and a mechanical accuracy of $3''$. The weight of each telescope, including camera, drive systems and mirrors is about 60 tons.

CT 5 (Fig. 3.3, *bottom*) is considerably larger than the other four telescope. Currently, it is the largest optical telescope in the world. Its light collecting area of $32.6 \times 24.3 \text{ m}^2$ is equivalent to a 28 m circular dish. The elevation axis is placed at 24 m height. The drive systems are different for the two axis. In azimuth, four motors drive 4 of the 12 wheels on a 36 m diameter rail. The maximum speed is $200^\circ/\text{min}$. The range is $\pm 280^\circ$ from the park position. The elevation drive is a rack-and-pinion system on semi-circular structures on both sides of the telescope, moved by two drive units with two motors each. The maximal speed is $100^\circ/\text{min}$. The range is $-125^\circ / + 90^\circ$ from the vertical. The greater speed and wider movement range allow for a repointing between any two positions in the sky in less than 50 seconds. The total weight of CT 5 amounts to 580 tons.

3.1.4 MIRRORS

The CT 1-4 mirrors (Bernlöhr et al. 2003) are constituted of a segmented reflector. It is composed of 380 round facets arranged with Davies-Cotton optics² (Davies & Cotton 1957). Each facet has a diameter of 60 cm, for a total reflecting area of about 107 m^2 . Due to shadowing from the

²In a Davies-Cotton optics, the facets are arranged on a sphere of radius f , which corresponds to the focal length of the facets and of the whole telescope, as well. This design provides good off-axis imaging (reduced coma aberration), which is important for a uniform response over the large field of view required for observations of extended sources.

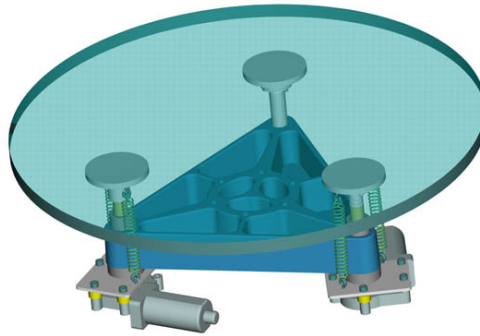


Figure 3.4: Drawing of a HESS-I mirror with its anchorage system. The same method is used for the HESS-II mirrors. From <https://www.mpi-hd.mpg.de/hfm/HESS/>.

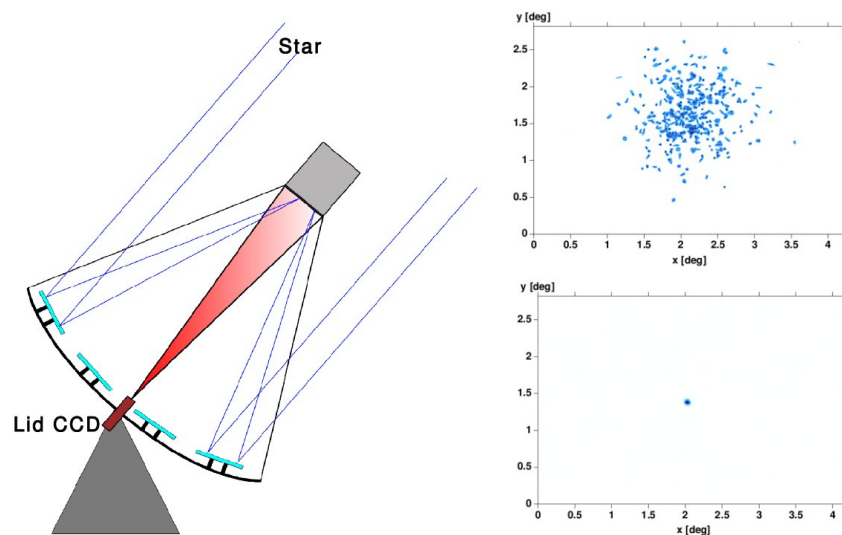


Figure 3.5: Mirror alignment technique. *Left:* a star is observed with a CCD camera positioned at the center of the dish, viewing the closed lid of the PMT camera. *Top-right:* star image before alignment. *Bottom-right:* star image after alignment (Cornils et al. 2003).

camera arms, the effective area is reduced to about 95 m^2 . The mirror facets are made with quartz-coated aluminized ground glass with a reflectivity of at least 80% for wavelengths between 300 and 600 nm. 80% of the reflected light must fall inside 1 mrad diameter at the distance of the 15 m focal length.

As for CT 1-4, the CT 5 mirror is a segmented reflector, as well. In this case, the mirror facets are mounted in a parabolic shape³. 875 hexagonal quartz-coated aluminized glass mirrors are used. They have a flat-to-flat width of 90 cm, for a total mirror area of 614 m^2 , and a focal length of 36 m.

³A Davis-Cotton mounting for CT 5 would have introduced too large anisochronisms between the arrival times of the photons from the center or from the border of the reflector, which would have resulted in a significant degradation of the signal to background ratio. The parabolic shape increases the off-axis aberration.

For all five telescopes, the anchorage of the mirrors to the dish is made on three points (Fig. 3.4). One is fixed, while the other two are movable through motor-driven actuators. This allows for their remote alignment, which is performed as follows (Cornils et al. 2003). A bright star is imaged on the close lid of the camera and viewed with a CCD camera in the center of the dish. When misaligned, every mirror will generate a spot on the lid (Fig. 3.5, *top-right*). Every facet is then moved in both axis until all the spots converge into a single star centered at the main focus at the center of the telescope camera (Fig. 3.5, *bottom-right*).

The optical point spread function (PSF) of the resulting image is defined as the radius of a circle enclosing 80% of the spot intensity. It depends on both the offset from the camera center (because of spherical aberrations) and on the elevation of the telescope (because of deformations of the dish structure). For all practical observations it is well within the pixel size (Fig. 3.6).

3.1.5 CAMERAS

The H.E.S.S. cameras have an hexagonal shape and are located in the focal plane of the reflector. They are supported by a quadrupod, the "nose" of the telescopes. They consist of photomultiplier tubes (PMTs) organized in "drawers" (Fig. 3.7, *left*). Each drawer contains 16 PMTs with the associated electronics. Each PMT represents a camera pixel. PMTs have been chosen above other alternatives due to their quick response, needed to catch Cherenkov flashes that last only for a few ns. Up to now⁴, they are the most appropriate light sensors for IACT cameras, despite a quantum efficiency of 25-30%. In order to reduce the insensitive area of the cameras due to

⁴Currently, the FACT collaboration (<http://isdc.unige.ch/fact/>) is successfully testing Geiger-mode avalanche photodiodes (G-APDs) as photosensors for an IACT camera. Compared to PMTs, G-APDs use a much lower operation voltage, are more robust and have a higher efficiency. They also can be operated during strong moon light. As a consequence, they are very well suited to improve the sensitivity of the instruments and are ideal for a monitoring telescope, providing a larger duty cycle.

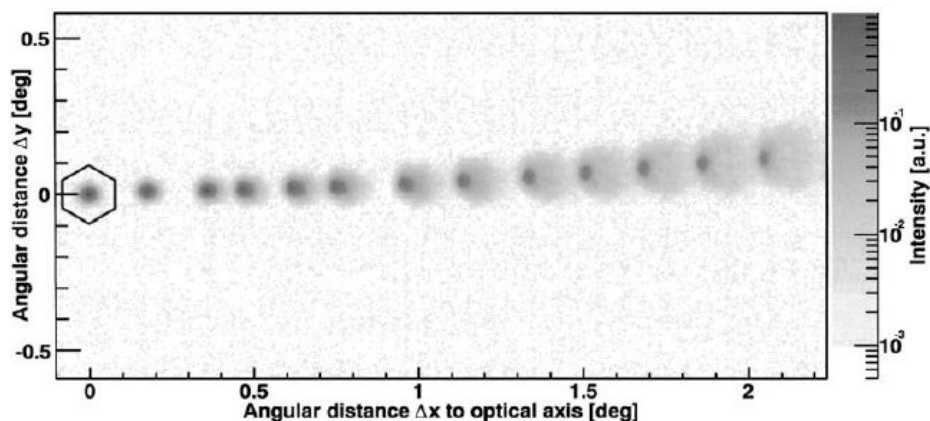


Figure 3.6: HESS-I PSF size of a star as function of the offset from the optical axis. The pixel size is indicated, as well (Cornils et al. 2003).



Figure 3.7: *Left:* a "drawer", consisting of 16 PMTs and all associated electronics. *Right:* front image of a HESS-I camera. In the upper half the hexagonal Winston cones are already in place, while in the lower half, one can see the bare PMTs. From <https://www.mpi-hd.mpg.de/hfm/HESS/>

the circular shape of the PMTs, hexagonal Winston cones (Fig. 3.7, *right*, Welford & Winston 1989) are used to funnel the light into the PMTs. The cones also limit the solid angle viewed by the PMTs and reduce the noise due to stray light and albedo. The trigger and readout electronics as well as the high voltage supply are contained in the rear part of the camera body. All H.E.S.S. cameras follow this concept. However, the CT 5 camera is redesigned and highly improved with respect to the older ones.

The HESS-I cameras (Fig. 3.8, *left*, Punch & H.E.S.S. Collaboration 2001) consist of 960 PMTs divided in 60 drawers. Each pixel has an angular size of 0.16° , yielding a total field of view (FoV) of the camera of about 5° of diameter. This combination allows for the observation of extended sources and for the resolution of image details. The image recording rate is 300 Hz. The cameras have a diameter of about 1.6 m and a length of 1.5 m. They weight around 800 kg.

The CT 5 camera is almost three times larger than the HESS-I cameras. Its is 2.3 m wide, 2.4 m high and 1.8 m deep for a total weight of 2.8 tons. Its 2048 PMTs cover an angular size of 0.067° each, yielding a total field of view of 3.2° of diameter in the sky. The image recording rate is 3600 Hz. The significantly smaller field of view makes CT 5 not suitable for the observation of extended sources or for observation strategies like the Galactic Plane survey. A special system allows for the loading and unloading of the camera for an easier maintenance and protection inside the shelter (Fig. 3.8, *right*).

3.1.6 TRIGGER SYSTEM

The H.E.S.S. trigger system (Funk et al. 2004) has been developed to optimize the use of the stereoscopy. It requires a coincident signal from at least two of the five telescopes in order for the event to be processed. This requirement significantly suppresses the rate of background events. They are mostly hadronic showers, which have a more inhomogeneous light pool than



Figure 3.8: *Left:* HESS-I camera with open lid inside its support (from <https://www.mpi-hd.mpg.de/hfm/HESS/>). *Right:* CT5 camera being unloaded from the quadrupod as demonstration during the inauguration in September 2012.

the γ -ray photons and therefore are less likely to fulfill the coincidence. Single muons are also almost completely rejected because their light pool is in general too small to trigger more than one telescope. The event rejection at the hardware level additionally allows for the reduction of the requirements for the network, the disc space and the CPU time needed. The coincidence permits to lower the camera trigger thresholds, and consequently the energy threshold of the instrument (that scales roughly with the pixel threshold), by a factor 2 compared to single telescope operations.

The trigger system is subdivided in two stages. The first is at the telescope level, the second involves a central trigger system (CTS). Here, the trigger system of the HESS-I telescopes is briefly described as an example. The CT5 trigger follows the same principles, but the same numerical values do not apply, being its camera larger and the whole electronics more advanced.

For the local trigger, each camera is subdivided in overlapping sectors containing 64 pixels. It is required that the photoelectric signal in a predefined number M of pixels (*sector threshold*, typically 2 to 4 pixels) exceeds a certain value N (*pixel threshold*, typically a few photoelectrons, p.e.). The overlapping sectors ensure a homogeneous trigger efficiency across the entire camera. This multiplicity trigger must be fulfilled in a short time window of usually 1.3 ns.

The signal from every PMT is sampled at 1 GHz and stored in buffers of 128 cells. When the conditions for the multiplicity trigger are met, the buffer content is integrated in a time window of 16 ns around the signal and the camera is read out. The total camera dead time for the process is 446 μ s.

The trigger signal is sent from the camera via optical fiber to the CTS, for the multiple-telescope coincidence requirement. If this is met, a readout signal is sent back to the cameras and the data are registered. Otherwise, a reset signal is sent, and the camera discards the event.

In addition to this, to allow for CT5 Mono observations, any signal coming from this telescope is recorded, as well. A second level local trigger (L2) is present to avoid that one event is



Figure 3.9: The Automated Telescope for Optical Monitoring (ATOM)

recorded as both Mono and Stereo event. It also prevents too high trigger rates caused by muons and night sky background through a first level pattern analysis of the recorded images.

3.2 AUTOMATED TELESCOPE FOR OPTICAL MONITORING (ATOM)

The Automated Telescope for Optical Monitoring (ATOM, Hauser et al. 2004) is also part of the H.E.S.S. experiment. ATOM (Fig. 3.9) is a 75 cm altazimuth telescope built by the German company Carl Zeiss GmbH in the late 1970s. It has a focal length $f = 600$ cm and an aperture ratio of $f/8$.

Initially, the telescope was mounted and operated at the Heidelberg State Observatory (Landessternwarte, LSW) on the Königstuhl in Heidelberg, Germany. With the start of the H.E.S.S. project, it was decided to relocate it to the H.E.S.S. site as support for multiwavelength (MWL) observations. The telescope was then upgraded to work in robotic mode. The mechanical components required a modest redesign, while the entire electronics were replaced.

ATOM is equipped with an Apogee Alta U47 camera (Apogee Alta E47+ until 2011) with a FoV of $8'$. It is mainly used for the optical monitoring of variable γ -ray sources and can trigger target of opportunity (ToO) observations for H.E.S.S. if a source is found in a high state.

Table 3.1: Comparison of the technical characteristics of the five Cherenkov telescopes of the H.E.S.S. array (from https://www.mpi-hd.mpg.de/hfm/HESS/pages/about/HESS_I_II/).

	CT 5	CT 1-4
	Mount	
Mount type	alt-az	alt-az
Azimuth drive system	12 wheels in 6 bogies on 36 m diameter rail; 4 wheels driven by servo motors, plus backup motors; peak positioning speed 200°/min; range 560°.	Friction drive using separate circular rail, with servo motor and backup motor; peak positioning speed 100°/min; range 540°.
Elevation drive system	Toothed ring on either side of the dish; 2 drive units with 2 motors each, plus backup motors; peak positioning speed 100°/min; range -125° / + 90° from vertical.	Friction drive using circular rail, with servo motor and backup motor; peak positioning speed 100°/min; range -125° / + 90° from vertical.
Height of elevation axis	24 m	10 m
	Dish	
Dimensions	32.6 × 24.3 m ² ; equivalent to a 28 m circular dish	12.0 m flat-to-flat (hexagonal, $\varnothing = 13$ m).
Shape of reflector	Parabolic	Davies-Cotton
Focal length	36 m	15 m
Total mirror area	614 m ²	108 m ²
Mirror facets	875 hexagonal facets of 90 cm (flat-to-flat) size; quartz-coated aluminized glass; weight per facet ≈ 25 kg	382 round facets of 60 cm size; quartz-coated aluminized glass; weight per facet ≈ 15 kg
Facet alignment	Each facet equipped with 2 actuators with 2 μ m positioning step size	Each facet equipped with 2 actuators with 3 μ m positioning step size
	Camera	
Photo sensors	2048 1-1/4' PMTs	960 1-1/4' PMTs
Packaging	128 drawers of 16 PMTs each; each drawer includes digitization, trigger, slow control and high voltage generation.	60 drawers of 16 PMTs each; each drawer includes digitization, trigger, slow control and high voltage generation.
Pixel size	42 mm flat-to-flat, hexagonal (Winston cones), equivalent to 0.067°.	42 mm flat-to-flat, hexagonal (Winston cones), equivalent to 0.16°.
Sensitive area/FoV	$\varnothing \approx 200$ cm, equivalent to 3.2° on the sky.	$\varnothing \approx 130$ cm, equivalent to 5.0° on the sky.
Signal recording	1 GHz signal sampling; 2 gain channels for each pixel for large dynamic range; records signal amplitude, timing, and shape.	1 GHz signal sampling; 2 gain channels for each pixel for large dynamic range; records signal amplitude.
Effective exposure time	16 ns	16 ns
Image recording rate	3600 images/s	300 images/s
Power consumption	8 kW	5 kW
Dimensions of camera body	227 × 240 × 184 cm (W × H × D)	160 × 160 × 150 cm (W × H × D)
Camera weight	2.8 tons	0.8 tons
Camera support	Quadrupod	Quadrupod
Weight of complete telescope	580 tons (incl. mirrors, camera)	60 tons (incl. mirrors, camera)

Every source in the ATOM database is observed typically once every three nights in R and B bands. Observations in V and I bands are also possible. The data collected are analyzed with an automatic pipeline that performs standard reduction, photometry and source calibration. For the photometry, an aperture of 4'' radius is used. Reference stars present on the same frame are used for the calibration. These in turn are calibrated using standard stars. The observation of standard stars can be used also for measuring the evolution of the atmospheric transmission on the H.E.S.S. site.

CHAPTER 4

DATA COLLECTION AND ANALYSIS

In this chapter, it will be explained how observations with IACT are done, how the data are collected and analyzed and how the signal is reconstructed. Two reconstruction methods are described, following the implementation adopted in the software framework used in this work, as well as the different procedures for the background rejection. Finally, the spectral, temporal and morphological analyses are presented.

4.1 OBSERVATION METHODS

Observations with IACTs are usually carried out only during the moonless part of the night, the so called “dark time”. One reason is the moonshine, which would hinder the detection of the very faint flashes of Cherenkov light. Another reason is the serious risk of damaging the cameras, would too much light enter the PMTs. This leads to the loss of about 50% of the night time, significantly limiting the duty cycle of the telescopes. In order to reduce the lost hours, some IACTs make use of UV filters that permit the observation during periods with (partial) moon coverage, at the expenses of a higher energy threshold. During the night, the dark time is subdivided in “runs”, single observations with a typical exposure of 28 minutes.

The original observation strategy used with the first IACTs was the so called ON/OFF mode. This method consists in alternating runs on the actual target (ON run) and on an empty part of the sky that will be used to derive a background estimation (OFF run). In order to keep the observation conditions of the two runs as similar as possible, the telescope is moved 30 minutes in Right Ascension, but maintained at the same Zenith angle. This strategy is particularly useful for single telescope instruments with relatively small FoV. It has the advantage that the target is placed at the center of the camera, which is the most sensitive part. The main disadvantage is the need to spend half of the available dark time off-source.

Modern IACTs have a larger FoV and their cameras have a more homogeneous response.

The wobble mode observation method is hence more appropriate: it allows the simultaneous recording of ON and OFF data (see sec. 4.7). In wobble mode, the telescope is pointed slightly offset from the observed target, which is kept in the FoV at all times. The offset is typically between 0.5° and 1.0° and is alternated in four different directions in Right Ascension and Declination with respect to the target position. When one axis is moved, the other is kept at the target nominal position. For each set of four observations, the ON region is in the middle of the total FoV. The striking advantage of the wobble mode is the suppression of dedicated OFF source observations, with the consequent doubling of ON source time. Another benefit is the fact that ON and OFF data are taken under the exact same conditions. The biggest disadvantages occur for very extended sources or for crowded regions (as it is the case in the Galactic Plane), for which it becomes difficult to find usable background regions.

4.2 SHOWER IMAGING

The Cherenkov radiation emitted by the particles in the air showers is collected by the large mirrors and reflected onto the PMT cameras. The resulting image on the focal plane is a two dimensional projection of the shower with an elongated elliptical shape.

In Fig. 4.1 the mapping of an air shower is sketched. In the left panel one can see how the orientation of the image depends on the inclination of the shower axis with respect to the telescope optical axis. In the right panel, the shape of the light distribution in the camera is explained. The length of the image is determined by $\Delta\phi = \phi_2 - \phi_1$, its position by the distance R between the telescope and the shower axis and its width by the shower lateral extent. This implies that the farther a shower is from the telescope, the more its image will be elongated and nearer to the border of the camera. The elongation also depends on the Zenith angle of the observation: for the same impact distance from the telescope, showers from larger Zenith angles will produce more elongated images.

Once the shower image has been collected, the original particle that ignited the air shower must be reconstructed. In the next two sections two different methods used for this work will be briefly described.

4.3 HILLAS RECONSTRUCTION

The first and most simple method used for the event reconstruction is based on the Hillas parameterization of the shower image (Hillas 1985) and is based on the fact that the images of γ -ray photons are to good approximation elliptical. This is not true for most hadron induced showers because in hadronic interactions the transferred lateral momentum is larger and leads to a much larger lateral spread of the shower. Its footprint is more irregular and shows several isolated clusters. This difference is useful for the background rejection.

The values of all the parameters needed for the event reconstruction can be determined from a single shower image. However, the stereoscopic approach greatly improves the determination

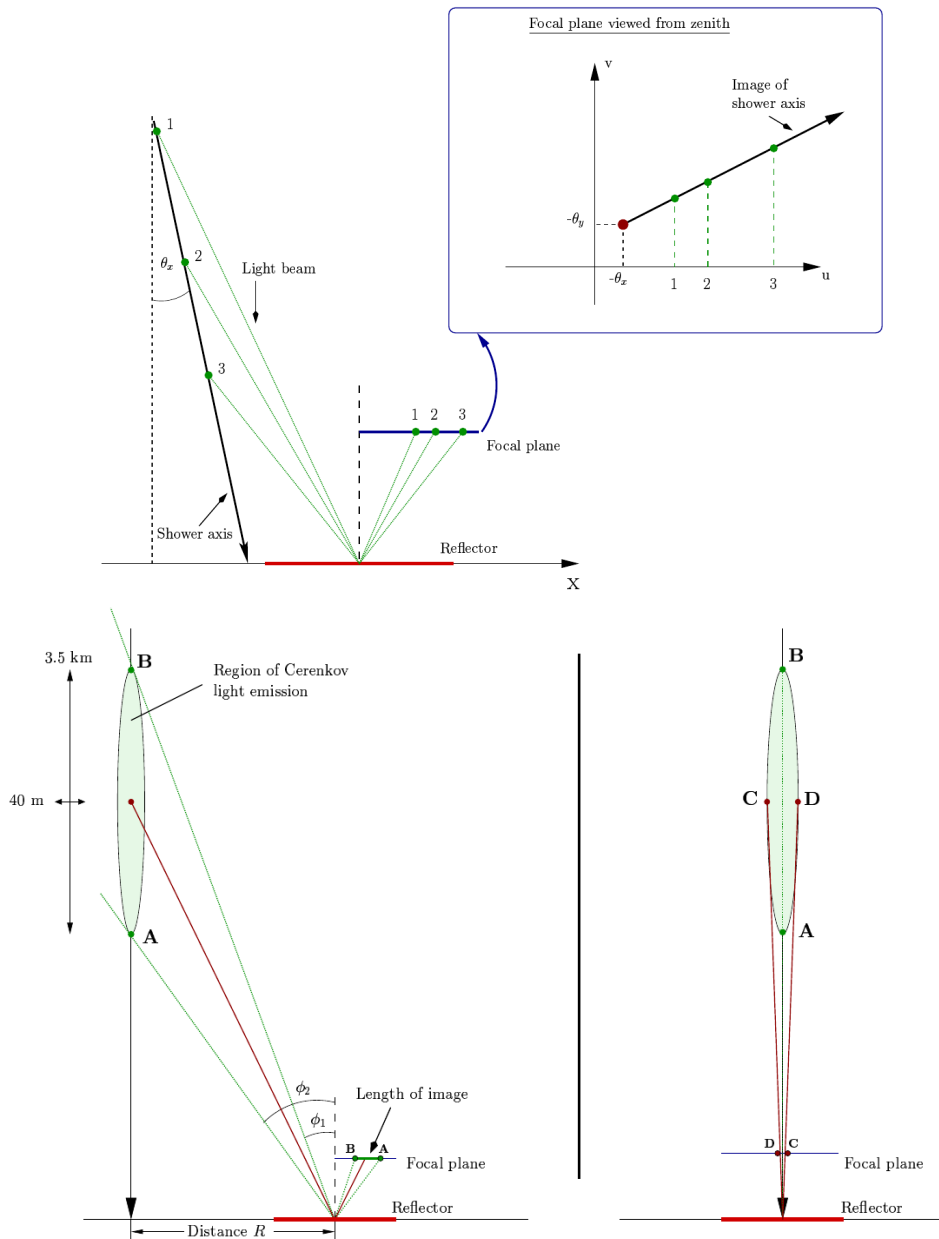


Figure 4.1: Mapping of an air shower onto the telescope camera. *Top:* the orientation of the image depends on the inclination of the shower axis with respect to the telescope optical axis. *Bottom:* the shape and size of the distribution depends on $\Delta\phi = \phi_2 - \phi_1$, R and the width of the shower (from Berge 2006).

of the shower direction and of the impact parameter, thus yielding a more precise reconstruction.

The parameters are the following (Fig. 4.2):

- the length L and width w of the ellipse;
- the image amplitude (*size*) as number of p.e.;

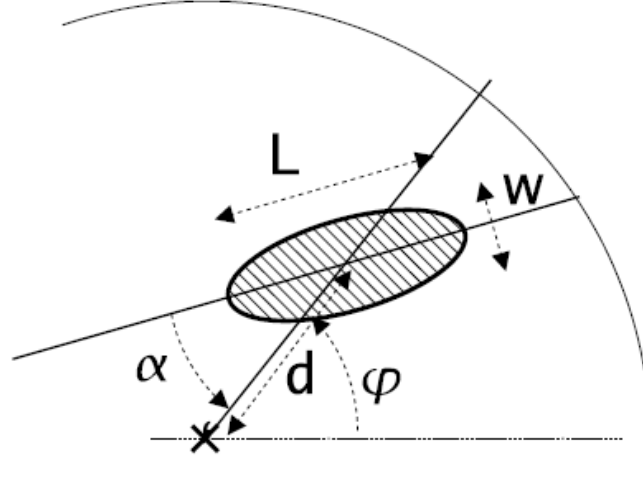


Figure 4.2: Schematic representation of the Hillas parameters (from De Naurois 2012).

- the nominal distance d . It is the distance, measured in degrees, between the center of the camera and the center of gravity (COG) of the image;
- the azimuthal angle of the image main axis φ ;
- the orientation angle α .

They can be expressed analytically using the measured intensity q_i and the position (x_i, y_i) of each pixel. From the first and second moments one has

$$\langle x \rangle = \frac{\sum_i x_i q_i}{\sum_i q_i} \quad \langle y \rangle = \frac{\sum_i y_i q_i}{\sum_i q_i} \quad (4.1)$$

$$\langle x^2 \rangle = \frac{\sum_i x_i^2 q_i}{\sum_i q_i} \quad \langle y^2 \rangle = \frac{\sum_i y_i^2 q_i}{\sum_i q_i} \quad \langle xy \rangle = \frac{\sum_i x_i y_i q_i}{\sum_i q_i} \quad (4.2)$$

and the respective variances and covariances

$$\sigma_{x^2} = \langle x^2 \rangle - \langle x \rangle^2, \quad \sigma_{y^2} = \langle y^2 \rangle - \langle y \rangle^2, \quad \sigma_{xy} = \langle xy \rangle - \langle x \rangle \langle y \rangle. \quad (4.3)$$

One can define the variables

$$\chi = \sigma_{x^2} - \sigma_{y^2} \quad (4.4a)$$

$$z = \sqrt{\chi^2 + 4\sigma_{xy}} \quad (4.4b)$$

$$b = \sqrt{\frac{(1 + \chi/z)\langle x \rangle^2 + (1 - \chi/z)\langle y \rangle^2 - 2\sigma_{xy}\langle x \rangle \langle y \rangle}{2}} \quad (4.4c)$$

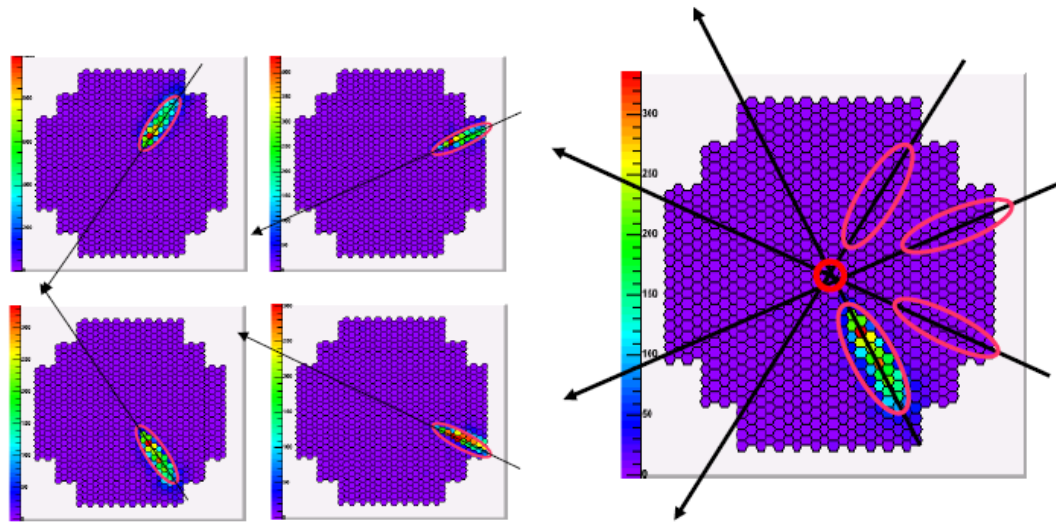


Figure 4.3: Shower images seen from the single telescopes in stereoscopic observations (*left*) and their superposition (*right*). The direction of the primary particle is given by the intersection of the main axes (from De Naurois 2012).

The Hillas parameters are then simply

$$d = \sqrt{\langle x \rangle^2 + \langle y \rangle^2} \quad (4.5a)$$

$$L = \sigma_x^2 + \sigma_y^2 + z \quad (4.5b)$$

$$w = \sigma_x^2 + \sigma_y^2 - z \quad (4.5c)$$

$$\alpha = \arcsin\left(\frac{b}{d}\right) \quad (4.5d)$$

In this parameterization, only the pixels contained in the shower image must be taken into account. An image cleaning is therefore needed to remove pixels with intensities unrelated to the shower, likely due to PMT noise or to NSB. The algorithm considers two intensity thresholds $T_{high} = 10 \text{ p.e.}$ and $T_{low} = 5 \text{ p.e.}$. Only the pixels that have an intensity above one of the two thresholds and at least one neighboring pixel above the other threshold are kept. An additional cut is made on the nominal distance d to avoid images too close to the edge of the camera, that could be truncated and hence misreconstructed.

For stereoscopic observations, the direction of the primary particle is given by the intersection of the main axes of the shower images seen by the single telescopes. Being these main axes non perfectly precise, one will have for N telescopes $N(N - 1)/2$ intersections. Therefore, the “true” value is calculated as a weighted¹ average of the multiple intersections. The shower impact point is calculated in a similar way, considering the geometrical intersection of the planes in the sky that contain the telescopes and the shower track.

¹The weight depends on the *size*, L and w parameters.

4.3.1 ENERGY RECONSTRUCTION

The estimation of the particle energy must rely on lookup tables, derived from Montecarlo (MC) simulations, which assume that all particles are γ -ray photons.

Firstly, a complete air shower is simulated, as well as the response of the H.E.S.S. array to the emitted Cherenkov light². The shower images depend on the true event energy, on the impact parameter, on the Zenith angle of the observation and on the off-axis angle (the offset between the camera center and shower position). For this reason, the simulations are computed in the energy range 30 GeV - 80 TeV for 20 Zenith angles bands, 6 off-axis angles bands and 7 optical efficiencies bands. Since the Earth magnetic field influences the development of the showers, also two Azimuth angles are taken into account. Secondly, the impact point and the image size of every shower are reconstructed for every telescope. The tables are created binning each event as function of these two parameters. For every bin, the average value and the variance of the *true* energy of the particles are finally computed.

The particle energy is estimated for each telescope using the impact parameter calculated from the full array³, interpolating the values in the lookup tables. The single values are then averaged over all telescopes, weighting over the uncertainties of the single measurements.

The typical energy resolution is of the order of 15-20%. The energy reconstruction becomes more precise with increasing primary energy. On the one hand, this is due to the fact that more light is collected by each camera, leading to smaller statistical fluctuations in the image size. On the other hand, the intrinsic shower fluctuations decrease with increasing energy. Significant biases exist below 100 GeV and above 20 TeV.

4.3.2 γ -HADRON SEPARATION

Most of the events detected with IACTs are not photons, but hadronic particles. Hadronic events exceed γ -ray events of a factor 10^3 to 10^4 . It is therefore necessary to find a way to suppress them. The use of stereoscopy helps avoiding single telescope events. Other methods involve applying cuts on the clean images. Again, the properties of the shower can be exploited. As discussed in sec. 2.4.1, the air showers generated by hadronic interactions are less regular, broader and less luminous than the showers generated by γ -ray photons of the same energy. Two kinds of cuts are used: *size* cuts and *shape* cuts. The first ones require the image size to be above a certain p.e. value. Usually thresholds of 40, 80 and 200 p.e. are used. The second ones rely on the use of two variables, the mean reduced scaled width (MRSW) and the mean reduced scaled length

²The system response takes into account a large series of parameters: the reflector layout, its orientation with respect to the air shower, the shadow of the camera support structure, the mirror reflectivity, the transmission of the Winston cones, the optical PSF, the quantum efficiency of the PMTs and the pulse shape of the PMT signals.

³Since the amount of Cherenkov light at a given distance from the shower axis is approximately proportional to the primary energy, a precise reconstruction of the impact distance is important.

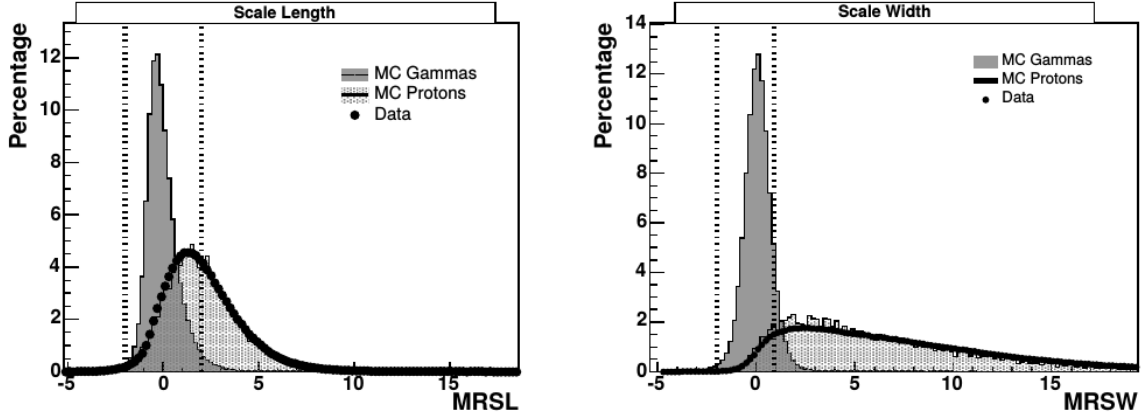


Figure 4.4: Distributions of the MRSL (*left*) and MRSW (*right*) variables for MC simulated γ -ray photons (gray histogram) and protons (hatched histogram) and for real off-source data (black points). The dashed vertical lines indicate the minimum and maximum cut values (from Funk 2005).

Table 4.1: Cuts configurations used in the Hillas analysis. The θ^2 cut is given for point-like sources. “c.u.” indicates source flux in units of the Crab Nebula flux.

Config.	MRSL		MRSW		θ^2 [deg ²]	<i>size</i> [p.e.]	Nom. dist. [deg]	Optimization
	min	max	min	max				
<i>Hard</i>	-2.0	2.0	-2.0	0.7	< 0.01	> 200	2.0	Faint sources ($\sim 1\%$ c.u.) with hard spectra ($\Gamma \sim 2.0$). For discovery and morphological analysis.
<i>Standard</i> (<i>Std</i>)	-2.0	2.0	-2.0	0.9	< 0.0125	> 80	2.0	Luminous sources ($\sim 10\%$ c.u.) with Crab-like spectra ($\Gamma \sim 2.6$). For spectral analysis.
<i>Loose</i>	-2.0	2.0	-2.0	1.2	< 0.04	> 40	2.0	Low energy sources with soft spectra ($\Gamma \sim 3.0$). For spectral analysis.

(MRSL), defined as

$$\text{MRSW} = \frac{1}{N_{tel}} \sum_{i=1}^{N_{tel}} \frac{w_i - \langle w \rangle_{MC,i}}{\sigma_{MC,i}} \quad \text{MRSL} = \frac{1}{N_{tel}} \sum_{i=1}^{N_{tel}} \frac{L_i - \langle L \rangle_{MC,i}}{\sigma_{MC,i}} \quad (4.6)$$

where MC refers to the values expected from MC simulations. As it can be seen in Fig. 4.4, photons and hadrons have very different MRSW and MRSL distributions. Minimum and maximum values can be defined, and all events falling outside this range are rejected. Most of the rejection is provided by the maximum value of MRSW. However, the *shape* cuts cannot eliminate completely the hadronic component. What remains after cuts is referred to as γ -like events. For the spectral analysis, an additional cut on the angular distance from the source position is used. It depends on the instrument PSF and on the source size and it is usually defined as the 68% containment radius. These cuts are combined in cuts configurations, which are optimized for sources with different characteristics. They are summarized in Table 4.1.

4.4 MODEL RECONSTRUCTION

A more sophisticated reconstruction method is represented by the Model Analysis (de Naurois & Rolland 2009). Here, the raw camera image is compared directly with the shower image predicted by a semi-analytical model. This technique was first investigated in Le Bohec et al. (1998) and was later further developed including a fit algorithm based on a log-likelihood minimization. The Model reconstruction, although it requires longer computing time, has several advantages with respect to the simpler Hillas reconstruction, outperforming it in basically every aspect of the analysis. In the following, the bases and the most important features of the model will be briefly described (for the details and the equations of the analytical parameterization please refer to de Naurois & Rolland 2009).

The shower images predicted by the semi-analytical model are obtained from the parameterization of the Cherenkov light pool of the simulated air showers (sec. 2.4.1). The light distribution depends on the longitudinal, lateral and angular distribution of the charged particles in the shower. The depth of the first interaction is taken into account, as well, in order to reduce the discrepancy between shower images and model predictions. The particle air showers are simulated at energies of 10 GeV, 50 GeV, 100 GeV, 500 GeV, 1 TeV, 5 TeV, 10 TeV and 20 TeV to cover the dynamical range of H.E.S.S. In addition, the noise from NSB is modeled for every pixel and enters the likelihood fit. Thus, an image cleaning procedure is not needed.

The light density can be calculated for every pixel in the camera with an eight-dimensional integral that depends on:

- the depth of the shower (longitudinal development);
- the electron/positron energy in the shower;
- the particle direction with respect to the telescope (two parameters);
- the particle position with respect to its direction (two parameters);
- the Cherenkov photon wavelengths;
- the azimuthal angle of the Cherenkov light around the electron (fixed for a given particle energy).

Moreover, the telescope response and the environmental conditions must be taken into account as well: PSF, electronic response of the PMTs, geometric light collection efficiency, atmospheric absorption, reflectivity and wavelength-dependent quantum efficiency. All these values are available in look-up tables. The telescope response is obtained with detailed simulations.

The shower models (Fig. 4.5) are generated for sets of different parameters:

- 40 Zenith angles θ_z ;
- 40 impact distances from the telescope between 0 and $440/\cos(\theta_z)$ m;
- 65 energies between $50/\cos(\theta_z)$ GeV and $20/\cos(\theta_z)$ TeV;
- 6 first interaction depths between 0 and 5.

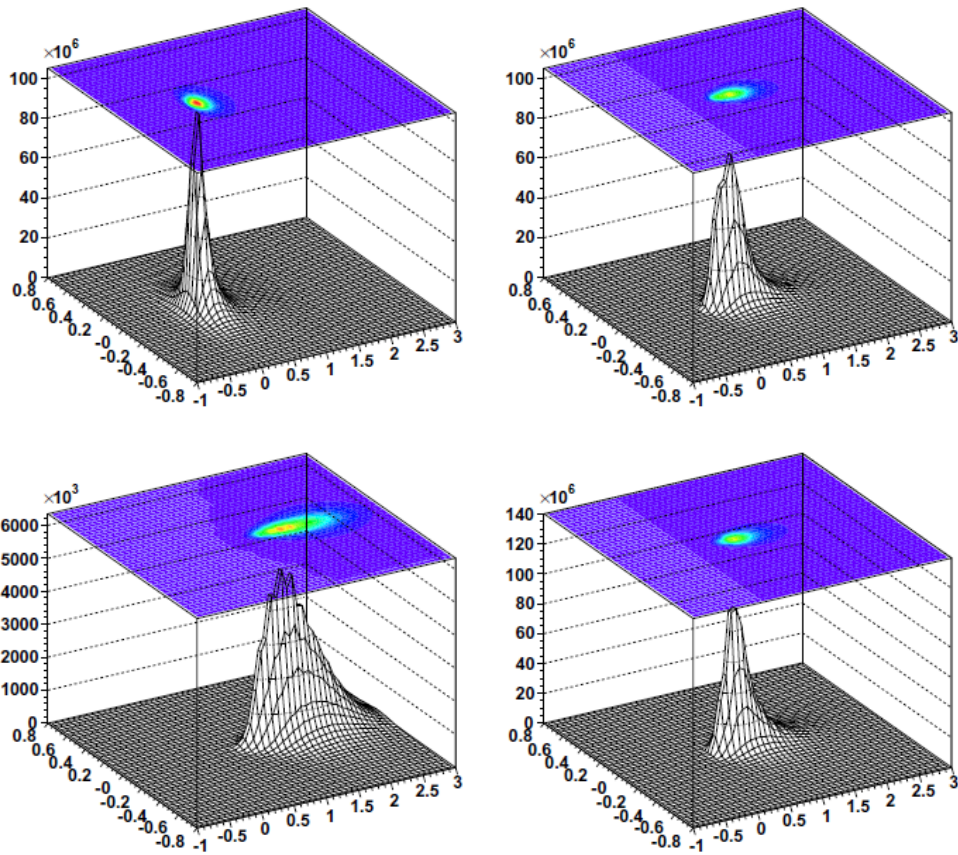


Figure 4.5: Model of a 1 TeV shower started at one radiation length and falling 20 m (*top-left*), 100 m (*top-right*) and 250 m (*bottom-left*) away from the telescope. *Bottom-right*: same as *top-right* but with a first interaction point at three radiation lengths. The x and y axis are in degrees in the camera frame. Note that the vertical scale differs (from de Naurois & Rolland 2009).

The comparison between the raw camera image and the generated parametrized models is done with a log-likelihood minimization procedure under the hypothesis that the particle is a γ -ray photon. The fit is performed on the whole camera, comparing the intensities from every pixel, each of them yielding a log-likelihood value. The total telescope log-likelihood is the sum of the pixels log-likelihood.

The best fit parameters (and their uncertainties) for the primary photon energy, the impact distance (two parameters), the photon direction (two parameters) and the depth of the first interaction are obtained with a minimization procedure.

4.4.1 γ -HADRON SEPARATION

As for the Hillas reconstruction, cuts must be used in order to discriminate between the γ -ray signal and the dominating hadronic background. Again, the differences between hadronic and electromagnetic showers can be exploited. As already mentioned, hadronic showers are more

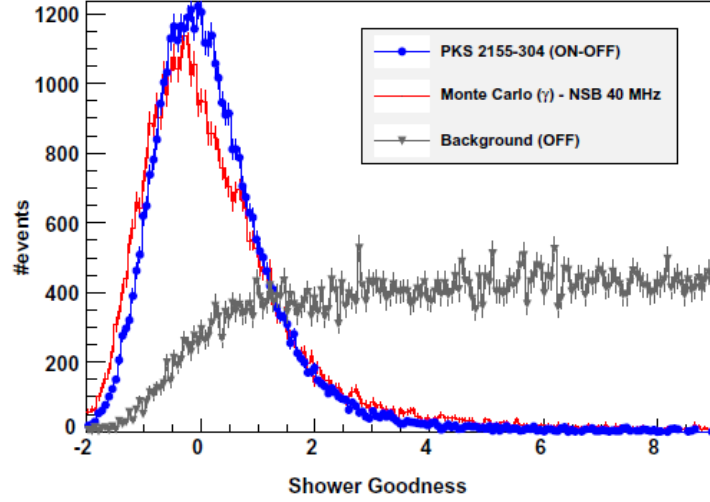


Figure 4.6: Distribution of the *ShowerGoodness* for real data (PKS 2155-304, excess events in blue, background events in grey), compared to a simulation with a similar night sky background level (red histogram). The shapes recall those of the MRSW and MRSL of the Hillas analysis (from de Naurois & Rolland 2009).

irregular, contain several sub-showers, have a larger lateral spread and emit less Cherenkov light compared to an equally energetic electromagnetic primary particle. As a consequence, images are fainter, more spread out in the camera and often exhibit several separated clusters.

The γ -hadron separation in the Model reconstruction is based on the *goodness-of-fit* approach, which checks the compatibility of the recorded image with the null hypothesis of a γ -ray event. The *goodness-of-fit* is defined as

$$G = \frac{\sum_{\text{pixel } i} [\ln L(s_i | \mu_i) - \langle \ln L \rangle |_{\mu_i}]}{\sqrt{2 \times \text{NdF}}} \quad (4.7)$$

where $\ln L(s_i | \mu_i)$ is the pixel log-likelihood of a signal s_i given an expected value μ_i , $\langle \ln L \rangle |_{\mu_i}$ is the pixel expectation value and NdF is the number of degrees of freedom (number of pixels - 6 parameters). The *goodness-of-fit* behaves asymptotically like a χ^2 distribution and G is expected to behave like a normal variable with $\langle G \rangle = 0$ and $\sigma^2(G) = 1$.

In order to exploit the differences between the γ and hadron shower images, the *ShowerGoodness* (SG) and the *BackgroundGoodness* (BG) discriminators were implemented. They are both based on eq. 4.7, but involve two different groups of pixels instead of the whole camera:

- *ShowerGoodness*: it takes into account the pixels belonging to the shower core. This is defined as the pixels with a predicted amplitude above 0.01 p.e., together with three rows of neighboring pixels. This variable is much more sensitive to discrepancies between model prediction and actual shower image than the *goodness-of-fit* thanks to the much smaller number of the NdF.
- *BackgroundGoodness*: it takes into account all remaining pixels. This variable is sensitive

Table 4.2: Cuts configurations used in the Model analysis for CT 1-4 data. The θ^2 cut is given for point-like sources. c.u. indicates source flux in units of the Crab Nebula flux.

Config.	MSSG		θ^2 [deg ²]	<i>size</i> [p.e.]	Nom. dist. max [deg]	Primary depth		NSBL min	Optimization
	min	max				min	max		
<i>Faint</i>	-3.0	0.4	0.005	120	2.0	-1.0	4.0	-1.0	For sources fainter than few c.u.
<i>Standard</i>	-3.0	0.6	0.01	60	2.0	-1.0	4.0	-1.0	
<i>Loose</i>	-2.0	0.9	0.0125	40	2.0	N/A	N/A	N/A	Maximizes the γ -ray efficiency for strong sources; poorer background rejection

For all cuts configurations, at least two telescopes must pass the shape cuts.

A value of BG < 2 is used in all cut configurations for safety (it gives no background rejection).

to hadronic clusters, hadronic rains and other irregularities outside the main image.

The distribution of the SG is similar to those of the MRSW and MRSL for the Hillas reconstruction, and is shown in Fig. 4.6. After applying cuts on the SG, the BG loses its background rejection power. It can still be useful as a safety check.

Initially, the *ShowerGoodness* and the *BackgroundGoodness* were not implemented in the Model reconstruction, which was often combined with other reconstruction methods and respective cuts in order to increase the sensitivity. With the introduction of these new discriminators, the combination lost all effects and the upgraded Model analysis was renominated as Model++ (in short M++). This new name will be used in the following chapters of this work.

As for the Hillas analysis, several sets of cuts has been defined (Table 4.2). A *MeanScaled-ShowerGoodness* is used instead of the SG. In addition, a similar variable on the NSB (*NSBLikelihood*, NSBL) has been implemented. It is defined as the comparison between two hypothesis: the image results from the shower, or the image results only from NSB fluctuations ($\mu = 0$):

$$\text{NSBL} = \frac{\sum_{\text{pixel } i} [\ln L(s_i | \mu_i) - \ln L(s_i | \mu_i = 0)]}{\text{NdF}} \quad (4.8)$$

With the addition of CT 5 and the consequent use of Mono and Stereo analyses, other cuts were required (Table 4.3). In particular, one cut on the minimum containment fraction of the model image inside the camera and one on the minimum number of pixels above 5 p.e. in the shower were introduced. In addition, the NSBL variable was substituted by the *NSBGoodness* (NSBG), which checks how good is the null hypothesis of the image resulting only from NSB. It has the same form of eq. 4.7:

$$\text{NSBG} = \frac{\sum_{\text{pixel } i} [\ln L(s_i | \mu_i = 0) - \langle \ln L(s_i | \mu_i = 0) \rangle]}{\sqrt{2 \times \text{NdF}}} \quad (4.9)$$

Table 4.3: Cuts configurations used in the Model Mono and Stereo analyses with Prod6 DSTs and software version paris-0-8-30 (see sec. 4.11). The θ^2 cut is given for point-like sources.

Config.	MSSG		θ^2 [deg ²]	<i>size</i> [p.e.]	Nom. dist. max [deg]	Primary depth		NSBG min	Min.cont. fraction	#pixels > 5 p.e.
	min	max				min	max			
Stereo										
<i>Faint</i>	-4.0	0.9	0.005	120	2.0	-1.1	3.4	60	0.5	5
<i>Standard</i>	-4.0	0.9	0.006	60	2.0	-1.1	3.4	28	0.5	5
<i>Loose</i>	-4.0	0.9	0.008	40	2.0	-1.1	3.4	15	0.5	5
<i>VeryLoose</i>	-4.0	0.9	0.010	20/40 [†]	2.0	-1.1	3.4	N/A	0.5	0
Mono										
<i>Safe</i>	-4.0	0.6	0.015	60	1.4	-1.1	1.3	40	0.5	5
<i>Standard</i>	-4.0	0.6	0.015	60	1.4	-1.1	1.3	32	0.5	5
<i>Loose</i>	-4.0	0.6	0.015	60	1.4	-1.1	1.3	24	0.5	5

[†] 20 p.e. for CT 1-4 and 40 p.e. for CT5

For all cuts configurations of the Stereo analysis, at least two telescopes must pass the shape cuts.

A value of BG < 2 is used in all cuts configurations for safety (it gives no background rejection).

A direction error < 0.2° for Stereo and < 0.3° for Mono is used for safety (it gives no background rejection).

It has to be noted here that the Mono/Stereo cuts are actually very different and in some aspects much harder than the CT 1-4 cuts, despite having similar names. This leads to different event selections which can reject events accepted by the CT 1-4 analysis. A direct comparison based on the cut name is therefore meaningless.

4.4.2 COMPARISON MODEL VS. HILLAS RECONSTRUCTION

The performances of the semi-analytical approach with log-likelihood minimization of the Model reconstruction are much better than those of the simpler Hillas parameter reconstruction. In the following, results of the Model analysis with *Standard* cuts are compared to the results of the Hillas analysis with both *Standard* and *Hard* cuts. In general, the semi-analytical model outperforms the simpler one on every aspect of the event reconstruction.

The effective area plot in the left panel of Fig. 4.7 show similar values for the Model and Hillas reconstructions using *Standard* cuts. The Model analysis loses acceptance at high energies because the shower models are generated only up to 20 TeV. Nonetheless, for a given γ -ray efficiency, the Model reconstruction yields a much higher background rejection than the Hillas analysis (Fig. 4.7, *right*). This characteristic improves the sensitivity by a factor more than 2.

The energy resolution⁴ of the Model *Standard* analysis (Fig. 4.8) is comparable to the Hillas *Hard* cuts analysis at low energies and a factor 2 better at high energies. The resolution is better than 15% in the whole energy range and better than 10% above 1 TeV. The energy bias is also

⁴The energy resolution is defined as the RMS of the $\Delta E/E$ distribution.

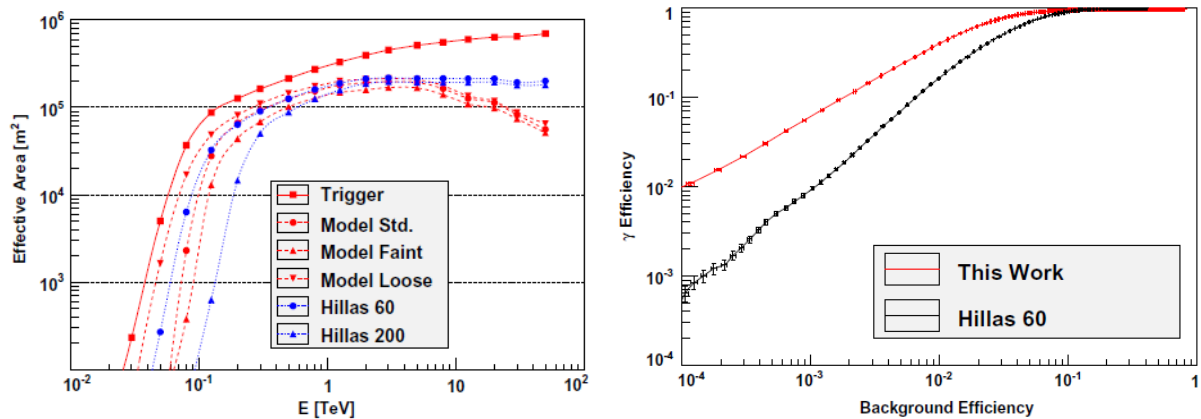


Figure 4.7: *Left:* Effective areas as function of energy, at zenith. In red, the values for the Model analysis for three different cuts, compared to the Hillas analysis, in blue. *Right:* Model γ -ray efficiency (red) as function of the background rejection for a selection based on *ShowerGoodness* only, after shape cuts, compared to the results of the standard Hillas reconstruction (black) using the MRSW and MRSL variables. From de Naurois & Rolland (2009).

better than 5% on a wide energy range and is always better than for the equivalent Hillas analysis.

The angular resolution⁵ of the Model reconstruction is smaller than 0.1° both as function of the energy and of the Zenith angle (Fig. 4.9). It is relatively constant around 0.06° in a large energy range and up to at least 50° Zenith angle. It is more stable than in the case of the Hillas analysis and a factor 2 better compared to the equivalent cut. As a consequence, the resulting θ^2 distributions are twice as much peaked, as can be seen in the comparison in Fig. 4.10 for the analysis of Crab Nebula data. This yields an improved sensitivity for point-like sources and for morphological studies.

⁵The angular resolution is defined as the 68% containment radius.

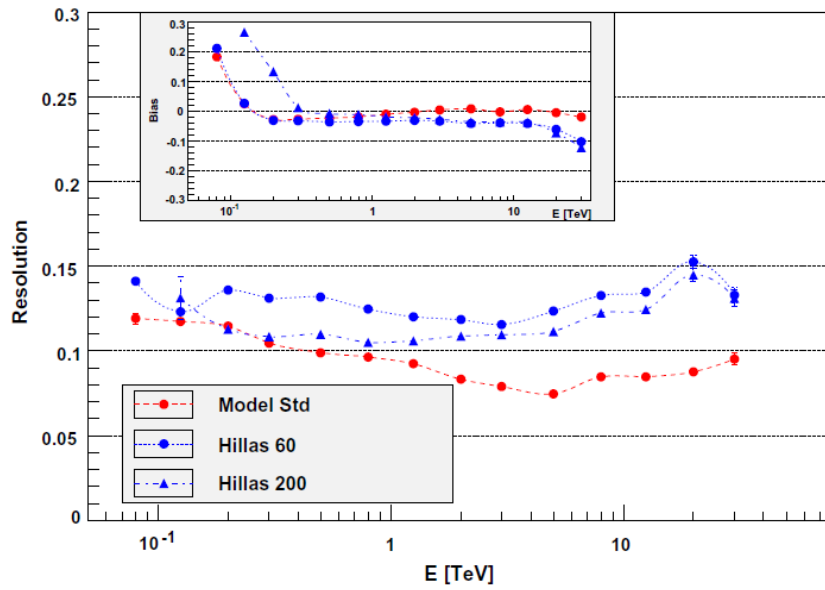


Figure 4.8: Energy resolution (main plot) and bias (inset) as function of energy, at zenith, for the Model (red) and Hillas (blue) reconstructions. From de Naurois & Rolland (2009).

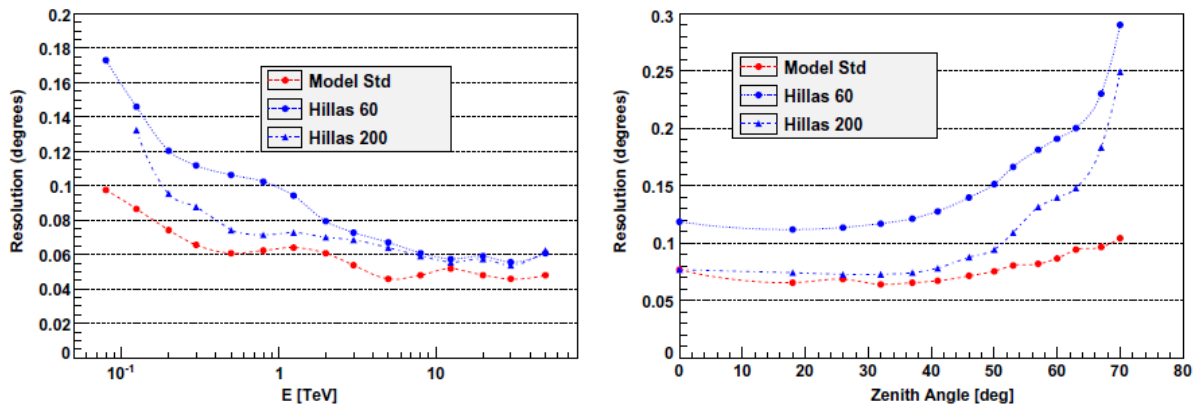


Figure 4.9: *Left:* angular resolution as a function of the energy, at zenith, for the Model analysis (red) compared to the values obtained for the Hillas analysis. *Right:* average angular resolution for a E^{-2} spectrum, as a function of zenith angle. From de Naurois & Rolland (2009).

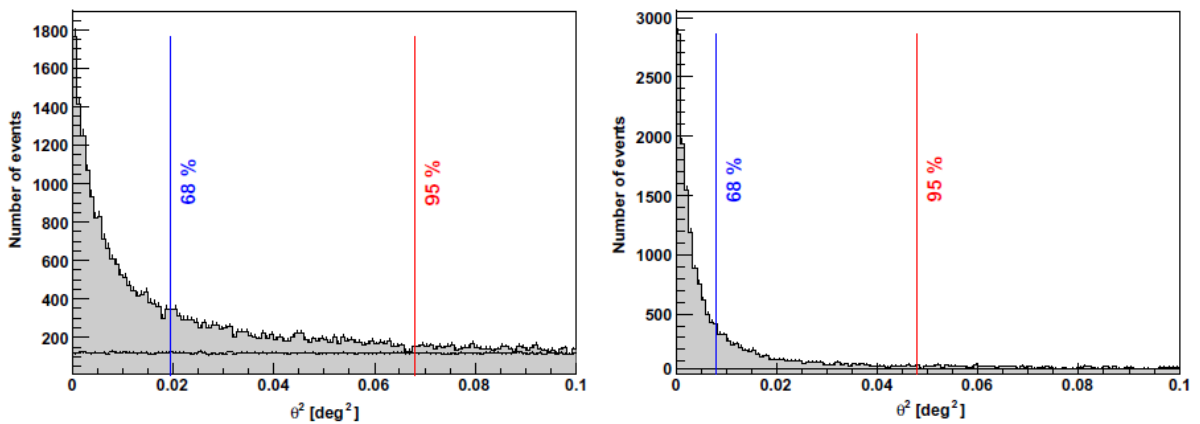


Figure 4.10: Squared angular distribution of Crab Nebula data for the Hillas analysis with *Standard* cuts (*left*) and for the Model analysis (*right*). From de Naurois & Rolland (2009).

4.5 SIGNAL EXTRACTION

The cuts applied on the reconstructed images help separating the γ -ray candidates from the cosmic ray (CR) events. However, it is not possible to reject all background because the γ -ray and CR distributions overlap and because of the presence of electrons and positrons. Their showers are purely electromagnetic and are hardly distinguishable from the γ -ray induced ones. Therefore, the background component ought to be determined (see sec. 4.7) and subtracted from the signal in the region of interest. Given N_{ON} and N_{OFF} events in the source and background regions, respectively, the true γ -ray signal N_γ is defined as

$$N_\gamma = N_{ON} - \alpha N_{OFF} \quad (4.10a)$$

$$\Delta N_\gamma = \sqrt{N_{ON} + \alpha^2 N_{OFF}} \quad (4.10b)$$

where ΔN_γ is the poissonian error estimation and α is a normalization factor that takes into account the difference of area and instrument response between the ON and OFF regions. For a dataset containing i runs, one will have

$$N_\gamma = \sum_i N_{\gamma,i} = \sum_i N_{ON,i} - \alpha' \sum_i N_{OFF,i} \quad \text{with} \quad \alpha' = \frac{\sum_i \alpha_i N_{OFF,i}}{\sum_i N_{OFF,i}} \quad (4.11)$$

The statistical significance S_γ of the excess N_γ is given by the LiMa statistics (Li & Ma 1983)

$$S_\gamma = \sqrt{-2 \ln \lambda} \quad (4.12)$$

$\lambda = P_0(H_0)/P(H)$ is the likelihood ratio between two hypothesis:

- the *null hypothesis* H_0 , for which the N_{ON} events consist only of background ($\alpha \times B$);
- the hypothesis H to be tested, for which the N_{ON} events consist of background ($\alpha \times B$) plus signal (S).

The probabilities in the two cases are, respectively:

$$P_0(N_{ON}, N_{OFF}|B) = \frac{e^{-\alpha B} (\alpha B)^{N_{ON}}}{N_{ON}!} \times \frac{e^{-B} B^{N_{OFF}}}{N_{OFF}!} \quad (4.13a)$$

$$P(N_{ON}, N_{OFF}|S, B) = \frac{e^{-(S+\alpha B)} (S + \alpha B)^{N_{ON}}}{N_{ON}!} \times \frac{e^{-B} B^{N_{OFF}}}{N_{OFF}!} \quad (4.13b)$$

Maximizing the likelihood for S , B and B_0 (for the null hypothesis), one obtains the optimal values for the three parameters:

$$S = N_{ON} - \alpha N_{OFF} \quad B = N_{OFF} \quad B_0 = \frac{N_{ON} + N_{OFF}}{\alpha + 1} \quad (4.14)$$

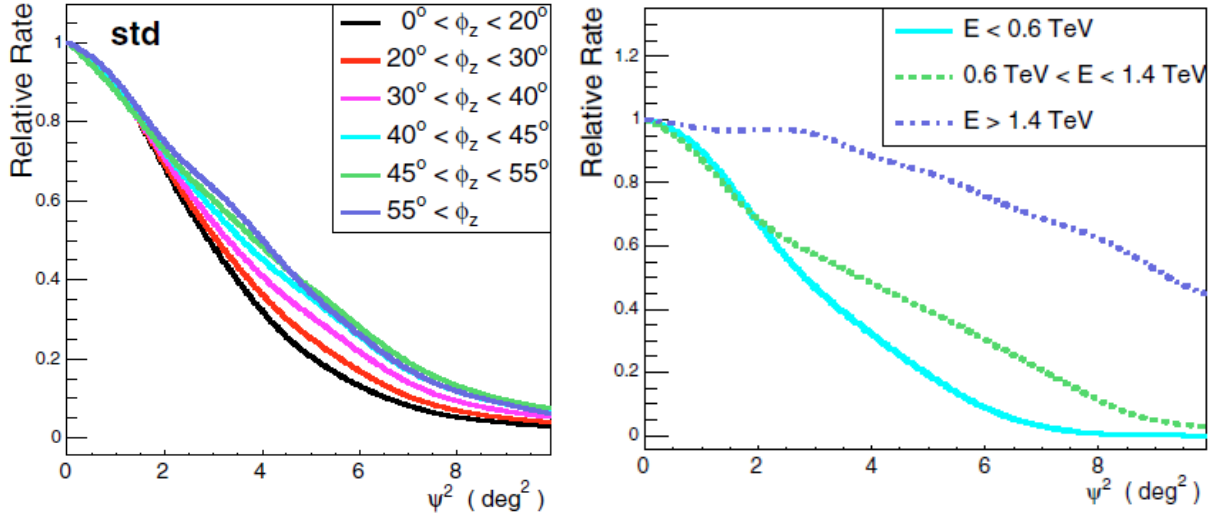


Figure 4.11: Radial acceptance from OFF source observations as function of the off-axis angle squared Ψ^2 for different Zenith angles of the observation (*left*) and γ -ray energy (*right*), for the Hillas reconstruction using Standard cuts (from Berge et al. 2007). Note that in the text the off-axis angle is referred to with θ .

The final formula of the significance reads:

$$S_\gamma = \sqrt{2} \left\{ N_{ON} \ln \left[\frac{1 + \alpha}{\alpha} \left(\frac{N_{ON}}{N_{ON} + N_{OFF}} \right) \right] + N_{OFF} \ln \left[(1 + \alpha) \left(\frac{N_{OFF}}{N_{ON} + N_{OFF}} \right) \right] \right\}^{1/2} \quad (4.15)$$

The distribution of S_γ follows a Gaussian distribution of mean 0 and width 1, provided that the statistical fluctuation on N_{ON} and N_{OFF} can be considered Poissonian. N_{ON} and N_{OFF} should be $\gtrsim 10$ in order for the formula to work properly. To claim the detection of a signal, usually a significance of at least 5 standard deviations (σ) is required. This implies a probability of $\sim 6 \times 10^{-5}$ for the signal to be a statistical fluctuation.

4.6 SYSTEM ACCEPTANCE

The system acceptance characterizes the probability that one event of given energy and type is “seen” by the telescope⁶. In general, for a given reconstruction method and cuts, it is a function of the position (θ_x, θ_y) , of the Zenith angle and of the exposure time:

$$\mathcal{A} = \mathcal{A}(\theta_x, \theta_y, \phi_z, t) \quad (4.16)$$

It also depends on the event type, i.e. if the particle is a photon or a CR. The acceptance for γ -rays is obtained from simulations and is needed in the computation of the energy spectrum. The acceptance for γ -like background events (mostly CR) and for hadron-like events must be es-

⁶Here it is meant that the event must trigger the system, be reconstructed and be selected according to its class.

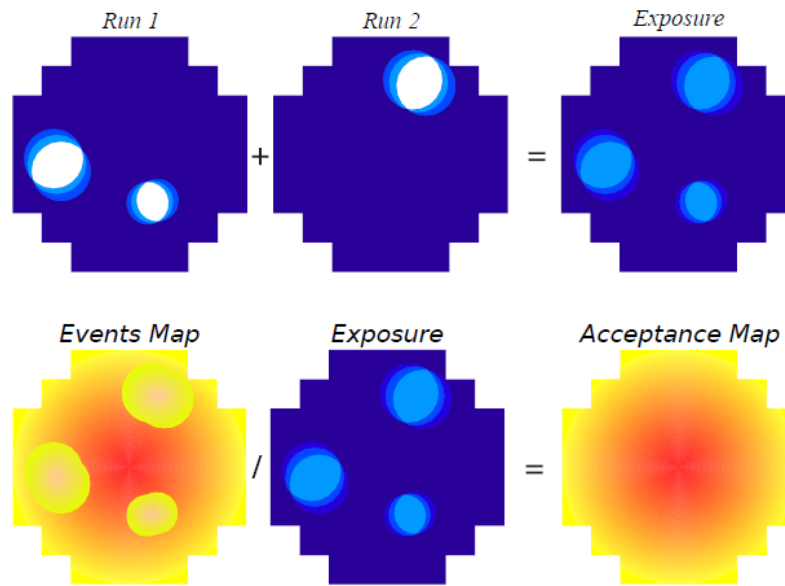


Figure 4.12: *Top:* run-wise exposure maps are summed together to create a cumulative averaged exposure map in the nominal system. *Bottom:* the nominal system acceptance map is derived dividing the event map by the exposure map (from De Naurois 2012).

timated from the data. It is required to correctly estimate the background in the region of interest. Figure 4.11 shows how the acceptance for background events is not homogeneous over the FoV and instead strongly deteriorates with the distance from the camera center. For this reason, the acceptance is calculated on a run-wise basis. For the calculation, the easiest assumption is that the acceptance is radially symmetric, so that the radial acceptance is simply $\mathcal{A} = \mathcal{A}(\theta)$. Regions with known γ -ray emission cannot enter directly the calculation and are substituted with a weight that corrects for the covered area as a function of the off-axis angle. The limits of this approximation derive from the fact that the camera is not circular and does not have a homogeneous response. More importantly, the Zenith angle varies across the FoV, introducing a gradient. This is negligible for observations close to the Zenith, but can become important for larger Zenith angle values. The gradient needs therefore to be corrected as well. Finally, the acceptance cannot be calculated if an exclusion region⁷ covers the center of the FoV.

More robust is the 2D acceptance model. Here, the acceptance is first computed in the nominal system (i.e. in the camera), then the cumulative average camera acceptance is used to compute the acceptance on the sky, taking into account the pointing of each run. The process is the following:

- an exposure map is calculated for every run: the distribution of background-like events is computed once for the whole camera, and once excluding the events that fall into an exclusion region⁸. The ratio of the two maps gives the fraction of time for which any point

⁷Regions in the sky with known γ -ray sources must be excluded from the background estimation to avoid contamination. This is done using a mask for every source in the FoV, so called exclusion region.

⁸Being the nominal system fixed, the exclusion regions move through the FoV.

in the camera has been inside an exclusion region (Fig. 4.12, *top*, Run1 and Run2);

- the run-wise exposure maps are weighted by the number of events in the run and summed together to obtain a cumulative exposure map (Fig. 4.12, *top*, Exposure);
- an event map is done in the same way for the raw distribution of γ -like events in the camera FoV. Here, only the events outside the exclusion regions are used (Fig. 4.12, *bottom*, Events Map);
- the event map is divided by the total exposure map to obtain the camera acceptance map (Fig. 4.12, *bottom*, Acceptance Map);
- the acceptance in the sky can now be calculated from the averaged cumulative acceptance map of the nominal system. For every run, the average position in the nominal system corresponding to every test position in the sky is computed. The obtained run acceptances are weighted by the number of events in each run and summed together.

This calculation can be done for both γ -like and background-like events. In order to take into account the response as function of the Zenith angle, the 2D acceptance maps are calculated in (usually 20) Zenith angle bands.

4.7 BACKGROUND EVALUATION

In order to retrieve from the data important information on the region of interest, the amount of background present therein has to be estimated. As explained in sec. 4.3.2 and 4.4.1 not all background can be removed by the cuts, and the remaining γ -like events continue to dominate above the source signal. The first method used has been the ON-OFF method (sec. 4.1). Although very simple, it has some negative draw-backs, the most important being the fact that half of the available dark time has to be spent off source. Secondly, it is not possible to reduce the statistical fluctuations and the statistical error on the background. Other methods have therefore been developed in order to resolve these issues. Here, the two relevant for the spectral analysis and the map generation done in this work are briefly presented.

4.7.1 REFLECTED REGION BACKGROUND MODEL

As seen in the previous section, the camera acceptance is not homogeneous over the whole FoV (Fig. 4.11). It strongly depends on the off-axis angle, as function of the particle energy and of the Zenith angle of the observation. When deriving the background for a spectral analysis, these dependencies must either be taken into account, or circumvented. The first option could in principle be done, but is practically not feasible. In fact, one should calibrate the detector response on γ -like cosmic ray events (which is highly complicated) and repeat it for every energy and Zenith angle band. The second option, instead, can be done easily by either observing in ON-OFF mode, or by using the Reflected Region Background model (Berge et al. 2007) when observing in wobble mode (sec. 4.1).

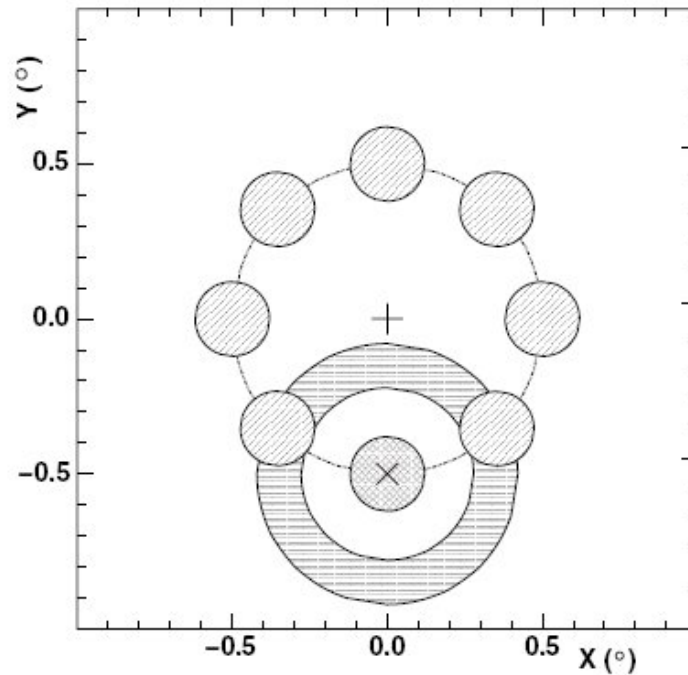


Figure 4.13: Schematic illustration of the Ring and Reflected Region Background models. The telescope pointing position lies at the image center, marked by a cross. The target position is at the center of the cross-hatched circular region and is marked with \times . The OFF region of the Ring Background method is the annular region filled by horizontal lines. The OFF regions determined with the Reflected Region Background method are the diagonally hatched circular regions on a circle around the pointing position. In this example, the OFF areas of the two models are equal (from Aharonian et al. 2006a).

The Reflected Region Background model (Fig. 4.13) relies on the assumption of a radially symmetrical acceptance. The background is estimated on a run-by-run basis and is extracted from positions in the camera with the same acceptance as the ON region. Several OFF regions with the same size as the ON region are defined on a circle with the radius of the wobble offset. To prevent γ -ray contaminations, a minimum distance between the ON and the OFF regions is required. For the same reason, exclusion region must be placed on known γ -ray sources, as well. If one or more OFF regions intersect an exclusion region, they must be excluded from the background evaluation. The normalization factor α is simply the inverse of the number of OFF regions ($\alpha = 1/N_{OFF}^{reg}$).

There are two main advantages deriving from this model. The first is the fact that ON and OFF events share the same acceptance, that have not to be taken into account. The second is the fact that, through the use of several OFF regions, the fluctuations and the statistical error of the background can be greatly reduced.

The main disadvantage is the fact that the wobble offset must be bigger than the source extension, otherwise no OFF region can be found. It is also possible that, in crowded fields with several exclusion regions or with extended sources (like in the Galactic Plane), no OFF region can be found. However, with this method is not possible to estimate the background over the

complete FoV.

4.7.2 RING BACKGROUND MODEL

To overcome the impossibility to estimate the background in the whole FoV of the instrument, the Ring Background model (Berge et al. 2007) can be used. This technique is used mostly for the creation of skymaps. Since it samples regions with different acceptances, it is not used to determine the background for the energy spectrum, due to the difficulties mentioned above.

The Ring Background model (Fig. 4.13) is employed on a binned skymap, filled with all the events of the cumulative dataset detected in the instrument FoV. An ON area and a ring around it are defined. For every bin in the map, the background is evaluated integrating over all bins that fall inside the ring centered in it. The same is done for the signal inside the ON region. As for the Reflected Region Background model, exclusion regions have to be placed on known γ -ray sources and on the target position in order to avoid contamination. If part of the ring intersects an excluded region, that part is not considered in the background evaluation. The exclusion regions are ignored when integrating over the ON area since this is meant to be the detected γ -ray signal.

Contrary to the previous method, the normalization factor α cannot be merely taken as the ratio of the ON and OFF areas, because the acceptance within the ring is not constant. In order to take this into consideration, the 2D-radial acceptances of all runs are projected onto the sky and then summed together. The total acceptances for the ON and the OFF regions are obtained as before integrating over the ON region and the ring. The normalization α will be the ratio of the two integrated acceptances ($\alpha = \sum_i \mathcal{A}_{ON,i} / \sum_j \mathcal{A}_{OFF,j}$).

The Ring Background method, although completely ignoring the energy dependence of the acceptance, has the important advantage of being able to estimate the background in any point of the FoV. This makes it very suitable for the creation of sky-maps and for morphological studies.

4.8 SPECTRAL ANALYSIS

The spectral analysis provides valuable information about the physical processes taking place inside a source. In the case of γ -ray sources, one can study the particles acceleration mechanisms, as well as the absorption mechanisms that exist between the source and the observer. The differential energy spectrum is defined as the number N_γ of γ -rays per unit of time dt , area dA and energy dE . N_γ is usually determined using the Reflected Region Background model, in order to avoid the calculation of an energy dependant normalization α . In this work, an upgraded version of the forward folding technique described in Piron et al. (2001) is used, and its analysis principles are briefly described below.

The forward folding technique relies on the assumption of a spectral shape $\Phi(E_{true})$ that is compared via a log-likelihood fit to the data. Several shapes are implemented, the ones used in this work are the following:

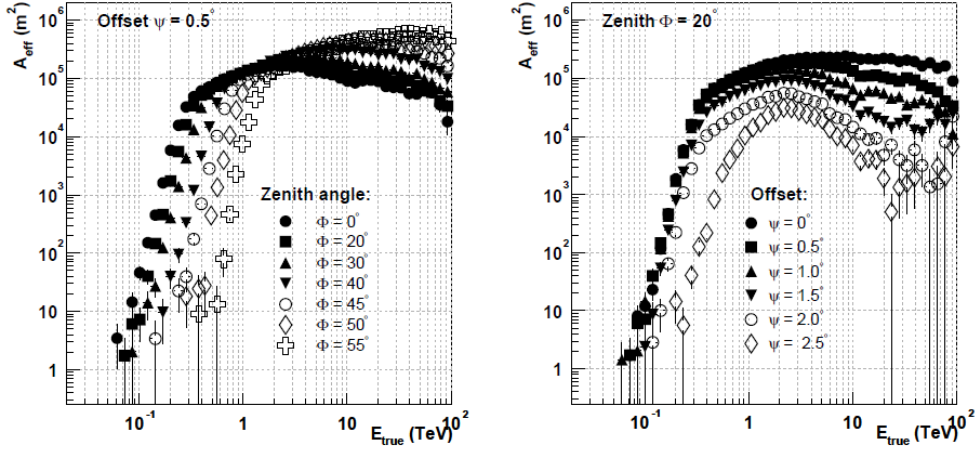


Figure 4.14: Effective area as function of the true energy for different Zenith angles and fixed off-axis angle (*left*) and for different off-axis angles and fixed Zenith angle (*right*). These are calculated for Hillas reconstruction and Standard cuts. Note that here the Zenith angle is referred to with Φ and the offset with Ψ (from Funk 2005).

Power-Law spectrum (PL)

$$\frac{dN}{dE} = N_0 \left(\frac{E}{E_0} \right)^{-\Gamma} \quad (4.17)$$

Curved Power-Law spectrum (CPL)

$$\frac{dN}{dE} = N_0 \left(\frac{E}{E_0} \right)^{-\alpha - \beta \log(E/E_0)} \quad (4.18)$$

Power-Law with Exponential cut-off spectrum (ECPL)

$$\frac{dN}{dE} = N_0 \left(\frac{E}{E_0} \right)^{-\Gamma} \times \exp\left(-\frac{E}{E_{cut}} \right) \quad (4.19)$$

As for the system acceptance, the effective area of the instrument is a function of the true energy E_{true} , the Zenith angle ϕ , the off-axis angle θ and the optical efficiency ϵ : $\mathcal{A}_{eff} = \mathcal{A}_{eff}(E_{true} | \phi, \theta, \epsilon)$. It is calculated from simulations and is tabulated as function of these parameters. The effective area also depends on the reconstruction method and on the cuts used. Examples of effective areas are depicted in Fig. 4.14. A function that relates the true photon energy with its reconstructed value is also needed. The resolution function $\mathcal{R}_{eff}(E_{rec}, E_{true} | \phi, \theta, \epsilon)$ gives the probability density of measuring a reconstructed energy E_{rec} for a given true energy E_{true} . Like the effective area, it is calculated from simulations, and depends on the reconstruction method and on the cuts used.

In order to compute the spectrum, the expected number of γ -ray events in a reconstructed

energy bin is calculated:

$$n_\gamma = \int_{E_{rec,1}}^{E_{rec,2}} dE_{rec} \int_0^\infty dE_{true} \mathcal{R}_{eff}(E_{rec}, E_{true} | \phi, \theta, \epsilon) \times \mathcal{A}_{eff}(E_{true} | \phi, \theta, \epsilon) \times \Phi(E_{true}) \quad (4.20)$$

To ease the calculation, the data are divided in Zenith angle, off-axis and efficiency bands, to form a grid. In every (ϕ, θ, ϵ) bin one has:

- the number of events from the ON dataset, N_{ON} ;
- the number of events from the OFF dataset, N_{OFF} ;
- the livetimes of the two subsets, T_{ON} and T_{OFF} ;
- the normalization $\beta = T_{ON}/T_{OFF}$;
- the expected number of γ and *hadron* events n_γ and n_h .

While n_γ is given by eq.4.20, n_h is obtained maximizing the probability of observing N_{ON} and N_{OFF} when expecting n_γ photons and n_h hadrons. It is given by:

$$n_h = \frac{C + \Delta}{2\beta(\beta + 1)} \quad (4.21)$$

where

$$C = \beta \times (N_{ON} + N_{OFF}) - (1 + \beta) \times n_\gamma \quad (4.22)$$

$$\Delta^2 = C^2 + 4\beta(\beta + 1) \times N_{OFF} \times n_\gamma \quad (4.23)$$

These log-likelihood is then maximized against the parameters of the spectral shape used. Finally, one obtains the best spectral fit parameters and their uncertainties, the covariance matrix between the parameters, the number of expected events in each bin and a likelihood values that measures the goodness of the fit. From the spectral parameters and the covariance matrix one can derive the uncertainty on the flux. The residual in each energy bin are used to calculate the spectral points. These are therefore only a product of the spectral fit, and do not contribute to its determination.

For the actual calculation of the spectrum, some additional cuts and thresholds are used. In particular, it is required that $N_{ON} \geq 1$ and $N_{OFF} \geq 5$ in every bin for it to participate actively in the fit. A threshold on the effective area is also set at 10% of its maximum (15% for Mono) to avoid steep gradients at low energies.

4.9 LIGHTCURVE DETERMINATION

The determination of lightcurves uses the same method described in the previous section. In this case, the spectral shape and its values are fixed to those derived in the spectral analysis. In each time bin, the optimal value of background events is determined. The likelihood is then

maximized against the γ -ray excess in that bin. This procedure can use all events, also the ones below the run-wise safe energy threshold. The best estimation is obviously provided when the spectral shape does not vary.

4.10 MORPHOLOGICAL ANALYSIS

As for the spectral analysis, also the morphological analysis make use of the log-likelihood forward folding technique. Here, a source morphology is assumed, instead of a spectral shape. Together with the instrument angular response, one can determine the expected number of γ -like events in every bin of a spatial map. The difference between the number of expected and observed events can be minimized against the morphological parameters. The expected number of γ -like events is

$$n_\gamma = \int \int dx dy PSF(r) \times \Phi(x, y) \quad (4.24)$$

where $PSF(r)$ is the radially symmetrical point spread function of the instrument and $\Phi(x, y)$ is the spatial source luminosity. For a point-like source one has

$$\Phi(x, y) = \sum_{i=1}^{N_{bins}} \Phi_i \delta(x - x_i) \delta(y - y_i) \quad (4.25)$$

The main advantage of the forward folding technique is that the true source shape can be estimated, and not only its convolution with the PSF as for a simple fit of the event distribution. The morphological fit of point-like sources is used to accurately determine the source position. More complex shapes are used to characterize the morphology of extended sources.

4.11 *ParisAnalysis* SOFTWARE

The analysis methods presented in this chapter follow their implementation of the *ParisAnalysis* software. Same or similar modules are implemented differently in other software environments developed by the members of the H.E.S.S. collaboration.

Several versions of *ParisAnalysis* have been used for this work, the most important being paris-0-8-24 and paris-0-8-30. The major difference between the two versions is the ability to handle HESS-II data, i.e. data collected in Mono and Stereo mode. The software version paris-0-8-24 can only analyze data from the HESS-I sub-array. This means, either data collected with the original HESS-I array, or CT 1-4 data extracted from HESS-II observations, after all information from CT 5 has been discarded. CT 1-4 data from CT 1-5 observations are referred to as HESS-I style. The software version paris-0-8-30 can in principle analyze data coming from all possible telescope sub-arrays. In practice, HESS-I (style) analysis is not possible due to the lack of implementation of the correct cuts.

The data are calibrated and saved in DST files. There are different DST productions, fol-

Table 4.4: Combination of software, sub-arrays and data production.

Sub-array	Name	Software version	DST production	Comments
CT 1-4 [†]	HESS-I HESS-I style	paris-0-8-24	Prod26	HESS-I style data obtained discarding CT 5 information from Stereo data
CT 5	Mono	paris-0-8-28	Prod4	Mono and Stereo DSTs separate; software cannot handle Prod6 DSTs; HESS-II analysis only
CT 1-5 [‡]	Stereo	paris-0-8-30	Prod6	Single Mono+Stereo DSTs; upgraded software; optimized cuts used in the analysis; HESS-II analysis only

[†] or combinations of at least 2 telescopes

[‡] or combinations of CT 5 and at least one other telescope

lowing (re-)calibrations and sub-arrays. The DST production 26 (Prod26) is used for HESS-I and HESS-I style data. The DST productions 4 and 6 (Prod4 and Prod6) are used for Mono and Stereo data. These differ for the calibration (in particular the treatment of the optical efficiencies) and for the fact that the Prod6 contains both Mono and Stereo data, whereas Prod4 DSTs are produced separately for the two sub-arrays. A previous software version (paris-0-8-28) is needed for the analysis of Prod4 DSTs. It cannot handle Prod6 DSTs. Different cuts are used in paris-0-8-28 and paris-0-8-30.

In Table 4.4 the various combinations of sub-arrays, DST productions and software versions are summarized.

CHAPTER 5

GALACTIC CENTER

The γ -ray emission towards the Galactic Center is of unknown origin. One of the possibilities is that the source is linked to the SMBH at the center of the Galaxy. The conclusive association of the radiation with the black hole would hint towards an AGN nature of Sgr A*, even if jets are lacking. In fact, it is still debatable whether the high energy emission from known AGN originates from the jets or from the central compact object.

The Galactic Center region was one of the primary targets of the early observations for the H.E.S.S. Galactic Plane survey (Aharonian et al. 2006d). A compact point-like source, later named HESS J1745-290, was detected in the direction of the Galactic Center (Aharonian et al. 2004b). TeV γ -ray emission from the same region had been previously detected also by Whipple (Kosack et al. 2004) and CANGAROO (Tsuchiya et al. 2004). Because of the several potential VHE emitter in the vicinity, the identification of HESS J1745-290 with one of these objects is difficult. Aharonian et al. (2004b) suggested the Galactic SMBH Sgr A* ($M > 4 \times 10^6 M_{\odot}$, Ghez et al. 2008; Gillessen et al. 2009), coincident within $1'$ with the H.E.S.S. source. However, other scenarios were proposed, among others, particle acceleration in the region of the SNR SgrA East (Crocker et al. 2005), or in the PWN G359.95-0.04 (Wang et al. 2006), and curvature radiation of protons near the black hole (Levinson 2000; Liu et al. 2006). Also dark-matter annihilation has been taken into consideration, but seems to be ruled out (Aharonian et al. 2006b). The association with the SNR SgrA East has been ruled out, as well, after the reduction of the systematic uncertainties in the determination of the H.E.S.S. centroid position (van Eldik et al. 2008).

In an attempt to link the γ -ray emission to the central black hole, Aharonian et al. (2008a) looked for correlated variability in simultaneous X-ray and VHE observations of Sgr A*. The absence of a significant increase in the γ -ray flux during an X-ray flare suggested that the two

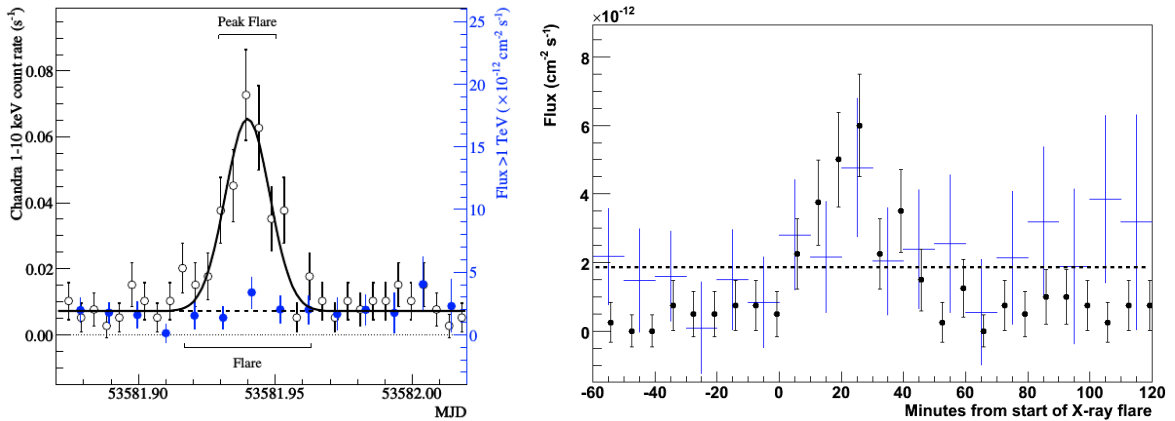


Figure 5.1: Simultaneous VHE and X-ray lightcurves during the X-ray flaring event reported in Aharonian et al. (2008a) as it appears in the publication (*left*) and with a shorter 10 minutes time bin (*right*, H.E.S.S. internal communication). In both plots, blue symbols are H.E.S.S. observations, black symbols are *Chandra* observations.

radiations were not produced by the same particle population, but could not exclude Sgr A* as the central engine. In Aharonian et al. (2009b) further variability studies were carried out. No significant variation was found and a flux increase of a factor of two was calculated to be required for a 3σ detection in an hour. This result did not rule out, however, that HESS J1745-290 could be variable on fast time-scales shorter than 30 min, as they have been detected in the IR and X-ray bands.

5.1 CHANDRA 3 Ms VISIONARY PROJECT

In Aharonian et al. (2008a), a 15 minutes time bin was adopted. The use of a shorter 10 minutes time bin for the γ -ray lightcurve shows that exactly at the peak of the X-ray flare, the VHE flux might have had its maximum level (Fig. 5.1). This suggests that joint variability studies would be promising. Even if the amplitude of VHE variations would not be higher than that shown in Fig. 5.1, the significance of correlations would be boosted in multi-event correlation studies.

In 2012, a large consortium was awarded a 3 Ms (~ 830 h) exposure on Sgr A* with *Chandra* (Baganoff et al. 2012). This represented a unique opportunity to look for correlated VHE and X-ray variability. The allocated time for *Chandra* observations was an order of magnitude larger than for any previous studies. For this reason, a corresponding increase in the number of detected X-ray flares was expected, as well as an increment of the chance of simultaneous X-ray and γ -ray detections. In the case of a positive correlation, (part of) the VHE emission would have been conclusively associated with Sgr A* and it could have been possible to provide constraints for the emission mechanism responsible for the flaring emission of the SMBH in the Galactic Center.

5.2 H.E.S.S. OBSERVATIONS AND ANALYSIS

H.E.S.S. observations have been carried out for the whole visibility window of Sgr A* in 2012, both as part of the multiwavelength campaign with *Chandra* and as part of other projects. 139 runs were collected in total and 114 pass the standard quality cuts over good weather, good camera conditions and telescope system stability. The total livetime of 45.7 h (38.3 h when corrected for acceptance). The analysis has been performed with Prod26 DSTs using the M++ analysis with Std cuts and the software version paris-0-8-24. The background has been determined using the *Reflected Region Background* method for the spectral and temporal analyses, and the *Ring Background* method for the skymaps (sec. 4.7). The source is detected with a significance of 51.6σ .

In Fig. 5.2, the excess and significance maps are displayed on the top row, together with the significance distribution. The source is clearly visible at the center of the maps, together with diffuse emission along the Galactic Plane. The last is visible also in the θ^2 distribution in the bottom-left panel.

5.3 SPECTRAL ANALYSIS

The 2012 VHE spectrum is best fit by a ECPL or a BPL¹. The ECPL fit (Fig. 5.3, *right*) yields $\Gamma = 1.89 \pm 0.07$, $E_{cut} = 5.21 \pm 1.16$ TeV and a normalization $N(1 \text{ TeV}) = 3.07 \pm 0.11 \times 10^{-12} \text{ cm}^{-2} \text{ s}^{-1} \text{ TeV}^{-1}$. The integrated flux above 1 TeV is $(2.33 \pm 0.20) \times 10^{-12} \text{ cm}^{-2} \text{ s}^{-1}$.

The BPL fit (Fig. 5.3, *left*) yields $\Gamma_1 = 2.04 \pm 0.05$, $\Gamma_2 = 2.83 \pm 0.19$, $E_{cut} = 2.33 \pm 0.45$ TeV and a normalization $N(1 \text{ TeV}) = 2.99 \pm 0.11 \times 10^{-12} \text{ cm}^{-2} \text{ s}^{-1} \text{ TeV}^{-1}$. The integrated flux above 1 TeV is $(2.37 \pm 0.16) \times 10^{-12} \text{ cm}^{-2} \text{ s}^{-1}$.

The BPL spectrum is perfectly compatible with the analogous results given in Aharonian et al. (2009b). Only the integrated flux is slightly higher, which could hint towards an increased emission. The parameter values of the ECPL fit, instead, are marginally compatible with results of the 2005 dataset of Aharonian et al. (2009b), with a harder spectral index and a smaller cut-off energy.

5.4 TEMPORAL ANALYSIS

In order to link the γ -ray emission to the central black hole, model-independent evidence that ultra-relativistic particles exist close to Sgr A* can be provided by the observation of variability at TeV energies. No significant variability is detected on the time scales useful for the comparison with the X-ray emission. In Fig. 5.4 the run-wise and 15 minutes bin lightcurves are shown. The probability for a constant fit are 0.17% ($\chi^2/\text{d.o.f.} = 119/105$) and 0.91% ($\chi^2/\text{d.o.f.} = 158/183$) respectively.

¹BPL = Broken Power-Law

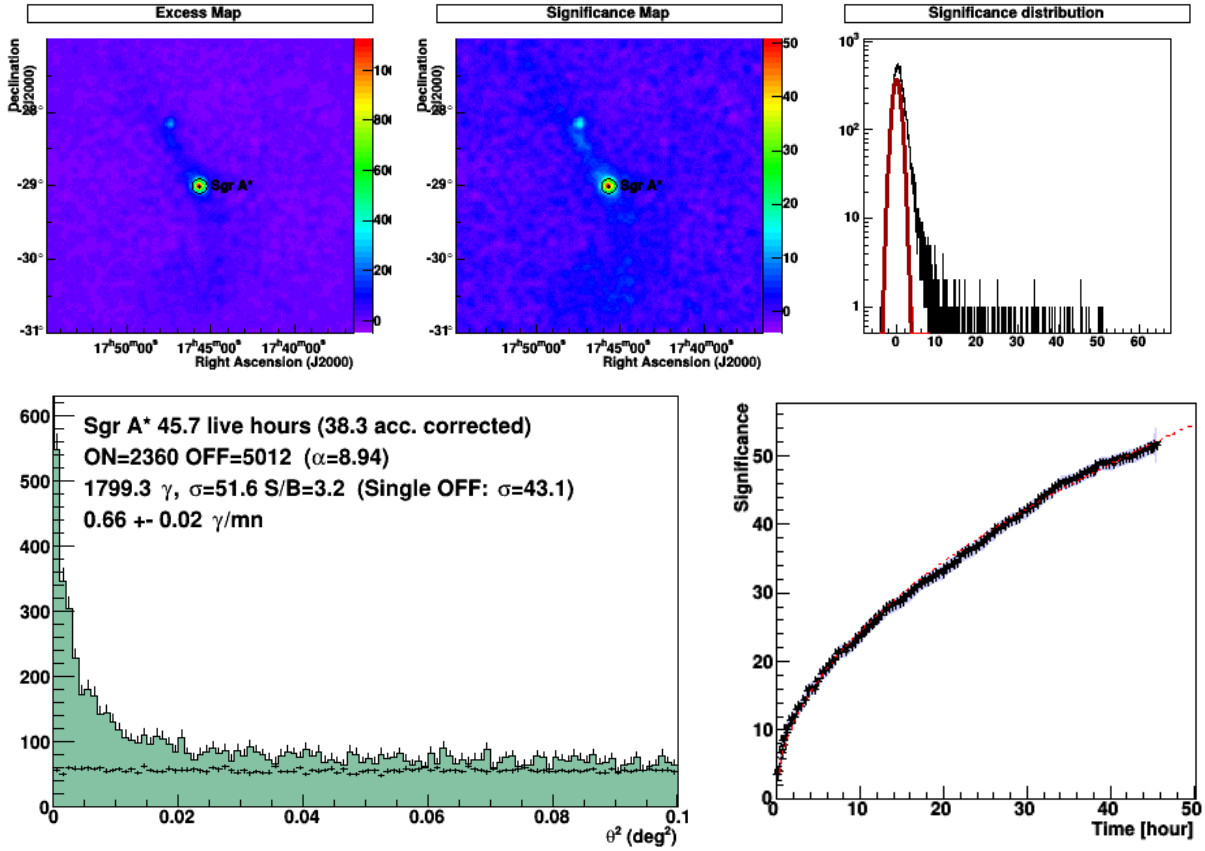


Figure 5.2: *Top* (from left to right): excess and significance maps, and significance distribution. Diffuse emission is visible along the Galactic Plane. *Bottom*: θ^2 distribution (*left*) and significance distribution as a function of the observation time (*right*). One can see emission over the background because of the presence of a γ -ray diffuse component in the Galactic plane. The significance follows the typical distribution for a constant emitter $\sigma \propto \sqrt{t}$ (red dotted curve).

The results of the *Chandra* observations are presented in Neilsen et al. (2013). Several flares have been detected, with different intensities. In Fig. 5.5 the *Chandra* lightcurve for the nights with contemporaneous H.E.S.S. observations (whose time windows are displayed in red) is shown. The periods of X-ray flaring states are marked in green. Only in three occasions VHE observations were carried out during X-ray flares. In the first night, the VHE observations do not pass the quality cuts and must therefore be discarded. The X-ray flare (MJD 56067.863 to 56067.888) was 2.3 times brighter than the one reported in Aharonian et al. (2008a). In the second night, *Chandra* started observing while the flaring event was already undergoing (MJD 56126.979 to 56127.038), therefore it is truncated. Only two runs were collected with H.E.S.S. and no variability could be seen (Fig. 5.6). In the third night, the X-ray flare is 70% brighter than the 2005 one. It evolves between MJD 56130.906 and 56130.921, which is exactly in the small gap between the H.E.S.S. observations (Fig. 5.7).

Given the absence of significant short term variability and of a sufficient number of flaring

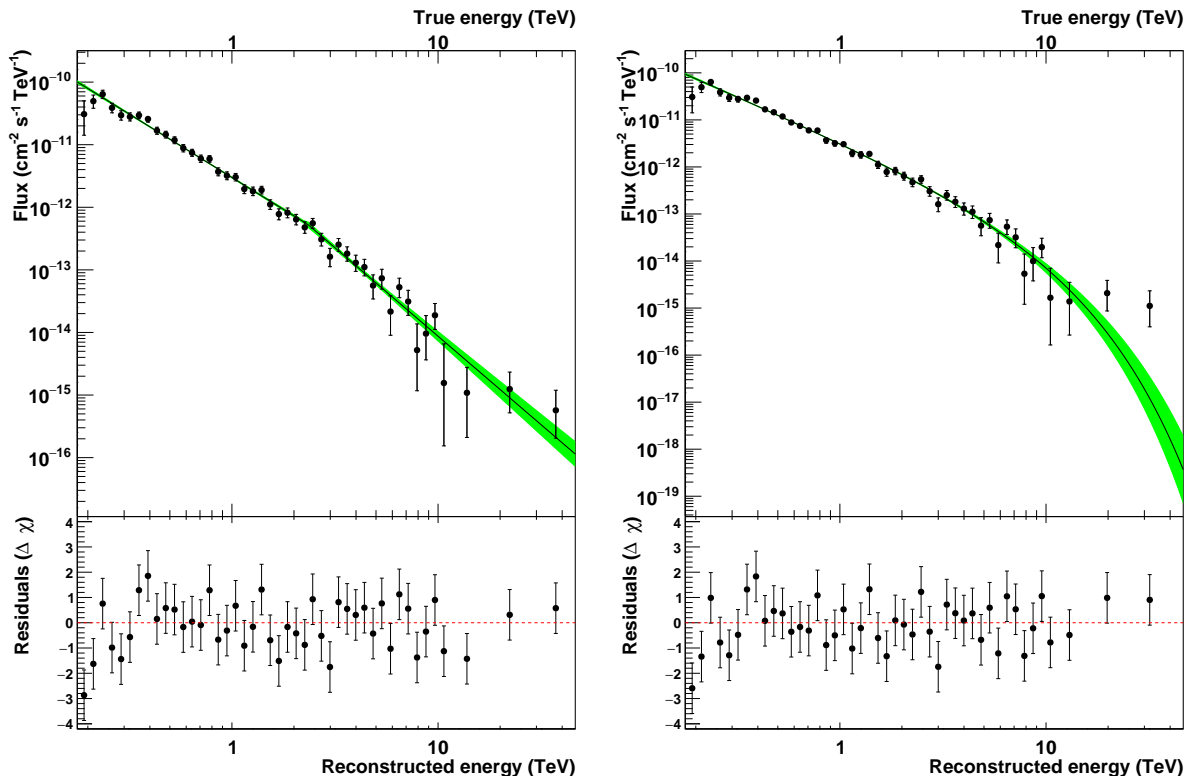


Figure 5.3: BPL (*left*) and ECPL (*right*) spectral fits of the 2012 VHE data of Sgr A*.

events that could be used for correlation studies, it is not possible to answer the question at the base of this study, whether or not the γ -ray source HESS J1745-290 is related to the black hole in the Galactic Center. Nonetheless, it is interesting to notice that in the last night, the TeV flux of the 15 minutes bin lightcurve seems to increase before the X-ray flare and decrease afterwards. However, all the points involved are well within fluctuation values.

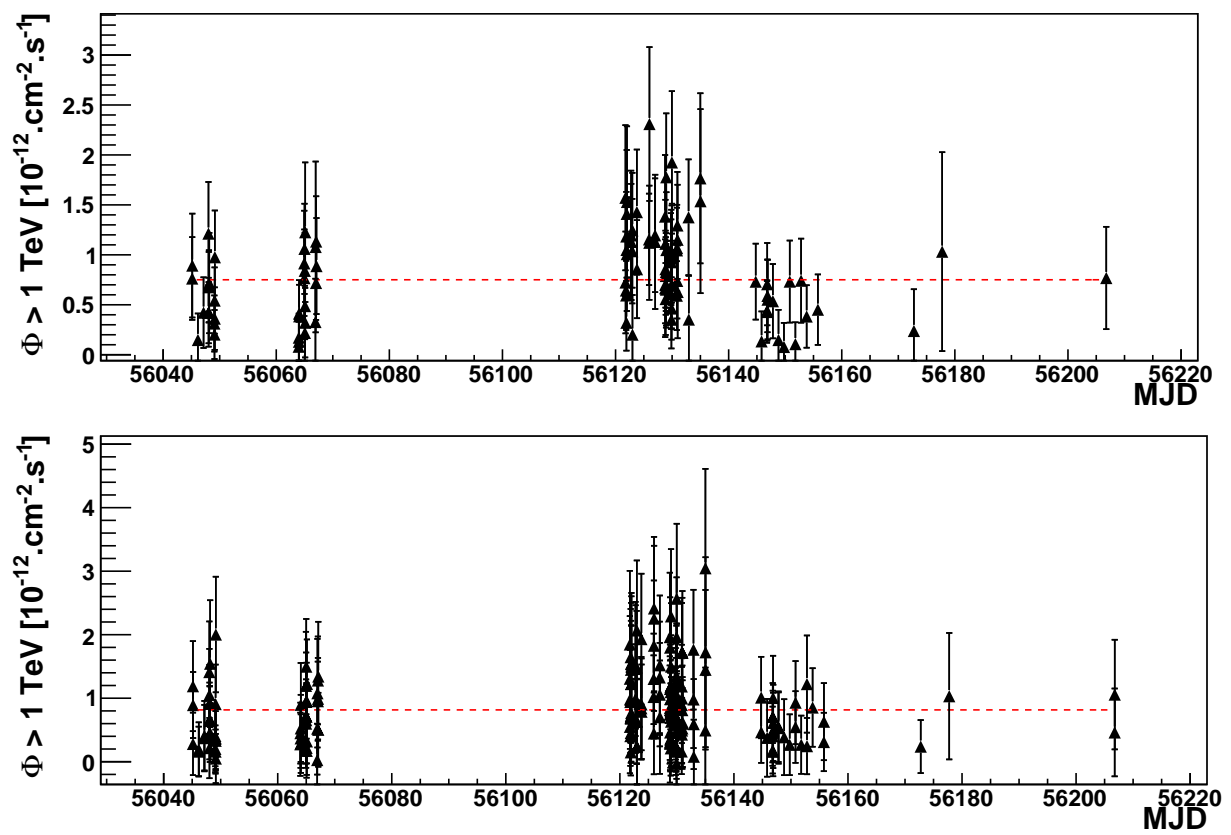


Figure 5.4: Runwise (*top*) and 15 minutes bin (*bottom*) VHE lightcurves of Sgr A*.

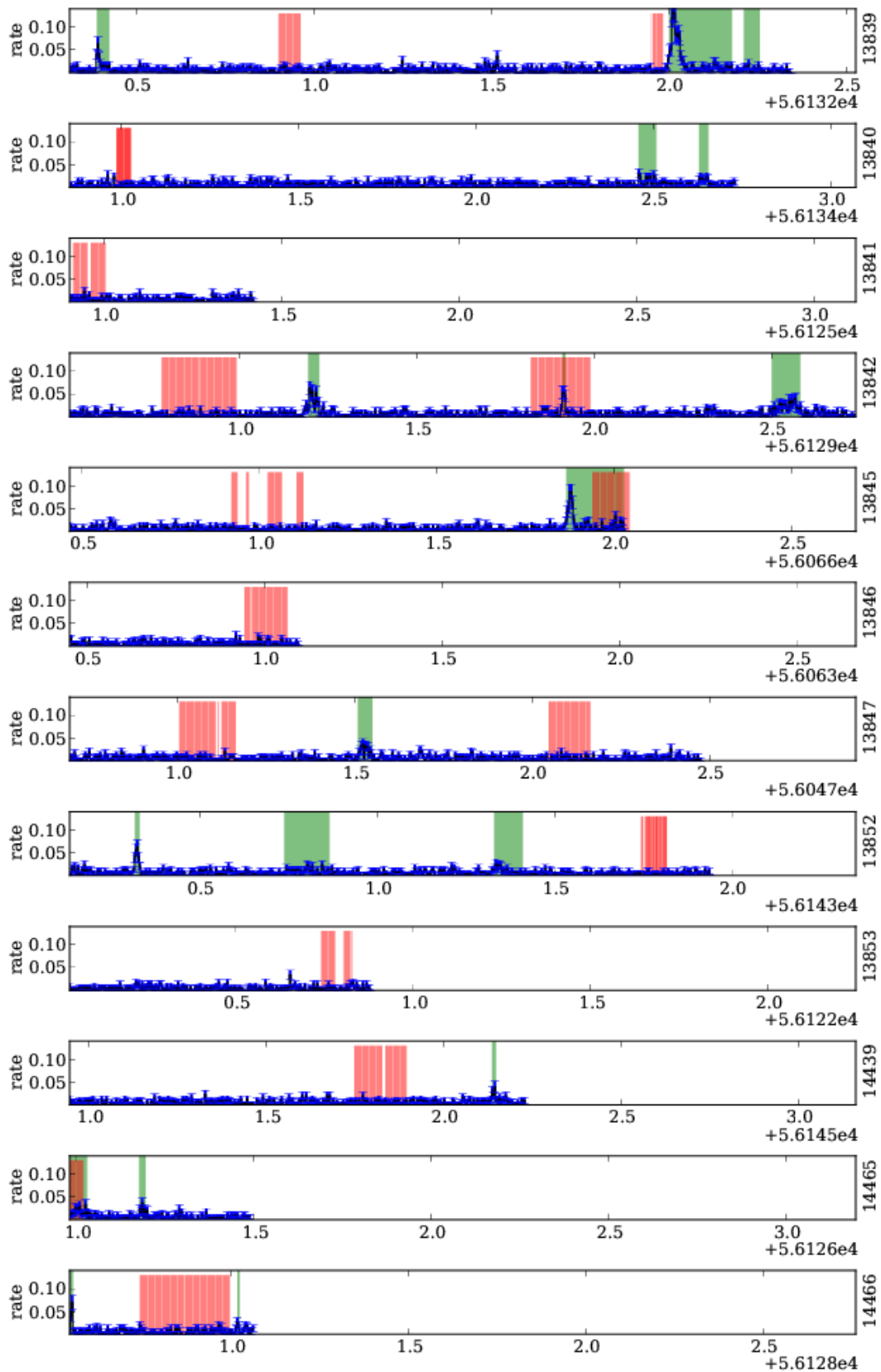


Figure 5.5: *Chandra* lightcurve of the 3 Ms campaign on Sgr A* for the nights with simultaneous H.E.S.S. observations. In green the times of X-ray flares are given, while in red the times of H.E.S.S. observations (Karl Kosack, H.E.S.S. internal communication).

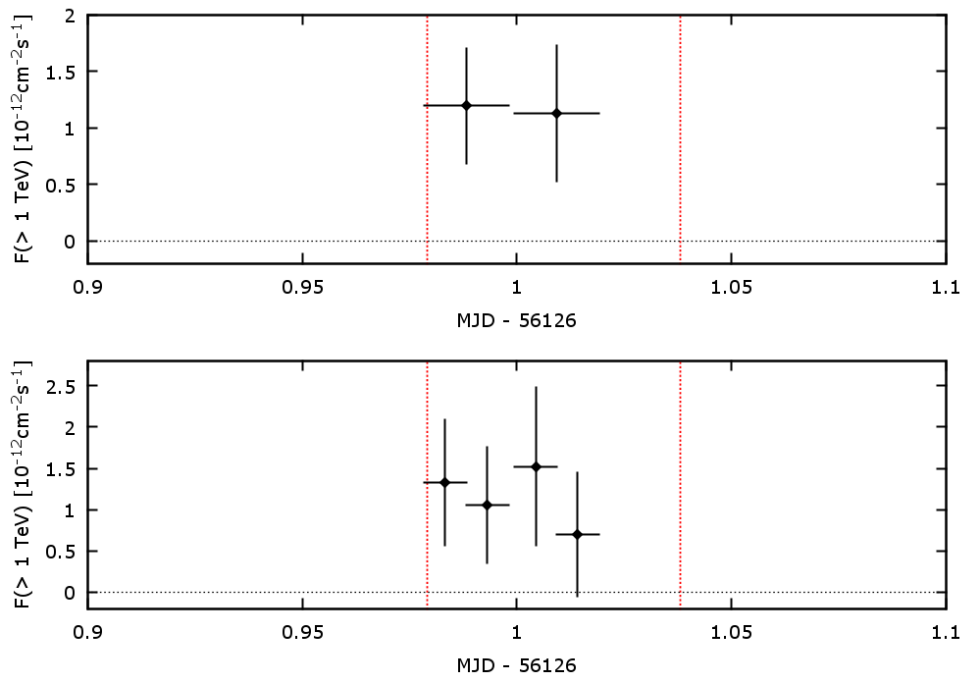


Figure 5.6: Runwise (*top*) and 15 minutes bin (*bottom*) VHE lightcurves simultaneous to the X-ray flare between MJD 56126.979 and 56127.038 (red dotted lines). The X-ray flare is truncated, since *Chandra* starts observing after it started. It covers the whole period of H.E.S.S. observations.

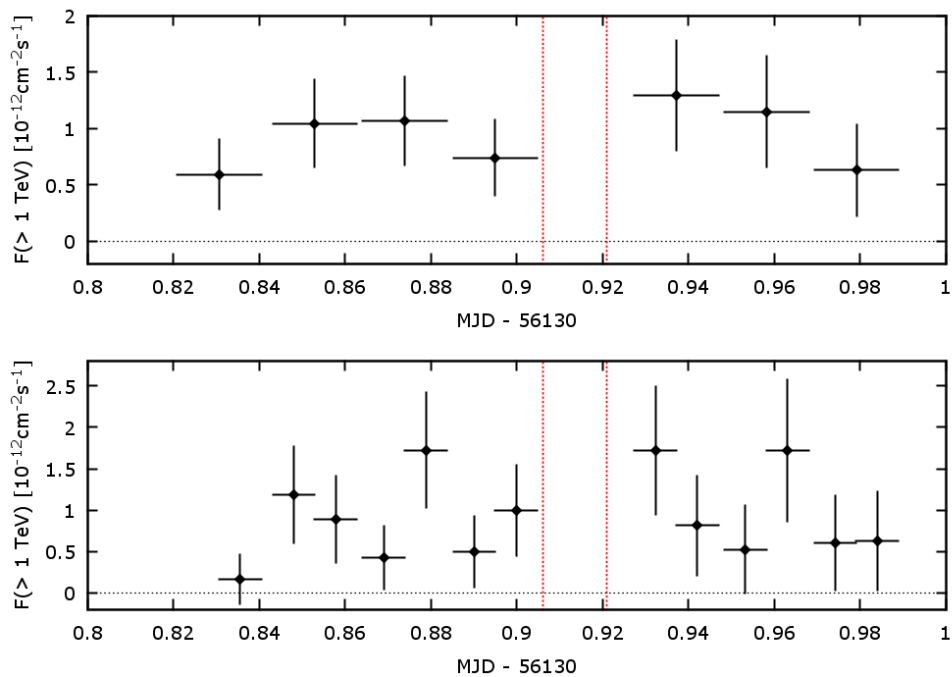


Figure 5.7: Runwise (*top*) and 15 minutes bin (*bottom*) VHE lightcurves simultaneous to the X-ray flare between MJD 56130.906 and 56130.921 (red dotted lines). The X-ray flare evolves exactly in the few minutes not covered by H.E.S.S. observations.

5.5 CONCLUSIONS

In this chapter, the determination of the nature of the galactic γ -ray source HESS J1745-290 has been attempted, under the hypothesis that its emission is linked to the SMBH at the center of the Galaxy. Simultaneous multiwavelength observations at TeV and X-ray energies with H.E.S.S. and *Chandra* have been carried out in order to catch the source in high state. Unfortunately, only two flares were observed by both instruments, so that no correlation study could be realized. Additionally, no significant variability was detected in the H.E.S.S. dataset. In conclusion, it was not possible to associate the γ -ray emission with the Galactic black hole Sgr A*.

CHAPTER 6

1ES 0229+200

Thanks to the combination of its hard spectrum reaching 10 TeV and its considerable distance (for a TeV source), 1ES 0229+200 has been one of the key sources for deriving constraints on the extragalactic background light (EBL, HESS07) and on the intergalactic magnetic field (IGMF, e.g. Tavecchio et al. (2010, 2011); Neronov & Vovk (2010); Dermer et al. (2011); Dolag et al. (2011); Taylor et al. (2011); Vovk et al. (2012)), as well as on pair halos, direct consequence of the IGMF (Ahlers 2011; H. E. S. S. Collaboration et al. 2014). The spectrum allows one to probe the near- and mid-infrared wavelengths of the EBL ($\sim 2 - 20 \mu\text{m}$) at high optical depths ($\tau \sim 1 - 6$ for γ -ray energies between $\sim 1 - 10$ TeV). This is unique, since only a few other sources have been observed at these energies. In HESS07, a low EBL level near to the lower limits derived from galaxy counts was found, in agreement with previous findings (Aharonian et al. 2006c, 2007c) and in contrast with some contemporary EBL models. For the IGMF studies, a multi-TeV hard spectrum in combination with high optical depths implies that a considerable part of the emitted TeV photons will be absorbed via pair production through their interaction with the EBL and re-emitted at (typically) GeV energies, causing a surplus of HE emission. Lower limits on the IGMF have been derived in the range $B > 10^{-18} - 10^{-15}$ G, depending on the assumptions on the source unknown parameters and the model used (semi-analytical, simulations).

6.1 1ES 0229+200: THE SOURCE

1ES 0229+200 is a blazar, and a member of the high frequency peaked BL Lac objects (HBL) subclass (Giommi et al. 1995). It is located at $\text{RA}_{\text{J2000}} = 02^{\text{h}}32^{\text{m}}48.616^{\text{s}}$, $\text{Dec}_{\text{J2000}} = 20^{\circ}17'17.45''$ (Rector et al. 2003) in a giant elliptical galaxy ($M = 10^{11.93 \pm 0.06} M_{\odot}$) at redshift $z = 0.1396$ (Falomo & Kotilainen 1999; Woo et al. 2005). Scarpa et al. (2000a) describe the host galaxy as “*well described by a de Vaucouleurs law*” and “*absolutely normal*”, with no visible companion for the AGN. Hyvönen et al. (2007) suggest that it is “*dominated by old stellar populations, with no*

Table 6.1: Observed and absolute optical magnitudes in different bands for the 1ES 0229+200 and its host galaxy. The values are taken from: (a) Scarpa et al. (2000b), (b) Scarpa et al. (2000a) and Urry et al. (2000), (c) Falomo & Kotilainen (1999), (d) Hyvönen et al. (2007)

band	m_{tot}	m_{nuc}	m_{host}	M_{nuc}	M_{host}
H ^a	13.56	16.0±0.2	12.8±0.1	-23.89	-27.1
R ^b	15.82	18.58±0.35	15.85±0.01	-21.72	-24.61
R ^c		18.25	15.76	-21.91	-24.53
V ^d		19.67	17.58	-19.9	-22.2
B ^d		19.58	18.57	-20.2	-21.9
U ^d		19.22	18.83	-20.6	-21.5

evidence for a young population”, as can be inferred by its colors. The host overshines the AGN in the optical band, especially towards the red and infrared, as can be seen in Table 6.1. Because of this, it is difficult to detect variability (which seems to be low intrinsically, as shown at other wavelengths) in this energy band (e.g. Fig. 6.4). The optical emission is constant within errors. The AGN is a supermassive black hole with $M = 10^{8.68 \pm 0.13} M_{\odot}$ (Woo et al. 2005).

1ES 0229+200 was first discovered in X-rays between 0.4 and 4.0 keV with the *Einstein* satellite in 1992 (Elvis et al. 1992). The source is bright in this energy range, and has a hard photon index $\Gamma_X \lesssim 2.0$ which flattens with increasing energy (Fig. 6.1). The synchrotron emission peaks around or above 10 keV (e.g. Kaufmann et al. 2011; Aliu et al. 2014) and reaches 100 keV and possibly up to 200 keV (Cusumano et al. 2014). The peak is also possibly flat for some tens of keV. The emission in the 2-10 keV band is variable by at least a factor of 2 (Kaufmann et al. 2011).

1ES 0229+200 is faint in radio, where it shows parsec and kiloparsec scale jets (Rector et al. 2003; Giroletti et al. 2004). The parsec-scale jet extends to the south, with a position angle (P.A.) of $+170^{\circ}$ and a weak evidence for a broad jet opening angle of $\sim 30^{\circ}$. The kiloparsec-scale jet is two-sided to the north (P.A. = -10°) and to the south (P.A. = $+180^{\circ}$), with both sides curved toward west. The small scale jet is well aligned with the southern jet.

The emission in γ -rays, especially at high energies (HE) is very faint. Vovk et al. (2012) reported for the first time a detection at HE between 1 and 300 GeV after more than three years of *Fermi* observations. The reported photon index was hard ($\Gamma_{GeV}^{Vovk} = 1.36 \pm 0.25$) and only an upper limit could be derived between 1 and 3 GeV. The source was later included in the 4-year *Fermi* Gamma-ray LAT Point Source Catalog (3FGL) (Acero et al. 2015), but it did not appear either in the First, nor in the Second LAT High-Energy Catalog (1FHL and 2FHL, Ackermann et al. 2013; The Fermi-LAT Collaboration 2015). The energy range covered in the 3FGL (0.1 - 100 GeV) is significantly different than the one in Vovk et al. (2012), and the reported photon index is much softer ($\Gamma_{GeV}^{3FGL} = 2.03 \pm 0.15$) and inconsistent with the previous one (Fig. 6.1). However, the spectral points in the common energy range are compatible. The 3FGL spectrum is also incompatible with the VHE spectrum derived by both HESS and VERITAS. These two points hint towards a concave HE spectrum or a spectral break around 1 GeV, which is difficult

to detect due to the faintness of the source.

In 1996, Stecker et al. predicted 1ES 0229+200 to be a VHE γ -rays emitter. Observations with the first generation of IACTs (HEGRA, Whipple, Milagro) provided only upper limits (Aharonian et al. 2000, 2004a; de la Calle Pérez et al. 2003; Horan et al. 2004; Williams 2005).

Its discovery above 500 GeV was finally reported by the H.E.S.S. Collaboration in 2007 (Aharonian et al. 2007a, hereafter HESS07). The spectrum was well fit with a simple hard power-law ($\Gamma_{\text{HESS}} = 2.50 \pm 0.19_{\text{stat}} \pm 0.10_{\text{sys}}$) reaching above 10 TeV and no significant flux variability was detected. The EBL-deabsorbed spectrum was very hard, almost reaching the theoretical limit of 1.5 ($\Gamma_{\text{HESS}}^{\text{deabs}} = 1.58 \pm 0.22$). Such a spectrum is compatible with the HE one of Vovk et al. (2012), hence suggesting the absence of intrinsic curvature in the IC peak from 1 GeV up to at least 10 TeV. Hints of flux variability on yearly and monthly timescales were claimed by the VERITAS Collaboration in 2014 (Aliu et al. 2014, hereafter VER14). The photon index was compatible with the one derived by HESS ($\Gamma_{\text{VERITAS}} = 2.59 \pm 0.12_{\text{stat}} \pm 0.26_{\text{sys}}$) and was found not to change significantly with flux ($\Gamma_{\text{VERITAS}}^{\text{high}} = 2.53 \pm 0.11_{\text{stat}} \pm 0.25_{\text{sys}}$, $\Gamma_{\text{VERITAS}}^{\text{low}} = 2.64 \pm 0.19_{\text{stat}} \pm 0.26_{\text{sys}}$).

In Fig. 6.1 an SED is shown with data taken from the literature. The data are not contemporaneous and several spectra are averaged over a prolonged period of time. However, the most important features described above are clearly visible. The synchrotron emission peaks in the X-rays at 10 keV or above and it reaches at least 100 keV. The GeV-TeV intrinsic emission above 1 GeV seems to be a single hard power-law, which is then absorbed by the EBL. This means that the peak of the intrinsic IC emission lies beyond the energies testable with H.E.S.S. in the tens of TeV, at least. If this picture is true, the enhancement of the emission in the MeV range, together with the apparent increase of the hard X-ray flux seen by *Swift*-BAT above 60 keV, leads to the intriguing hypothesis that the synchrotron peak extends all the way up to the GeV range, or that an additional component in the soft γ -rays exists.

6.2 VHE OBSERVATIONS WITH H.E.S.S.

H.E.S.S. observations have been carried out almost yearly between 2004 and 2013, with the only exceptions of 2010 and 2012. 354 observation runs were collected in wobble mode. They have been subject to quality control over good weather, good camera conditions and telescope system stability: 311 runs pass these quality cuts, for a total livetime of 133 h (122 h when corrected for acceptance). They have a mean Zenith angle of 45.2° and a mean offset from the pointing position of 0.51° . The exposure was not homogeneous over the years, ranging from 3.8 h in 2004 to 47.1 h in 2006. Refined quality selection criteria allowed for a larger dataset for the years 2004-2006 than the one published in Aharonian et al. (2005b) and HESS07.

Part of the 2009 and 2013 data belong to multiwavelength (MWL) campaigns. The first one was organized with XMM-*Newton* and ATOM on August 21 and 23, 2009, the second one with *NuSTAR*, *Swift*-XRT, MAGIC and VERITAS on October 1, 5 and 11, 2013. The two datasets comprise 21 and 13 good quality runs, respectively.

In 2013, 35 out of the 354 total runs were taken with the full HESS-II array. After quality

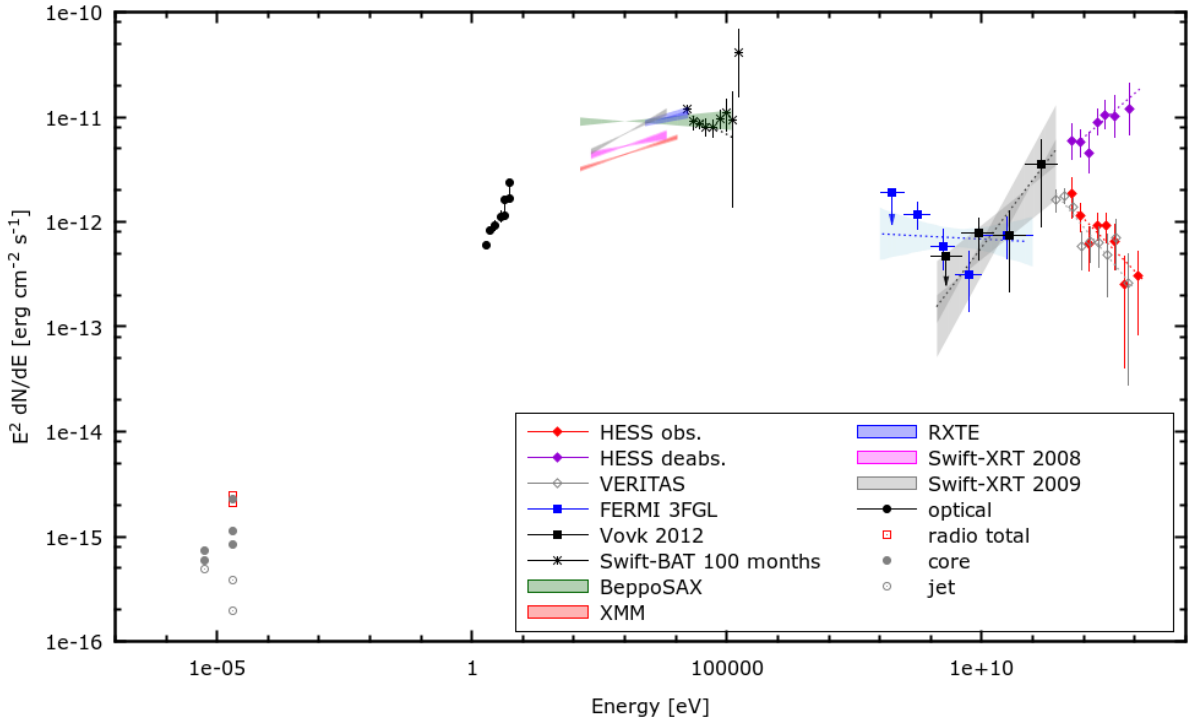


Figure 6.1: Historical SED with data taken from the literature. The radio data (filled and open gray circles, and red open squares) are taken from Schachter et al. (1993), Perlman et al. (1996), Rector et al. (2003) and Giroletti et al. (2004), the optical and UV data (black filled circles), as well as the XMM-Newton and Swift-XRT (red, pink and gray bands) are from Kaufmann et al. (2011). Other X-ray data are the *BeppoSAX* spectrum from Donato et al. (2005, green band) and the *Swift*-BAT spectral points from the 100 months Palermo Catalogue (black stars, Cusumano et al. 2014). The *Fermi* data are from the 3FGL catalog (blue squares and band) and from Vovk et al. (2012, black squares and band). The upper limits are 95% and 90% confidence level, respectively. The observed (red diamonds) and EBL-deabsorbed (violet diamonds) HESS datapoints are taken from HESS07. The VERITAS points (open gray diamonds) are from VER14.

cuts, 28 and 27 runs remain for the Mono and Stereo subarrays, respectively (5 and 5 in the MWL campaign).

6.3 OBSERVATIONS OUTSIDE THE VHE BAND

6.3.1 HIGH ENERGIES

HE data have been collected by the Large Area Telescope (LAT) onboard the *Fermi* satellite starting August 4, 2008. Data up to April 27, 2015 have been analyzed¹ with the Science-Tool software package version v10r0p5. Only events belonging to the 'Source' class within

¹The analysis has been provided by Mahmoud Mohamed.

a region of interest (RoI) of 15° from the position of 1ES 0229+200 were selected. Cuts on the Zenith angle (90°), rocking angle (52°) and distance from the Sun (5°) were applied, as well. For the binned maximum-likelihood spectral analysis, the instrument response functions P8R2_SOURCE_V6 were used, together with the publicly available standard Isotropic and Galactic diffuse emission background models iso_P8R2_SOURCE_V6_v06.txt and gll_iem_v06.fits².

1ES 0229+200 is detected with a significance of 9.5σ in the energy range 100 MeV - 500 GeV, compared to the 6.7σ between 1 and 300 GeV in Vovk et al. (2012). The spectrum is described by a PL with index $\Gamma_{\text{PL}}^{\text{Fermi}} = 1.86 \pm 0.13$.

More complex spectral shapes which could describe the possible spectral upturn in the MeV range are not significantly better than the simple PL. The broken power-law (BPL) yields a softer and a harder photon indices $\Gamma_{1\text{BPL}}^{\text{Fermi}} = 2.17 \pm 0.23$ and $\Gamma_{2\text{BPL}}^{\text{Fermi}} = 1.69 \pm 0.19$ for a fixed $E_{\text{br}}=3.5$ GeV. The CPL shows a concave spectrum with $\Gamma_{\text{CPL}}^{\text{Fermi}} = 2.14 \pm 0.02$ and a curvature parameter $\beta = -0.054 \pm 0.006$.

The simple PL spectrum is marginally compatible with the 3FGL one. Contrary to this last one, it is more compatible with the VHE emission. The hard component of the BPL spectrum would be compatible with the findings of Vovk et al. ($\Gamma_{\text{GeV}}^{\text{Vovk}} = 1.36 \pm 0.25$). The comparison of the three spectra is shown in Fig. 6.2.

The low flux in the *Fermi*-LAT band does not permit detailed temporal studies on monthly timescales. Studies with the variability index test³ do not show any significant variability. Lightcurves with 3 months, 6 months and 1 year bins do not show any variability as well.

The same test applied to the monthly lightcurve obtained from a previous analysis with P7REP_SOURCE_V15 and presented in Cologna et al. (2015b) yielded a value of 157 for 81 degrees of freedom, which indicates variability at the 5σ level. The difference with the newest results is explained by the incorrect treatment of two sources in the RoI. One soft source at 4.5° distance from 1ES 0229+200 was kept fixed to its catalog values, but was found to be flaring in the first 200 days of observations. A second source at 3.5° distance was instead not listed in any *Fermi* catalogs and was not accounted for in the analysis. The incorrect treatment of these two sources also affected the derivation of the spectrum. A BPL or CPL spectral shapes were preferred at almost 3σ due to the excess emission in the MeV range.

6.3.2 X-RAYS

In this work, X-ray data from *Swift*, *RXTE* XMM-*Newton* and *NuSTAR* are used (Fig. 6.13, third and fourth panels). The 30-days bin *Swift*-BAT lightcurve between 15 and 85 keV is derived from the 15-days bin one in the 66 months Palermo BAT Catalog (Cusumano et al. 2013). The 2008 and 2009 XMM-*Newton* and *Swift*-XRT, as well as the 2010 *RXTE* data are taken from Kaufmann et al. (2011), while the whole 2010-2011 *RXTE* lightcurve is taken from Rivers et al. (2013). Finally, the most recent *Swift*-XRT data have been collected between the nights of

²<http://fermi.gsfc.nasa.gov/ssc/data/access/lat/BackgroundModels.html>

³ $\text{TS}_{\text{var}} = 2\sum_i [\text{Log}\mathcal{L}_i(F_i) - \text{Log}\mathcal{L}_i(F_{\text{const}})]$ where F_{const} and F_i are the average source flux and the flux of the i -th time bin. The test can be carried out without requiring limits on the significance of every time bin.

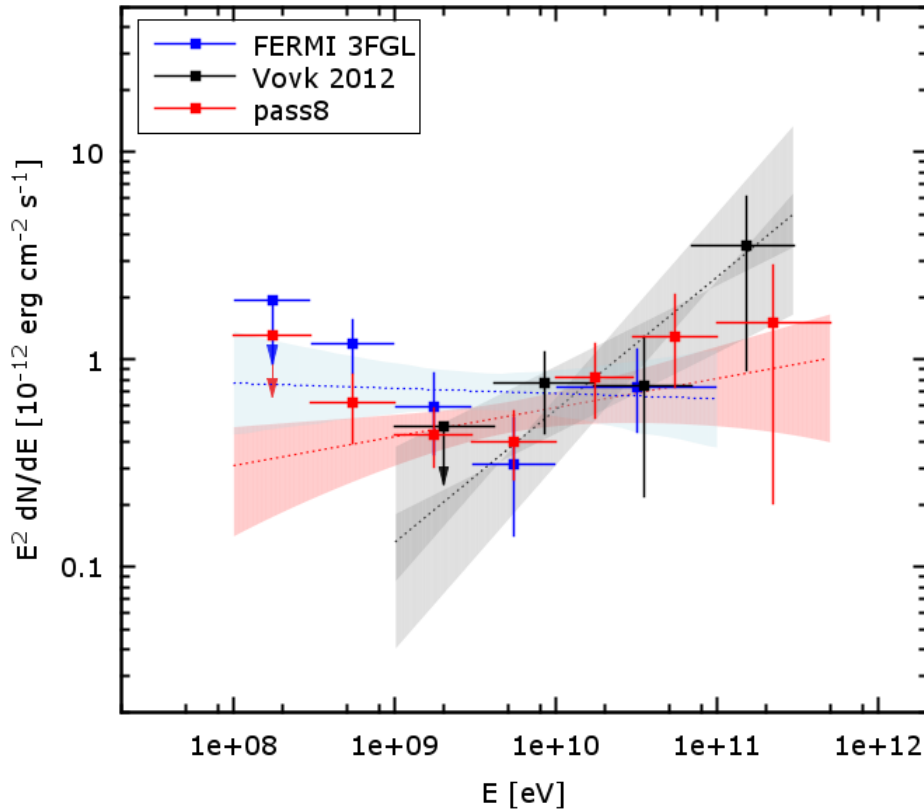


Figure 6.2: Comparison of the three available *Fermi* spectra from Acero et al. (2015, blue), Vovk et al. (2012, black) and of the current analysis (red). Despite a BPL fit over the whole energy range is not significantly better than a PL, one can see that above 3 GeV the spectrum is harder than the global fit suggests.

October 1-2 and 10-11, 2013 during the aforementioned MWL campaign.

All the available *Swift*-XRT data collected between 2008 and 2015 (ObsIDs 00031249001-00031249050 and 00080245001-00080245006) were analyzed⁴ using the HEASoft software package v. 6.16⁵ with CALDB v. 20140120. All the events were cleaned and calibrated using the *xrtpipeline* task and the data in the 0.3-10 keV energy range with grades 0-2 for WT mode and 0-12 for PC mode were analyzed. The photons were grouped in bins with at least 30 counts using the *grappa* tool and then fit using XSPEC v. 12.8.2 with a single PL model and Galactic hydrogen absorption fixed to $n_H = 8.06 \times 10^{20} \text{ cm}^{-2}$ (Kalberla et al. 2005). The PL fits the data satisfactorily. The lightcurve flux points were calculated from the spectra of single snapshots integrating between 2 and 10 keV.

The *NuSTAR* observations were collected on October 2, 5 and 10, 2013 (ObsIDs: 60002047002, 60002047004 and 60002047006). All data were analyzed³ using the NuSTARDAS software package v.1.4.1. available within HEASoft package v. 6.16⁴ with CALDB v. 20140414. The data

⁴The analyses have been provided by Alicja Wiercholska.

⁵<http://heasarc.gsfc.nasa.gov/docs/software/lheasoft>

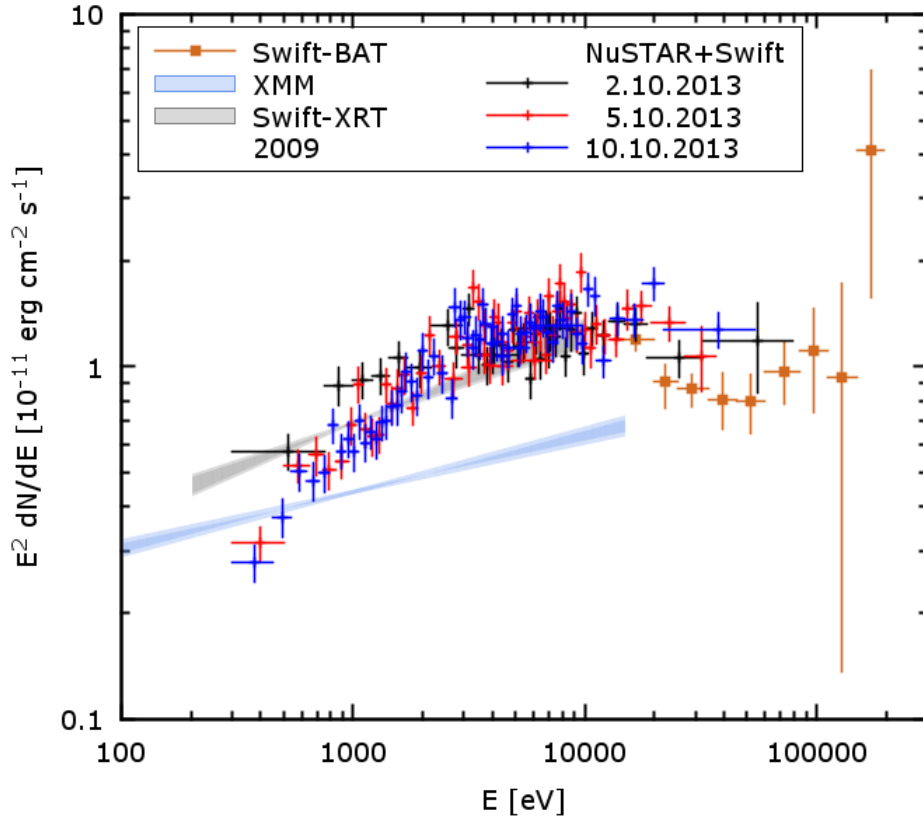


Figure 6.3: SED of the synchrotron peak with the contemporaneous *NuSTAR* and *Swift*-XRT data of the MWL campaign in October 2013. As a comparison, the lowest and the highest fluxes measured by *XMM-Newton* and *Swift*-XRT in 2009 (Kaufmann et al. 2011) are shown, together with the 100 months *Swift*-BAT spectrum (Cusumano et al. 2014).

were processed using the `nupipeline` and `nuproducts` tasks. For each observation, the combined spectra from the A and B detectors were grouped to have a minimum of 30 counts/bin and fitted with a single PL model using `XSPEC` v. 12.8.2. This fit the data reasonably well.

For these three nights, also a combined fit of the *Swift*-XRT and *NuSTAR* spectra has been done, which allows the contemporaneous characterization of the synchrotron peak between 0.3 and 79 keV. In this case, the spectra were clearly curved beyond the Hydrogen absorption and were fit with a CPL model. The combined observations of the MWL campaign are plotted in Fig. 6.3 together with some historical data.

6.3.3 OPTICAL

Optical monitoring of 1ES 0229+200 has been carried out with ATOM between 2007 and 2012. Observations in B and R bands took place typically once every three nights during the August-December visibility window.

During the 2013 MWL campaign ATOM was not operational and data were collected with

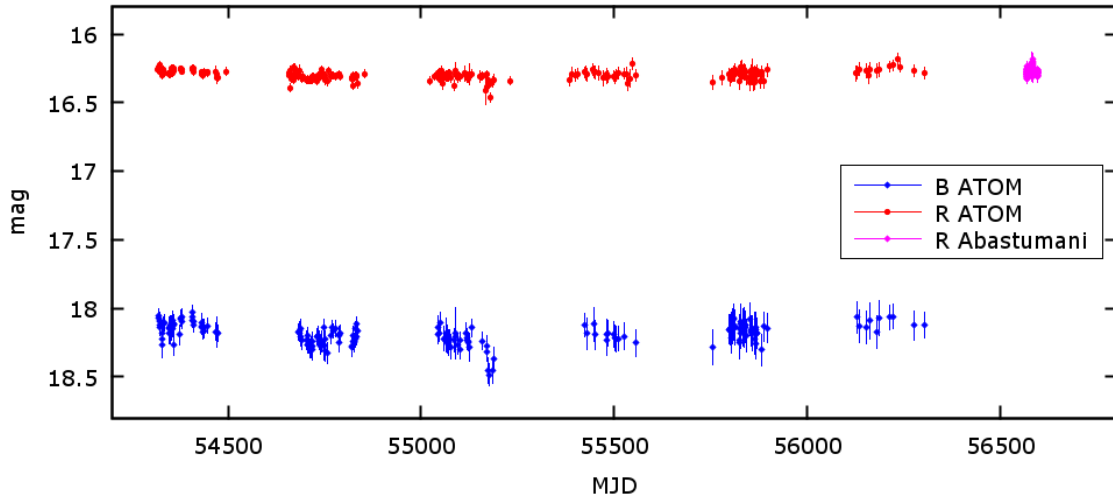


Figure 6.4: Optical R and B band lightcurve from ATOM and Abastumani for the 2007-2013 period. During the 2013 MWL campaign (around MJD 56570) no observation with ATOM was possible.

Table 6.2: Statistics of the yearly and total H.E.S.S. observations.

Period	Dates (MJD)	Live Time (h)	ON counts	OFF counts	excess	Significance (σ)	Flux (> 580 GeV) ($10^{-13} \text{ cm}^{-2} \text{ s}^{-1}$)
2004 - 2013	53259 - 56606	134.7	1879	14419	715	18.4	6.2 ± 0.5
2004	53259 - 53317	3.8	48	368	17	2.8	3.5 ± 1.9
2005	53613 - 53649	16.4	177	1575	45	3.6	2.5 ± 1.0
2006	53967 - 54088	47.1	769	4784	370	15.6	9.0 ± 0.8
2007	54322 - 54336	10.5	142	1112	49	4.5	5.6 ± 1.7
2008	54681 - 54789	12.2	154	1454	33	2.7	4.0 ± 1.6
2009	55063 - 55151	19.0	216	1852	62	4.5	5.2 ± 1.4
2011	55801 - 55909	7.8	124	990	42	4.1	3.0 ± 1.8
2013	56514 - 56606	17.8	249	2284	97	6.9	7.4 ± 1.3

Note: the normalization factor β between the ON and OFF area is 1/12 for all years with the exception of 2013 1/15. Errors on the flux are statistical only. The systematic error is estimated to be 20% of the flux.

the 70 cm telescope of the Abastumani Observatory (Georgia), equipped with an Apogee 6E camera. Observations taken with a R Cousins filter have been analyzed with the Daophot II reduction software using an aperture diameter of $10''$.

The lightcurve of the 2007-2013 period is pictured in Fig. 6.4. No significant variability can be detected.

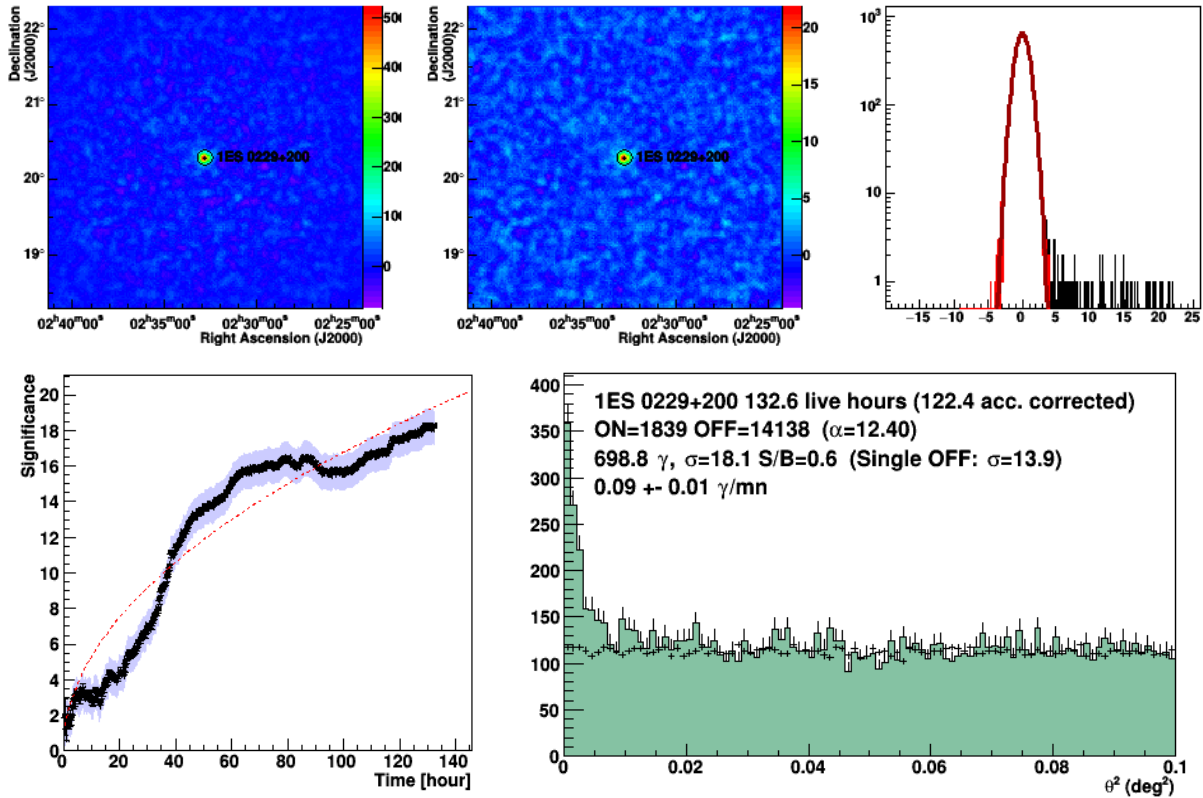


Figure 6.5: *Top:* from left to right, excess map, significance map and significance distribution of the 2004–2013 dataset of 1ES 0229+200. *Bottom:* significance as function of the time (*left*) and theta square distribution (*right*)

6.4 H.E.S.S. DATA REDUCTION

The HESS-I style analysis has been performed on Prod26 DSTs using the Model analysis (sec. 4.4, hereafter M++) with *Std* cuts and the software version paris-0-8-24. The background has been determined using the *Reflected Region Background* method for the spectral and temporal analyses, and the *Ring Background* method for the skymaps (see sec. 4.7). The source is detected with a significance of 18.1σ for the whole dataset. In Figure 6.5, the excess and significance maps are displayed on the top row, together with the significance distribution. One can see that the background is homogeneous and well normalized and the source is clearly visible at the center of the maps. The distribution of the significance as function of the time does not follow the usual $\sigma \propto \sqrt{t}$ shape typical of a constant source. The θ^2 distribution in the bottom panel of Fig 6.5 shows the point-like nature of the emission and again the good normalization of the background. The numerical results for the total dataset and for every year of observation can be found in Tab.6.2, as well as for every observing periods in Tab.6.3.

The 2013 HESS-II data have been analyzed using Prod6 DSTs and the software version paris-0-8-30 with *Std* cuts for both the Mono and Stereo subarrays. For Mono, *Safe* cuts were applied as well: they allow for a stronger background suppression leading to a larger detection

Table 6.3: Statistics of the observation periods.

Period	Dates (MJD)	Live Time (h)	ON counts	OFF counts	excess	Significance (σ)	Flux (> 580 GeV, $10^{-13} \text{ cm}^{-2} \text{ s}^{-1}$)	UL (68% c.l.)
2004								
September	53259 - 53265	3.0	34	292	10	1.8	2.8 ± 2.1	–
November	53316 - 53316	0.8	14	76	8	2.5	5.6 ± 4.2	–
2005								
September	53613 - 53621	10.5	96	904	20	2.1	1.0 ± 1.1	–
October	53644 - 53648	5.9	81	671	25	3.0	5.0 ± 2.0	–
2006								
August	53967 - 53977	13.5	230	1653	92	6.8	8.1 ± 1.6	–
September	53994 - 54005	16.0	337	1887	180	11.8	12.2 ± 1.6	–
November	54048 - 54063	12.5	150	860	78	7.6	6.9 ± 1.4	–
December	54077 - 54088	5.1	52	384	20	3.1	6.8 ± 2.0	–
2007								
August	54322 - 54335	10.5	142	1112	49	4.5	5.6 ± 1.7	–
2008								
August	54681 - 54687	4.7	49	509	7	1.0	0.8 ± 2.3	< 3.2
September	54733 - 54737	6.2	96	796	30	3.3	7.9 ± 2.5	–
November	54787 - 54788	1.4	9	149	-3	-1.0	-2.8 ± 3.5	< 1.6
2009								
August	55063 - 55074	9.3	72	829	3	0.3	-0.5 ± 1.5	< 1.1
October	55115 - 55121	5.1	73	568	26	3.3	7.0 ± 2.9	–
November	55145 - 55151	4.6	71	455	33	4.6	16.6 ± 3.8	–
2011								
August	55801 - 55811	4.8	79	667	23	2.8	1.8 ± 2.3	–
September	55835 - 55835	1.3	21	122	11	2.8	6.9 ± 4.3	–
October	55854 - 55854	0.9	9	84	2	1.0	3.4 ± 5.7	–
December	55908 - 55908	0.8	15	117	5	1.5	3.3 ± 5.6	–
2013								
August	56514 - 56520	3.8	72	399	39	5.5	15.6 ± 3.5	–
September	56536 - 56536	0.4	5	40	2	0.8	1.6 ± 8.6	< 11.5
October	56566 - 56573	5.5	61	463	22	3.2	5.7 ± 2.1	–
November	56591 - 56605	8.1	111	1382	34	3.6	5.1 ± 1.9	–

Note: the observing periods are defined by the lunar cycle and do not always strictly match the given month, which is given for an easier identification.

The normalization factor β between the ON and OFF area is 1/12 for all periods, with the exception of November 2013 1/18. Errors on the flux are statistical only. The systematic error is estimated to be 20% of the flux.

Table 6.4: Statistics of the 2013 observations in Mono and Stereo mode.

Subarray	Live Time (h)	ON counts	OFF counts	excess	Significance (σ)	Flux (> 580 GeV) ($10^{-13} \text{ cm}^{-2} \text{ s}^{-1}$)
Mono <i>Safe</i>	12.5	769	6953	160	6.0	11.1 ± 0.2
Mono <i>Std</i>	12.5	1051	9980	172	5.4	11.0 ± 0.2
Stereo <i>Std</i>	10.7	290	2945	138	9.6	13.4 ± 0.2

Note: Errors on the flux are statistical only. The systematic error is estimated to be 20% of the flux.

significance and better normalized skymaps at the expense of a slightly higher energy threshold. The results are reported in Table 6.4. The source is firmly detected in Stereo with almost 10σ in less than 10 hours livetime. In Mono, 5.4 and 6.0σ are obtained with *Std* and *Safe* cuts, respectively, in 12.5 hours livetime. The difference in livetime larger than the duration of the single run missing in the Stereo runlist is due to the fact that the CT5 camera operates at a higher frequency than the small telescopes cameras, hence has shorter deadtime. It is evident how the Stereo observations greatly ease the detection of a faint source like 1ES 0229+200 with respect to the observation with the HESS-I subarray only. On the other hand, Mono observations alone yield a lower significance. It could be caused by the worse background rejection capabilities of the Mono observations with respect to Stereo because of the lack of stereoscopy. This effect worsens in case of low signal to noise ratios, especially when the spectra of source and background have a similar slope.

6.5 H.E.S.S. SPECTRAL ANALYSIS

The spectral analysis has been carried out using the forward-folding technique. A simple PL spectral shape was fit to the total dataset (Fig. 6.6, *top*). More complex shapes do not fit the data as well as the PL. The photon index is $\Gamma = 2.87 \pm 0.12$. It is significantly softer than the one published in HESS07 ($\Gamma_{\text{HESS}} = 2.50 \pm 0.19$). One can argue that this could be due to the significantly larger dataset used, in case of spectral variability. For this reason, analyses have been done with the data collected in the same period covered by HESS07 only. Two runlists were used: the same one used for the paper, and a larger one containing all the 2005 and 2006 runs passing the current standard quality cuts. Again, the photon indices of both fits are significantly softer than the published value: $\Gamma_{05-06 \text{ pap}} = 2.90 \pm 0.17$ and $\Gamma_{05-06} = 2.96 \pm 0.15$ for the two lists, respectively (Fig. 6.6, *bottom*). One should notice that already at the time of the publication, the cross-checks provided by Mathieu de Naurois with a development version of the Model analysis showed a photon index not consistent within the $1\text{-}\sigma$ error ($\Gamma_{\text{x-checks}} = 2.92 \pm 0.23$)⁶. When considering the stability of the results presented here, they have always been consistent disregarding changes of three different software versions and likewise DST calibrations and productions.

The HESS07 results were derived from an Hillas analysis. In order to obtain results (in

⁶Other cross checks done with different methods were consistent within the $1\text{-}\sigma$ statistical error

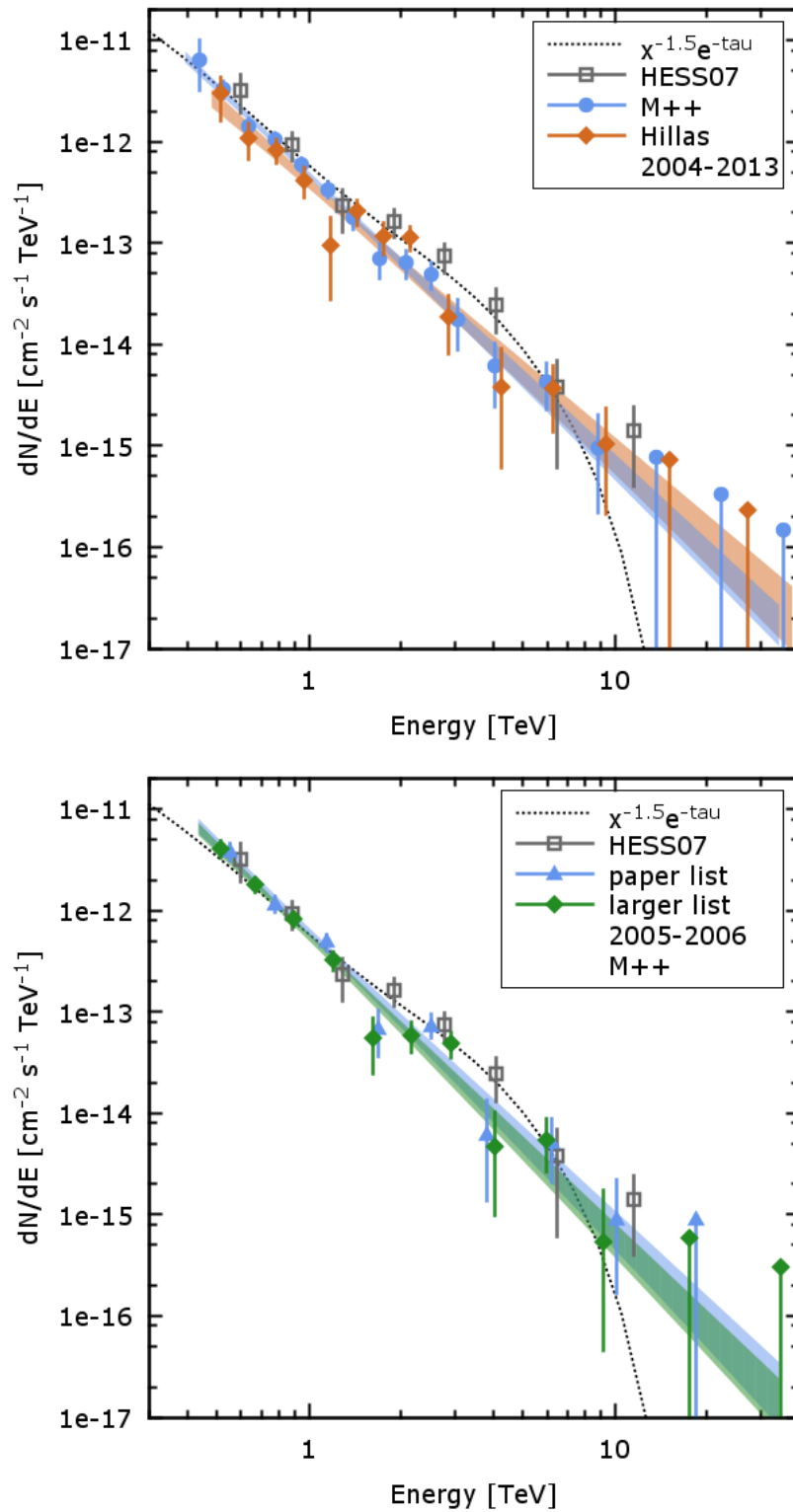


Figure 6.6: Spectra of the 2004-2013 (*top*) and 2005-2006 (*bottom*) analyses compared with the one from HESS07. An hypothetical absorbed hard intrinsic emission with $\Gamma = 1.5$ is also shown.

Table 6.5: Values of the photon indices Γ of a PL fit of the H.E.S.S. data for different analysis methods and datasets. VER14 results are also given for comparison. Only statistical errors are reported. Systematic errors are quantified in 10% of the central value in all cases. (a) The Model Hybrid analysis was one of the cross-checks for the HESS07 publication. (b) This work.

Analysis	2005 - 2006 paper runlist	2005 - 2006 larger runlist	2009 - 2012	2004 - 2013	no 2006
HESS07	2.50 ± 0.19				
Model Hybrid ^a	2.92 ± 0.23				
M++ ^b	2.90 ± 0.17	2.96 ± 0.15		2.87 ± 0.12	2.79 ± 0.19
Hillas ^b	2.69 ± 0.29	2.57 ± 0.18		2.65 ± 0.18	2.76 ± 0.35
VER14	all		2.59 ± 0.12		
	high state		2.53 ± 0.11		
	low state		2.64 ± 0.19		

principle) as similar as possible and at the same time test the M++ ones, Hillas analyses were performed on the 2005-2006 runlists described above. This can be done in the same paranalysis framework as for the M++ analysis, using the same DSTs, which also contain all the necessary information. The paper runlist yields a significance slightly smaller than the published one (5.9 vs 6.6σ). The spectrum is softer and has larger errors ($\Gamma_{\text{Hillas}}^{05-06\text{pap}} = 2.69 \pm 0.29$). It is compatible with both M++ and HESS07. The larger dataset yields a harder photon index $\Gamma_{\text{Hillas}}^{05-06} = 2.57 \pm 0.18$, which is not consistent with the respective M++ result. The analysis of the whole 2004 to 2013 dataset gives again a slightly softer spectrum ($\Gamma_{\text{Hillas}}^{04-13} = 2.65 \pm 0.18$), compatible with both the M++ and published results. The spectral values derived from the Hillas analysis are compatible with the VERITAS ones reported in section 6.1. The comparison of the indices is summarized in Table 6.5.

The apparent softening of the central value of all new Hillas results with respect to HESS07 could be explained by the completely different software framework, data calibration and spectral analysis technique used. Nonetheless, all indices are compatible within the $1-\sigma$ error.

As said, the spectra derived from the M++ analysis are softer than the others. In some cases they are compatible within the $1-\sigma$ error, sometimes they are significantly different. There are some consideration that can be done about these differences:

- M++ and the Hillas analysis are intrinsically very different. The former is much more sensitive than the latter, especially at low energies, with much higher background rejection capabilities. As an example, the detection significance for the 2004-2013 dataset is 18.4 and 8.9σ for the two analyses, respectively. The higher sensitivity leads to smaller statistical errors in the low energy spectral bins, and this can affect the spectral analysis even in the case of compatible spectral points. This concerns also the results published in HESS07 and VER14, both derived from Hillas analysis.

- In the bottom panel of Fig. 6.6, one can see that the M++ spectral points are perfectly compatible with HESS07 up to ~ 1 TeV. At higher energies, they do not show the clear wiggles in the spectrum with the same intensity. Instead, they show a deficit in the emission around 2 and 4 TeV. The effect is even more apparent for the 2004-2013 analysis. Interestingly, also the Hillas analysis cannot reproduce the same shape.
- The harder VERITAS spectrum could be partly expected because of the lower energies reached (240 versus 500 GeV, circa) thanks to the smaller Zenith angle of their observations. As it can be seen in Fig. 6.1, the maximum of the observed IC emission is expected to lie around a few hundreds GeV, meaning that the spectral slope naturally hardens towards lower energies.
- The last two spectral points in HESS07 at 6.5 and 11.5 TeV are not significant (less than 1.5σ). If the speculations about the IC peak done in Sec. 6.1 are true, and no further emission component exists above 10 TeV, the highest energy point is unrealistic and most likely only a statistical fluctuation. Modeling a hard intrinsic PL with $\Gamma = 1.5$ and absorbing it with the EBL model of Franceschini et al. (2008, hereafter FR08) shows that the highest energy flux should be smaller by a factor 50. Softer indices would increase this discrepancy. Despite the low significance, this possibly wrong flux affects the spectral fit for a combination of reasons:
 - the fit has been performed using a least-squares method (less sophisticated than the forward folding technique used in this work);
 - only 8 points enter the fit;
 - all points have low significance ($< 3.5\sigma$).

For such a fit, a point at the one end of the spectrum with a significance similar to that of the point at 11.5 TeV, but with a very different flux, strongly influences the value of the photon index. Correcting the flux by a factor 10 already causes an increase of 0.3 in the photon index, making it compatible with all other indices discussed above.

- If the last spectral point is indeed a statistical fluctuation, this would explain the lack of detection above 10 TeV in the M++ analysis of the same dataset, despite the M++ higher sensitivity. The 10 TeV point in the bottom panel of Fig. 6.6 is only 0.8σ . It spans between 8.5 and 15.5 TeV and is dominated by events below 10 TeV. The same explanation could hold for the larger H.E.S.S. and VERITAS datasets, although the flux variability (sec. 6.7) could play a role, as well. For VERITAS, the lack of detection could be due also to the fact that at high energies it has a smaller effective area than H.E.S.S. due to the smaller Zenith angle of their observations.
- The most recent cross-checks of the current M++ analysis carried out with a Boosted Decision Tree Hillas based analysis (BDT or TMVA, Ohm et al. 2009) provide spectra with indices $\Gamma \sim 2.8 \pm 0.15$, well compatible with the M++ values.
- If the hypothesis about the wrong flux is not correct, then the issue remains. A yearwise

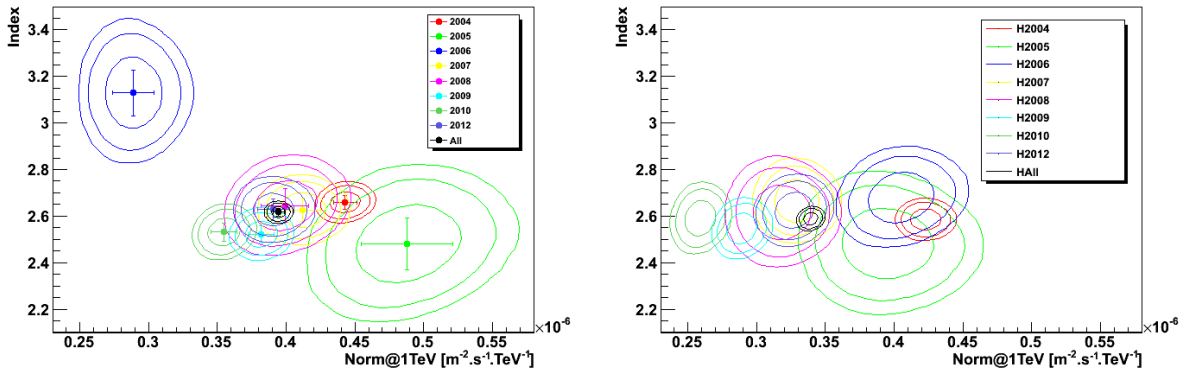


Figure 6.7: Yearly comparison of the Crab Nebula PL spectra between 0.7 and 7 TeV for M++ (*left*) and Hillas (*right*) analysis (Gianluca Giavitto, H.E.S.S. internal communication). In 2006, the M++ photon index is significantly softer than in all other cases.

comparison of the Crab Nebula spectra with M++ and Hillas analysis⁷ shows that the 2006 M++ spectrum is significantly softer than all others (Fig. 6.7). Such spectral variability is not expected because the Crab Nebula is considered a standard candle for TeV astronomy. This could hint towards calibration issues for the M++ DSTs of that period, due to a particularly hazy atmosphere caused by bush fires, which often burst on the Kohmas Highlands at the end of the Summer, beginning of the Autumn due to the prolonged drought. For uniform atmospheric conditions, the lightcurve of the hadronic background (cosmic rays) is expected to be flat. The one in Fig. 6.8, instead, is not, and reflects the hypothesis of an hazy atmosphere. It could be possible that, being M++ more sensitive than Hillas, it is also more sensible to strong atmospheric variations. 2006 is the year in which more than 1/3 of all observations of 1ES 0229+200 have been taken (Tab. 6.2) and which is characterized by a flux higher than average (sec. 6.7). It therefore dominates all analyses containing it. If an error affects these data, it is likely that all results will be affected by it. However, this seems not to be the case. A spectral fit excluding the 2006 data yields a compatible photon index $\Gamma_{\text{no2006}} = 2.79 \pm 0.19$.

- A last possibility is that the data are wrongly calibrated astrometrically, which is known to be the case at least of some periods of observations. This can be a problem because it affects the event and the energy reconstruction, leading to a loss of signal. It is not clear, however, whether or not it affects a consistent part of the dataset used. A dedicated recalibration exists on a source-by-source basis, but it has never been completed for 1ES 022+200 and could not be used. This issue concerns both M++ and Hillas models. It could possibly explain the common deficit of emission between 2 and 4 TeV and the slightly lower flux of the Hillas results. However, this bug should affect only the latest used DST production. The fact that the results remained stable disregarding the use of previous DST versions weakens this point.

⁷This comparison has been done by Francois Brun and reported by Gianluca Giavitto.

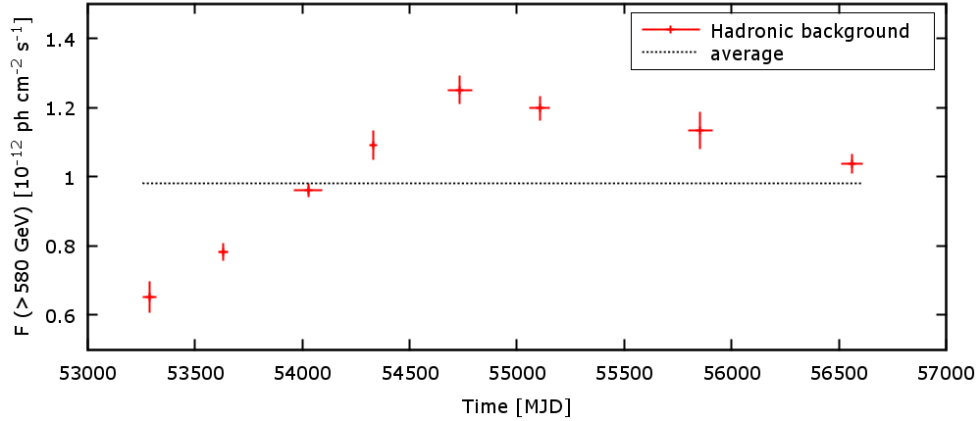


Figure 6.8: M++ yearly lightcurve of the hadronic background for the 1ES 0229+200 observations. Together with 2004 and 2005, in 2006 (MJD ~ 54000) the hadronic flux is significantly lower than in the following years. Given the amount of hours collected in 2006, a calibration error for this year could strongly affect the analysis of the whole dataset.

In the end, it is not completely clear what is the source of the different photon index values. Possibly, all of the hypothesis described above play a role. The fact that all analysis and cross checks, irrespective of the combination of softwares and datasets, show indices softer than in HESS07 demonstrates that the published value is indeed too hard. All of the analyses also fail to reproduce the spectral wiggles that were interpreted as EBL imprint in HESS07.

In order to detect a possible spectral variability, fits were carried out on the yearly and monthly datasets, as well. No spectral variability is detected on a yearly nor monthly timescale (Fig. 6.9, *top*). No spectral variability can be seen as function of the flux, either (Fig. 6.9, *bottom*). In Table 6.6, all spectral fits derived from a M++ analysis are summarized.

As mentioned at the beginning of the section, more complex spectral forms like CPL or ECPL do not improve the fit. They resemble a PL: both β and $1/E_{\text{cut}}$ are consistent with zero. It is not possible to determine, inside the tested energy range, a cut-off in the observed emission that indicates a cut-off in the underlying electron population or to the onset of the Klein-Nishina regime. Given the 3σ detection between 4 and 10 TeV in the M++ spectrum, both must be well above 10 TeV. In order to reach these energies, the underlying electron population must be very energetic. Here, the Thomson limit is valid only for low energy photons, and a cut-off due to the transition to the Klein-Nishina regime is expected at $E = \gamma mc^2 \delta$ (with δ the Doppler factor). In order to avoid a cut-off below 10 TeV, γ must be much larger than $2 \times 10^7 / \delta$, or alternatively have a very large Doppler factor.

Spectral analyses were conducted also on the Mono and Stereo datasets. For Mono, both *Safe* and *Std* cuts yield spectra that have a significant curvature ($\sim 3\sigma$). A comparison of the three spectral shapes is shown in the top-left panel of Fig 6.10 for the *Safe* cuts analysis. The CPL indices derived for the two cuts are not compatible (see Table 6.7), but their contours match well thanks to the different strength of the curvatures β (Fig. 6.10, *top-right*). The ECPL fits yield unphysically hard photon indices and very small cut-off energies, although the $1-\sigma$ contours still

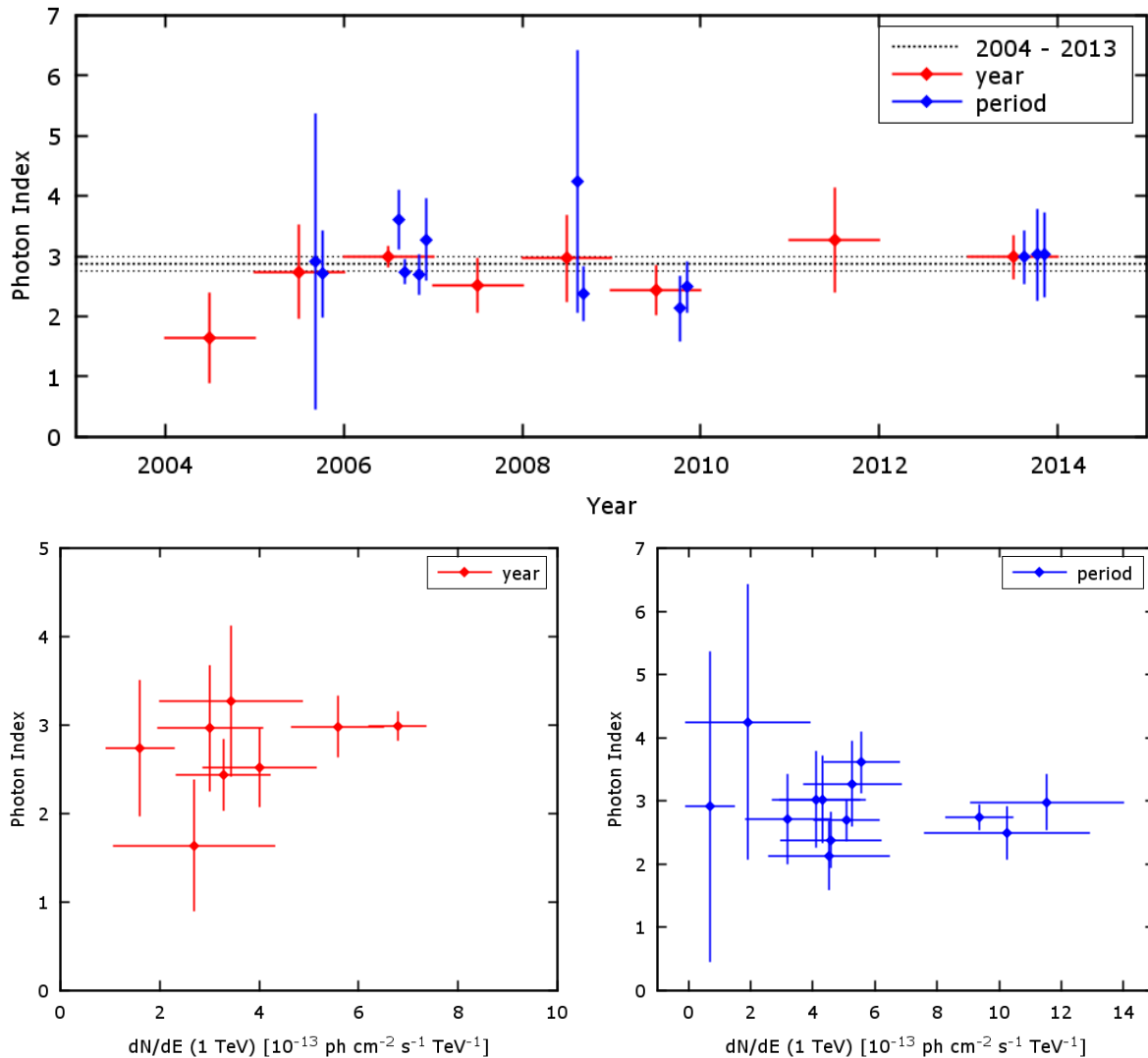


Figure 6.9: Photon index variability as function of the time (*top*) and of the flux normalization (*bottom*) for the yearly (*red*) and periodwise (*blue*) spectral fits. No variation can be seen in any of the plots. In 2004 and 2007 observations have been taken in a single period only, therefore they appear as yearly spectra only. No meaningful spectra can be derived for November 2008, August 2009, September 2013 and for all four periods in 2011, so they are not reported here. The dotted lines in the upper plot represent the 2004 - 2013 average photon index and $1\text{-}\sigma$ error.

match the CPL ones.

For Stereo, the PL is the better fit (Table 6.7 and Fig. 6.10, *bottom-left*). The photon index is very hard ($\Gamma_{\text{Stereo}} = 2.30 \pm 0.17$) and is incompatible with the HESS-I results, for both M++ and Hillas. This could be explained as a consequence of the different energy range involved. It starts at an energy about 100 GeV^8 lower than for HESS-I and reaches smaller high energies.

⁸The HESS-I spectrum starts at 390 GeV , but in the first 100 GeV the source is detected for just $\sim 1\sigma$.

Table 6.6: Spectral fits for different periods of H.E.S.S. observations. In 2004 and 2007 observations have been taken in a single period only, therefore they appear as yearly spectra only. No meaningful spectra can be derived for November 2008, August 2009, September 2013 and for all four periods in 2011, so they are not reported here. For the 2005-2006 dataset marked with (a), the analysis has been performed on the same dataset as in HESS07.

Period	Γ	$dN/dE(@ 1 \text{ TeV})$ [$10^{-13} \text{ cm}^{-2} \text{ s}^{-1} \text{ TeV}^{-1}$]	Energy range	$\chi^2/d.o.f.$ (prob)
2004 - 2013	2.87 ± 0.12	4.75 ± 0.31	0.39 - 34.37	59.8/64 (0.62)
2005 - 2006 ^(a)	2.90 ± 0.17	6.16 ± 0.59	0.44 - 34.37	30.9/40 (0.85)
2005 - 2006	2.96 ± 0.15	5.47 ± 0.45	0.44 - 34.37	43.5/56 (0.89)
2004	1.64 ± 0.74	2.69 ± 1.62	0.39 - 7.75	10.7/ 9 (0.30)
2005	2.74 ± 0.76	1.60 ± 0.67	0.48 - 31.12	16.0/20 (0.72)
2006	2.99 ± 0.16	6.79 ± 0.57	0.48 - 37.96	25.1/30 (0.72)
2007	2.52 ± 0.44	4.01 ± 1.14	0.48 - 31.12	14.9/19 (0.73)
2008	2.96 ± 0.70	3.01 ± 1.04	0.48 - 25.51	25.1/13 (0.02)
2009	2.44 ± 0.40	3.28 ± 0.93	0.59 - 17.15	27.9/21 (0.14)
2011	3.27 ± 0.85	3.44 ± 1.43	0.48 - 17.15	13.1/14 (0.52)
2013	2.98 ± 0.34	5.58 ± 0.92	0.48 - 31.12	9.3 /12 (0.68)
Sept. 2005	2.91 ± 2.44	0.69 ± 0.77	0.48 - 9.41	14.4/17 (0.64)
Oct. 2005	2.71 ± 0.70	3.19 ± 1.36	0.48 - 31.12	8.7/11 (0.63)
Aug. 2006	3.61 ± 0.48	5.58 ± 1.22	0.48 - 37.96	17.0/21 (0.71)
Sept. 2006	2.73 ± 0.19	9.35 ± 1.07	0.48 - 14.06	25.6/24 (0.37)
Nov. 2006	2.69 ± 0.31	5.10 ± 1.04	0.48 - 25.51	5.1/11 (0.93)
Dec. 2006	3.27 ± 0.67	5.28 ± 1.56	0.48 - 4.27	9.5/10 (0.48)
Aug. 2008	4.25 ± 2.16	1.92 ± 1.99	0.48 - 20.92	6.5/ 8 (0.59)
Sept. 2008	2.38 ± 0.44	4.58 ± 1.59	0.48 - 25.51	13.8/11 (0.24)
Oct. 2009	2.13 ± 0.53	4.52 ± 1.93	0.59 - 17.15	2.7/11 (0.99)
Nov. 2009	2.49 ± 0.41	10.3 ± 2.64	0.59 - 14.06	18.0/15 (0.26)
Aug. 2013	2.98 ± 0.43	11.5 ± 2.45	0.48 - 14.06	3.9/ 8 (0.86)
Oct. 2013	3.02 ± 0.75	4.10 ± 1.41	0.48 - 3.50	11.2/ 8 (0.19)
Nov. 2013	3.02 ± 0.68	4.32 ± 1.37	0.48 - 9.45	20.9/10 (0.02)

When comparing the Stereo and the Mono spectra (Fig. 6.10, *bottom-right*), it appears obvious that above 1 TeV they are not compatible. The Mono spectrum is significantly curved in an energy range where neither Stereo nor HESS-I show anything similar. The spectral point at 800 GeV also seem to have a too large flux. Such a strong curvature is not expected from anything known from the literature, as well. It is therefore likely that, at the moment, the Mono

Table 6.7: Mono and Stereo spectral fits.

		Γ	β/E_{cut}	$dN/dE(@ 1 \text{ TeV})$ [$10^{-12} \text{ cm}^{-2} \text{ s}^{-1} \text{ TeV}^{-1}$]	Energy range	$\chi^2/d.o.f.$ (prob)
Mono	PL	2.67 ± 0.27		1.03 ± 0.23		47.8/27 (0.01)
<i>Safe</i>	CPL	1.74 ± 0.53	1.14 ± 0.67	1.70 ± 0.38	0.22 - 10.4	38.2/26 (0.06)
	ECPL	0.28 ± 1.31	0.38 ± 0.24	1.80 ± 0.41		37.9/26 (0.06)
Mono	PL	2.53 ± 0.26		1.05 ± 0.24		44.5/28 (0.03)
<i>Std</i>	CPL	2.89 ± 0.53	1.28 ± 0.72	1.76 ± 0.40	0.20 - 10.4	32.8/27 (0.20)
	ECPL	0.1 ± 1.4	0.31 ± 0.20	1.75 ± 0.41		32.5/27 (0.21)
Stereo	PL	2.30 ± 0.17		1.06 ± 0.13		28.8/29 (0.48)
<i>Std</i>	CPL	2.20 ± 0.30	0.10 ± 0.20	1.11 ± 0.17	0.32 - 18.9	28.6/28 (0.43)
	ECPL	2.28 ± 0.40	85 ± 1376	1.06 ± 0.15		28.8/28 (0.42)

spectrum is affected by some systematics and is not reliable for 1ES 0229+200.

Beside this issue, the two Mono and Stereo spectra are also clearly incompatible with both the 2004-2013 and 2013 HESS-I spectra, as it can be seen in the top panels of Fig. 6.11. Their fluxes are off of a factor 2. This cannot be justified by variability, since the 2013 dataset are very similar. When considering the toy model of the absorbed intrinsic emission introduced earlier (shown in all panels as reference) one can see that it reproduces the *Fermi* and 2013 HESS-I spectra fairly well, at least up to 2 TeV. Above, the HESS-I spectrum is affected by the same deficit described above as the long term spectra. Interestingly, the Stereo spectrum seems to follow the same shape of the toy model, only at higher energies. This could hint towards an energy shift as described in Chapter 8. There, it is shown that a systematic bias exists between the energies reconstructed with the different analyses. It is therefore likely that the inconsistency shown here depends on the energy calibration issue. The same test was repeated for 1ES 0229+200. It shows the same results as for the Crab Nebula⁹ (sec. 8.2.2): a 20% bias is expected for Mono, and none for Stereo. An energy bias seems to be excluded. Nonetheless, correcting the Stereo spectrum of a factor 0.8 in energy seems to fix the problem (Fig. 6.11, *bottom*). The effect of this correction is better visible in the energy spectrum plots. The Stereo spectral points are consistent with both the toy model and the 2013 HESS-I points at least up to 2 TeV. With all the caveats discussed before, the same is valid for the Mono spectrum, as well. It has to be noted here that the value of 20% is empiric and cannot be based on the outcomes of the test on the energy bias. This simple scaling does not take into account any possible energy dependencies during the spectral fit, like those on the effective area. For this reason, it can be seen as a rough first order correction.

At last, one could consider the systematic error on the flux, which is evaluated to be around 20%. This would not be enough to make up for the 50% difference in the flux.

⁹1ES 0229+200 has a similar declination as the Crab Nebula and the two sources are not too far apart in R.A.

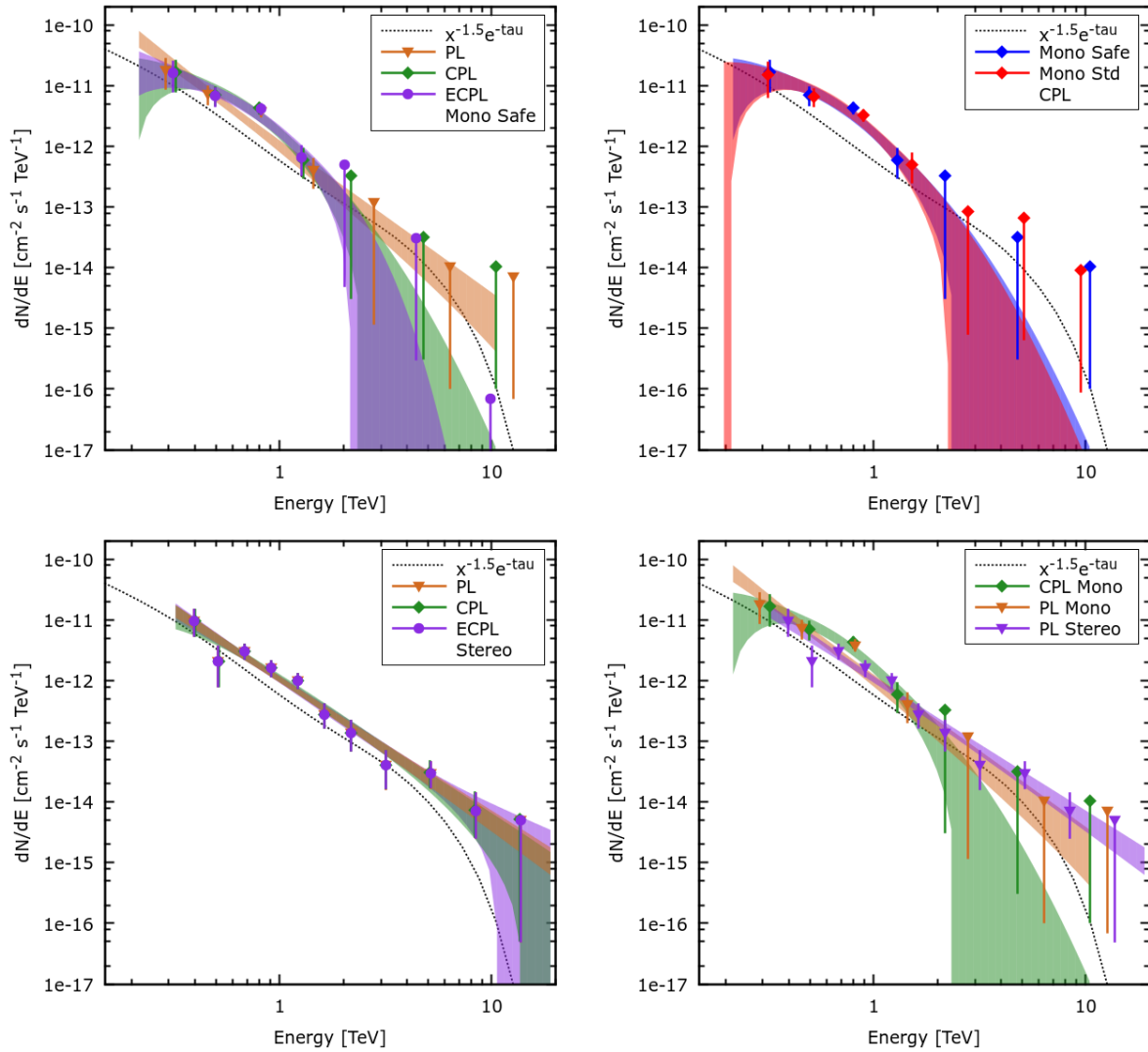


Figure 6.10: *Top-right:* Mono spectrum fit with three spectral shapes. Curved spectral shapes are significantly better than a simple PL. *Top-right:* comparison of the Mono *Safe* and *Std* CPL spectrum. The two are equivalent. *Bottom-left:* Stereo spectrum fit three spectral shapes. No curvature can be seen. *Bottom-right:* comparison of the best Mono and Stereo spectra. The two are hardly compatible. The Mono PL is shown as reference, as well.

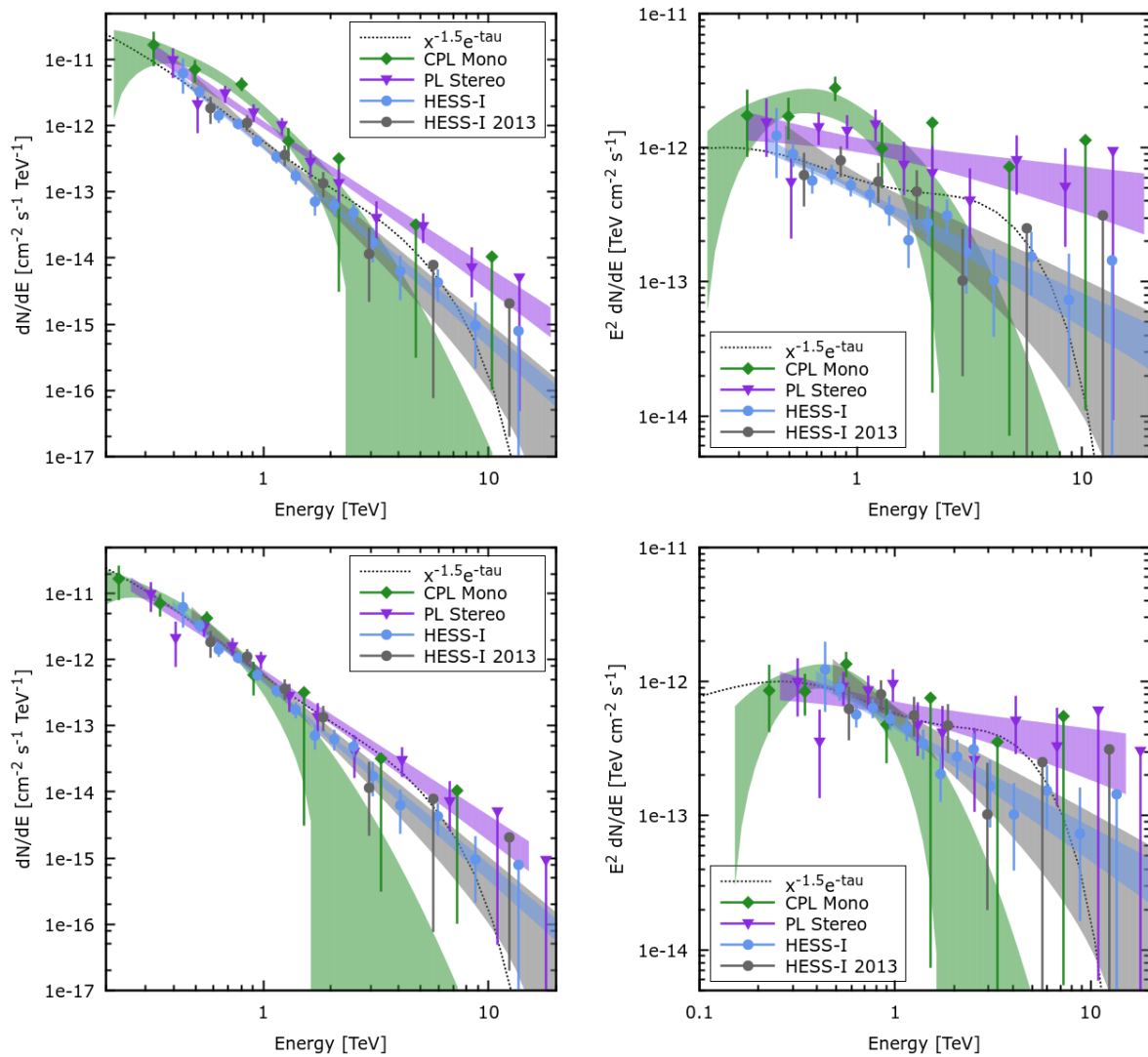


Figure 6.11: *Top:* comparison of the HESS-I and the Mono and Stereo spectra in flux (*left*) and energy flux(*right*) representation. The HESS-I and HESS-II spectra are clearly incompatible. *Bottom:* same as above, but with the Mono and Stereo energies multiplied by a factor 0.7 and 0.8 respectively.

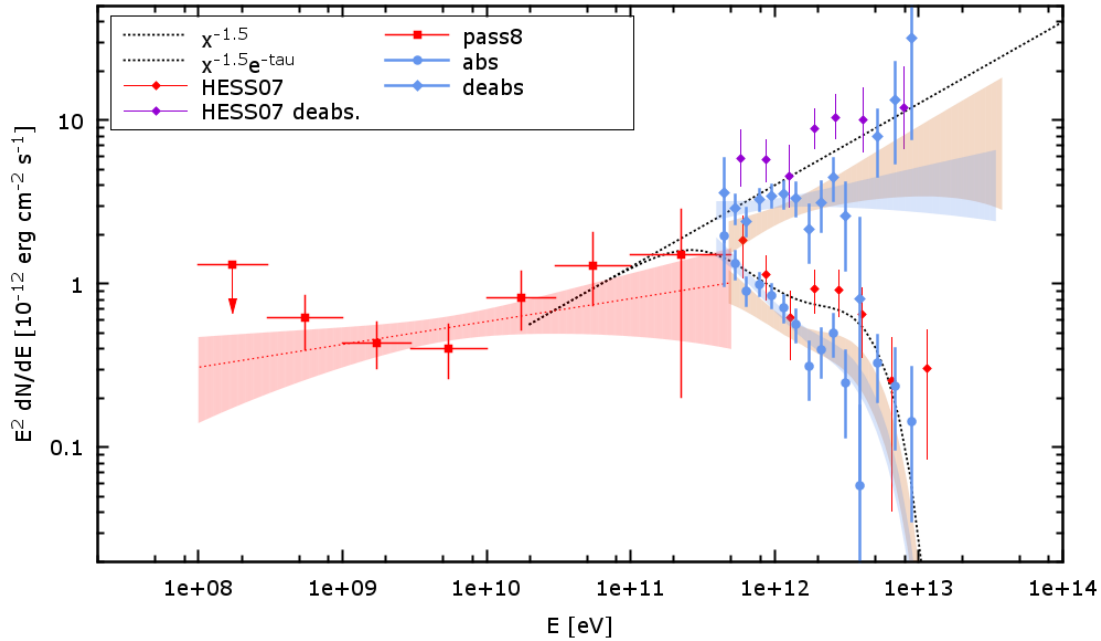


Figure 6.12: SED of the HE and VHE component of 1ES 0229+200.

6.6 SPECTRAL ANALYSIS WITH EBL ABSORPTION

The spectra derived up to here are all observed spectra. It is known that they are absorbed by the EBL. In order to reconstruct the shape of the intrinsic emission from the AGN, they need to be deabsorbed. This can be done using EBL models, which predict the density of the background light as function of the wavelength and of the redshift. In HESS07, the model of Primack et al. (2005) scaled by a factor 1.6 was used. They found that the data could be fit with a simple hard PL with intrinsic photon index $\Gamma_{\text{HESS}}^{\text{deabs}} = 1.58 \pm 0.22$. The index is compatible with the ones derived at GeV energies by Vovk et al. (2012, $\Gamma_{\text{GeV}}^{\text{Vovk}} = 1.36 \pm 0.25$) and H. E. S. S. Collaboration et al. (2014, $\Gamma_{\text{HESS 2014}}^{\text{Fermi}} = 1.5 \pm 0.3$), as well as with the newest results presented in sec. 6.3.1 ($\Gamma_{\text{PL}}^{\text{Fermi}} = 1.86 \pm 0.13$ for the simple PL and $\Gamma_{\text{2BPL}}^{\text{Fermi}} = 1.69 \pm 0.19$ for a BPL above 3.5 GeV). These results support the hypothesis of a single hard PL spectrum going from a few GeV up to at least 10 TeV.

In the previous section, it has been shown how the new HESS-I spectra derived with M++ are significantly softer than the one in HESS07. It is therefore interesting to see how the intrinsic spectrum changes. Spectral fits comprising EBL absorption were carried out on the datasets 2004-2013 and 2005-2006 datasets described above, for both M++ and Hillas. The EBL model of FR08 was used. The same attempt to define the best EBL normalization as in sec. 7.6, and hence determine a more precise intrinsic spectrum, was done on the full dataset. Unfortunately, the inclusion of the EBL absorption did not improve the goodness of the fit. It did not improve or worsen significantly for all EBL normalizations tested, either. For this reason, only the results obtained with the unmodified FR08 model and reported in Table 6.8 will be discussed.

Table 6.8: EBL spectral fits. (a) indicates the runlist used in HESS07.

	Dataset	Γ_{int}	$\text{dN/dE}(@ 1 \text{ TeV})$ [$10^{-12} \text{ cm}^{-2} \text{ s}^{-1} \text{ TeV}^{-1}$]
HESS07	2005 - 2006 ^(a)	1.58 ± 0.22	
M++	2004 - 2013	1.85 ± 0.13	1.91 ± 0.13
	2005 - 2006 ^(a)	1.96 ± 0.19	2.54 ± 0.25
	2005 - 2006	1.99 ± 0.16	2.26 ± 0.19
Hillas	2004 - 2013	1.62 ± 0.21	1.62 ± 0.21
	2005 - 2006 ^(a)	1.76 ± 0.35	1.85 ± 0.36
	2005 - 2006	1.56 ± 0.22	2.06 ± 0.29
Mono <i>Safe</i>		1.75 ± 0.27	4.35 ± 0.96
Mono <i>Std</i>	2013	1.64 ± 0.27	
Stereo <i>Std</i>		1.34 ± 0.18	4.34 ± 0.54

The intrinsic photon indices derived with Hillas are well compatible with HESS07. They support the hypothesis of a continuous hard PL described above. In this interpretation, the 2004-2013 flux does not match perfectly the level shown by *Fermi*, but in principle this can be explained with flux variability (see sec. 6.7), since the observations are not contemporaneous.

The M++ intrinsic indices, on the other hand, are much softer and just marginally compatible with all Hillas derived ones. The H.E.S.S. and *Fermi* spectra can match inside the statistical errors only in three cases:

- when considering the PL fit of the *Fermi* spectrum, the two indices are exactly the same. To match the two spectra, an increase of the *Fermi* flux of a factor 3 is needed;
- when considering the hard component of the HE BPL fit, the two spectra match only if the *Fermi* flux is increased of a factor 2 and the harder limit of the H.E.S.S. photon index is used;
- a curvature or a break exists in the intrinsic spectrum around few hundred GeV.

The first two options are unlikely because, even if flux variations of a factor 2 or 3 have been detected in the VHE emission (Fig. 6.13, top panels), the long term H.E.S.S. spectrum is an average of all these states. There is also no reason to believe that in the periods without H.E.S.S. observations the source should have been mainly in a low state, so to justify this large discrepancy. If the hypothesis made in sec. 6.7 about the correlation of the X-ray and γ -ray emission are correct, one can see from the two bottom panels in Fig. 6.13 that such large corrections are not justified. Nor the other way around, reducing the H.E.S.S. flux of the same factor. It must be

noted also that the renormalization of the fluxes works in opposite ways for the M++ and Hillas spectra. This means, they are mutually exclusive¹⁰ since the dataset is the same.

The third option is interesting, but is also likely to be incorrect. As can be seen in Fig. 6.12, the last three deabsorbed points are not compatible with the contour of the spectrum. Their combined significance is more than 3σ . This means that the resulting spectral point deviates significantly from the soft spectrum. It would be compatible, instead, with a harder spectrum similar to the Hillas one or to the toy model. The points up to 1.5 TeV would be compatible with such a spectrum, as well. Again, the deficit between 2 and 4 TeV strongly affects the results.

Like it has been done in the previous section for the observed spectra, it is interesting to check if there are hints of curvature or cut-off beyond the EBL absorption. Even if more complex spectral shapes are not significantly better than an absorbed PL, they could still point towards the presence of a spectral feature. Again, this is not the case. They both resemble an absorbed PL, with β and $1/E_{\text{cut}}$ consistent with zero. It is not possible to determine, inside the tested energy range, a cut-off in the intrinsic IC emission or the onset of the Klein-Nishina regime. Both must be well above 10 TeV.

In spite of the possible lower flux, it seems that the slope of the Hillas spectrum describes better the source emission. That the spectrum is harder than the M++ ones is also hinted by the deabsorbed Mono and Stereo spectra, despite all caveats mentioned in the previous section. The Stereo intrinsic photon index is very hard, but is compatible with the theoretical limit of 1.5 and with the Hillas result. The Mono spectrum is affected by excessive curvature, but a simple absorbed PL yields indices compatible with the harder results.

Fits comprising EBL absorption of the HESS-II data using more complex spectral shapes give unphysical results and are therefore ignored.

Taking into account the harder values, the VHE intrinsic photon index converge around a value of $\Gamma = 1.6 \pm 0.2$. This value depends obviously on the EBL model used, here FR08. However, as it will be discussed in sec. 7.6 and as it has been shown in Biteau & Williams (2015), the FR08 model describes adequately the true shape of the EBL.

6.7 TEMPORAL ANALYSIS

The lightcurves (see sec 4.9) of the whole decade of observations were derived using the average 2004 - 2013 spectrum evaluated in sec.6.5. The integral flux was obtained integrating over energies above a common threshold of 580 GeV. The monthly and yearly lightcurves are shown in the top two panels of Fig. 6.13.

In HESS07, no flux variability was claimed. During the 2009 MWL campaign, the source could not be detected, despite the amount of hours of observation collected should have allowed that. This was a strong hint that 1ES 0229+200 was variable.

The Model analysis is more sophisticated and sensitive than the Hillas analysis used in that publication. Its use permits therefore to have a much higher sensitivity to small flux variations.

¹⁰Systematic effects on the data calibration that could affect only one analysis are not considered here.

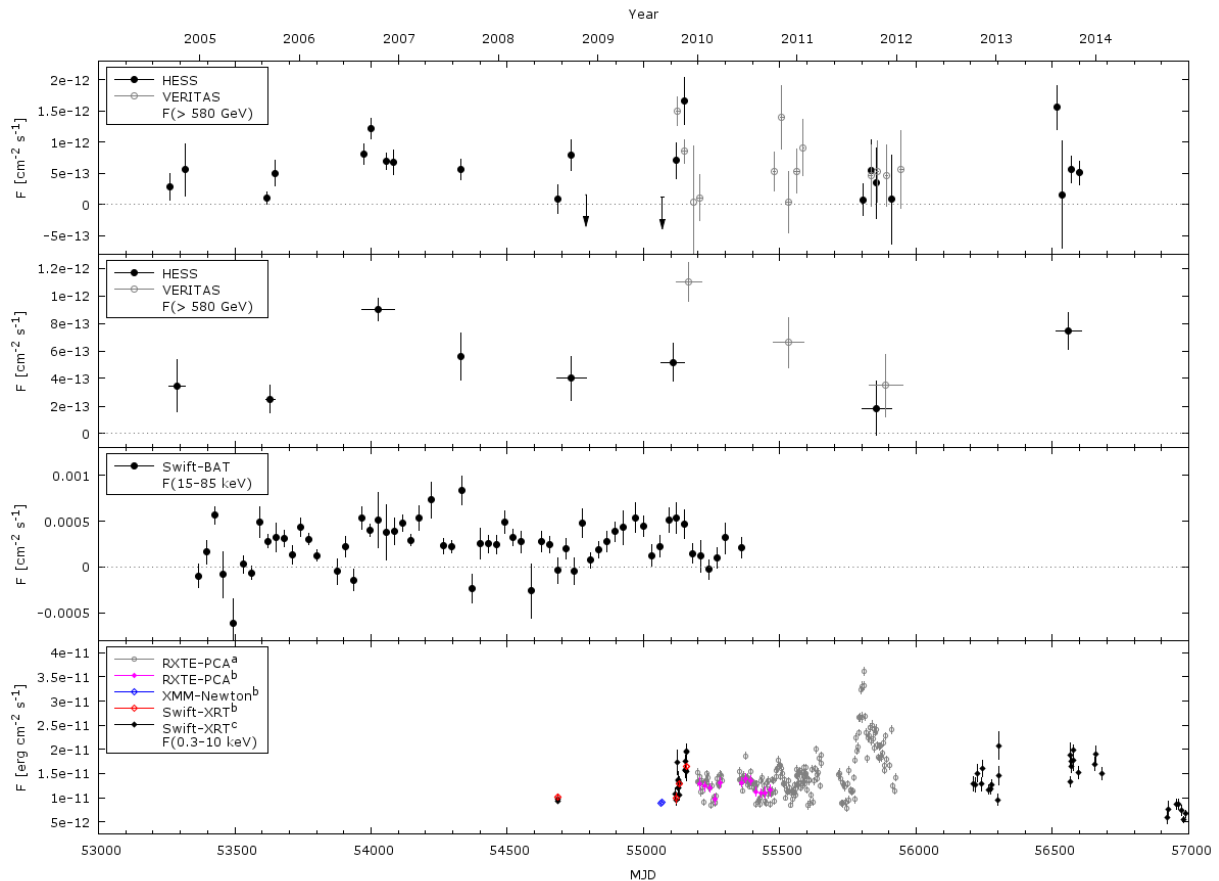


Figure 6.13: Lightcurves of the BL Lac object 1ES 0229+200 in different energy bands between 2004 and 2013. From *top to bottom*: monthly and yearly H.E.S.S. lightcurves above 580 GeV - the VERITAS values from VER14 are also depicted as comparison; hard X-rays monthly lightcurve between 15 and 85 keV from *Swift*-BAT (Cusumano et al. 2013); soft X-ray lightcurve between 2 and 10 keV for different instruments: *a*) 2010-2012 *RXTE* dataset from Rivers et al. (2013), *b*) *XMM-Newton*, *Swift*-XRT and *RXTE* data from Kaufmann et al. (2011), *c*) *Swift*-XRT data analysed in this work. The source is clearly variable in all energy bands. The discrepancy between the H.E.S.S. and VERITAS points in 2009 is explained by the non identical observation windows of the two instruments (see text). Three points at MJD 53831, 55331 and 55377 have been removed for clarity from the *Swift*-BAT plot because of their large negative fluxes or error bars.

Together with the much larger dataset available, it is possible to detect variability in this faint source. The monthly and yearly VHE lightcurves (top two panels of Fig. 6.13) show an emission which is not constant, neither on a yearly, nor on a monthly timescale. A fit to a constant value yields a χ^2 of 84.3 (33.3) for 22 (7) degrees of freedom for the monthly (yearly) lightcurve. This translates into a probability of 3×10^{-9} and 2×10^{-5} respectively. The fractional variability (Vaughan et al. 2003, but the errors are estimated as in Poutanen et al. 2008) yields values of 0.60 ± 0.15 and 0.39 ± 0.11 . Variability is detected on a monthly timescale also in smaller energy ranges. The probability of a constant flux is 1×10^{-4} between 0.58 and 1 TeV and 2×10^{-5} above 1 TeV.

In 2009, H.E.S.S. and VERITAS observed the source contemporaneously (though on different nights). The time range spanned by the VERITAS observations was significantly longer than the H.E.S.S. one. Taking the windows into account, the measurements of both experiments are consistent with an increasing flux that reaches its maximum just before MJD 55150 and then decreases. The comparison of the VHE and X-ray data in 2009 (Kaufmann et al. 2011) is very interesting. The source is in very low state for both H.E.S.S. and XMM-*Newton* during the MWL campaign (MJD \sim 55065). In the following three months, *Swift*-XRT detects a flux increase of a factor ~ 2 (Kaufmann et al. 2011), which is also seen by *Swift*-BAT in the hard X-ray band. This is mirrored by an enhancement in the γ -ray emission of a factor 2 or 3 (Fig. 6.13). In all three wavebands, this state is followed by a decrease in the emission. Despite the limited sensitivity of *Swift*-BAT, it is interesting to notice that the three periods of low VHE fluxes in 2008 and 2009 are mirrored also in its energy band. The R and B bands optical lightcurves, instead, are constant within the errors and do not show any variations. During the second MWL campaign in 2013 (MJD \sim 56570), 1ES 0229+200 seems to be relatively bright in X-rays and on its average value in TeV.

A correlation in the X-ray-VHE emission is expected by the SSC model, implying that the two components are generated by the same electron population. On the other hand, the big peak shown by *RXTE* in 2011 (MJD \sim 55800) does not have a clear correspondence in TeV. There are at least four possible explanations for this behaviour:

- the very low exposure in three out of the four periods of H.E.S.S. observations. However, assuming the same VHE to X-ray ratio as in 2009, it seems unlikely that such a prolonged period of high activity would be completely missed by both H.E.S.S. and VERITAS. It is even more unlikely if one considers the 2010-2011 VERITAS observations, when the VHE emission closely follows the evolution of the *RXTE* lightcurve.
- a period of high activity of one of the other X-ray sources present in the field of view of *RXTE*, like 1RXS J023558.0+201215, 1RXS J023427.5+192247 or one of the numerous XMM sources.
- the presence in 1ES 0229+200 of a second X-ray emitting zone, unrelated to any γ -ray emission.
- under certain conditions, the γ -ray emission could be prevented by Klein-Nishina suppression.

6.8 INTERGALACTIC MAGNETIC FIELD (IGMF) DETERMINATION

The interaction of the VHE emission with the EBL leads to the production of beams of energetic e^-e^+ pairs through photon-photon collisions. The particles have Lorentz factors γ typically of the order of $10^6 - 10^7$. They are expected to upscatter the cosmic microwave background (CMB) photons via IC to GeV energies. The reprocessed emission will add to the source intrinsic HE emission, generating a surplus. However, up to now there is no evidence in any source for the detection of a reprocessed component. To explain this lack, IGMFs have been invoked. They should deflect the e^-e^+ pairs out of their original path parallel to the primary VHE photons, reducing the amount of secondary emission that reaches the observer proportionally to the field strength. Lower limits on the IGMF can therefore be computed under some assumptions.

Thanks to its hard multi TeV intrinsic spectrum, 1ES 0229+200 is one of the key sources for the determination of lower limits on the IGMF. Values in the range $10^{-18} - 10^{-14}$ G have been derived by several authors (Neronov & Vovk 2010; Tavecchio et al. 2010, 2011; Ahlers 2011; Dermer et al. 2011; Dolag et al. 2011; Taylor et al. 2011; Vovk et al. 2012). The difference in the results derives not only by the method adopted for the calculation of the reprocessed emission, but also on the assumptions on the unknown physical parameters of the source. New constrains on the IGMF can qualitatively be determined by comparing these works with the results on the VHE flux variability and on the refined GeV spectrum presented in the previous sections. Here, the two models of Taylor et al. (2011) are considered:

- the “minimal” case: the fraction of absorbed VHE emission (and hence of reprocessed HE emission) is minimized through the use of a lower bound of the cut-off energy of the intrinsic TeV spectrum. For 1ES 0229+200, $E_{\text{cut}} = 5$ TeV and a photon index $\Gamma = 1.2$ have been used (“hard” case). In Vovk et al. (2012) a “soft” case has been tested, as well, with $\Gamma = 1.5$;
- the “maximal” case: the fraction of absorbed VHE emission (and hence of reprocessed HE emission) is maximized through the use of a high energy cut-off and a hard photon index. For 1ES 0229+200, $E_{\text{cut}} = 100$ TeV and $\Gamma = 1$ have been used.

As a sort of “maximal” model can be considered also the hadronic scenario. It has been stated that the HE-VHE γ -rays from 1ES 0229+200 could be explained by proton cascade emission (e.g. Essey & Kusenko 2010; Essey et al. 2010, 2011a,b).

6.8.1 EFFECTS OF THE VHE VARIABILITY

Reprocessing causes an energy dependent delay in the arrival time of the secondary photons (sec. 2.4.4). Even the reprocessed emission of monochromatic photons will be spread in both energy and time due to how and when the actual absorption of the primary γ -rays and the re-emission of the secondary photons will take place. Because of the time delay, no variability is expected to be seen and the observed reprocessed emission corresponds to the time-averaged original VHE emission. The IGMF constrains rely hence on the assumption of a steady VHE flux on time scales of these delays. Is the VHE flux variable, average values can be used as long

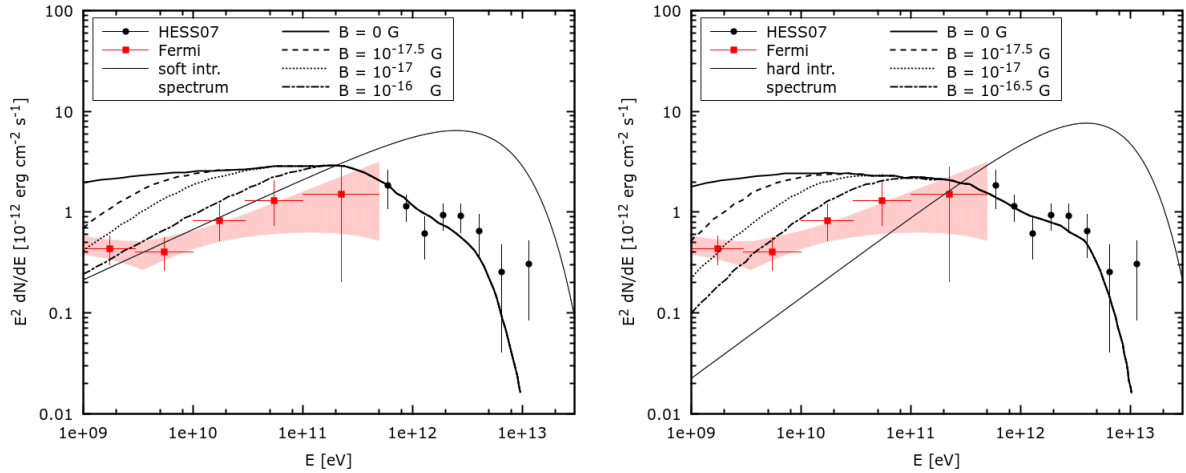


Figure 6.14: Comparison of the “soft” (*left*) and “hard” (*right*) models with the new *Fermi* spectrum. The two plots are taken from Vovk et al. (2012), the updated *Fermi* spectrum is added in red.

as the variability is shorter than the reprocessing time delay.

As shown in sec. 6.7, VHE variability on monthly timescales has been detected above 580 GeV, as well as above and below 1 TeV. For the maximal case, if the ~ 600 GeV emission consists of secondary photons, then a measurement of the IGMF can actually be done. From both eq. 2.53 and Fig. 2 in both Taylor et al. 2011 and Arlen et al. 2014, one gets IGMF values of the order of $B_{\text{IGMF}} \sim 5 \times 10^{-17} \text{ G}^{11}$.

However, the detected variability above 1 TeV implies that the radiation of this source is dominated by primary γ -rays. This challenges the “maximal” models and those proton-cascade models that require the TeV emission to be constant and consisting of secondary radiation only (although under some circumstances monthly and yearly variability could be detected, Prosekin et al. 2012). The derivation of an IGMF strength with such models would therefore not be correct.

6.8.2 LIMITS FROM THE REVISED *Fermi* SPECTRUM

The revised GeV spectrum presented in sec. 6.3.1 is more precise and reaches higher energies than the one used in Vovk et al. (2012), thanks to the much larger dataset. New limits on the IGMF can be determined by simply comparing the current *Fermi* spectrum with the levels of secondary emission presented in that publication. This is done in Fig. 6.14. Here, the contours of the BPL fit are shown, so to consider an energy range more similar to the one in Vovk et al. (2012).

In the “soft” case, the best fit is given by the intrinsic spectrum itself. A minimum value of $B_{\text{IGMF}} > 10^{-16} \text{ G}$ is needed for the secondary emission to be at the level of the errors of the *Fermi* spectral points. In the “hard” case, it must be $B_{\text{IGMF}} > 3 \times 10^{-16} \text{ G}$. Though, such a strength

¹¹Due to the uncertainties and model dependence of the calculation of the time delay, only a rough estimate can be done, between 10^{-17} and 10^{-16} G .

would underestimate the flux between 1 and 3 GeV. Both models underestimate the emission at even lower energies, requiring an additional component.

The models used here have been constructed in such a way that the resulting limits are very conservative. A cut-off at 5 TeV in the VHE spectrum finds no support in the H.E.S.S. data. As shown in sec. 6.5 and 6.6, the intrinsic emission remains hard at least up to 10 TeV. A cut-off at higher energies implies a larger amount of primary radiation being absorbed, hence an increase of the emission of reprocessed radiation. The strength of the IGMF needed to fit the GeV spectrum would be higher. Most models used by other authors rely on “hard” and/or “maximal” type models with $\Gamma_{\text{int}} < 1.2$. They need strong magnetic fields $B_{\text{IGMF}} > 10^{-14}$ G in order to not exceed the measured GeV emission. However, such strong fields are mostly constrained by the emission above 50 GeV and all fail to reproduce the emission at lower energies. This suggests that a “soft/minimal” model best describes the intrinsic emission.

All the limits derived depend obviously on the EBL density. A smaller density would allow for less absorption, less re-emission and hence for the need for a weaker IGMF. On the contrary, stronger IGMF would be needed to reduce the secondary emission caused by an increased absorption from a higher EBL level.

6.8.3 COMMENTS ON PLASMA EXCITATION THEORIES

Plasma excitation theories (e.g. Schlickeiser et al. 2012a,b, 2013; Broderick et al. 2012; Supsar & Schlickeiser 2014; Chang et al. 2014; Menzler & Schlickeiser 2015) show how the e^-e^+ pairs produced by photon-photon interaction in the cosmic voids will cause oblique instabilities in the intergalactic medium (IGM). Because of said instabilities, the pairs will lose their energy and heat up the IGM itself. For sufficiently bright VHE sources at $z < 4$, the cooling rates of the plasma instabilities dominate the IC cooling above 1 TeV by orders of magnitude (e.g. Broderick et al. 2012, Fig. 2 and 3). The lack of an excess in the GeV emission is hence unavoidable and independent from the presence of an IGMF. As a consequence, it is also not possible to determine lower bounds on the IGMF with the methods used in the previous section.

In the case of 1ES 0229+200, even the most conservative scenario (Chang et al. 2014, Fig. 3) implies that the cooling due to plasma instabilities dominates over the IC cooling for primary photon energies above 0.8 TeV. No secondary emission is then expected. Menzler & Schlickeiser (2015) show that the GeV emission of 1ES 0229+200 can be explained without the need for an IGMF of any strength. In the case of a “soft-minimal” scenario, the reprocessed component is nonexistent. This supports the interpretation made in section 6.6 about the IC spectrum: a single hard ($\Gamma \sim 1.5$) PL which extends from a few GeV up to at least 10 TeV.

6.9 CONCLUSIONS

In this chapter, the BL Lac object 1ES 0229+200 has been presented. This source is unique and important because of the combination of its hard spectrum reaching 10 TeV and its considerable distance. These characteristics make of 1ES 0229+200 one of the key sources for deriving constraints on the EBL and on the IGMF.

The 10 years long H.E.S.S. monitoring between 2004 and 2013 has been analyzed in a MWL context. Clear variability is detected at VHE on monthly and yearly timescales. The lightcurves in different energy bands hint towards a correlation between TeV and X-ray emission. The overall shape of the VHE lightcurve mimics the evolution of the lightcurve in the soft X-ray band. This supports an SSC emission model for the X-ray and VHE emission in 1ES 0229+200. VHE variability is detected both above and below 1 TeV. This suggests that the emission is primary, putting constraints on the derivation of the IGMF strength.

For the spectral analysis, the results from two different models were used: M++ and Hillas. The M++ spectrum (and in lesser way the Hillas spectrum) fails to reproduce the expected characteristic whiggles, sign of the EBL imprint, that were well defined in HESS07, and shows a deficit in the emission between 2 and 4 TeV. This result does not depend on the dataset used. While the Hillas PL photon index is compatible with HESS07 and VER14, the M++ index is significantly softer, probably a consequence of the aforementioned deficit. No spectral variability has been detected as a function of the flux or of the time on a monthly or yearly timescale.

The Mono and Stereo spectra show harder PL photon indices, in line with the Hillas results and expected by the natural hardening at low energies in the connection region between the *Fermi* and H.E.S.S. bands. The Mono spectrum is significantly curved at the 3σ level, but the strong curvature is incompatible with both Stereo and HESS-I spectra. It seems not to be reliable. The HESS-II spectra show a higher flux than HESS-I. For Mono, this seems to be at least partly caused by a shift of the energy calibration of $\sim 20\%$ towards higher energies. The Stereo energies have no bias, but an empirical correction factor of 0.8 removes the disagreement with HESS-I.

When considering the EBL absorption, the Hillas intrinsic photon index supports the hypothesis of a continuous hard PL from few GeV up to at least 10 TeV. The deabsorbed M++ spectrum, instead, is softer and is not compatible with the *Fermi* spectrum. A hard intrinsic emission is supported also by the deabsorbed Stereo spectrum.

From both HESS-I absorbed and deabsorbed spectra was not possible to determine a lower limit for an intrinsic spectral curvature. This suggests that a cut-off in the electron energy distribution, or the onset of the Klein-Nishina regime must be well beyond the 10 TeV. A very energetic particle population (or a large Doppler factor) with $\gamma > 2 \times 10^7/\delta$ is hence needed to avoid a cut-off in the spectrum below 10 TeV.

New constraints on the IGMF rely on the VHE monthly flux variability and on the refined GeV spectrum. The flux variability is detected also above 1 TeV. It implies that the radiation is dominated by primary γ -rays. This disfavors those proton-cascade models and “maximal” type cascade models in general that require the TeV emission to be constant and consisting of secondary radiation only. Nonetheless, if under some circumstances the emission at ~ 600 GeV

can be assumed to be of secondary photons, a measurement of the IGMF can be obtained: $B_{\text{IGMF}} \sim 3 \times 10^{-16}$ G. The detection of variability in the HE range would put further constraints on B_{IGMF} , increasing the lower limits.

Comparing the new *Fermi* spectrum with the IGMF models found in the literature, under the hypothesis of a “minimal” case where the VHE is primary emission, one sees that the contribution of the reprocessed radiation to the GeV spectrum must be low, if not completely absent. The constraint is primarily given by the last spectral point between 100 and 500 GeV.

The *Fermi* spectrum is compatible with the “soft” model in Vovk et al. (2012) for B_{IGMF} a few times 10^{-16} G, similar to the value derived for the “maximal” case. The range $0.3\text{-}3 \times 10^{-15}$ G is excluded by H. E. S. S. Collaboration et al. (2014), even if for a different energy range considered here. Other models would be consistent with this spectrum for values of B_{IGMF} of at least $\times 10^{-14}$ G. It cannot be excluded that the spectral softening below 1 GeV is due to reprocessed emission.

CHAPTER 7

MRK 501

7.1 SOURCE DESCRIPTION

Markarian 501 (Mrk 501, also known, among others, as 4C 39.49, B2 1652+39 and 4U 1651+39) is one of the objects classified by the Armenian astrophysicist Benjamin "Benik" Egishevitch Markarian in the First Byurakan Spectral Sky Survey, or Markarian Survey (Markarian 1967). The survey started in 1965 with the aim of classifying nearby galaxies which showed anomalous spectra with strong ultraviolet (UV) continuum emission in the central regions. This was thought to be non-thermal and originating from the galactic nuclei. More than 200 Seyfert galaxies and hundreds of starburst galaxies were discovered in this survey (Petrosian et al. 2007). The particular object Mrk 501 was first listed in the fifth paper of the series (Markaryan & Lipovetskii 1972) and it was described as

"501. Spheroidal galaxy with faint corona. Extended almost along δ . In the red part the continuous spectrum is very strong, and in the blue it is strong and extends to the far ultraviolet. H_α and λ 3727 observed in the spectrum. Judging from the spectrum, it must have a star-like nucleus. Some indication of Seyfert characteristics."

In the paper, it was associated with the optical galaxy MCG 07-35-002 (Vorontsov-Vel'Yaminov & Arkhipova 1964), which had a radio counterpart in 4C 39.49 (Caswell & Wills 1967).

Based on its flat high-frequency radio spectra, Mrk501 was chosen by Ulrich et al. (1975) for optical spectral, photometric and polarimetric studies. It showed a stellar-like nucleus hosted in an elliptical galaxy. Ulrich et al. (1975) did not find evidence of emission lines despite their weak detection in Markaryan & Lipovetskii (1972) and later on in, e.g., Moles et al. (1987). They derived a redshift $z = 0.0337$ based on absorption lines. Later works from e.g. Kondo et al. (1981); Moles et al. (1987); de Vaucouleurs et al. (1991); Fouqué et al. (1992); Stickel et al. (1993); Grazian et al. (2000); Healey et al. (2008) confirmed it, giving values in the range 0.033

to 0.034. Their photo-polarimetric observation showed a degree of (possibly variable) linear polarization between 2 and 3%. The overall radio-to-UV characteristics showed similarities with other variable radio objects like BL Lac and OJ 287 with no Seyfert nature, again at odds with Markaryan & Lipovetskii (1972) and Moles et al. (1987).

The composite nature of the source was studied further by Maza et al. (1978), who found a wavelength dependent optical polarization which significantly decreased towards the red. They interpreted this behavior as polarized non-thermal emission from a BL Lac-type object (where the polarization is wavelength independent) diluted by different amounts by the light of the host galaxy. As in Ulrich et al. (1975), they found a possible variation of the polarization degree and furthermore discovered a significant change in its position angle. The latter had no wavelength dependence, suggesting the presence of a single source of polarized light, likely the non-thermal nucleus. They calculated that the non-thermal component dominates the U and B bands and gives a significant contribution to the V band. Further studies on optical surface brightness profiles by Hickson et al. (1982) confirmed that the star-like compact object is hosted in a normal elliptical galaxy. van Breugel & Schilizzi (1986) discovered a small scale radio jet aligned with the preferred optical polarization angle, with better agreement closer to the nucleus.

Despite the classification as a BL Lac object would suggest large and fast flux variability, Mrk 501 showed a quite stable emission at all energies in the first years of observations. Slow flux variations were finally discovered in optical B band by Barbieri & Romano (1977) in data collected between 1967 and 1976, although it was not possible to detect a significant short term variability.

Mrk 501 became the first BL Lac object known to emit in X-rays when Schwartz et al. (1978) confirmed with HEAO 1 observations the association of the X-ray source 4U 1651+39 (Forman et al. 1978) with the optical counterpart. They tried to interpret the X-ray emission as IC on the radio photons. This was excluded by Snijders et al. (1979) for frequencies below 10 GHz. They suggested a synchrotron spectrum with a break between UV and X-rays, although they did not exclude that the X-rays could be produced by IC on microwave to UV photons. Kondo et al. (1981) found that both synchrotron and IC scenarios in the optical to X-ray range were reasonable and consistent with the data. A further step towards the correct identification of the X-ray emission as synchrotron rather than IC radiation was made by Mufson et al. (1984). In addition to a spherically symmetric, homogeneous SSC model, they suggested a jet model, that described the data accurately and provided tighter constraints on the physical parameters.

In 1995 Mrk 501 was finally detected at Very High Energies (VHE, $E > 100$ GeV) above 300 GeV by the Whipple Collaboration (Quinn et al. 1996). It was the second extragalactic source to show emission in this energy range (the first being Mrk 421, Punch et al. 1992). The detection of these two sources definitely proved the existence of VHE emitting objects outside of our own Galaxy and gave impetus to the development of extragalactic TeV astronomy. Confirmation came from the 1996 HEGRA CT1 observations above 1.5 TeV (Bradbury et al. 1997). In the same year it was also discovered at High Energies (HE, $E > 100$ MeV) with EGRET (Kataoka et al. 1999).

In 1997, Mrk 501 underwent a prolonged period of high activity, with VHE fluxes ≥ 1 Crab Unit (c.u.) for several months. This permitted its detection with various TeV instruments: Whipple (Catanese et al. 1997; Samuelson et al. 1998; Quinn et al. 1999), HEGRA (Aharonian et al. 1997, 1999a,b,c, 2001b), CAT (Djannati-Atai et al. 1999), Milagro (Atkins et al. 1999), Telescope Array (Hayashida et al. 1998), TIBET (Amenomori et al. 2000). The historical highest γ -ray flux ($F(> 250 \text{ GeV}) \sim 8.3 \cdot 10^{-10} \text{ cm}^{-2} \text{ s}^{-1}$) was recorded with CAT on April 16, 1997. They found a correlation between spectral hardness and source intensity between 0.3 and 13 TeV. This was not confirmed with HEGRA, although in a smaller energy range (1 to 5 TeV). The flaring states were covered by MWL observations, which were reported in, e.g., Pian et al. (1998), Lamer & Wagner (1998) and Petry et al. (2000). At radio and optical wavelengths, Mrk 501 showed again only small variations. In the X-rays, instead, the source was extremely variable. Its spectrum was extraordinary hard. The synchrotron peak shifted for two orders of magnitude to higher energies and reached for the first time up to 100 keV.

The monitoring of Mrk 501 at VHE continued in 1998 and 1999 with Whipple (Quinn et al. 1999) and HEGRA (Aharonian et al. 2001a). During these two years, the source was in low state, with the exception of a flaring event in June 1998 (Sambruna et al. 2000), which was significantly less pronounced than the 1997 ones. The source was observed again at VHE starting from 2004. Only upper limits could be derived from the 2004 and 2006 HESS observations (1.8 and 2.2 h livetime, Aharonian et al. 2005b, 2008b). Observations with MAGIC and VERITAS have been carried out almost yearly from 2005 onwards (Albert et al. 2007; Anderhub et al. 2009; Aleksić et al. 2015; Acciari et al. 2011), leading to firm detections between ~ 0.1 and ~ 5 TeV. Flux levels comparable to the 1997 big flare have been reached on June 30, 2005 (Albert et al. 2007), June 9, 2012 (Borracci et al. 2013) and June 23, 2014 (this work).

Since August 2008, Mrk 501 is regularly observed at HE with the *Fermi* satellite. During a MWL campaign in 2008-2009, a flux dependant spectral variability was detected above a few GeV, while none was seen below (Abdo et al. 2011). This can indicate the presence of two components in the IC peak.

All the aforementioned characteristics let Mrk 501 be classified as a blazar belonging to the subclass of the high frequency peaked BL Lac objects (HBL). Because of the impressive shift of its synchrotron peak, it is sometimes referred to as an extreme HBL.

7.2 VHE OBSERVATIONS WITH H.E.S.S.

Observation of Mrk 501 are challenging for H.E.S.S.. Mrk 501 is the most northern source ever observed with H.E.S.S. up to date. With its declination of $+39^{\circ}45'36.61''$, it culminates at less than 27° altitude, exceeding the previous very large Zenith angle observations of Mrk 421 (Aharonian et al. 2005a) by more than 1.5° . Such extreme Zenith angles imply a large (~ 2 TeV) low energy threshold, which in turn requires the source to be very bright or to have a relatively hard spectrum in order to be detected. However, a positive consequence of large Zenith angles observations is a significantly larger effective area at high energies when compared to standard observations. Despite these technical difficulties, being Mrk 501 known for its variability and

very bright flaring states, it was observed by H.E.S.S. in a few occasions, in the hope of catching it in an high state.

H.E.S.S. observations have been carried out in four different epochs between 2004 and 2014. The dataset comprises 34 runs taken in wobble mode in 2004 (4 runs), 2006 (5 runs) and 2012 (4 runs) with the HESS I array and in 2014 (21 runs) with the full HESS II array. The mean zenith angle is 63.7° and the mean offset from the pointing position is 0.50° .

The 2004 and 2006 runs were collected as part of two MWL campaigns (Gliozzi et al. 2006; Anderhub et al. 2009) on the nights of June 15-16, 2004 and July 18-19, 2006. Due to the low state of the source, only upper limits could be derived in the original analyses and the results were published separately (Aharonian et al. 2005b, 2008b).

The 2012 observations have been triggered as ToO following a flaring state¹ in the TeV domain. It was detected by MAGIC during an ongoing long term MWL campaign on the source. Only two runs in two consecutive nights were taken (11-13 June).

In 2014, observations were triggered by two flare alerts from the FACT Collaboration (Anderhub et al. 2013) on June 19 and July 28¹. They were carried out on several nights between June 19-25 and on the night of July 29-30.

The data has been subject to quality control over good weather, good camera conditions and telescope system stability. All 2004, 2006 and 2012 runs pass these standard quality cuts. In order to have a telescope-homogeneous dataset for the whole monitoring period, HESS I style DSTs have been produced for the 2014 observations. Only events detected with the CT1-4 telescopes were extracted from the data, and all the information coming from CT5 were discarded. 18 good quality runs remain after quality cuts. Similarly, Mono style DSTs have been produced taking into account CT5 information only. 15 runs remain after quality cuts. 15 good quality runs exist for the CT1-5 Stereo data.

7.3 OBSERVATIONS AT LOWER ENERGIES

In order to present the H.E.S.S. results in a MWL context, observations in optical and X-rays have been collected.

7.3.1 X-RAYS

X-ray coverage has been ensured by the Rossi X-ray Timing Explorer (*RXTE*) and *Swift* satellites. The lightcurve of the former has been retrieved from Rivers et al. (2013)². The data from the X-ray telescope (XRT) onboard of the latter have been analyzed for this work³. They were collected in WT mode between May 12 and July 30, 2012 (obsIDs: 00030793177-00030793201)

¹Private communication, within the agreement between H.E.S.S., MAGIC (MAGIC/FACT in 2014) and VERITAS for notifications about ongoing VHE flaring activities of AGN.

²<http://cass.ucsd.edu/~rxteagn/>

³The analysis has been provided by Alicja Wiercholska

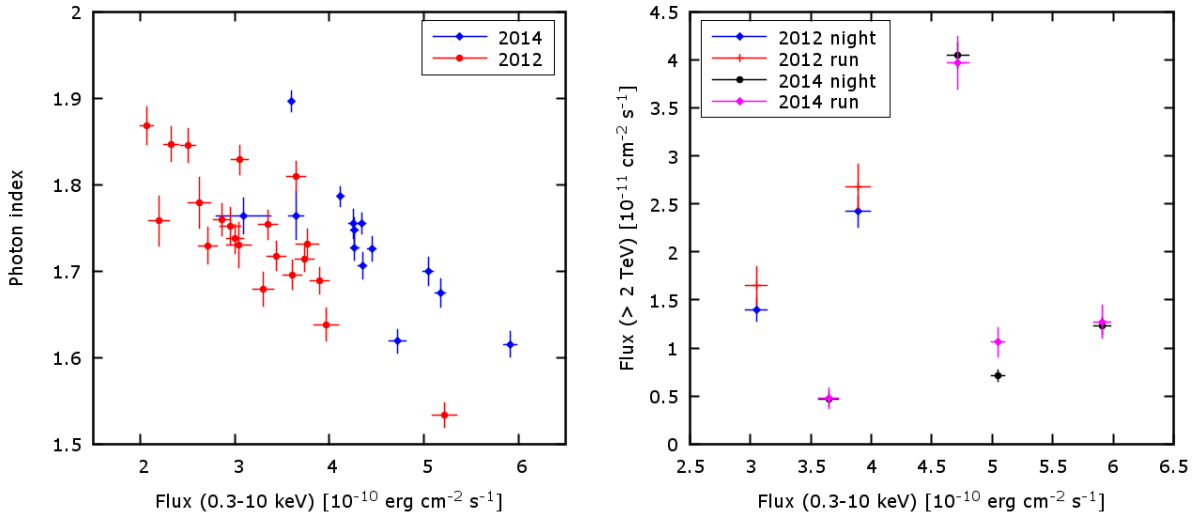


Figure 7.1: *Left:* X-ray photon index as function of the energy flux between 0.3 and 10 keV. A clear harder when brighter behavior is visible. *Right:* Scatter plot of the integral VHE flux above 2 TeV as function of the X-ray energy flux between 0.3 and 10 keV for the whole nights of H.E.S.S. observations and for the run temporally closer to the *Swift*-XRT snapshot. The left-most red point represents the strictly simultaneous observations during the 2012 flare. No common trend is visible.

and between May 31 and June 28, 2014 (obsIDs: 00035023035-00035023047). The analysis was done as described in sec. 6.3.2. The Galactic hydrogen absorption was fixed to $n_H = 1.58 \times 10^{20} \text{ cm}^{-2}$ (Kalberla et al. 2005). A clear harder-when-brighter behavior is detected (Fig. 7.1, *left*), as it was expected from the literature (e.g. Pian et al. 1998). Contemporaneous X-ray and H.E.S.S. observations exist in some nights. The typical time offset between them is ~ 90 minutes. An exception is June 12, 2012, when strictly simultaneous observations exist. Because of the fast variability of the source in both wavelengths, it is not possible to determine any correlation (Fig. 7.1, *right*).

7.3.2 OPTICAL

Optical data are obtained with the 70 cm telescope of the Abastumani Observatory (Georgia). It is equipped with an Apogee 6E camera (between 1997-2006 a SBIG ST-6 camera). Observations were taken with a R Cousins filter and cover the 1997-2014 period. They have been analyzed with the Daophot II reduction software using an aperture diameter of $10''$. Some nights of contemporaneous exposure with H.E.S.S. exist, and strictly simultaneous observations have been taken during the peak of the flare on June 23, 2014.

Table 7.1: Count values for *Std*, *Loose* and *Faint* cuts for every year of observation.

	nON	nOFF	excess	significance	LiveTime (# runs)
<i>Std</i> cuts					
2004	52	136	41	8.2σ	1.8 h (4)
2006	25	134	14	3.4σ	2.3 h (5)
2012	358	106	347	35.3σ	1.8 h (4)
2014	1367	483	1329	71.5σ	7.7 h (18)
tot	1801	859	1730	77.9σ	13.6 h (31)
<i>Loose</i> cuts					
2004	109	375	72	8.8σ	1.8 h (4)
2006	81	416	39	5.1σ	2.3 h (5)
2012	579	358	536	37.8σ	1.8 h (4)
2014	2100	1436	1964	76.0σ	7.7 h (18)
tot	2868	2584	2611	82.0σ	13.6 h (31)
<i>Faint</i> cuts					
2004	20	35	18	6.7σ	1.8 h (4)
2006	5	28	3	1.9σ	2.3 h (5)
2012	165	33	162	26.4σ	1.8 h (4)
2014	668	125	661	56.7σ	7.7 h (18)
tot	858	221	844	61.8σ	13.6 h (31)

7.4 H.E.S.S. DATA REDUCTION

The reduction of the H.E.S.S. data has been performed using the M++ analysis. The software versions paris-0-8-24 was used to analyze the HESS I style DSTs (Prod26), while the version paris-0-8-30 was used for the HESS II style DSTs (Prod6).

For the HESS I style analysis, the *Std*, *Loose* and *Faint* cuts have been initially applied. The *Ring Background* and the *Reflected Region Background* methods (sec. 4.7) were used for the background determination. The 31 good quality runs have a total lifetime of 13.6 h (12.0 h when corrected for acceptance). The source is detected with a significance of 77.9σ with *Std* cuts. In Table 7.1 the results for each year and analysis cut are reported. Thanks to the higher sensitivity of M++ compared to a simpler Hillas analysis, Mrk 501 is detected also in the years 2004 and 2006, which were previously published as upper limits in Aharonian et al. (2005b, 2008b).

In Fig. 7.2 the θ^2 distribution derived with *Std* cuts (*left*) and the relative excess distribution with the superimposed point spread function (PSF, *right*) are shown. In the former, one can see that the emission is almost background-free, in the latter that the excess is well described as emission from a point-like source. In Fig. 7.3 the significance/excess distributions as function of

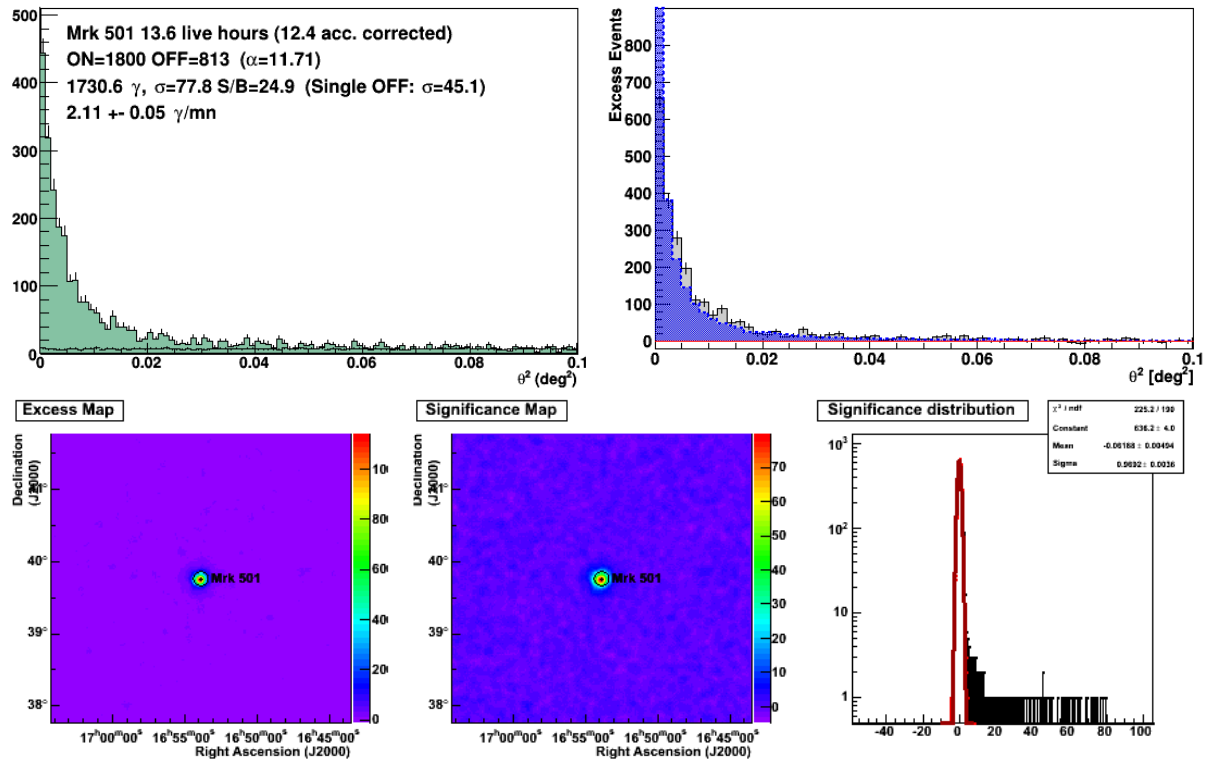


Figure 7.2: Top: theta squared distribution (left), and excess distribution in gray with superimposed PSF in blue (right) of Mrk 501 for the 2004-2014 analysis with *Std* cuts. Bottom: from left to right, excess map, significance map and significance distribution for the same analysis.

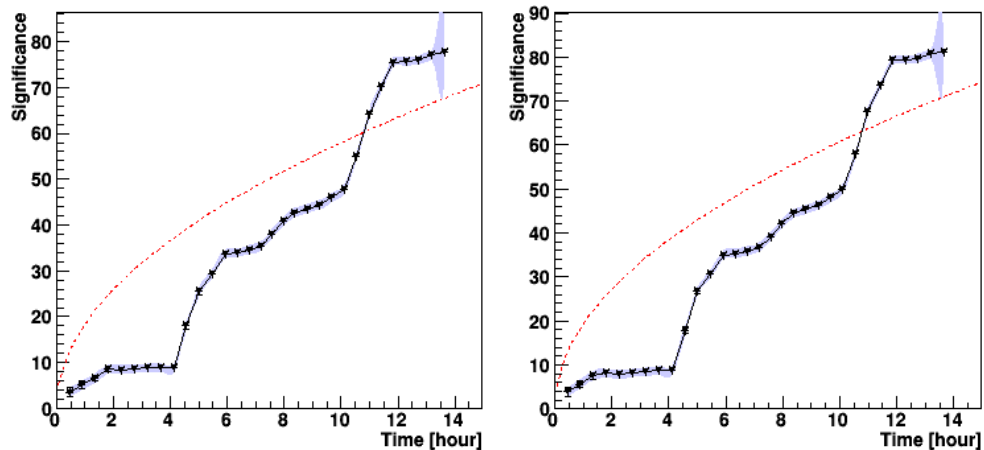


Figure 7.3: Significance distributions for *Std* (left) and *Loose* (right) cuts as a function of the time. The red dotted line is the $\sigma \propto \sqrt{t}$ expected for a constant emission. The non smooth behavior indicates a variable emission.

the nOFF/time are displayed. It is striking that they do not follow the $\sigma \propto \sqrt{t}$ trend which is expected for a constant emission. The large steps in short time indicate the presence of flaring activity.

7.5 SPECTRAL ANALYSIS

Spectral analyses have been carried out using the forward-folding technique. Given the small number of ON and OFF events, especially at high energies, the energy bin size of the spectrum has been adjusted for every data subset and cut following these criteria as long as possible:

- use a conservative low energy threshold nearer to the maximum of the ON and OFF events distributions to avoid low energy bins with few counts, which are more strongly affected by Zenith angle selection criteria;
- the bins should contain enough counts ($n_{\text{ON}} \geq 1$, $n_{\text{OFF}} \geq 5$) to be actively used in the fit procedure (this is important for high energies);
- all ON counts should be contained in one of these bins;
- the bins should show a significant excess;
- the number of bins should be maximized.

7.5.1 OBSERVED SPECTRA

7.5.1.1 CUMULATIVE DATASET

Fits with a PL spectral shape have been performed on the total dataset for each of the three cuts (*Std*, *Loose*, *Faint*). The quality of the fits was very poor, with χ^2_{red} values between 4 and 10. Therefore, two other spectral shapes (CPL and ECPL) were tested. These fits yielded much better χ^2 values than the PL fits, proving that the observed spectrum is curved. To test if these spectra are significantly better than the simple PL, the *LogLikelihood-ratio* test (LLRT) was used. It is defined as

$$\text{LLRT} = -2 * \left[\text{Log} \left(\mathcal{L}(H_0) / \mathcal{L}(H_1) \right) \right] \quad (7.1)$$

where H_0 is the null hypothesis (in this case a simple PL shape) and H_1 the hypothesis to be tested (the CPL or ECPL shapes). The significance is then calculated as $\sqrt{\text{LLRT}}$. The curved spectra are preferred at the $\sim 4 - 12\sigma$ level depending on the cut used (Fig 7.4, *left*). The significance increases with the widening of the energy range. The results are summarized in Table 7.2. In the right panels of Fig 7.4, the comparisons of the spectral shapes for different cuts are shown. One can see that the CPL and ECPL fits are consistent for all three cuts. The PL gets softer with increasing energy threshold (due to increasing cut hardness), as one can expect for a curved spectrum.

As mentioned before, the source shows a high flux variability during the monitored period. A flux dependent spectral variability at VHE is known from the literature, as discussed, e.g., in Djannati-Atai et al. (1999) and Albert et al. (2007). It is likely that the cumulative fits presented here show only an indication of the actual source spectrum at a given time. It is important to note that in the aforementioned papers spectra below 13 TeV and 7 TeV are shown. The spectral variability is determined mostly with energies below 2 TeV. This energy is approximately the energy threshold of the current H.E.S.S. spectra, as can be seen in Table 7.2. Will spectral variability

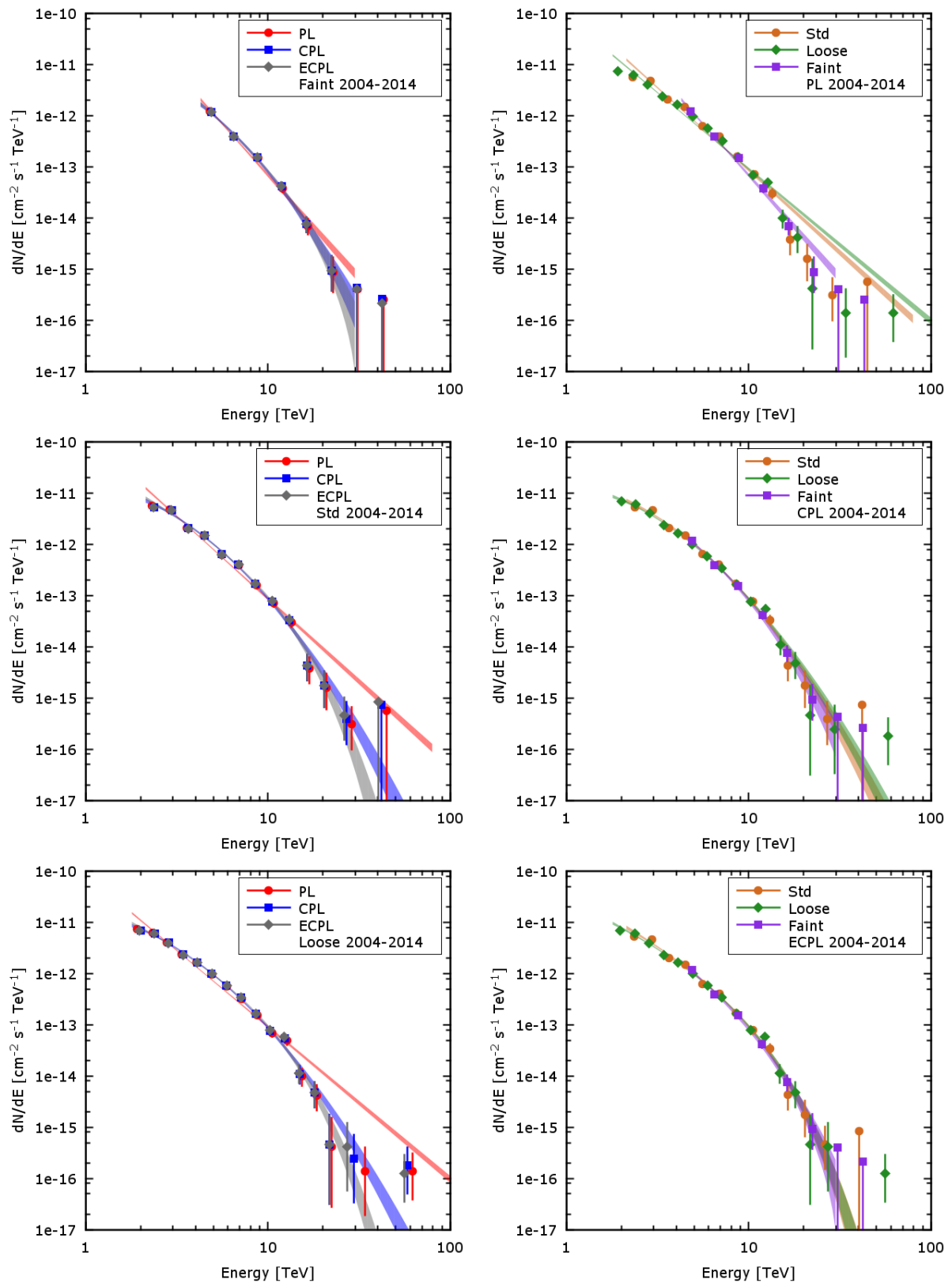


Figure 7.4: *Left:* comparison of the three spectral shapes for the fit to the total 2004-2014 dataset for *Faint* (top), *Std* (middle) and *Loose* (bottom) cuts. In all three cases one can see that the curved fits describe the data better than a simple PL. *Right:* comparison of the PL (top), CPL (middle) and ECPL (bottom) spectral shapes for the three different cuts. The CPL and ECPL fits are consistent for all cuts, while the PL gets softer with increasing energy threshold.

Table 7.2: Spectral results for the cumulative dataset 2004-2014 for the three cuts.

Γ	β/E_{cut}	$d\Phi/dE$ (3.5 TeV) [$10^{-12}cm^{-2}s^{-1}TeV^{-1}$]	E_{dec} [TeV]	Energy range [TeV]	$\chi^2/d.o.f.$ (prob)
<i>Std cuts</i>					
PL	3.22 ± 0.06	2.53 ± 0.08	4.20		110.4/11 ($1.5 \cdot 10^{-18}$)
CPL	2.47 ± 0.11	0.84 ± 0.12	2.68 ± 0.09	3.65	2.13 - 79.51 25.37/10 ($4.7 \cdot 10^{-3}$)
ECPL	1.55 ± 0.24	3.83 ± 0.59	2.58 ± 0.09	4.20	23.20/10 (0.01)
<i>Loose cuts</i>					
PL	2.98 ± 0.05	2.08 ± 0.05	3.87		161.5/16 ($4.2 \cdot 10^{-26}$)
CPL	2.20 ± 0.09	0.77 ± 0.09	2.47 ± 0.07	3.11	1.79 - 103.06 22.13/15 (0.11)
ECPL	1.41 ± 0.18	3.73 ± 0.47	2.37 ± 0.07	3.26	17.06/15 (0.32)
<i>Faint cuts</i>					
PL	4.01 ± 0.14	4.57 ± 0.44	5.90		16.10/4 ($2.9 \cdot 10^{-3}$)
CPL	3.37 ± 0.24	0.94 ± 0.37	2.77 ± 0.54	5.90	4.26 - 29.91 4.31/3 (0.23)
ECPL	2.15 ± 0.68	4.79 ± 1.90	3.05 ± 0.49	5.90	2.86/3 (0.41)

be detected in the current dataset, it would be the first time for an energy range significantly extending above 10 TeV, up to 20 TeV.

Table 7.3: Spectral results for the 2004 dataset for the three cuts.

Γ	β/E_{cut}	$d\Phi/dE$ (3.5 TeV) [$10^{-12}cm^{-2}s^{-1}TeV^{-1}$]	E_{dec} [TeV]	Energy range [TeV]	$\chi^2/d.o.f.$ (prob)
<i>Std cuts</i>					
PL	2.79 ± 0.40	0.31 ± 0.07	4.03	2.13 - 20.46	1.17/3 (0.76)
ECPL	2.76 ± 1.45	$inf \pm inf$	3.35		1.18/2 (0.55)
<i>Loose cuts</i>					
PL	3.47 ± 0.40	0.31 ± 0.06	2.63	1.79 - 57.76	4.79/5 (0.44)
CPL	3.79 ± 0.65	-0.28 ± 0.42	2.31		4.33/4 (0.36)
ECPL	3.46 ± 0.96	$inf \pm inf$	2.63		4.79/4 (0.31)

7.5.1.2 YEARLY DATASETS

In order to detect spectral variability, the data have been divided in smaller datasets of single years of observations. In 2012 and 2014, the high significance allows (and the different flux states invite) to perform analyses for each single night and for every run during the flares. These have been carried out using *Loose* cuts. The complete results are summarized in Tables 7.3 to 7.8 and visualized in Fig. 7.5 to 7.14.

In 2004 (Table 7.3 and Fig. 7.5, *top* and *middle*) and 2006 (Table 7.4 and Fig. 7.5, *bottom*), the source spectra are well described by PLs with a soft photon index of ~ 3.4 (using *Loose* cuts). In 2004, the *Std* cuts analysis yields a slightly harder (but still compatible within errors) index of 2.8. This can be caused by the narrower energy range, together with a relatively high 2σ flux point above 10 TeV, which is still compatible with statistical fluctuations. In all cases, the more complex spectral shapes resemble a PL, showing no significant curvature.

In 2012 (Table 7.5 and Fig. 7.6) and 2014 (Table 7.6 and Fig. 7.7) the *Loose* spectra are significantly curved. CPL and ECPL show hard photon indices between ~ 1.6 and 2.8 that strongly depend on the strength of the curvature. The shapes of the spectra are consistent for all cuts, as it can be seen from the left plots of Fig. 7.6 and 7.7. The PL fits become softer with increasing energy threshold, as it is expected when fitting a curved spectrum.

Table 7.4: Spectral results for the 2006 dataset for the three cuts.

Γ	β/E_{cut}	$d\Phi/dE$ (3.5 TeV) [$10^{-12}cm^{-2}s^{-1}TeV^{-1}$]	E_{dec} [TeV]	Energy range [TeV]	$\chi^2/d.o.f.$ (prob)
<i>Loose cuts</i>					
PL	3.42 ± 0.84	0.16 ± 0.05	3.04	2.01 - 82.71	1.14/5 (0.95)
CPL	1.24 ± 3.01	3.44 ± 5.61	2.68		0.07/4 (1.00)
ECPL	0.1 ± 9.02	1.08 ± 3.03	2.67		0.37/4 (0.99)

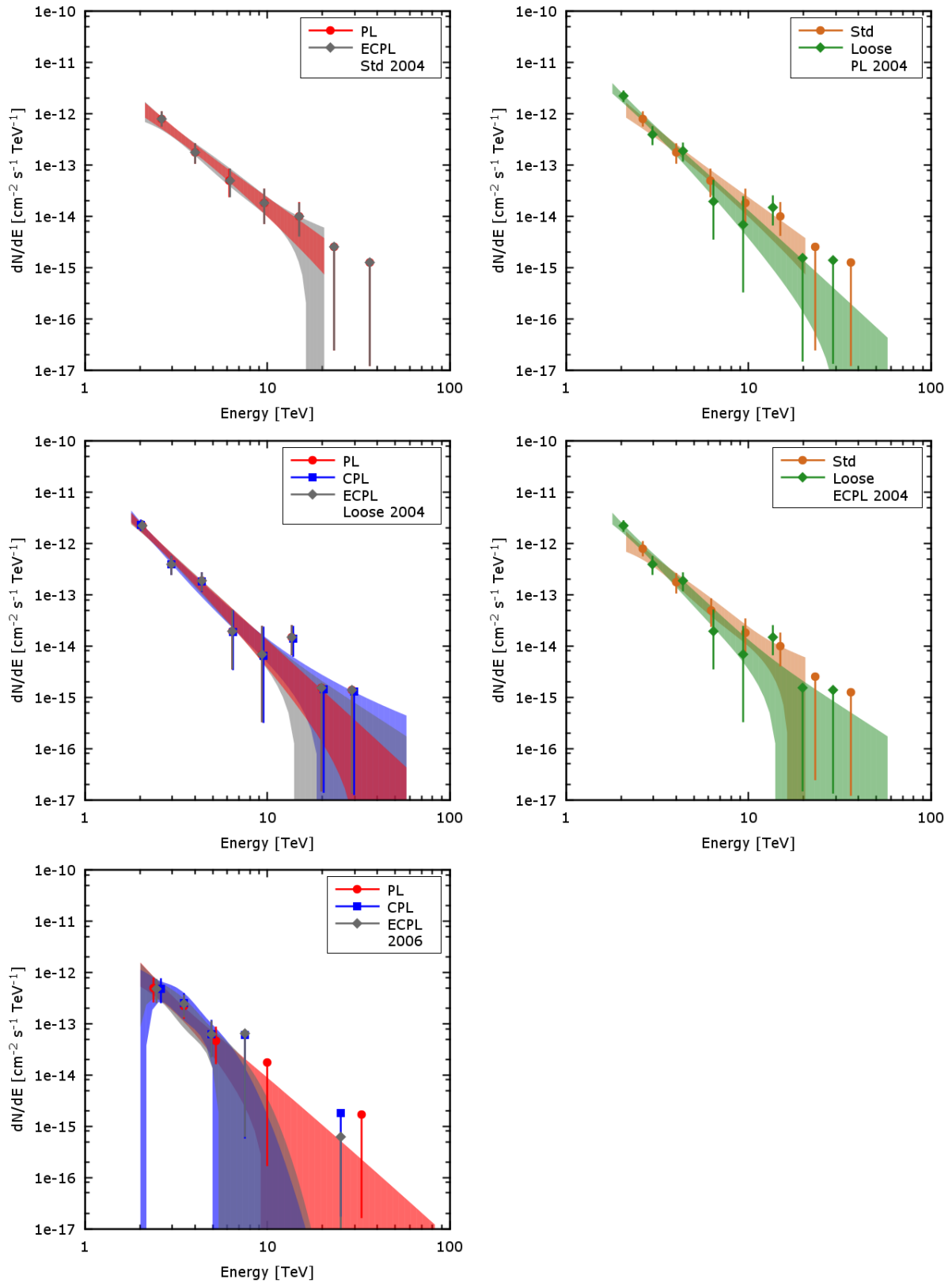


Figure 7.5: *Left:* comparison of the three spectral shapes for the fit to the 2004 dataset for *Std* (top) and *Loose* cuts (middle). The PL is a satisfactory description of the data. *Right:* comparison of PL (top) and ECPL (middle) spectral shapes for *Std* and *Loose* cuts. The wider energy range gives slightly softer spectra. *Bottom:* Comparison of the three spectral shapes for the fit to the 2006 dataset for *Loose* cuts.

Table 7.5: Spectral results for the 2012 dataset for the three cuts.

Γ	β/E_{cut}	$d\Phi/dE$ (3.5 TeV) [$10^{-12}cm^{-2}s^{-1}TeV^{-1}$]	E_{dec} [TeV]	Energy range [TeV]	$\chi^2/d.o.f.$ (prob)	
<i>Std cuts</i>						
PL	3.06 ± 0.15	3.63 ± 0.28	4.72		5.23/3 (0.16)	
CPL	2.75 ± 0.27	0.42 ± 0.34	3.65 ± 0.29	4.00	2.6 - 22.36	3.18/2 (0.20)
ECPL	2.15 ± 0.64	6.99 ± 5.02	3.60 ± 0.29	4.00		2.48/2 (0.29)
<i>Loose cuts</i>						
PL	2.93 ± 0.10	3.01 ± 0.15	3.87		45.59/10 ($1.7 \cdot 10^{-6}$)	
CPL	2.19 ± 0.19	0.68 ± 0.18	3.56 ± 0.23	3.02	1.88 - 102.36	17.28/9 (0.04)
ECPL	1.60 ± 0.36	4.53 ± 1.39	3.40 ± 0.20	3.42		15.35/9 (0.08)
<i>Faint cuts</i>						
PL	3.34 ± 0.37	4.53 ± 1.12	6.47	4.26 - 17.27	0/0 (0)	

In 2014, the *Std* and *Faint* spectra show significant curvature, as well. Harder cuts yield slightly stronger curvatures (7.7, right). CPL and ECPL fits of the same cut are practically indistinguishable (7.7, left). The ECPL tends to show a harder curvature at higher energies and has in general a slightly better χ_{red}^2 value.

Table 7.6: Spectral results for the 2014 dataset for the three cuts.

Γ	β/E_{cut}	$d\Phi/dE$ (3.5 TeV) [$10^{-12}cm^{-2}s^{-1}TeV^{-1}$]	E_{dec} [TeV]	Energy range [TeV]	$\chi^2/d.o.f.$ (prob)	
<i>Std cuts</i>						
PL	3.34 ± 0.07	3.92 ± 0.15	4.72		69.56/8 ($6.0 \cdot 10^{-12}$)	
CPL	2.65 ± 0.12	0.83 ± 0.14	4.20 ± 0.17	3.65	1.93 - 68.89	8.45/7 (0.29)
ECPL	1.66 ± 0.28	3.66 ± 0.66	4.05 ± 0.16	3.79		7.58/7 (0.37)
<i>Loose cuts</i>						
PL	3.05 ± 0.05	3.13 ± 0.08	3.80		99.47/14 ($6.0 \cdot 10^{-15}$)	
CPL	2.47 ± 0.09	0.56 ± 0.08	3.65 ± 0.12	2.96	1.54 - 68.63	24.25/13 (0.03)
ECPL	1.88 ± 0.17	4.90 ± 0.77	3.54 ± 0.11	3.43		15.78/13 (0.26)
<i>Faint cuts</i>						
PL	4.23 ± 0.17	7.58 ± 0.87	6.21		8.50/3 (0.04)	
CPL	3.41 ± 0.35	1.09 ± 0.46	4.36 ± 1.07	5.51	2.93 - 27.85	0.16/2 (0.92)
ECPL	2.20 ± 0.86	4.22 ± 1.88	4.96 ± 0.99	6.21		0.04/2 (0.98)

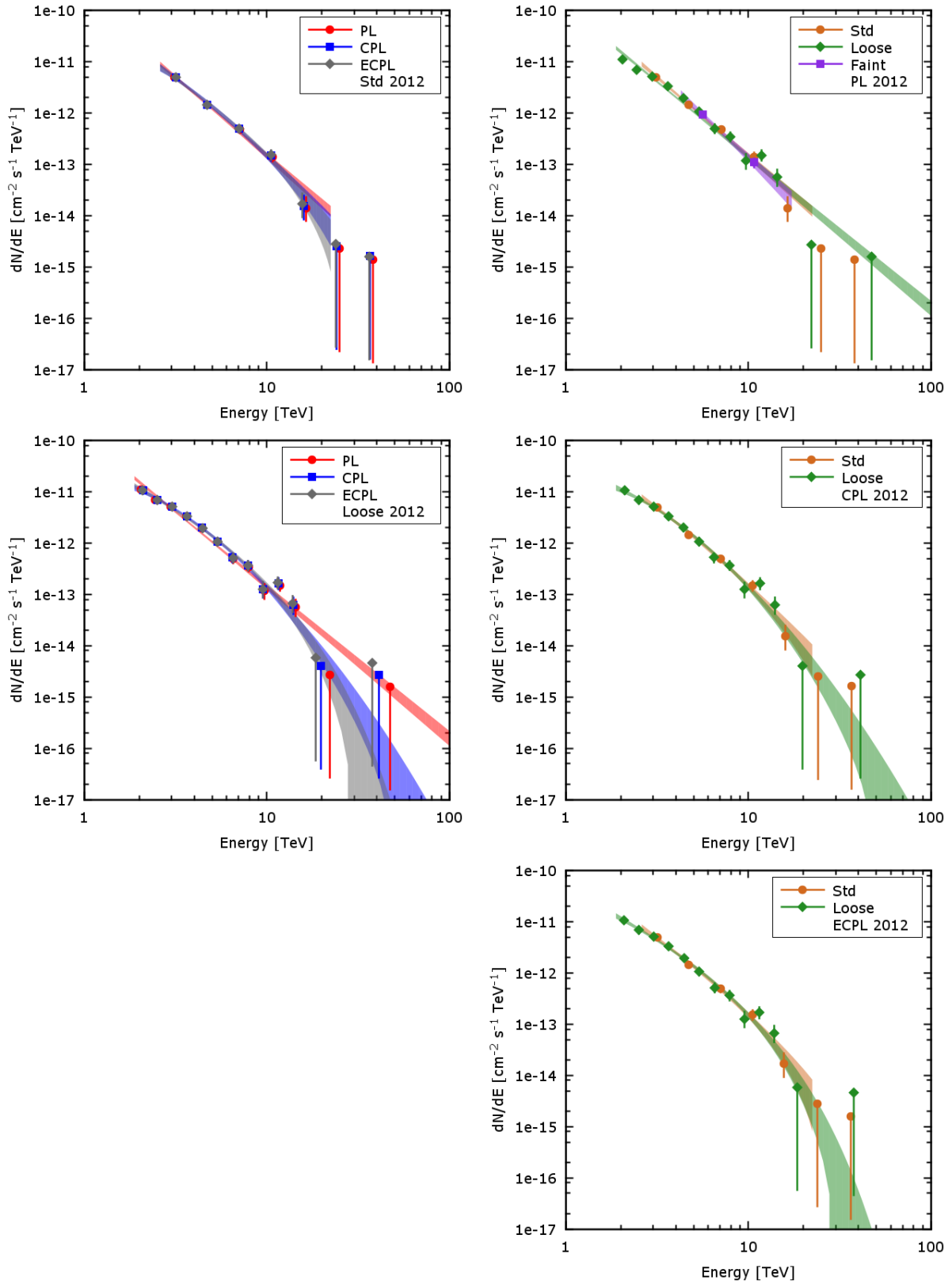


Figure 7.6: *Left:* comparison of the three spectral shapes for the fit to the 2012 dataset for *Std* (top) and *Loose* (middle) cuts. In the former case, despite hinting to a possible curved spectrum, CPL and ECPL are not significantly better descriptions of the data than the simple PL. In the latter, they are. *Right:* comparison of the PL (top), CPL (middle) and ECPL (bottom) spectral shapes for the three cuts. As for the total 2004-2014 dataset, the CPL and ECPL fits are consistent for all cuts, while the PL gets softer with increasing energy threshold.

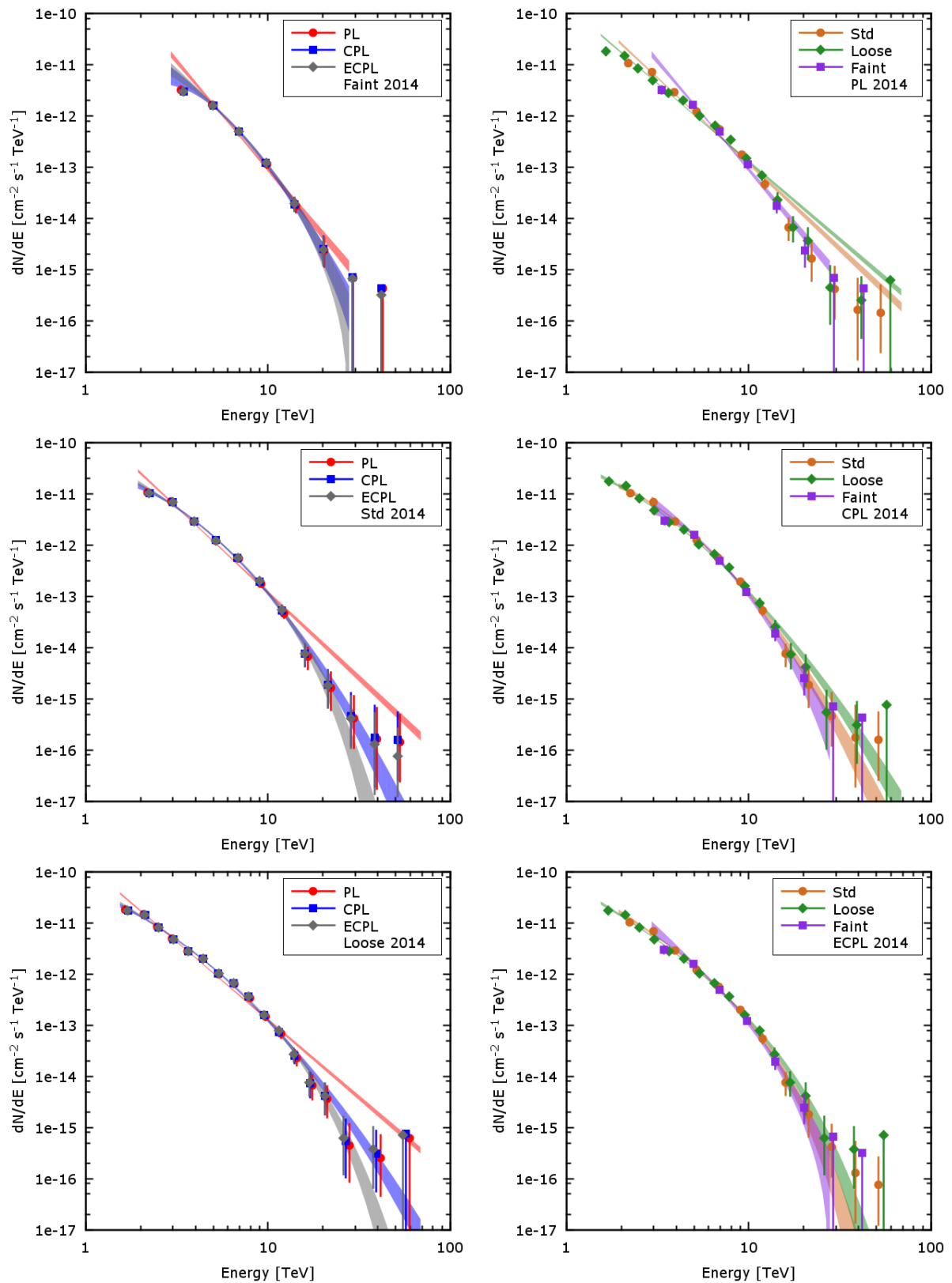


Figure 7.7: *Left:* comparison of the three spectral shapes for the fit to the 2014 dataset for *Std* (top), *Loose* (middle) and *Faint* (bottom) cuts. In all three cases one can see that the curved fits describe the data better than a simple PL. *Right:* comparison of the PL (top), CPL (middle) and ECPL (bottom) spectral shapes for the three cuts. As for the total 2004–2014 dataset, the PL gets softer with increasing energy threshold. The CPL and ECPL fits are consistent for all cuts, even though they seem to have a stronger curvature for harder cuts.

7.5.1.3 DAILY DATASETS

Up to this point it is not possible to determine the presence of a flux dependent spectral variability. To further test this hypothesis, *Loose* cuts fits were carried out on the two single nights in 2012 (Fig. 7.8 and Table 7.7) and on the six nights in 2014 (1 flaring state and 5 low state nights, Fig. 7.9, 7.10 and Table 7.8). The 2014 cumulative dataset for the low state nights was fit as well.

In 2012, the curved fits are significantly better than a simple PL only in the first night. In the second night, there is just an indication at the 2σ level. It is apparent from both figure and table that the spectra are not changing between the two nights, despite a 40% lower flux in the second night. The photon index is harder for the ECPL ($\Gamma \sim 1.8$) than for the CPL ($\Gamma \sim 2.3$), but the two fits are equivalent (Fig. 7.8, *left*).

In 2014, the flaring state and the cumulative low state spectra are curved. The CPL and ECPL fits are significantly better than the simple PL. The flaring state spectra are compatible with the 2012 nightly ones. The low state spectra are significantly softer. The difference in the photon index is 0.5 - 0.6. This clearly shows the existence of a flux dependent spectral variability at energies larger than 2 TeV!

The emission of the low state nights is well described by PL spectra with soft photon indices $\Gamma \sim 3.4$. An exception is the second night. A curved and harder spectrum as in the flare night is preferable. During this night the flux is higher than in the other nights, almost reaching the emission level of the first night in 2012.

Table 7.7: Night- and run-wise spectral results 2012 with *Loose* cuts.

		Γ	β/E_{cut}	$d\Phi/dE$ (3.5 TeV) [$10^{-12} cm^{-2} s^{-1} TeV^{-1}$]	E_{dec} [TeV]	Energy range [TeV]	$\chi^2/d.o.f.$ (prob)
night 1	PL	2.87 ± 0.12		3.74 ± 0.25	4.07		18.83/9 (0.03)
	CPL	2.37 ± 0.19	0.50 ± 0.20	4.20 ± 0.33	3.42	1.88 - 68.63	7.30/8 (0.51)
	ECPL	1.84 ± 0.40	6.39 ± 2.77	4.05 ± 0.30	3.42		5.70/8 (0.68)
night 2	PL	2.83 ± 0.17		2.41 ± 0.19	3.42		12.6/9 (0.18)
	CPL	2.30 ± 0.31	0.66 ± 0.33	2.82 ± 0.29	2.91	1.88 - 16.94	8.52/8 (0.38)
	ECPL	1.71 ± 0.63	4.29 ± 2.34	2.71 ± 0.26	3.05		9.40/8 (0.31)
run 1	PL	2.69 ± 0.20		3.49 ± 0.34	3.94		2.86/4 (0.58)
	CPL	2.46 ± 0.39	0.26 ± 0.40	3.70 ± 0.49	2.89	1.9 - 28.03	2.41/3 (0.49)
	ECPL	2.13 ± 0.76	8.98 ± 12.26	3.67 ± 0.44	3.08		2.31/3 (0.51)
run 2	PL	2.64 ± 0.19		4.44 ± 0.51	4.98		1.62/3 (0.65)
	CPL	2.80 ± 0.44	-0.15 ± 0.37	4.41 ± 0.50	3.46	1.9 - 68.73	1.47/2 (0.48)
	ECPL	2.66 ± 0.77	<i>inf</i> ± <i>inf</i>	4.46 ± 0.51	3.83		1.63/2 (0.44)
run 3	PL	2.55 ± 0.26		2.11 ± 0.25	3.87		7.69/3 (0.05)
	CPL	1.73 ± 0.58	1.10 ± 0.62	2.65 ± 0.41	3.07	1.9 - 20.78	3.78/2 (0.15)
	ECPL	0.63 ± 1.29	2.53 ± 1.63	2.51 ± 0.37	3.46		4.74/2 (0.09)
run 4	PL	3.17 ± 0.25		2.82 ± 0.31	3.46		2.17/5 (0.83)
	CPL	2.83 ± 0.50	0.37 ± 0.53	3.08 ± 0.49	2.67	1.9 - 15.41	1.58/4 (0.81)
	ECPL	2.37 ± 1.01	5.74 ± 7.42	3.07 ± 0.45	2.80		1.44/4 (0.84)

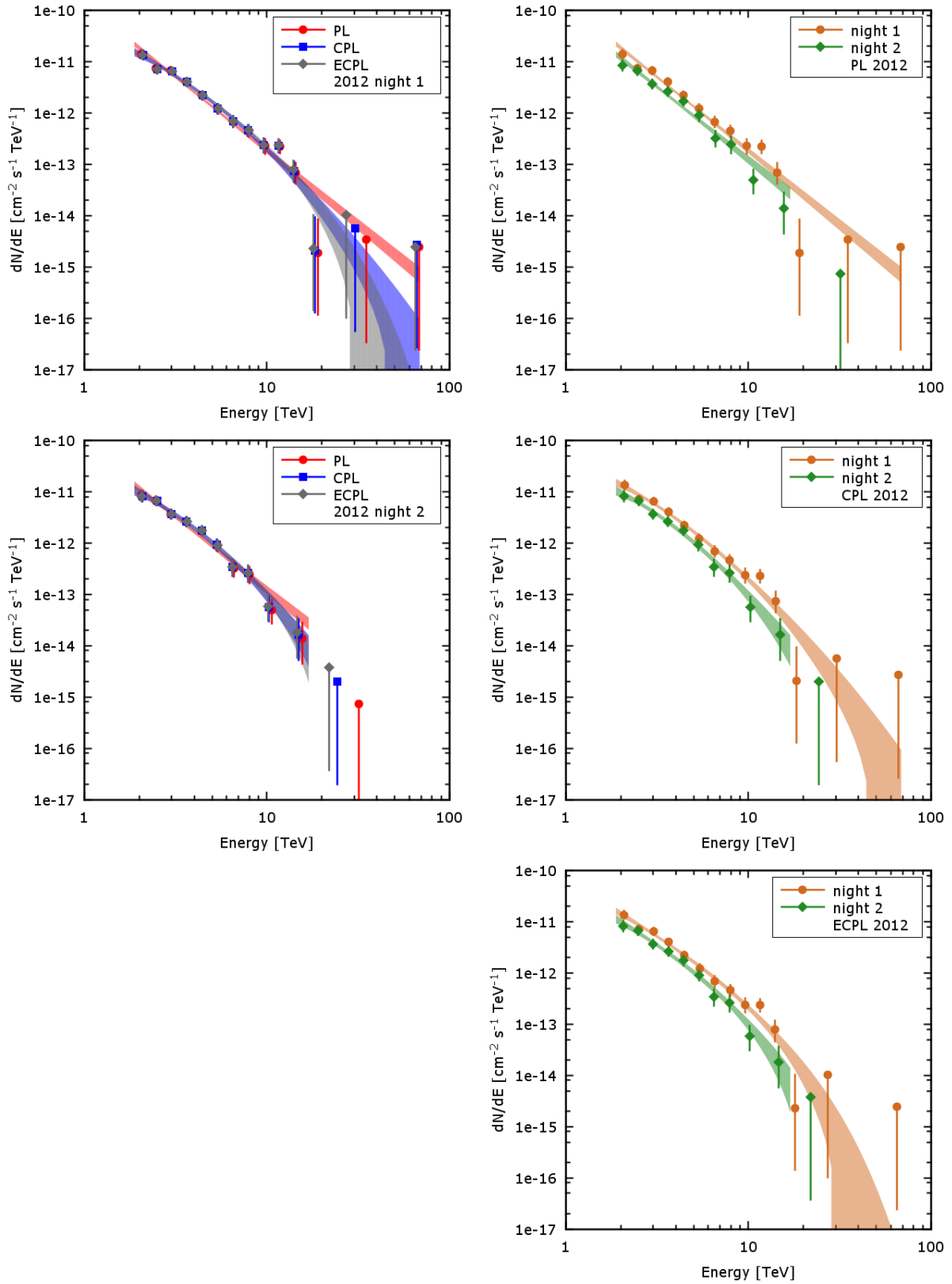


Figure 7.8: *Left:* comparison of the three spectral shapes for the *Loose cuts fits* to the first (*top*) and second (*middle*) night in 2012. The curved fits are significantly better than a simple PL in the first night, while this is just an indication for the second night. *Right:* comparison of the PL (*top*), CPL (*middle*) and ECPL (*bottom*) spectral shapes for the two nights. One can see that, despite the small but significant flux change, the fits are all compatible.

Table 7.8: Night- and run-wise spectral results 2014 with *Loose* cuts.

		Γ	β/E_{cut}	$d\Phi/dE$ (3.5 TeV) [$10^{-12}cm^{-2}s^{-1}TeV^{-1}$]	E_{dec} [TeV]	Energy range [TeV]	$\chi^2/d.o.f.$ (prob)
flare	PL	2.82 ± 0.06		8.48 ± 0.28	4.18		50.8/10 ($1.9 \cdot 10^{-7}$)
	CPL	2.26 ± 0.11	0.57 ± 0.11	9.61 ± 0.38	3.13	1.88 - 25.27	15.33/9 (0.08)
	ECPL	1.65 ± 0.21	4.90 ± 0.91	9.31 ± 0.34	3.34		10.34/9 (0.32)
low	PL	3.31 ± 0.09		1.55 ± 0.07	3.54		24.6/12 (0.02)
	CPL	2.85 ± 0.18	0.44 ± 0.17	1.73 ± 0.10	2.80	1.88 - 68.63	15.58/11 (0.16)
	ECPL	2.27 ± 0.37	4.94 ± 1.94	1.72 ± 0.10	2.80		13.82/11 (0.24)
Low state							
night 1	PL	3.43 ± 0.36		0.77 ± 0.12	3.43		6.19/5 (0.29)
	CPL	2.82 ± 0.82	0.52 ± 0.83	0.87 ± 0.20	2.54	1.88 - 27.92	5.39/4 (0.25)
	ECPL	2.19 ± 1.61	4.09 ± 6.25	0.87 ± 0.18	2.84		4.87/4 (0.30)
night 2	PL	2.96 ± 0.14		2.57 ± 0.19	3.91		13.19/7 (0.07)
	CPL	2.42 ± 0.22	0.65 ± 0.24	2.99 ± 0.26	3.42	1.88 - 50.85	2.62/6 (0.86)
	ECPL	1.67 ± 0.47	4.53 ± 1.80	2.88 ± 0.23	3.42		3.17/6 (0.79)
night 3	PL	3.29 ± 0.16		1.55 ± 0.12	3.45		8.52/11 (0.67)
	CPL	3.19 ± 0.28	0.09 ± 0.20	1.59 ± 0.16	2.80	1.88 - 37.68	8.36/10 (0.59)
	ECPL	3.21 ± 0.35	73 ± 268	1.56 ± 0.14	2.80		8.49/10 (0.58)
night 4	PL	3.45 ± 0.38		1.09 ± 0.16	3.42		2.70/5 (0.75)
	CPL	2.78 ± 0.82	0.82 ± 1.04	1.28 ± 0.29	2.68	1.88 - 15.33	1.68/4 (0.79)
	ECPL	1.67 ± 2.07	2.44 ± 3.05	1.28 ± 0.28	2.77		1.43/4 (0.84)
night 5	PL	4.03 ± 0.60		1.75 ± 0.44	4.66		4.46/3 (0.22)
	CPL	2.88 ± 1.54	1.53 ± 2.45	1.51 ± 0.49	3.99	1.88 - 27.92	3.56/2 (0.17)
	ECPL	0.77 ± 4.84	1.87 ± 3.08	1.50 ± 0.47	4.05		3.39/2 (0.18)
Flare night							
run 1	PL	2.75 ± 0.15		9.62 ± 0.84	4.66		2.92/3 (0.40)
	CPL	2.35 ± 0.30	0.45 ± 0.31	9.69 ± 0.87	3.80	1.9 - 28.03	0.58/2 (0.75)
	ECPL	1.84 ± 0.62	7.10 ± 4.82	9.54 ± 0.85	3.99		0.50/2 (0.78)
run 2	PL	2.89 ± 0.12		11.7 ± 0.69	3.97		1.30/4 (0.86)
	CPL	2.82 ± 0.26	0.07 ± 0.25	11.9 ± 0.94	2.93	1.9 - 20.78	1.21/3 (0.75)
	ECPL	2.67 ± 0.49	23.3 ± 51.3	12.0 ± 0.85	3.09		1.08/3 (0.78)
run 3	PL	2.81 ± 0.14		5.78 ± 0.41	3.88		27.4/4 ($1.7 \cdot 10^{-5}$)
	CPL	1.79 ± 0.26	1.06 ± 0.29	7.44 ± 0.67	3.04	1.9 - 15.41	4.92/3 (0.18)
	ECPL	0.57 ± 0.57	2.44 ± 0.69	7.11 ± 0.60	3.46		3.35/3 (0.34)
run 4	PL	2.98 ± 0.13		8.22 ± 0.58	4.16		16.46/6 (0.01)
	CPL	2.40 ± 0.22	0.67 ± 0.26	9.36 ± 0.80	3.46	1.9 - 20.78	4.86/5 (0.43)
	ECPL	1.58 ± 0.51	4.31 ± 1.73	9.02 ± 0.72	3.46		2.76/5 (0.74)

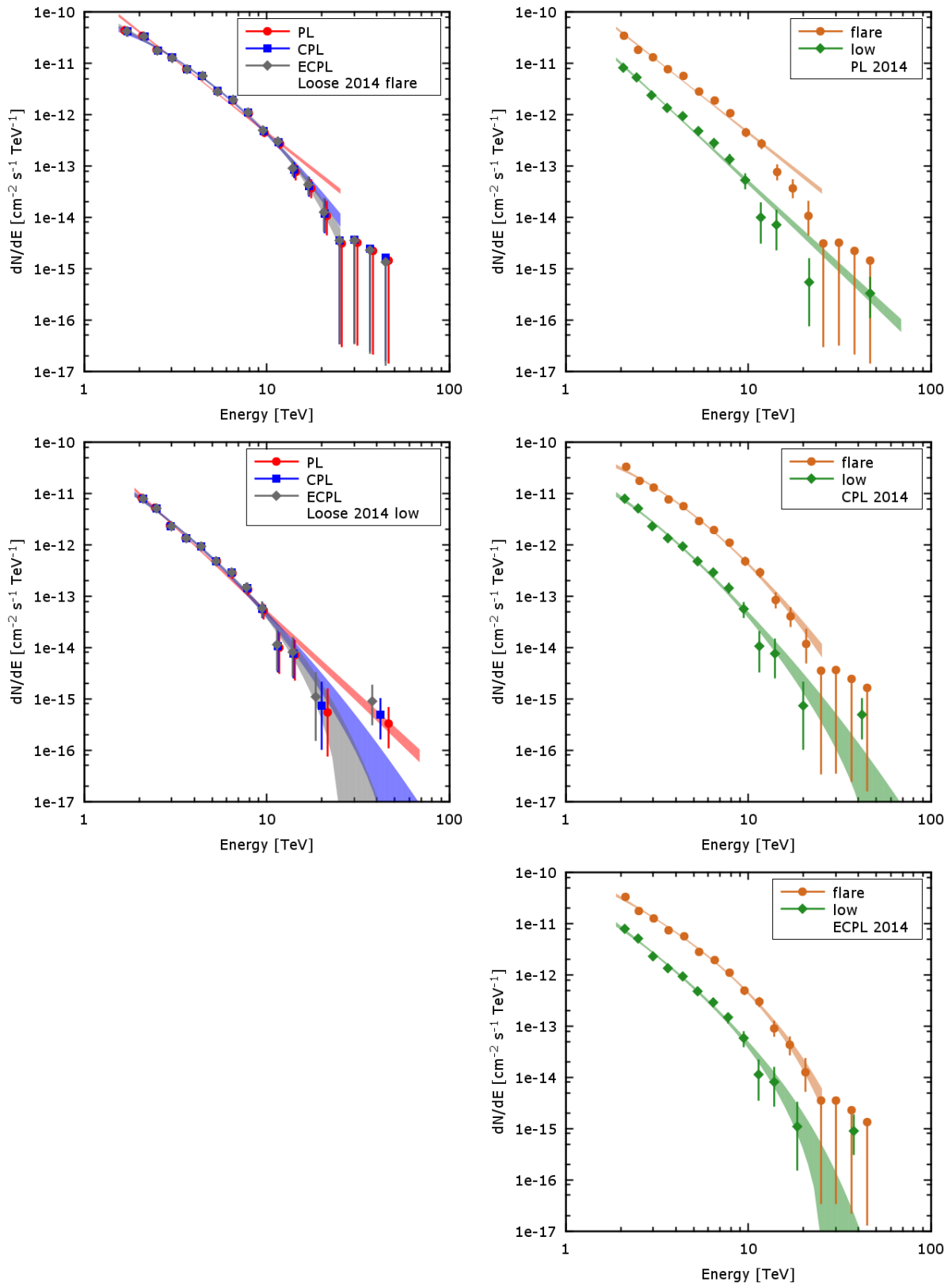


Figure 7.9: *Left:* Comparison of the spectral shapes for the flare (*top*) and low state (*middle*) in 2014. *Right:* Comparison of the 2014 flare and low states for the PL (*top*), CPL (*middle*) and ECPL (*bottom*) spectral shapes.

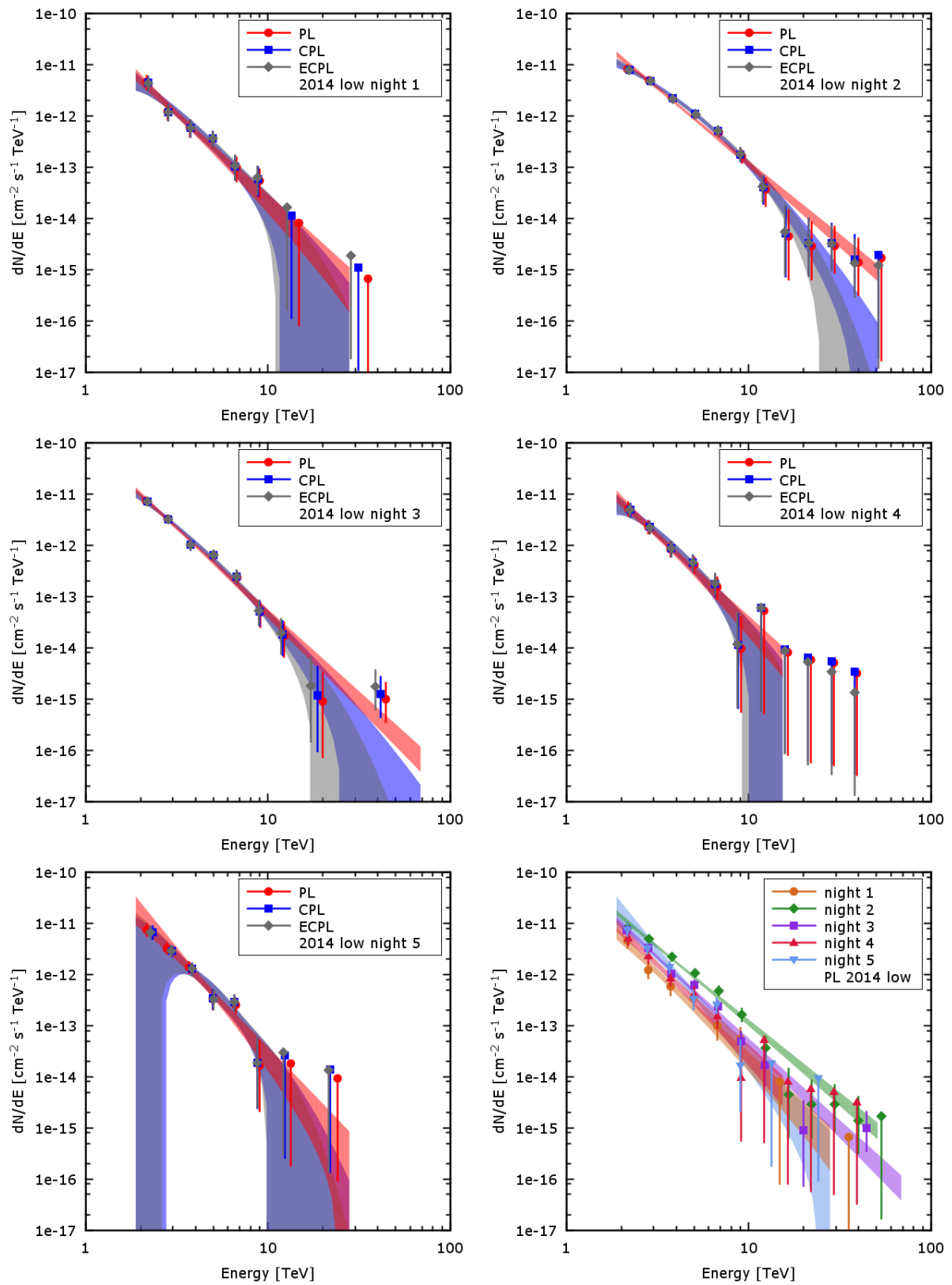


Figure 7.10: Comparison of the three spectral shapes for the five low state nights in 2014. The spectrum is significantly curved only in the second night (*top-right*). *Bottom-right*: comparison of the PL spectra of the five nights.

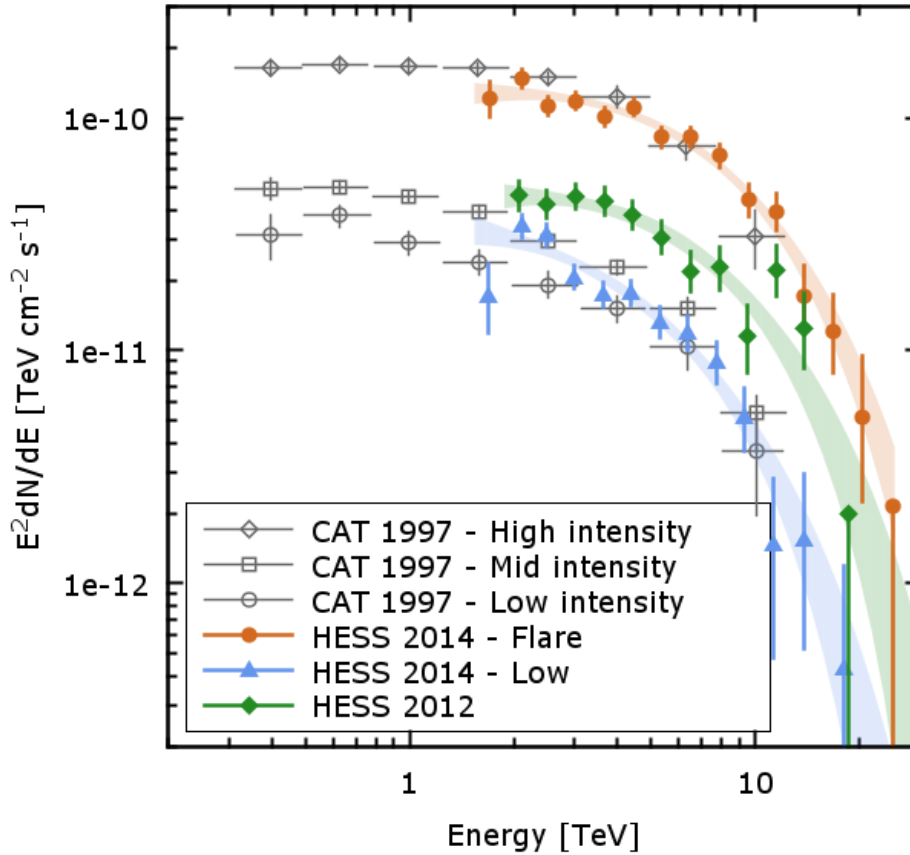


Figure 7.11: H.E.S.S. observed spectra for the 2014 and 2012 flare and low states. The 1997 CAT spectra (Djannati-Atai et al. 1999) are also shown for comparison.

In Fig. 7.11 the 2012 and 2014 H.E.S.S. spectra are compared to the three flux states detected with CAT in 1997 (Djannati-Atai et al. 1999). It is apparent how the 2014 flare state is perfectly compatible with the 1997 high intensity spectrum. The same is true for the two low states.

At this point it is interesting to check if spectral variability can be detected on even shorter timescales. Runwise spectra have been derived for the datasets of the 2012 (Fig. 7.12, 7.14 *left* and Table 7.7) and 2014 flare nights (Fig. 7.13, 7.14 *right* and Table 7.8). The spectra are in general well described by a PL shape. The third and fourth run of the 2014 flare night are an exception. Hints of curvature exist also for the third run in 2012. Although not all photon indices are compatible within the $1\text{-}\sigma$ statistical error, there is not enough evidence to claim spectral variability on this timescale. This is also supported by the fact that the spectra of the three nights considered here are compatible.

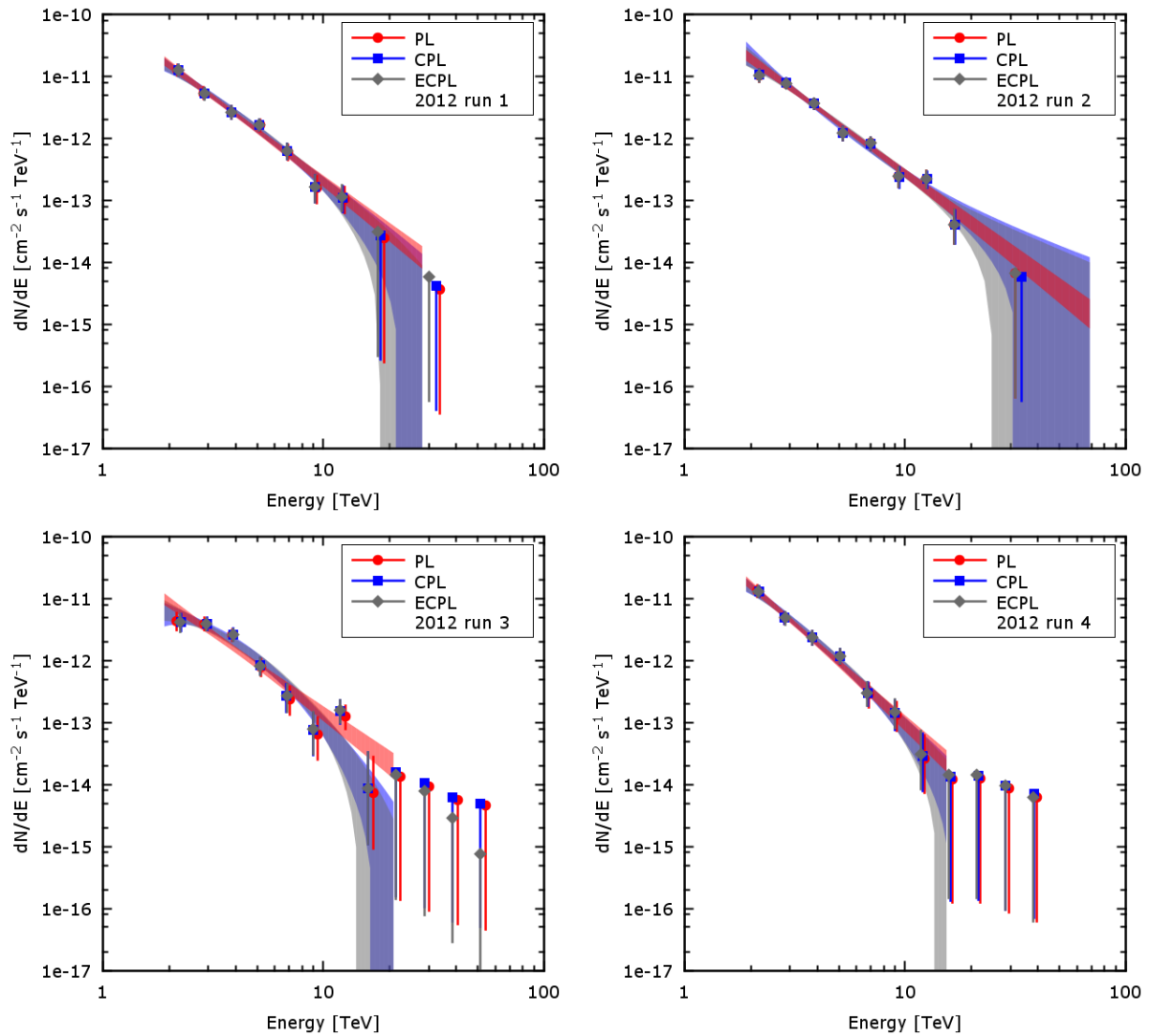


Figure 7.12: Comparison of the three spectral shapes for the *Loose* cuts fits for each run in 2012. The PL describes well the data in every case.

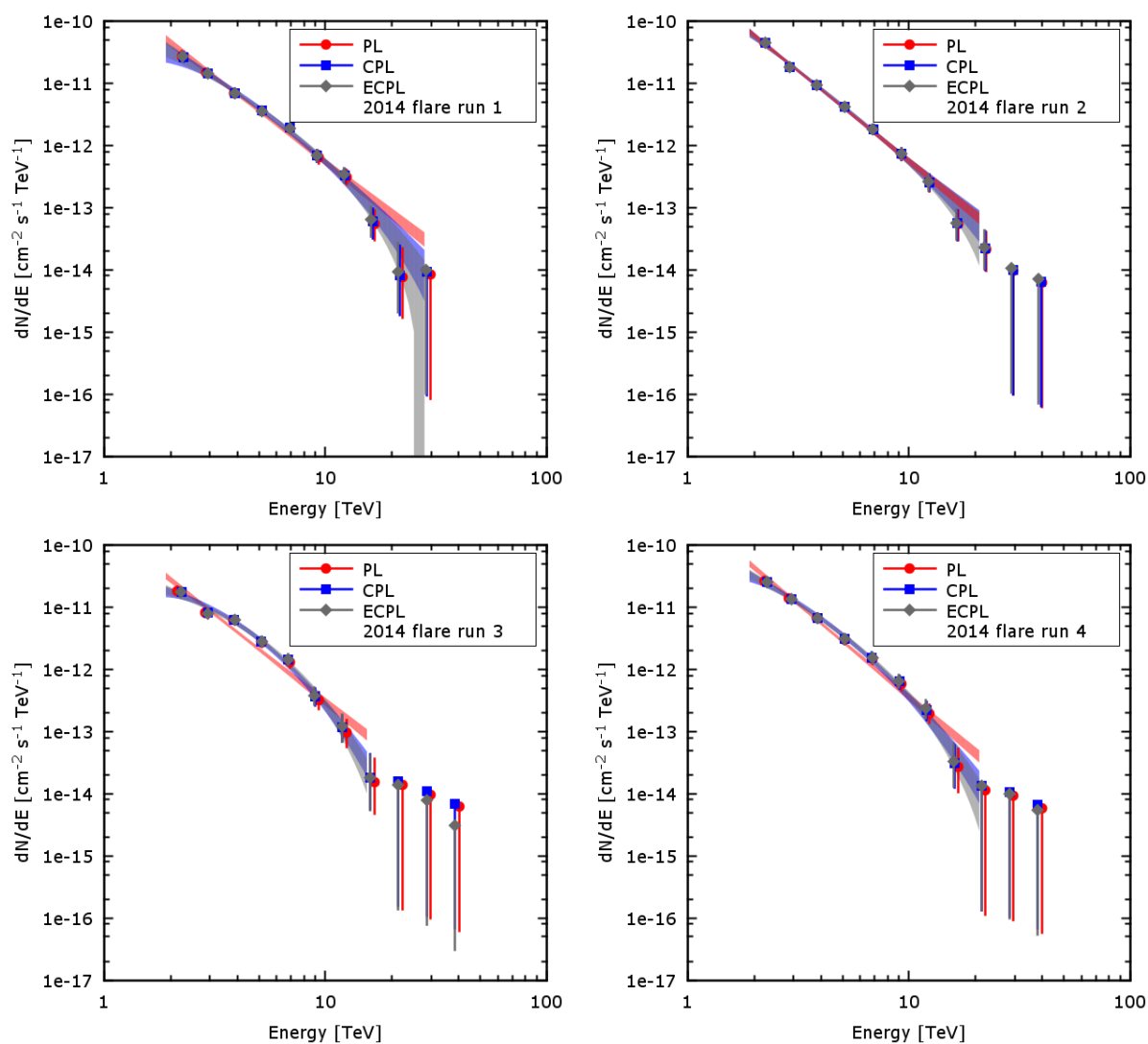


Figure 7.13: Comparison of the PL (*top left*), CPL (*top right*) and ECPL (*bottom*) spectral shapes for the four flare runs in 2014.

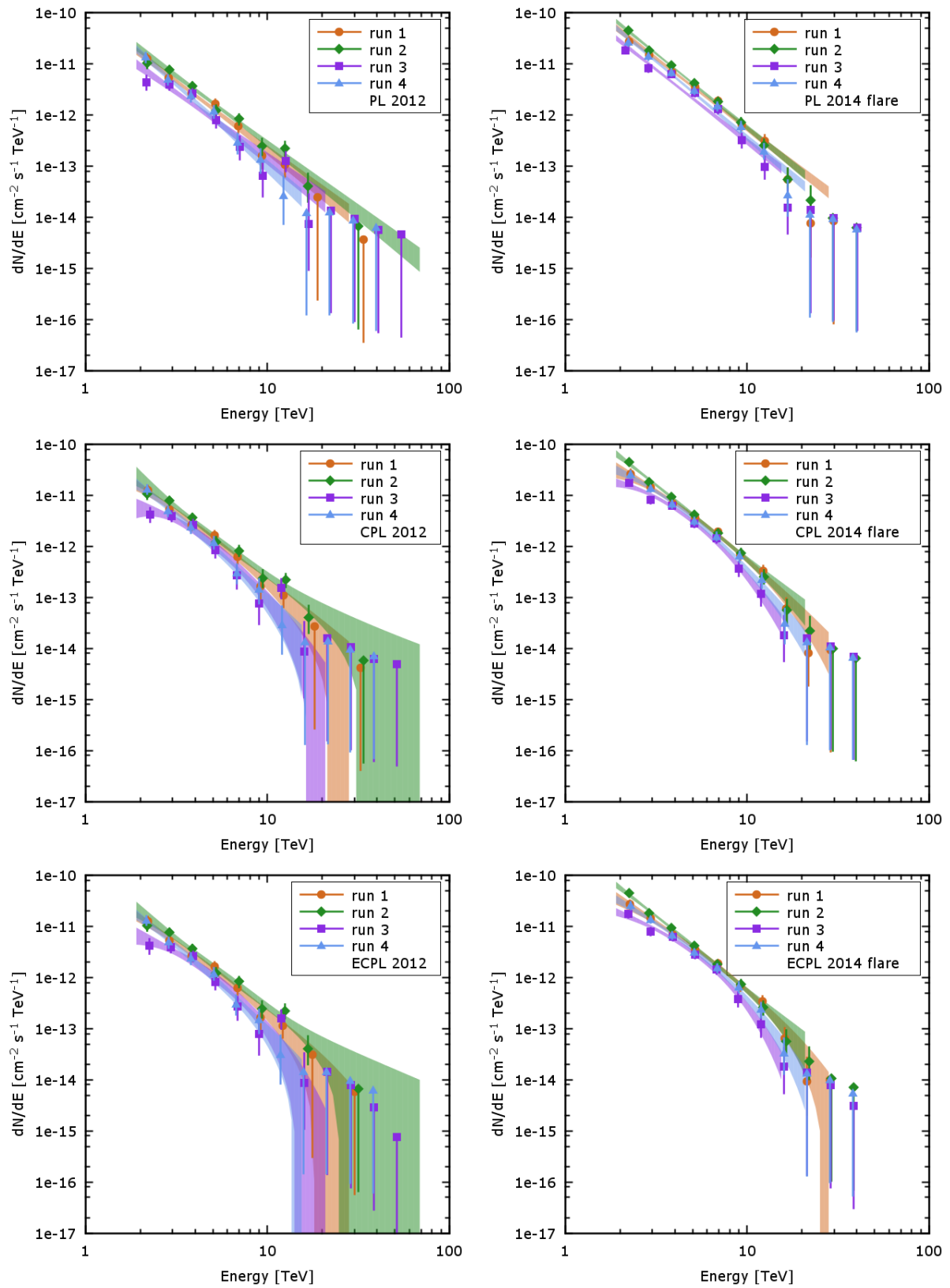


Figure 7.14: Comparison of the PL (*top*), CPL (*middle*) and ECPL (*bottom*) spectral shapes for the four runs of the 2012 (*left*) and 2014 (*right*) flare nights.

7.5.1.4 2006 DATASET: COMPARISON OF H.E.S.S. AND MAGIC SPECTRA

As reported in Sec. 7.2, the 2004 and 2006 data were collected as part of MWL campaigns (Gliozzi et al. 2006; Anderhub et al. 2009). Due to the low state of the source, they were published as upper limits in Aharonian et al. (2005b, 2008b). Thanks to the use in the current work of the more sensitive M++ analysis with *Loose* cuts, it was possible to obtain a detection for both datasets (Table 7.1). For the 2006 campaign, a VHE spectrum is provided by MAGIC and can be compared with the one derived here. The two spectra are displayed in Fig. 7.15. The photon indices of the two PL fits are marginally compatible ($\Gamma_{\text{HESS}} = 3.42 \pm 0.84$ vs $\Gamma_{\text{MAGIC}} = 2.79 \pm 0.12$). This result is not surprising because the two spectra cover complementary energy bands and because the spectrum is expected to be curved. The flux levels instead are offset by a factor of 2. This difference is unlikely to be explained by flux variability, since Mrk 501 is in low and relatively stable state over a longer period (see Fig. 3 in Anderhub et al. 2009) and the MAGIC spectrum is averaged over the three days of the MWL campaign. In any case, this cannot be completely excluded because the H.E.S.S. observations have been taken a few hours before the MAGIC ones (Rügamer et al. 2009). A plausible explanation could be the finite energy resolution of the two instruments of about $\sim 15\%$. Taking this into account, one can correct the energies and slightly shift the two spectra in opposite directions. Already with a 10% correction, the spectra match reasonably well.

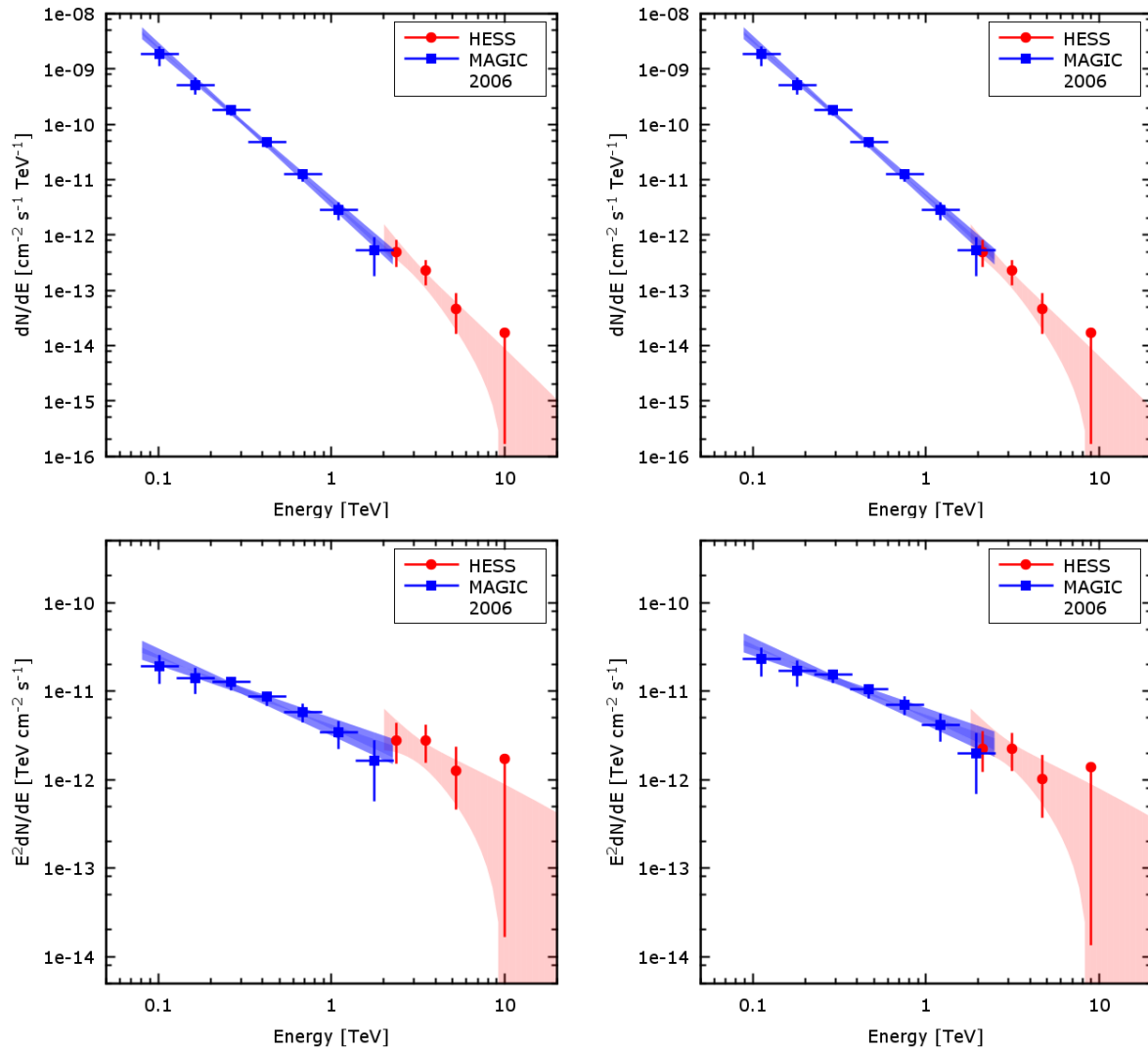


Figure 7.15: *Left:* Comparison of the H.E.S.S. and MAGIC spectra in 2006. The H.E.S.S. spectrum is slightly steeper than the MAGIC one, but a softening is expected at higher energies. The fluxes seem to be off by a factor of 2 and this seems not to be explained by the source variability. *Right:* Taking into account the energy resolution of the instruments, already a 10% correction to the energy scale of both spectra seems to solve the inconsistency. The MAGIC points are taken from (Anderhub et al. 2009). The butterfly is calculated from the fit parameters and their errors.

Table 7.9: Yearly *Loose* cuts spectral results with EBL.

	Γ	β/E_{cut}	$d\Phi/dE$ (3.5 TeV) [$10^{-12}cm^{-2}s^{-1}TeV^{-1}$]	E_{dec} [TeV]	Energy range [TeV]	$\chi^2/d.o.f.$ (prob)
2004						
PL	3.32 ± 0.49		0.54 ± 0.12	2.63	1.79 - 57.76	5.84/5 (0.32)
CPL	4.41 ± 0.71	-1.27 ± 0.48	0.40 ± 0.12	2.15		3.29/4 (0.51)
2006						
PL	2.97 ± 0.94		0.29 ± 0.10	3.04	2.01 - 82.71	0.82/5 (0.98)
2012						
PL	2.17 ± 0.10		5.69 ± 0.29	3.92	1.88 - 102.4	13.98/10 (0.17)
CPL	2.18 ± 0.19	-0.01 ± 0.19	5.68 ± 0.37	2.96		13.98/9 (0.12)
ECPL	2.24 ± 0.38	<i>inf</i> \pm <i>inf</i>	5.38 ± 0.33	3.42		15.91/9 (0.07)
2014						
PL	2.38 ± 0.05		5.94 ± 0.15	3.81	1.54 - 68.63	13.74/14 (0.47)
CPL	2.38 ± 0.09	-0.00 ± 0.09	5.94 ± 0.20	2.85		13.74/13 (0.39)
ECPL	2.37 ± 0.18	633 ± 14682	5.95 ± 0.19	3.05		13.74/13 (0.39)

7.5.2 INTRINSIC SPECTRA

As explained in Sec. 2.4.3, the Universe is filled with the EBL: optical and IR background radiation emitted by stars and dust, which interacts with and absorbs the very high energy γ -ray photons. This absorption usually does not affect much the emission of nearby sources like Mrk 501. Nonetheless, for the energies in play here, well above 10 TeV, every reasonable EBL model predicts a significant absorption, with optical depths $\tau > 1$. The question hence arises, if the curvature seen in the observed spectra discussed above is only due to the EBL absorption or if it has an intrinsic component. To determine which hypothesis is correct, spectral analyses comprising EBL absorption have been carried out on the datasets described above. Because spectral variability has been proven in the previous section, the total cumulative dataset has been excluded. Here, only *Loose* cuts are considered, since they provide higher significance and a broader energy range coverage. The EBL model from FR08 has been used.

The results for the yearly datasets are summarized in Table 7.9. All spectra are best described with an EBL absorbed PL. The more complex spectral shapes are not significantly better than this one. The ECPL fits do not always converge or show non significant cut-off energies E_{cut} outside the tested energy range. They tend to resemble simple PLs. With the exception of 2004, also the CPL fits give results compatible with simple PLs. The curvature parameter β is most of the times very small and/or compatible with zero. In some cases, it shows a tendency to an upwards curvature. The easiest explanation for an upward curvature is that the energy dependent optical depths reported for this redshift in FR08 could be slightly overestimated, as it is discussed in sec. 7.6. In this case, the CPL fit can compensate the excess of absorption with a negative

Table 7.10: Night- and run-wise spectral results 2012 with *Loose* cuts with EBL.

		Γ	β/E_{cut}	$d\Phi/dE$ (3.5 TeV) [$10^{-12} cm^{-2} s^{-1} TeV^{-1}$]	E_{dec} [TeV]	Energy range [TeV]	$\chi^2/d.o.f.$ (prob)
night 1	PL	2.08 ± 0.13		6.96 ± 0.47	4.08		5.87/9 (0.75)
	CPL	2.31 ± 0.24	-0.26 ± 0.23	6.57 ± 0.55	2.98	1.88 - 68.63	4.57/8 (0.80)
	ECPL	2.10 ± 0.47	<i>inf</i> \pm <i>inf</i>	7.00 ± 0.54	3.42		5.89/8 (0.66)
night 2	PL	2.35 ± 0.18		4.50 ± 0.36	3.42		10.58/9 (0.31)
	CPL	2.14 ± 0.32	0.30 ± 0.35	4.79 ± 0.51	2.87	1.88 - 16.94	9.95/8 (0.27)
	ECPL	2.00 ± 0.65	12.9 ± 22.3	4.65 ± 0.45	3.03		10.33/8 (0.24)
run 1	PL	2.21 ± 0.21		6.43 ± 0.64	3.92		2.42/4 (0.66)
	CPL	2.37 ± 0.40	-0.19 ± 0.41	6.17 ± 0.83	2.84	1.9 - 28.03	2.22/3 (0.53)
	ECPL	2.22 ± 0.80	<i>inf</i> \pm <i>inf</i>	6.22 ± 0.76	3.05		2.56/3 (0.46)
run 2	PL	1.89 ± 0.20		7.53 ± 0.88	4.95		6.26/3 (0.10)
	CPL	2.76 ± 0.44	-0.89 ± 0.39	7.25 ± 0.84	3.46	1.9 - 68.73	2.05/2 (0.36)
	ECPL	1.97 ± 0.90	<i>inf</i> \pm <i>inf</i>	7.79 ± 0.91	3.46		6.39/2 (0.04)
run 3	PL	2.06 ± 0.27		3.92 ± 0.47	3.87		6.07/3 (0.11)
	CPL	1.53 ± 0.58	0.76 ± 0.63	4.54 ± 0.71	3.05	1.9 - 20.78	4.46/2 (0.11)
	ECPL	0.89 ± 1.31	4.02 ± 4.22	4.33 ± 0.64	3.46		5.11/2 (0.08)
run 4	PL	2.75 ± 0.26		5.23 ± 0.57	3.46		1.31/5 (0.93)
	CPL	2.76 ± 0.50	-0.02 ± 0.54	5.21 ± 0.83	2.64	1.9 - 15.41	1.31/4 (0.86)
	ECPL	2.70 ± 1.03	94 ± 2015	5.25 ± 0.77	2.79		1.31/4 (0.86)

curvature, balancing the EBL absorption effect. Despite the upward curvature being significantly different from zero in 2004, the fit is not significantly better than a simple absorbed PL.

Focusing on the night- and run-wise fits (Tables 7.10 and 7.11), one can see that an absorbed PL is again the best fit in all cases, with a maximal deviation of 2σ for two runs. The same comments relative to the yearly fits also apply here. Inspecting the fit residuals in Fig. 7.16, however, one can notice that the spectra seem to soften at the highest energies, especially when lower fluxes are considered. Would this trend be true, one could explain the impossibility to detect an intrinsic curvature in this energy range with the low significance of the high energy bins and with the fact that the spectra cover significantly only one decade in energy between ~ 2 and 20 TeV, which is not broad enough.

When plotting the intrinsic photon index as function of the flux (Fig. 7.17), a soft-low state (top-left) and a hard-high state (bottom) can be recognized. This is a sign of a harder-when-brighter behavior which probably cannot be detected in its entirety because of the small number of points and because of the loose constrains on the photon index at low fluxes. In the hard state, the photon index remains stable around $\Gamma = 2.1 - 2.2$ for a broad range of flux values. This can be explained as being in the vicinity of the maximum of the IC peak, which is known to migrate towards higher energies during flares and periods of high activity.

Table 7.11: Night- and run-wise spectral results 2014 with *Loose* cuts with EBL.

		Γ	β/E_{cut}	$d\Phi/dE$ (3.5 TeV) [$10^{-12}cm^{-2}s^{-1}TeV^{-1}$]	E_{dec} [TeV]	Energy range [TeV]	$\chi^2/d.o.f.$ (prob)
Flare	PL	2.15 ± 0.06		15.72 ± 0.53	4.18		8.59/10 (0.57)
	CPL	2.20 ± 0.11	-0.06 ± 0.11	15.52 ± 0.63	3.07	1.54 - 25.27	8.28/9 (0.51)
	ECPL	2.16 ± 0.22	<i>inf</i> \pm <i>inf</i>	15.75 ± 0.59	3.29		8.59/9 (0.48)
Low	PL	2.67 ± 0.10		2.83 ± 0.13	3.49		20.80/13 (0.08)
	CPL	2.50 ± 0.18	0.24 ± 0.21	2.99 ± 0.19	2.81	1.54 - 68.63	19.12/12 (0.09)
	ECPL	2.21 ± 0.41	9.46 ± 8.34	2.97 ± 0.17	2.81		19.05/12 (0.09)
Low state							
night 1	PL	2.87 ± 0.37		1.46 ± 0.23	3.49		4.53/5 (0.48)
	CPL	2.97 ± 0.81	-0.11 ± 0.82	1.42 ± 0.33	2.54	1.88 - 27.92	4.50/4 (0.34)
	ECPL	2.69 ± 1.64	25 ± 238	1.48 ± 0.31	2.82		4.51/4 (0.34)
night 2	PL	2.29 ± 0.16		4.83 ± 0.35	3.88		4.56/7 (0.71)
	CPL	2.11 ± 0.30	0.21 ± 0.32	5.04 ± 0.49	2.93	1.88 - 50.85	4.11/6 (0.66)
	ECPL	1.88 ± 0.62	12.1 ± 18.7	4.99 ± 0.44	3.42		4.16/6 (0.66)
night 3	PL	2.82 ± 0.19		2.90 ± 0.23	3.42		5.61/7 (0.59)
	CPL	2.88 ± 0.37	-0.07 ± 0.39	2.86 ± 0.34	2.65	1.88 - 68.63	5.58/6 (0.47)
	ECPL	2.83 ± 0.74	<i>inf</i> \pm <i>inf</i>	2.88 ± 0.31	2.80		5.62/6 (0.47)
night 4	PL	3.05 ± 0.40		2.02 ± 0.30	3.42		1.76/5 (0.88)
	CPL	2.70 ± 0.84	0.45 ± 1.07	2.19 ± 0.50	2.66	1.88 - 15.33	1.50/4 (0.83)
	ECPL	1.99 ± 2.10	3.98 ± 8.24	2.20 ± 0.48	2.76		1.37/4 (0.85)
night 5	PL	3.26 ± 0.65		2.83 ± 0.75	4.70		3.60/3 (0.31)
	CPL	2.72 ± 1.63	0.80 ± 2.59	2.65 ± 0.83	3.94	1.88 - 27.92	3.43/2 (0.18)
	ECPL	1.38 ± 5.00	3.05 ± 8.56	2.62 ± 0.82	4.02		3.35/2 (0.19)
Flare night							
run 1	PL	1.97 ± 0.16		16.22 ± 1.46	4.66		1.29/3 (0.73)
	CPL	2.19 ± 0.31	-0.27 ± 0.33	16.12 ± 1.44	3.73	1.90 - 28.03	0.66/2 (0.72)
	ECPL	1.95 ± 0.68	<i>inf</i> \pm <i>inf</i>	14.54 ± 1.31	3.94		3.31/2 (0.19)
run 2	PL	2.38 ± 0.12		21.49 ± 1.27	3.98		2.58/4 (0.63)
	CPL	2.74 ± 0.26	-0.39 ± 0.25	19.89 ± 1.59	2.90	1.90 - 20.78	0.32/3 (0.96)
	ECPL	2.42 ± 0.52	<i>inf</i> \pm <i>inf</i>	21.38 ± 1.54	3.08		2.68/3 (0.44)
run 3	PL	2.10 ± 0.15		10.98 ± 0.78	3.91		7.21/4 (0.13)
	CPL	1.65 ± 0.28	0.54 ± 0.30	12.32 ± 1.15	2.97	1.90 - 15.41	3.58/3 (0.31)
	ECPL	0.97 ± 0.59	4.38 ± 2.34	12.10 ± 1.04	3.46		3.04/3 (0.39)
run 4	PL	2.23 ± 0.14		15.10 ± 1.08	4.18		1.14/6 (0.98)
	CPL	2.27 ± 0.27	-0.05 ± 0.27	14.97 ± 1.32	3.06	1.90 - 20.78	1.10/5 (0.95)
	ECPL	2.27 ± 0.54	<i>inf</i> \pm <i>inf</i>	14.71 ± 1.19	3.46		1.44/5 (0.92)

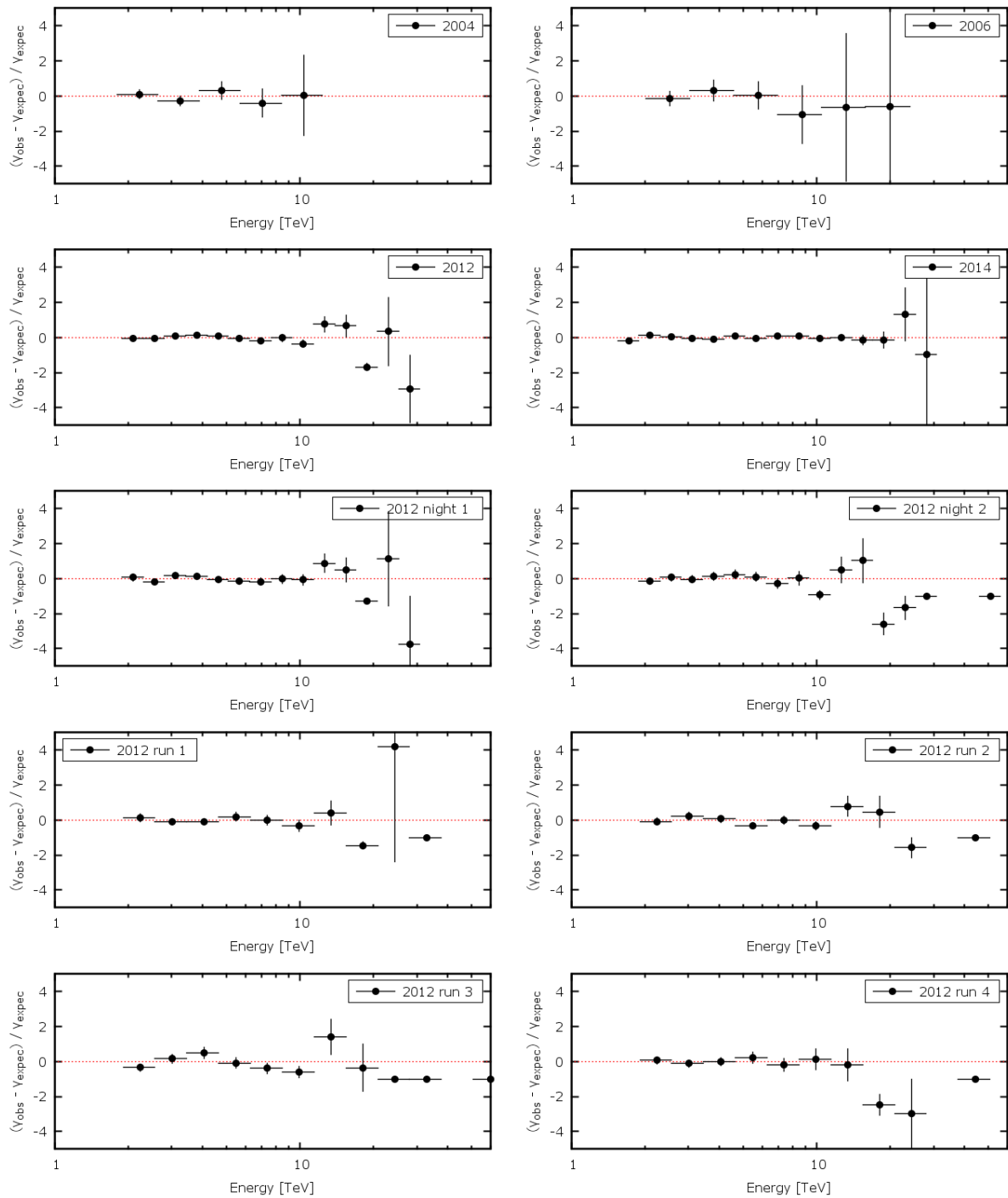


Figure 7.16: Residuals of the PL spectra comprising EBL absorption. From top to bottom, single years, 2012 subsets (*this page*) and 2104 subsets (*next page*). The y-axis range has been fixed for clarity reasons. Some very low significance bins (i.e. with very large errorbars) with large offset in the central value are therefore not displayed.

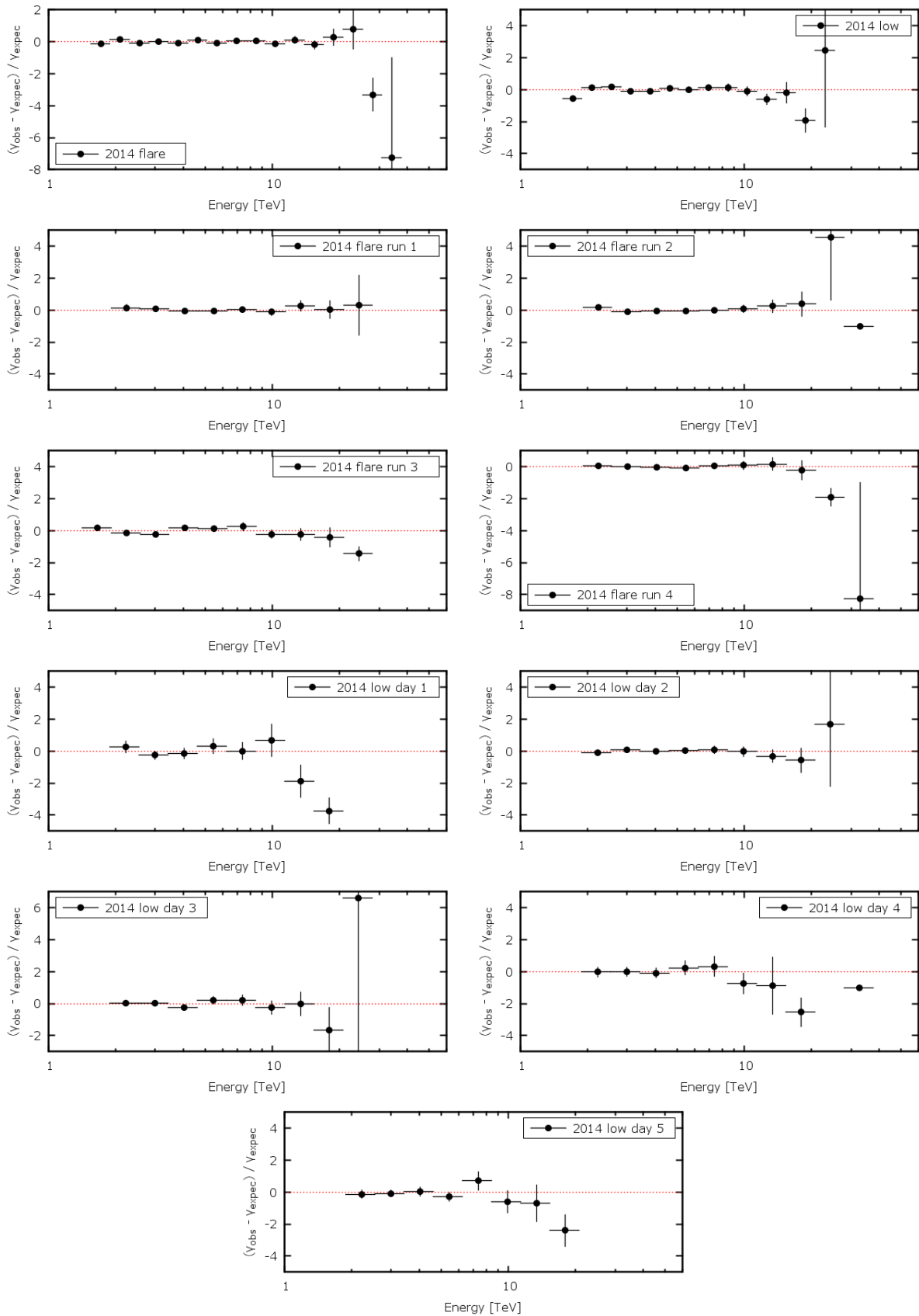


Figure 7.16: Continued.

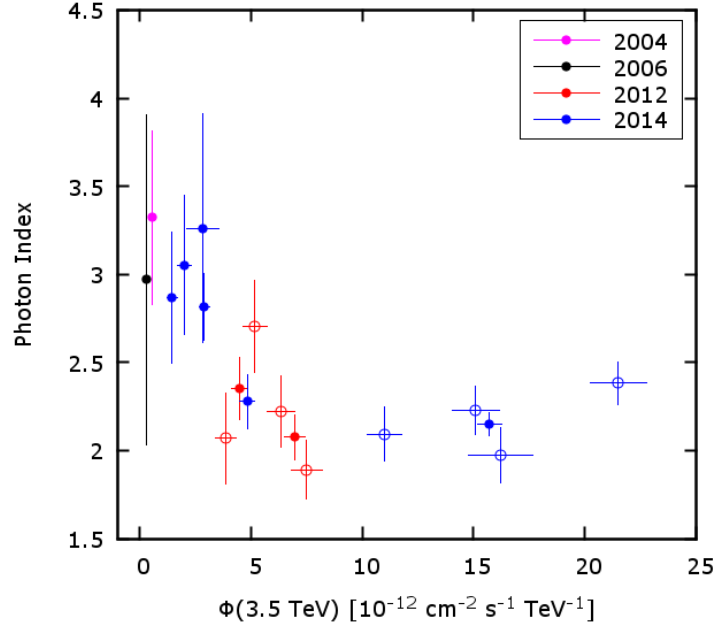


Figure 7.17: Intrinsic photon indices from EBL absorbed PL fits as function of flux. Values are given for single nights (full circles) and for single runs (open circles) during the flares. By high fluxes, the spectra are clearly hard.

The hard simple PL spectrum of the 2014 flare night extends above 20 TeV, indicating the absence of the predicted Klein-Nishina suppression. In fact, it is expected at these high energies that the Thomson limit for the scattering cross section does not hold anymore. For this to happen, eq. 2.29 must be fulfilled. Theoretically, it is still possible to reach 20 TeV without violating the limit if the electron distribution reaches at least $\gamma_e > 10^6$ and the Doppler factors are up to $\delta = 50$. In this case, however, only very low energy photons can be up-scattered. Their number is not sufficient to explain the VHE flare flux. The emission is more easily explained in the Klein-Nishina limit. Using eq. 2.32 it is possible to determine the minimum value of the maximal electron energy $\gamma_{e,max}$ from the highest observed energy in the H.E.S.S. spectrum, around 20 TeV: $\gamma_{e,max} = 4 \times 10^6 (10/\delta)$. Since in the Klein-Nishina limit all the electron energy is transferred in one scattering, a cut-off is expected near $\gamma_{e,max}$. The absence of a detectable cut-off implies that the underlying electron distribution must reach energies significantly larger than the one found here. From the combination of eq. 2.22 and 2.32, it is possible to constrain the magnetic field in the emission region:

$$B \sim 0.075 \left(\frac{\delta}{10} \right) \left(\frac{E_{syn}^{max}}{200 \text{ keV}} \right) \left(\frac{20 \text{ TeV}}{E_{IC}^{max}} \right)^2 \text{ G}. \quad (7.2)$$

E_{syn}^{max} has been taken at 200 keV from the *BeppoSAX* spectrum of the big flare in 1997. This choice is justified by the similarity of the VHE spectra during the 1997 and 2014 flares (Fig. 7.11). The physical parameters derived here are only a simple qualitative approximation. However, they are in the range of values that are used in the literature for SED fitting.

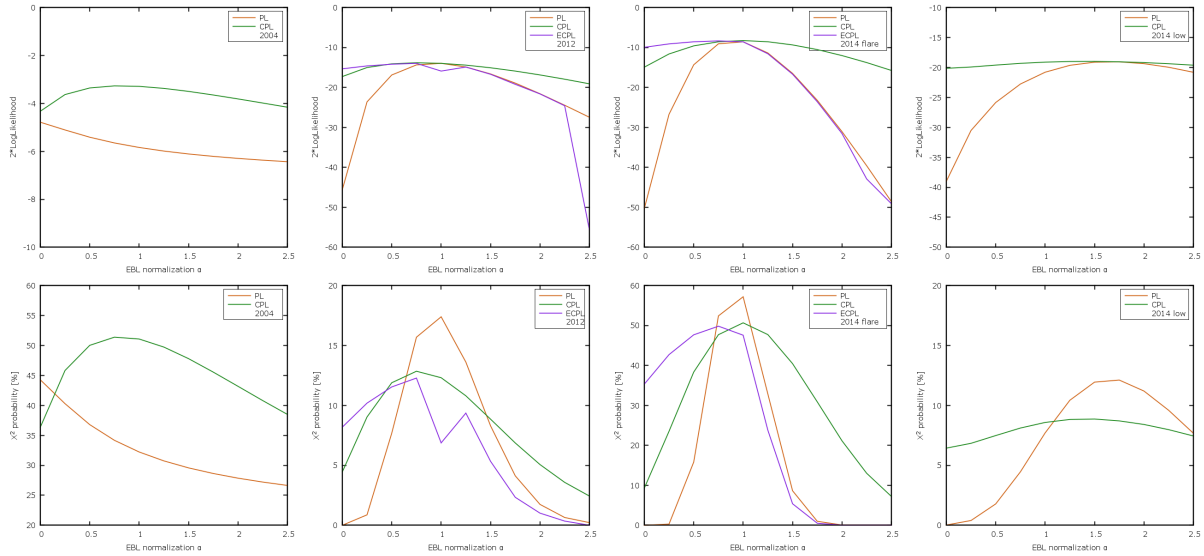


Figure 7.18: $\text{Log}(\mathcal{L})$ (top) and χ^2 (bottom) profiles for the four datasets used in this study. With the exception of the 2004 dataset, the $\text{Log}(\mathcal{L})$ profiles peak at similar values. The PL is preferred because it has more degrees of freedom. For clarity reasons, the y-axis do not have the same scale in all plots.

7.6 EBL DETERMINATION

The model of FR08 has been chosen because it describes an overall low optical depth, as it has been found to be the case for other sources (e.g. for 1ES 0229+200, Aharonian et al. 2007a), and because it is provided in fine binned tables in both energy and redshift. However, other models exist, which predict significantly lower or higher EBL densities, especially at high energies (e.g. Finke et al. 2010). It is hence possible that the optical depth derived from FR08 for the 2–20 TeV energy range at the redshift of Mrk 501 ($z \approx 0.034$) is not precise. With the availability of a spectral fit that comprises the effects of the EBL absorption, it is possible to effectively test this hypothesis simply applying a multiplicative factor α to the optical depth of the model τ_{model} and determine which value maximizes the significance of the fit with respect to $\alpha = 0$. The factor α is defined as the normalization between predicted and measured opacity: $\alpha = \tau_{\text{meas}}/\tau_{\text{model}}$. The procedure followed here is the one described in H.E.S.S. Collaboration et al. 2013 (hereafter HESS13), which in turn follows the steps of Abdo et al. (2010).

The source observed flux can be written in terms of the intrinsic source flux multiplied by an absorption coefficient, which depends on the optical depth $\tau(E, z, n)$, where E is the γ -ray photon energy, z is the source redshift and n the estimated EBL density:

$$\Phi_{\text{obs}}(E) = \Phi_{\text{int}}(E) \times e^{-\tau_{\text{meas}}(E, z, n)} \quad (7.3)$$

To describe the intrinsic spectra in the different flux states, the same three spectral shapes have been used again on the 2004, 2012, 2014 flare and low state datasets. The 2006 dataset has been discarded because the source is too faint to provide significant results.

One needs to determine which is the most complex spectral model that best describes each dataset. Hence, fits with all three absorbed spectral shapes have been performed varying the normalization α in the range $[0 : 2.5]$ with steps of 0.25. The respective LogLikelihood ($\text{Log}(\mathcal{L})$) and χ^2 probability profiles have been computed (Fig. 7.18). Although the Likelihood distributions peak at identical maximum values in three of the four cases, indicating a similar goodness of the fit, the simpler model is preferred by the χ^2 probability, since it has more degrees of freedom. Therefore, the PL has been chosen as the best shape, with the exception of the 2004 dataset, where a CPL has a better probability. On the other hand, the ECPL does not converge for all datasets and tends to a PL for normalizations $\alpha \geq 1$.

For the best intrinsic shapes, LLRT profiles have been computed⁴ and summed together (Fig. 7.19). As expected, the 2014 flare dataset gives the larger contribution, while the 2004 provides only a very marginal contribution. The sum of the LLRT profiles peaks at $\alpha = 0.99 \pm 0.15$, with a value of 92.6, which translates in a significance of 9.6σ . The null hypothesis of a non-existent EBL is hence excluded at more than 9σ level. The reported error is only statistical. A systematic error $d\alpha_{\text{sys}} = 0.25$ is taken from HESS13 and is justified by the use of the same tools used in that publication. The derived normalization is perfectly compatible with the model of FR08. Taking into account only the two major contributions, one derives $\alpha = 0.91_{-0.15}^{+0.16}$, while for the 2014 flare alone $\alpha = 0.90_{-0.17}^{+0.20}$. These are not compatible with $\alpha = 1.27_{-0.15}^{+0.18}$ calculated in HESS13. This can be explained by the fact that, although several sources have been used in HESS13, the major contribution is given by a single source, PKS 2155-304. Differences could therefore arise as dependencies on the redshift ($z_{\text{Mrk } 501} \simeq 0.034$ vs. $z_{\text{PKS } 2155-304} = 0.116$) and on the significantly different energy range covered ($\sim 2 - 20$ TeV vs. $\sim 0.15 - 7$ TeV). These dependencies were investigated by HESS13, so it is possible to make further comparisons. The low-redshift subset composed of Mrk 421 and PKS 2005-489 only ($\langle z \rangle = 0.051$) yields a value $\alpha_{\text{low-}z} = 1.6_{-1.1}^{+0.5}$ which is not very useful given its low precision. Moreover, the various subsets used there provide non significant LLRT values between -2 and 2. On the other hand, the present result is perfectly compatible with $\alpha_{\text{high-energy}} = 1.05_{-0.28}^{+0.32}$ derived for the high energy dataset, which covers the range between 0.95 and 14 TeV.

The results presented here are obviously valid only for the energy range common to all datasets used, which is 1.9 - 25.3 TeV. It is important to determine the wavelength of the EBL photons responsible for the absorption. From eq. 2.49 one has that the wavelength range for this analysis spans from 2.4 to $30 \mu\text{m}$. The corresponding flux densities for the total sum are basically the ones given by FR08: 8.6 ± 1.3 and $3.7 \pm 0.6 \text{ nW m}^{-2} \text{ sr}^{-1}$. For the 2014 flare dataset alone one gets instead $7.8_{-1.5}^{+1.7}$ and $3.3_{-0.6}^{+0.7} \text{ nW m}^{-2} \text{ sr}^{-1}$.

It is now possible to draw some considerations. Under similar conditions, this work and HESS13 are consistent. This also shows that the FR08 model is a good description of the actual EBL intensity. The 2014 flare LLRT profile could hint to a slight overestimation of the model, but the deviation is less than 1σ . This goes also in the direction of the work of Biteau & Williams (2015), who found a normalization $\alpha_{\text{Biteau2015}} = 1.05 \pm 0.07$ using 86 different spectra (mostly at significant lower energies than this work) from 30 sources up to $z = 0.287$. The use of models

⁴In this case, the EBL normalizations α are compared: $\text{LLRT} = -2 \cdot [\text{Log}(\mathcal{L}(\alpha = 0)/\mathcal{L}(\alpha))]$.

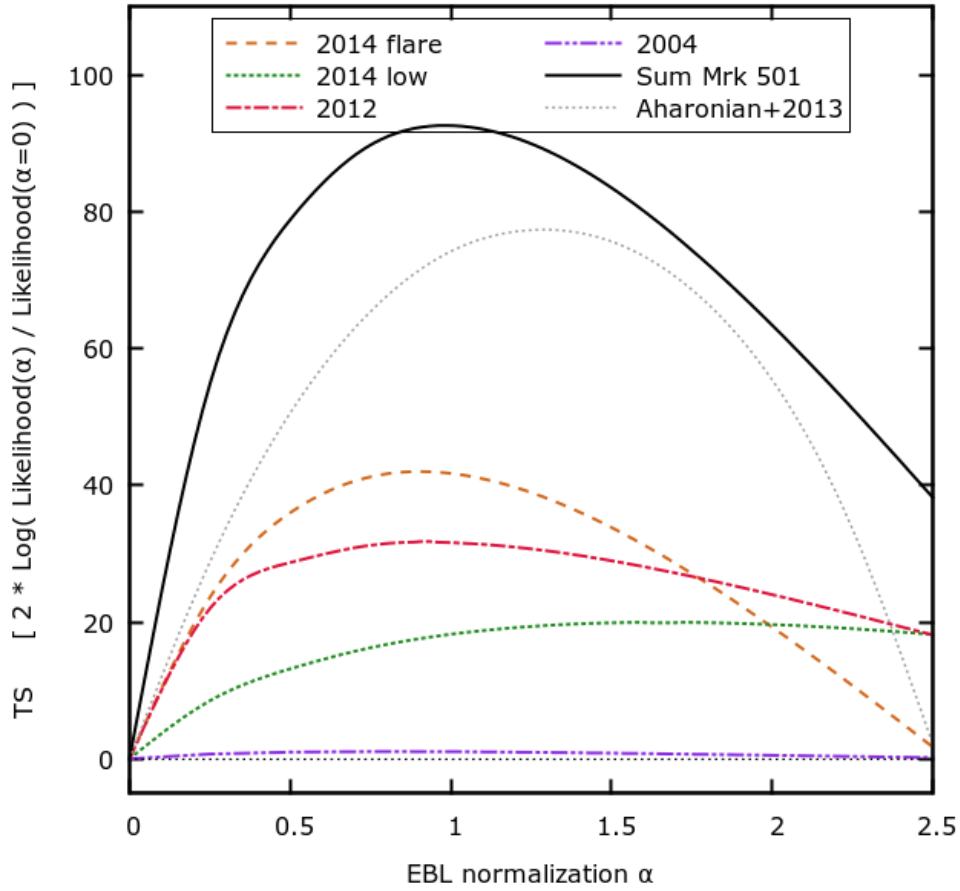


Figure 7.19: LLRT profiles of the four datasets used and their sum. The profile derived in HESS13 is also shown for comparison.

with EBL intensity significantly lower than required would directly affect the determination of the intrinsic spectrum. Accounting for less absorption, they would require a curvature or cut-off in the source intrinsic spectrum.

It is now interesting to take a look at the values of the spectral parameters as function of the normalization α for the three spectral shapes (Fig. 7.20). For the 2012 and 2014 flare/low state datasets, it is apparent how Γ_{CPL} is rather stable independently from α . The EBL absorption effect is mimicked and balanced by the curvature β . Keeping in mind the profiles of Fig. 7.18, it is now obvious that the better quality of the CPL fits for $\alpha \geq 1$ is only due to the possibility to counterweight the exceeding EBL absorption, as suggested in sec. 7.5.2. Would β be forced to be larger than 0, hence avoiding an upward curvature in the intrinsic spectrum, then the CPL fit would resemble a simple PL, as it is the case for the ECPL for $\alpha \geq 1$. Worth mentioning is the fact that the Γ s corresponding to the maxima of the profiles have all the same value (for a single dataset) for all three spectral shapes, and β and $1/E_{\text{cut}}$ are very close to and compatible with 0. This is a further evidence that the intrinsic spectra are simple PLs in the energy range that can be tested here.

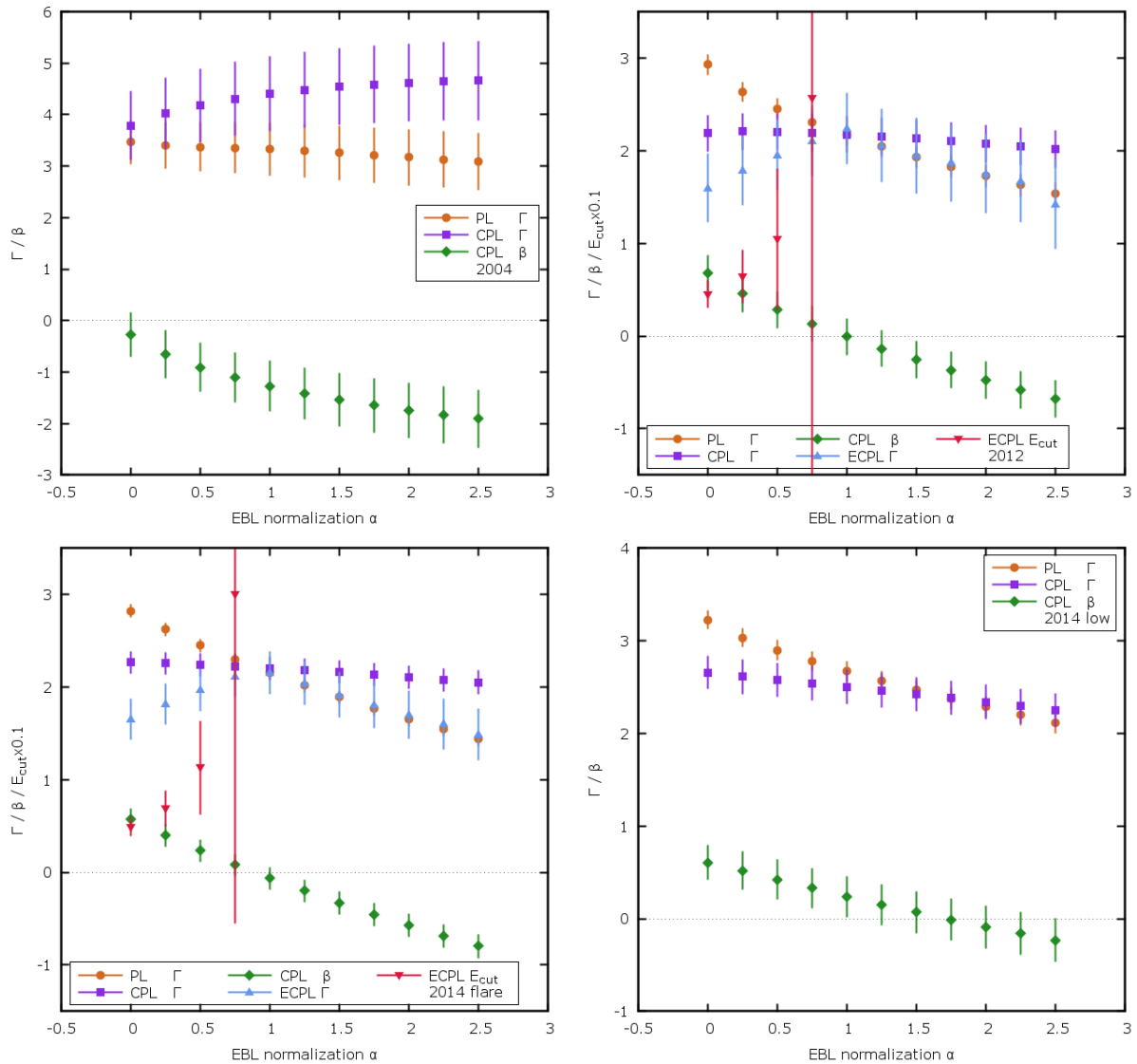


Figure 7.20: Γ , β , E_{cut} values as function of the EBL normalization α for the four datasets used here. The E_{cut} values have been divided by 10 for visualization purposes. For $\alpha \geq 1$ they tend to $+\infty$ and lie outside the plots.

7.7 TEMPORAL ANALYSIS

In the top panel of Fig. 7.21, the run-wise lightcurve above 2 TeV of the 2004–2014 H.E.S.S. observations is shown. Two clear flaring events can be seen in 2012 and in 2014, along with two quiescent states in 2004 and 2006 and a phase of moderate activity in 2014. Mrk 501 is clearly variable also in X-rays (middle panel) with 2–10 keV fluxes between $\sim (1.5 - 4) \times 10^{-10}$ erg cm $^{-2}$ s $^{-1}$ and in optical (lower panel). The comparison of the three lightcurves shows no obvious correlation in the flux variations of the different energy bands. The optical emission

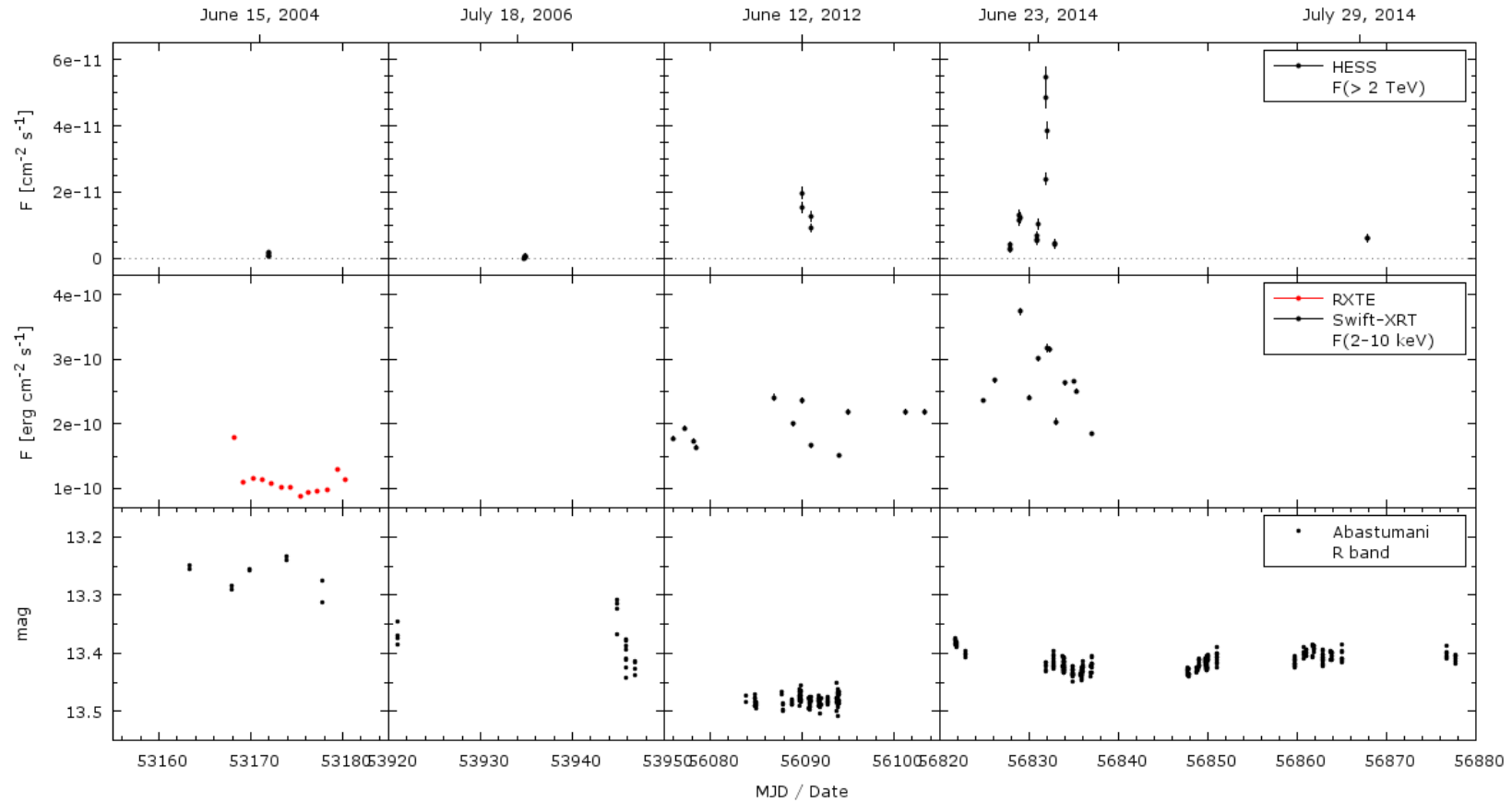


Figure 7.21: *Top:* H.E.S.S. run-wise lightcurve above 2 TeV. The flaring states in 2012 and 2014 are clearly visible (MJD \sim 56089-90 and 56831-32). It is also apparent that the "low" state in 2014 still represent a state of moderate activity when compared to the flux levels in 2004 and 2006. *Middle:* RXTE and Swift-XRT X-ray lightcurves in the energy range 2-10 keV showing high variability. *Bottom:* optical lightcurve from the Abastumani Observatory. No particularly high flux values or strong variability are detected in correspondence of the 2012 and 2014 TeV flares.

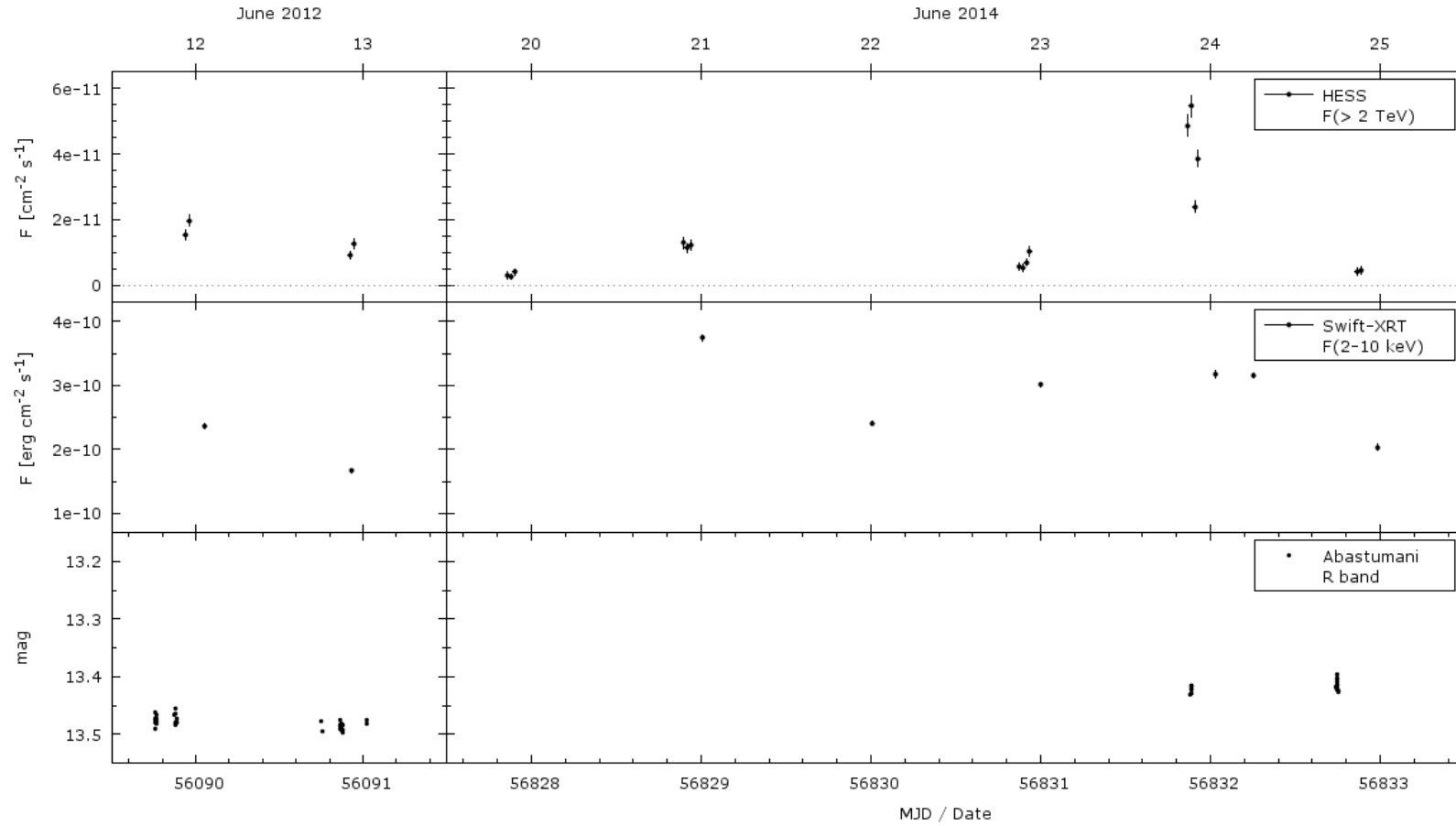


Figure 7.22: Zoom-in of the lightcurves of Fig. 7.21 for the years 2012 (*left*) and 2014 (*right*) for H.E.S.S., *Swift*-XRT and Abastumani (from *top* to *bottom*). The highest X-ray flux (June 21) and γ -ray flux (\sim June 24) find no matching high state in the other energy band. The strictly simultaneous optical measurements on June 24 show a relatively low state.

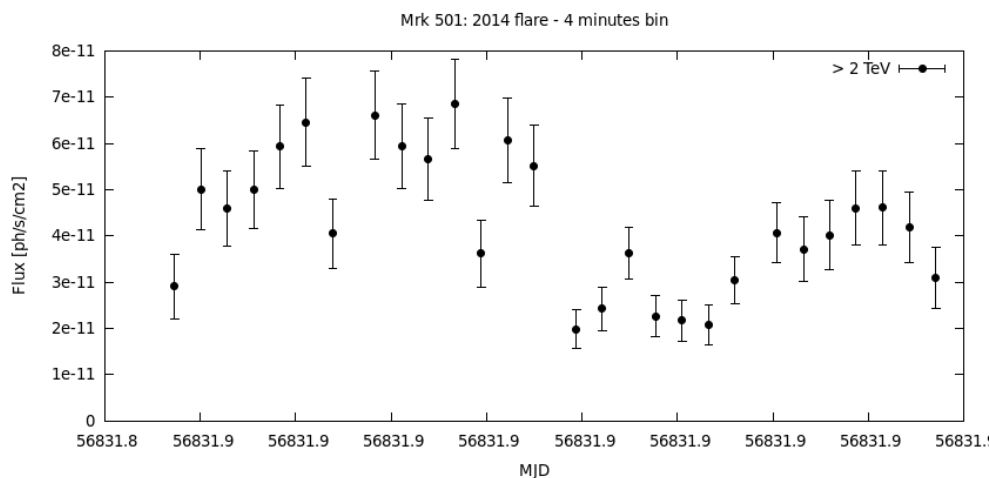


Figure 7.23: 240 s bin lightcurve of the 2014 flare.

is in an average/low state during both TeV flares (Fig. 7.22) and this is true also for the strictly simultaneous observations during the peak of the flare in 2014. This can be explained by the harder-when-brighter behavior detected in X-rays, since the variability at lower energy has a lower amplitude. On the other hand, the source is in higher optical state in 2004 and 2006, when the TeV emission is very low. This suggests that at least two zones or mechanisms are necessary to explain the flaring events in Mrk 501. The hypothesis of the presence of more than one emission zone is supported also by the discovery of off-axis jet structures in radio images at 43 GHz (Koyama et al. 2016). In particular, a component on the east side of the jet (NE' in the paper) is clearly visible in the snapshot of June 11, 2012, i.e. during the first day of H.E.S.S. observations, two days after the detection of a big VHE flare by MAGIC (Borracci et al. 2013).

In X-rays, the brightest event is recorded in the night of June 20-21, 2014 (MJD 56829), but does not show a correspondent maximum at VHE, as might be expected. Given the rapid variability in both energy bands, this could be explained by the non-simultaneity of the two observations (~ 90 minutes delay between them). The TeV flux is roughly constant during this night and is similar to the one recorded on June 12, 2012. On this date, strictly simultaneous X-ray observations show a 55% lower X-ray flux. Assuming an SSC emission model, a quadratic correlation between the two energy bands is expected. Thus, the source should be able to increase its γ -ray emission of almost a factor 4 in ~ 90 minutes. This can be easily achieved thanks to a flux doubling timescale shorter than 10 minutes (see below and Chakraborty et al. 2015). A similar behavior of high X-ray and low γ -ray emission is detected on the night of June 22-23, 2014. In this case the TeV flux roughly doubles in the ~ 2 hours of observations, suggesting a further increase to match the X-ray flux state. The opposite behavior is registered during the TeV flare on June 23-24, 2014 (MJD 56831): the X-ray emission is $\sim 20\%$ lower than the maximum reached three nights before, while the γ -ray flux is ~ 4 times higher.

The high significance allows one to look for very short timescales variability, as well as energy dependent variability. A four minutes interval has been chosen, so that at least $3\sigma/\text{bin}$

can be obtained for the 2012 and 2014 flare datasets (Fig. 7.23). For the latter, the source is detected in every single bin with at least 5σ . A subdivision in two energy bands 2 - 4.5 TeV and above 4.5 TeV is hence possible. The separation energy is defined as the median energy of the photons above 2 TeV. The fractional variability (Vaughan et al. 2003) was calculated on these lightcurves to quantify the flux variations. It is defined as

$$F_{var} = \sqrt{\frac{S^2 - \overline{\sigma_{err}^2}}{\bar{x}^2}} = \sqrt{\sigma_{NXS}^2} \quad \text{with error} \quad \Delta F_{var} = \sqrt{F_{var}^2 + \Delta\sigma_{NXS}^2} - F_{var}. \quad (7.4)$$

The uncertainty is calculated as in Poutanen et al. (2008), which uses Eq. 11 from Vaughan et al. (2003) for $\Delta\sigma_{NXS}^2$, the error on the normalized excess variance:

$$\Delta\sigma_{NXS}^2 = \sqrt{\frac{2}{N} \cdot \left(\frac{\overline{\sigma_{err}^2}}{\bar{x}^2}\right)^2 + \frac{\overline{\sigma_{err}^2}}{N} \cdot \left(\frac{2F_{var}}{\bar{x}}\right)^2}. \quad (7.5)$$

Here, S^2 is the sample variance, \bar{x} the arithmetic mean of the flux, $\overline{\sigma_{err}^2}$ the mean square error and N the number of observations. The results are depicted in Fig. 7.24. The fractional variability strongly varies as function of the dataset, spanning a range between 0.2 and 1.2. As one can expect, the presence of a flare is caused by itself of a large value: for the 2004-2014 dataset $F_{var} = 1.22 \pm 0.02$. Removing the 2014 flare, the fractional variability remains high $F_{var} = 0.78 \pm 0.04$. On the contrary, the variability intrinsic to each flux state is significantly lower: $F_{var}^{2012} = 0.27 \pm 0.06$, $F_{var}^{2014 \text{ flare}} = 0.29 \pm 0.03$, $F_{var}^{2014 \text{ low}} = 0.40 \pm 0.06$. No intra night bursts were detected. Looking at the 2 - 4.5 TeV and > 4.5 TeV energy ranges, one can see that the degree of variability is constant during the 2014 flare ($F_{var}^{2-4.5} = 0.29 \pm 0.05$, $F_{var}^{>4.5} = 0.32 \pm 0.05$) but changes during the 2012 high state ($F_{var}^{2-4.5} = 0.15 \pm 0.10$, $F_{var}^{>4.5} = 0.37 \pm 0.10$). The same is to be seen also for the whole 2014 dataset: $F_{var}^{2-4.5} = 0.87 \pm 0.04$, $F_{var}^{>4.5} = 1.12 \pm 0.04$. This hints towards spectral variability, as it has been found in the previous section.

Given a lightcurve, it is also possible to determine a flux doubling time scale⁵, defined as (following Zhang et al. 1999)

$$T_2^{j,k} = |\overline{\Phi}\Delta T/\Delta\Phi| \quad (7.6)$$

where $\overline{\Phi} = (\Phi_j + \Phi_k)/2$ is the mean flux of the j^{th} and k^{th} bin, and $\Delta T = T_j - T_k$ and $\Delta\Phi = \Phi_j - \Phi_k$ the time and flux difference of such bins, respectively. This method has been applied on the 4-minutes-bin lightcurve ($F > 2$ TeV) between June 19-25, 2014 since it is the largest quasi-continuous and most variable dataset. The error on $T_2^{j,k}$ is calculated propagating the error on the fluxes. The pairs with a relative error larger than 50% are discarded. As anticipated before, the shortest timescale detected is below 10 minutes. The minimal time difference between all the pairs $T_{2,min}$ is 6.5 ± 2.9 minutes, while the average of the five smallest values is $\overline{T}_{2,min} = 6.6 \pm 2.8$ minutes. This method only gives a rough estimate of the variability timescales, because it is not fully robust and is sensitive to the time binning and the sampling. Variabilities with a frequency

⁵This work has been done in collaboration with Nachiketa Chackraborty and is part of a common proceeding (Chackraborty et al. 2015).

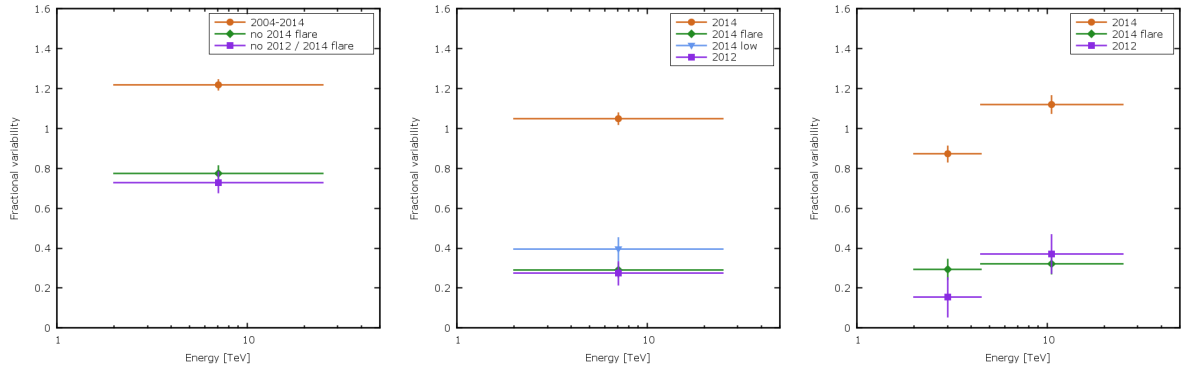


Figure 7.24: Fractional variability for the 4 minutes lightcurves calculated for different energy ranges and data subsets. *Left:* full dataset, without 2014 flare, without 2012 and 2014 flare for fluxes above 2 TeV. It is apparent that the 2014 flare is the cause of a large part of the F_{var} of the dataset. *Middle:* F_{var} for the 2012 and 2014 (all, flare, low) datasets for fluxes above 2 TeV. Again, most of the variability is due to the very different flux states in play. The variability inside of every single dataset is significantly lower. *Right:* same as the previous one, but for fluxes between 2 and 4.5 TeV and above 4.5 TeV. No energy dependence is to be seen during the 2014 flare. For the other datasets, F_{var} increases with energy, hinting towards spectral variability. For 2004 and 2006 it is not possible to derive F_{var} values.

higher than $1/(2 \cdot t_{bin})$ would not be detectable. So far, the observed variability on the few minutes timescale in Mrk 501 (e.g. Albert et al. 2007) was dominated by energies in the hundreds GeV range, well below the threshold taken into consideration here (2 TeV).

The detected variability and its energy dependence suggest that the electron distribution responsible for the γ -ray emission hardens during periods of high flux, increasing its maximal energy. From the doubling flux timescale it is possible to qualitatively derive constraints on the size of the emitting region. Because of causality, it cannot be larger than the light crossing time. One will have $R = c \Delta t \delta$, where δ is the Doppler factor. Now, considering a conservative flux doubling time $\Delta t = 10$ minutes and $\delta = 10$,⁶ one obtains $R = 1.8 \times 10^{14} (\Delta t/10 \text{ min})(\delta/10)$ cm. This value is comparable with the ones found in the literature for the SED modeling of the high states of Mrk 501, which are only a factor of a few larger.

7.8 LORENTZ INVARIANCE VIOLATION (LIV) STUDIES

The exceptional dataset provided by the 2014 flare can be exploited also for studies on fundamental physics. In spite of its low redshift ($z \sim 0.034$), Mrk 501 is a very promising source for Lorentz Invariance Violation (LIV) studies⁷ due to the high flux and high energies reached during the flare. The short scale variability can be used to set constraints on the Quantum Gravity (QG) scale through the search for LIV effects. QG theories predict the space-time to fluctuate on the

⁶This value is commonly used for the SED fit of blazars.

⁷The work on the LIV studies has been done by Agnieszka Jacholkowska and is part of a common proceeding (Cologna et al. 2015a)

Planck time and distance scales. This could affect the propagation of energetic photons, inducing an energy dependent change in the speed of light. Depending on the QM model, two cases exist, the sub-luminal and the superluminal motion, where the high energy photons propagate slower or faster than the low energy ones, respectively. The change in the velocity is given by a linear and a quadratic correction, in case the linear term equals to zero (H.E.S.S. Collaboration et al. 2011):

$$\frac{\Delta c}{c} = -\frac{\Delta E}{M_{QG}} \quad \text{and} \quad \frac{\Delta c}{c} = -\frac{\Delta E^2}{M_{QG}^2}. \quad (7.7)$$

It is hence possible to derive constrains on the QG mass M_{QG} measuring the difference in arrival time of photons at different energies. Since cosmological distances are considered, a correction is needed:

$$\tau_l = \frac{\Delta t}{\Delta E} \approx \frac{1}{M_{QG} H_0} \int_0^z \frac{(1+z') dz'}{\sqrt{\Omega_m (1+z')^3 + \Omega_\Lambda}} \quad (7.8)$$

for the linear case, and

$$\tau_q = \frac{\Delta t}{\Delta E^2} \approx \frac{3}{2M_{QG}^2 H_0} \int_0^z \frac{(1+z')^2 dz'}{\sqrt{\Omega_m (1+z')^3 + \Omega_\Lambda}} \quad (7.9)$$

for the quadratic case. Here, τ_l and τ_q are in s/GeV and s/GeV^2 , H_0 is the Hubble constant, Ω_m the matter density and Ω_Λ the dark energy density⁸. In order to detect the small time delays in play here, a burst or a flaring state is needed, so that it is possible to compare the shape of the lightcurves at different energies and see if they are shifted in time. The better constrains on M_{QG} are then obviously given comparing lightcurves with large difference in the median energy.

In this work, the study of energy dependent time-delays was performed within a deterministic scenario and with a Likelihood method following H.E.S.S. Collaboration et al. (2011). First, a low-energy template lightcurve (2 - 4.5 TeV) is constructed and parameterized. Then, in the likelihood fit procedure the template is injected with photons of energy above 4.5 TeV (~ 500 photons with a negligible background contribution below 0.5%) and is studied with dedicated simulations. Both linear and quadratic cases were considered and no significant time delay was found. One-sided 95% CL lower limits on the QG scale were computed for the sub-luminal and supra-luminal cases, including systematic uncertainties. They are listed in Table 7.12. Sources of uncertainty are the lightcurve template used in the binned fit, the energy calibration, the knowledge of the acceptance corrections and of the smearing factors in energy. The total contribution of the systematic effects was conservatively estimated to be below 100% of the statistical error. Source intrinsic energy-dependent effects that may lead to energy-dependent time lags are also cause of systematic uncertainties, but were not considered in this study.

The results obtained here are one of best constraints on the linear term derived from AGN observations and are comparable with with the PKS 2155-304 ones from the 2006 flare (H.E.S.S. Collaboration et al. 2011). They also are the best limits on the quadratic term obtained so far with both GRB (Vasileiou et al. 2013) and AGN (H.E.S.S. Collaboration et al. 2011) data. This is

⁸The values used here are $H_0 = 70.6 \text{ km s}^{-1} \text{ Mpc}^{-1} = 2.29 \times 10^{-18} \text{ s}^{-1}$, $\Omega_m = 0.3$ and $\Omega_\Lambda = 0.7$.

Table 7.12: One-sided 95% CL QG limits obtained in this work. The limits on the quadratic term are the best derived up to now with both GRB and AGN data. The best constrains found in the literature are also shown for comparison, together with the ones derived for previous flares of Mrk 501.

Limit type	Linear term M_{QG} (GeV)	Quadratic term M_{QG} (GeV)
Sub-luminal	8.5×10^{17}	1.15×10^{11}
Supra-luminal	6.4×10^{17}	1.0×10^{11}
PKS 2155-304 ^a (sub.)	2.1×10^{18}	6.4×10^{10}
GRB 090510 ^b (sub./sup.)	$1.8/3.2 \times 10^{19}$	$4.0/3.0 \times 10^{10}$
Mrk 501 ^c	2.1×10^{17}	2.6×10^{10}

^a H.E.S.S. Collaboration et al. (2011)

^b Vasileiou et al. (2013)

^c MAGIC Collaboration et al. (2008)

mostly due to the exceptional strength of the Mrk 501 2014 flare leading to a high number of photons in the energy range 10 - 20 TeV. Using the data collected for two flares in 2005, MAGIC Collaboration et al. (2008) claimed to have detected a non zero displacement at the 2.5σ level. They did not consider intrinsic source effects, though, and derived lower limits for the linear and quadratic case, which are both less constraining than the ones derived here. They also noted that, if source effects could explain the energy dependent time shift, their limits on M_{QG} would increase. This is fully in agreement with the findings presented here.

7.9 POSITION FIT

Being the first time that Mrk 501 is detected with H.E.S.S., it is interesting to determine how well the position of the γ -ray source matches the radio position (RA(J2000): 16h 53m 52.21668s, Dec(J2000): +39d 45m 36.6089s, Lanyi et al. 2010). For this scope, the skymaps of the 2012 and 2014 observations have been fit with a Likelihood procedure with a point-like source model convolved with the instrument PSF⁹:

$$\mathcal{L}(x, y) = \sum_i L_i \delta(x - x_i) \delta(y - y_i) \quad (7.10)$$

The two datasets were fit separately to avoid possible systematics arising from the fact that the observations were carried out with two different arrays. The good statistics of both samples allows this division. All three available cuts were used. The *Faint* cuts provide better angular resolution, at the expense of the statistics, while the *Loose* cuts are possibly better because of the much higher statistics. This is obviously important for the log-likelihood maximization. Being

⁹The PSF depends on the Zenith and offset angles of the observation and on the photon index of the energy spectrum. It is estimated from simulations and is tabulated in specific tables.

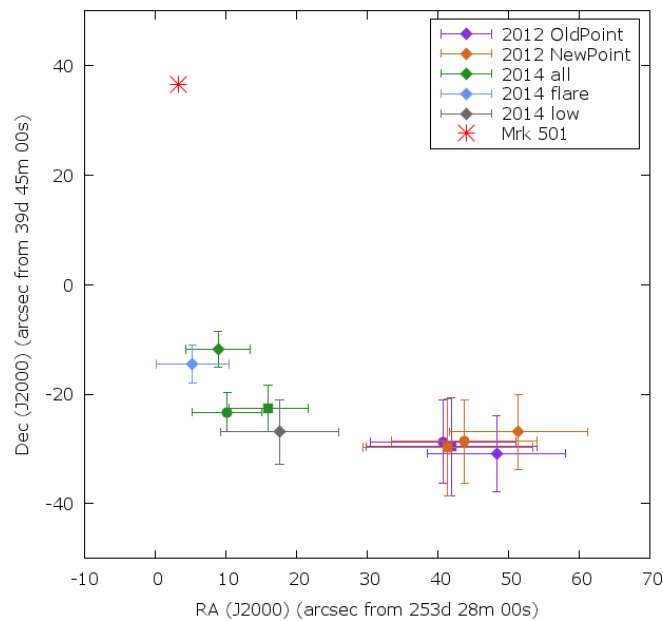


Figure 7.25: Fitted positions for different datasets as described in the text. The errors are 1σ statistical only. The years and subsets are divided by color. To each cut corresponds a different symbol: *Faint* cuts squares, *Loose* cuts diamonds, and *Std* cuts circles.

the source very faint in 2004 and 2006, these dataset have not been used.

For each dataset, the positions derived for the three cuts are all compatible, but none is compatible with the radio position, with distances larger than 1 arcminute. This can clearly be seen in Fig. 7.25 and in Table 7.13. The values are not compatible inside the 3σ error even considering the systematic uncertainties (fixed at 20 arcsec). This disagreement is obviously significantly larger than one would expect. It is probably due to the fact that no source is normally observed at such high Zenith angles, and the telescope pointing is therefore inaccurate. It is known that insufficient pointing corrections were used for some time for the DST calibration. These DSTs were then recalibrated with a better pointing model. In our case, the 2012 DSTs were reproduced, while the 2014 ones used already the corrected pointing model. No difference can be seen for the two pointing models in 2012. Instead, some shift in RA is to be seen between the 2012 and 2014 values, which clump ~ 30 arcsec apart. In the latter dataset, the RA is compatible with the one of the source. The 2014 dataset was divided again in flare and low state. They yield two positions that are almost 16 arcsec apart, with the flare dataset giving a position nearer to the actual source.

Being all the previous analyses done with a fixed position, an offset of one arcminute could be worrisome. Here, nonetheless, the 68% containment radius (c.r.) of the PSF is always smaller than the one used for the on-source regions, hence the possible loss of signal is negligible and does not affect the results.

Table 7.13: Fitted positions. The errors are statistical only. The systematic error is fixed at 20 arcsec. The distance in arcsec is given from the radio position RA(J2000): 16h 53m 52.21668s, Dec(J2000): +39d 45m 36.6089s (Lanyi et al. 2010). The 68% c.r. of the PSF is also given.

Dataset	Cuts	Pointing	RA(J2000)		Dec(J2000)		Distance [arcsec]	PSF 68% c.r. [arcmin]
			253d	28m ss	39d	44m ss		
2012	<i>Faint</i>	Old	41.9	± 12.1	30.4	± 9.0	72.6	4.1
	<i>Std</i>		40.7	± 10.3	31.3	± 7.6	71.4	4.5
	<i>Loose</i>		48.3	± 9.8	29.2	± 6.9	75.8	6.2
2012	<i>Faint</i>	New	41.4	± 12.0	30.3	± 8.9	72.5	4.1
	<i>Std</i>		43.8	± 10.3	31.4	± 7.6	72.3	4.5
	<i>Loose</i>		51.4	± 9.8	33.1	± 6.9	73.5	6.2
2014	<i>Faint</i>	New	16.0	± 5.6	37.4	± 4.2	60.0	3.6
	<i>Std</i>		10.2	± 4.9	36.7	± 3.6	60.1	4.5
	<i>Loose</i>		8.9	± 4.6	48.2	± 3.3	48.6	6.4
flare low	<i>Loose</i>	New	5.3	± 5.2	45.5	± 3.5	51.1	6.2
			17.6	± 8.4	33.1	± 5.9	64.5	6.4

7.10 MONO AND STEREO ANALYSIS WITH CT5

As mentioned in sec. 7.2, the 2014 observations have been carried out with the whole HESS-II array. They were analyzed with a HESS-I style analysis in order to have a telescope homogeneous dataset over all years. In addition, the analysis of HESS-II data has currently some unsolved problematics like the energy intercalibration between subsystems (Chapter 8). This mostly affects the Mono analysis. For the Stereo analysis, there is the additional issue of the incorrect handling of the telescope efficiencies in the spectral analysis: a single efficiency is used for the whole system, whereas CT 5 and CT 1-4 have different values. To overcome the problem, look-up tables with efficiency frozen to the values of January 2014 have been produced. These should yield correct results for data acquired around this period. It is not clear how well they can describe the system status five months later. Nonetheless, keeping in mind these caveats, it can be interesting to test the performances of the HESS-II analysis at very large Zenith angles and to compare the results with the HESS-I ones.

Mono and Stereo analyses have been performed on the 2014 dataset. All the available cuts were tested and the results are reported in Table 7.14, together with those of the HESS-I analysis, for comparison. In all cases, Mrk 501 is detected at very high significance. However, this appears to be due more to a better background rejection than to a higher number of detected photons. Contrary to what one could expect, the addition of CT 5 does not seem to significantly improve the statistics of the source photons, especially in Stereo mode. Comparing the number of events, the Stereo *Loose* cuts analysis is equivalent to the HESS-I *Std* analysis. In reality, only ~60% are

Table 7.14: Counts values for the Mono and Stereo analyses of the 2014 data for the different cuts used. The 2014 HESS-I results are also reported from Table 7.1 for comparison.

Cuts	nON	nOFF	excess	significance	LiveTime (# runs)
HESS-II Mono					
<i>Safe</i>	1666	554	1609	74.3 σ	
<i>Std</i>	1988	899	1894	77.3 σ	8.2 h (18)
<i>Loose</i>	2506	2557	2237	72.7 σ	
HESS-II Stereo					
<i>Std</i>	1242	369	1218	72.6 σ	
<i>Loose</i>	1389	473	1354	73.6 σ	7.7 h (18)
<i>Very-Loose</i>	1988	739	1925	84.1 σ	
HESS-I					
<i>Faint</i>	668	125	661	56.7 σ	
<i>Std</i>	1367	483	1329	71.5 σ	7.7 h (18)
<i>Loose</i>	2100	1436	1964	76.0 σ	

common events, as it will be shown in sec. 8.2. The 40% "missing" photons could partly explain why the addition of CT5 doesn't seem to have the expected effects.

The Mono *Loose* and Stereo *Very-Loose* cuts skymaps and the theta square plots are shown in Fig. 7.26 and 7.27. The maps appear well normalized and both theta square distributions show clear point-like shapes.

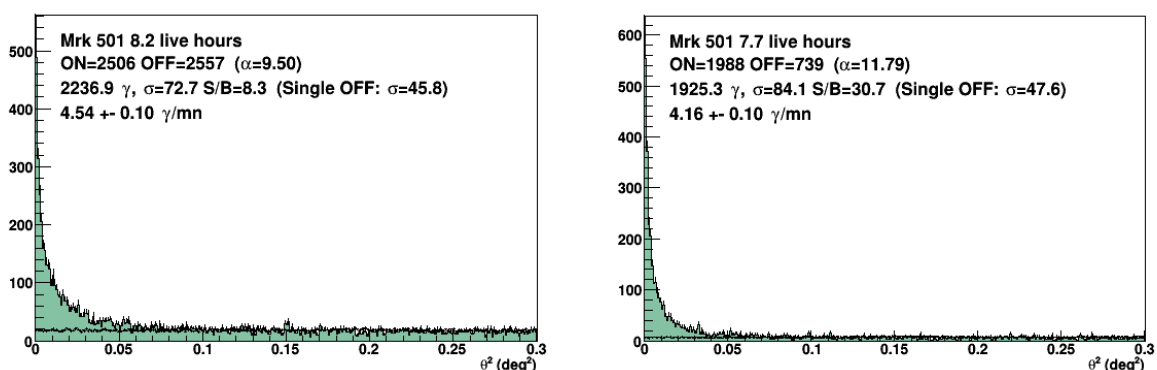


Figure 7.26: *Top:* Theta square distribution for the Mono *Loose* (*left*) and Stereo *Very-Loose* (*right*) analyses. In both cases, the background distribution is well normalized and the signal in the ON region has clearly a point-like shape.

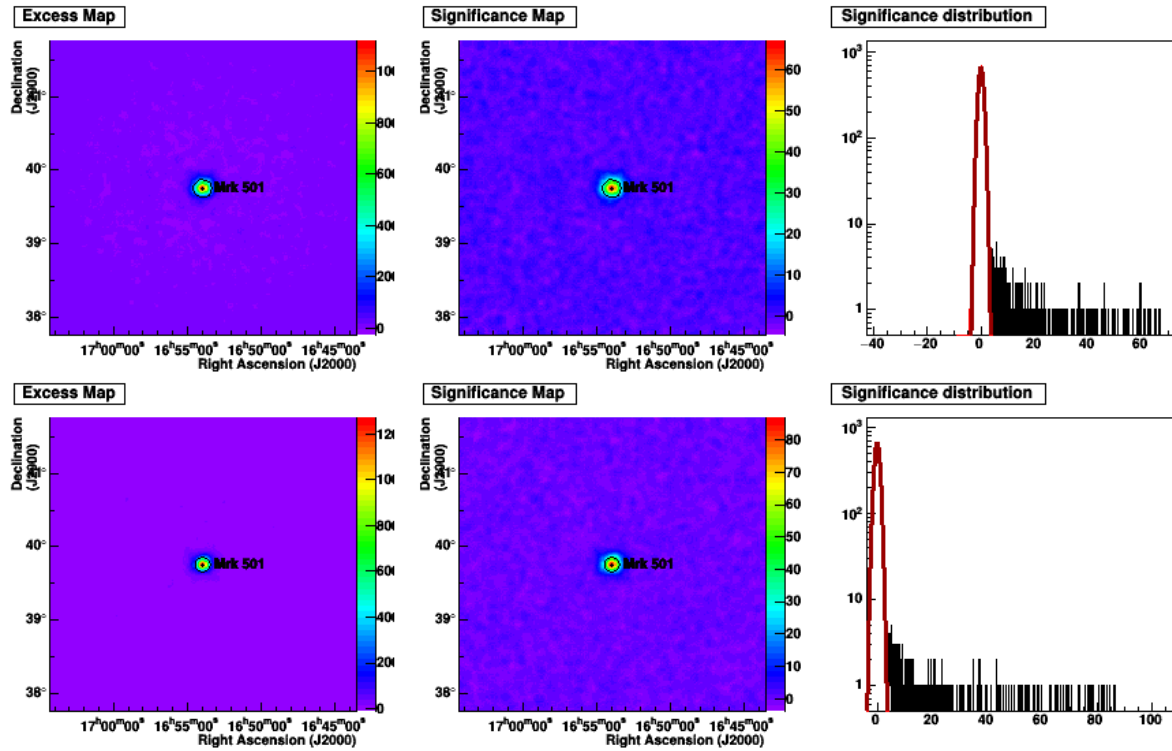


Figure 7.27: Skymaps from the Mono (*top*) and Stereo analyses (*bottom*).

7.10.1 MONO AND STEREO SPECTRA

Spectral analyses have been carried out as described in sec. 7.5. Here, spectra are derived for the Mono *Loose* and the Stereo *VeryLoose* analyses only. The results for the cumulative 2014 dataset, as well as for the flaring and low states are summarized in Table 7.15 and 7.16 and in Fig. 7.28 for Mono and Stereo, respectively. The cumulative 2014 spectra are significantly curved for both analysis, as expected from the HESS-I results. The Stereo data show very significant curvature also for the flaring and low state subsets. On the other hand, the curvature is only marginal in the Mono data. A comparison with the HESS-I results (Tables 7.6 and 7.8) shows that none of the spectra are compatible. In general, the Stereo spectra are harder at low energies and have a stronger curvature. The Mono spectra, instead, are softer with less curvature. The HESS-I spectra match better the Mono shape at low energies and the Stereo shape at high energies. The comparison is shown in Fig. 7.29 for the CPL and ECPL fits. The behavior can be best seen for the fits of the flaring state.

The possible origin of the inconsistencies at both low and high energies has already been outlined in sec. 7.10. An energy bias and an energy dependent ratio between Mono and HESS-I events (sec. 8.2.1) could affect the curvature of the Mono spectra at high energies. On the other hand, the issue with frozen look-up tables for the telescope efficiencies could well explain the too hard Stereo spectrum below 3 TeV. However, these are only hypothesis that at the moment cannot be tested. In addition, the HESS-II spectral analysis as a whole is still not fully understood, as well as its systematics.

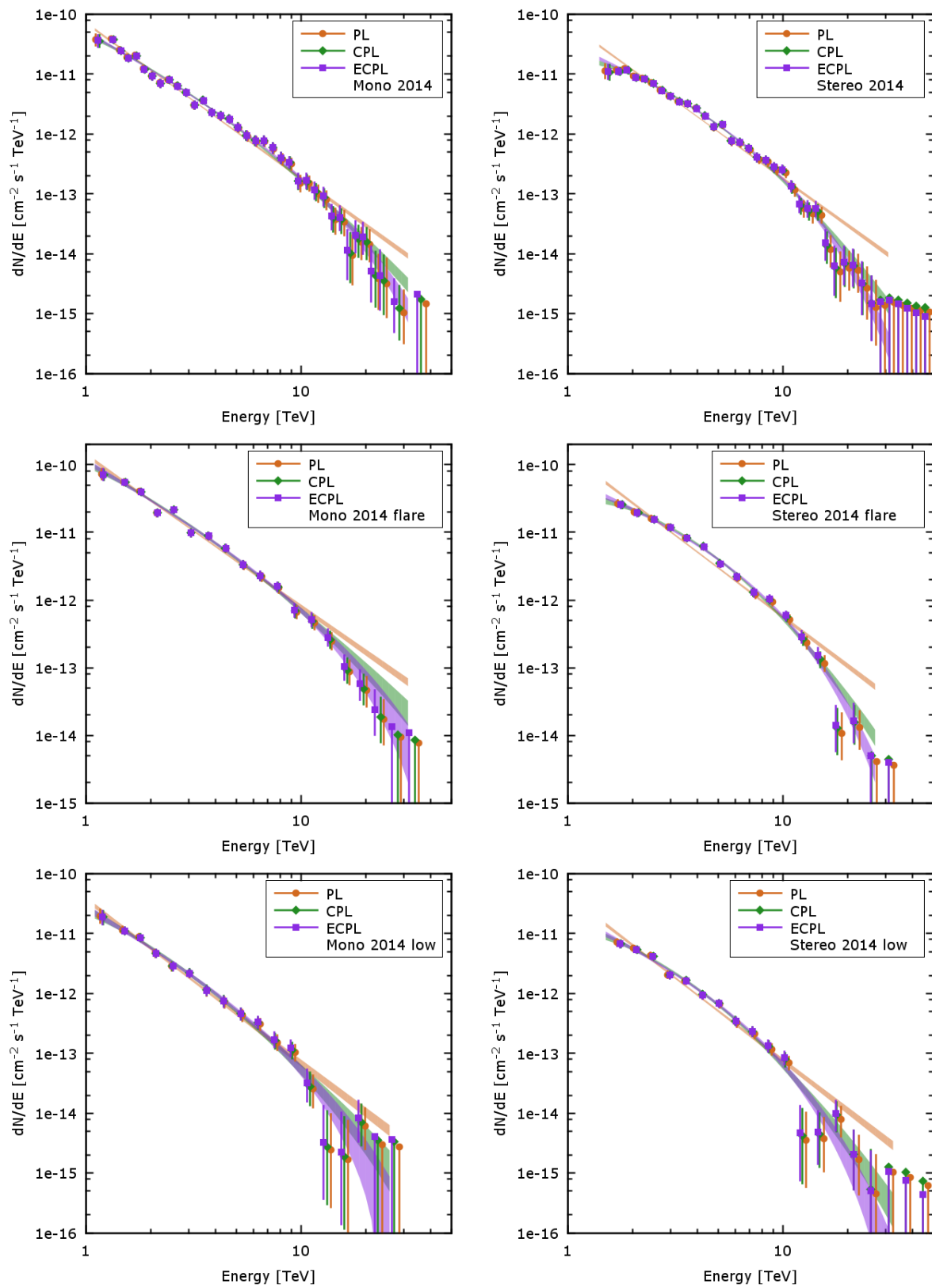


Figure 7.28: Comparison of the three spectral shapes for the Mono (*left*) and Stereo (*right*) spectra for the 2014 cumulative dataset (*top*), the flaring (*middle*) and the low states (*bottom*).

Table 7.15: Spectral results for the 2014 dataset with Mono *Loose* cuts.

Γ	β/E_{cut}	$d\Phi/dE$ (3.5 TeV) [$10^{-12}cm^{-2}s^{-1}TeV^{-1}$]	E_{dec} [TeV]	Energy range [TeV]	$\chi^2/d.o.f.$ (prob)
All					
PL	2.60 ± 0.04	2.76 ± 0.08	2.95		83.9/25 ($3 \cdot 10^{-8}$)
CPL	2.19 ± 0.08	0.30 ± 0.06	3.29 ± 0.13	2.09	1.1 - 31.4 44.7/24 (0.01)
ECPL	1.95 ± 0.11	7.81 ± 1.46	3.26 ± 0.12	2.32	33.5/24 (0.10)
Flare state					
PL	2.24 ± 0.06	8.43 ± 0.29	3.08		25.4/10 (0.01)
CPL	2.00 ± 0.11	0.23 ± 0.09	9.34 ± 0.47	2.14	1.1 - 31.4 17.8/9 (0.04)
ECPL	1.77 ± 0.18	8.93 ± 3.31	9.31 ± 0.45	2.31	17.3/9 (0.04)
Low state					
PL	2.73 ± 0.09	1.23 ± 0.07	2.64		19.0/12 (0.09)
CPL	2.34 ± 0.18	0.36 ± 0.16	1.43 ± 0.11	1.97	1.1 - 25.8 11.3/11 (0.42)
ECPL	1.96 ± 0.31	5.22 ± 2.22	1.45 ± 0.11	2.11	9.0/11 (0.62)

Table 7.16: Spectral results for the 2014 dataset with Stereo *VeryLoose* cuts.

Γ	β/E_{cut}	$d\Phi/dE$ (3.5 TeV) [$10^{-12}cm^{-2}s^{-1}TeV^{-1}$]	E_{dec} [TeV]	Energy range [TeV]	$\chi^2/d.o.f.$ (prob)
All					
PL	2.60 ± 0.04	2.76 ± 0.07	3.44		131/27 ($1 \cdot 10^{-15}$)
CPL	1.97 ± 0.08	0.62 ± 0.07	3.38 ± 0.11	2.84	1.4 - 30.9 29.5/26 (0.29)
ECPL	1.37 ± 0.15	4.42 ± 0.54	3.24 ± 0.10	3.04	24.4/26 (0.55)
Flare state					
PL	2.41 ± 0.05	7.08 ± 0.22	3.92		88.2/10 ($1 \cdot 10^{-14}$)
CPL	1.74 ± 0.10	0.68 ± 0.09	8.85 ± 0.35	2.93	1.5 - 26.8 8.8/9 (0.45)
ECPL	1.08 ± 0.18	4.17 ± 0.58	8.41 ± 0.31	3.12	7.7/9 (0.56)
Low state					
PL	2.76 ± 0.08	1.37 ± 0.06	3.24		50.0/13 ($3 \cdot 10^{-6}$)
CPL	2.14 ± 0.14	0.63 ± 0.14	1.70 ± 0.09	2.65	1.5 - 32.5 18.0/12 (0.12)
ECPL	1.51 ± 0.27	3.95 ± 0.90	1.64 ± 0.08	2.81	16.8/12 (0.16)

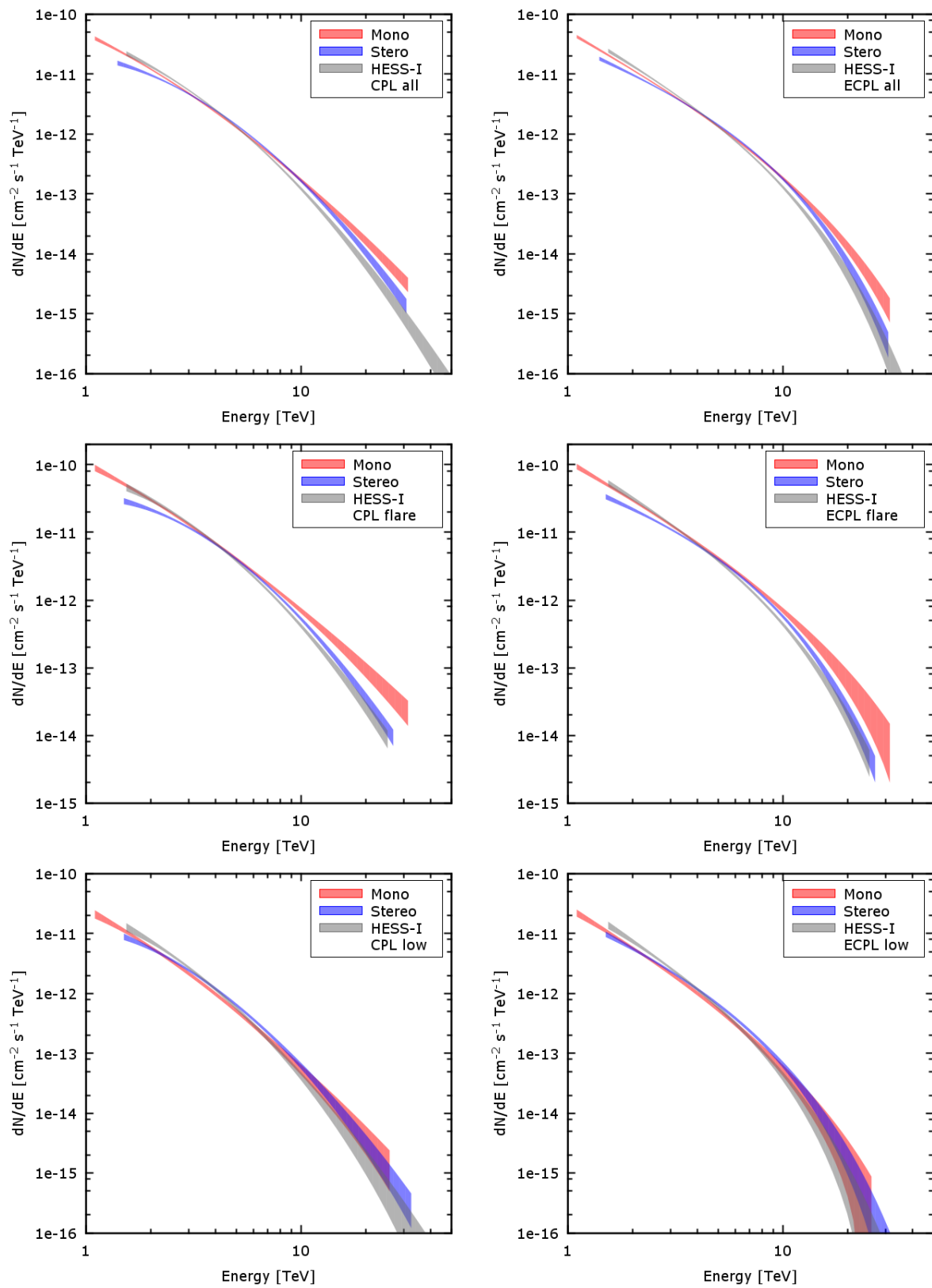


Figure 7.29: Comparison of Mono, Stereo and HESS-I spectra for the three flux states in 2014 and for CPL (*left*) and ECPL (*right*) fits. For sake of clarity, only the spectral contours are shown.

Table 7.17: Spectral results comprising EBL absorption for the 2014 dataset with Mono *Loose* cuts.

	Γ	β/E_{cut}	$d\Phi/dE$ (3.5 TeV) [$10^{-12} cm^{-2} s^{-1} TeV^{-1}$]	E_{dec} [TeV]	Energy range [TeV]	$\chi^2/d.o.f.$ (prob)
Flare state						
PL	1.84 ± 0.06		16.4 ± 0.6	3.09	1.1 - 31.4	18.5/10 (0.05)
CPL	1.90 ± 0.11	-0.06 ± 0.09	16.0 ± 0.8	2.10	1.1 - 31.4	18.1/9 (0.03)
ECPL	1.88 ± 0.19	$inf \pm inf$	15.7 ± 0.8	2.28	1.1 - 31.4	20.3/9 (0.02)
Low state						
PL	2.33 ± 0.09		2.41 ± 0.13	2.95	1.1 - 25.8	7.3/12 (0.84)
CPL	2.28 ± 0.18	0.05 ± 0.16	2.45 ± 0.19	1.93	1.1 - 25.8	7.2/11 (0.78)
ECPL	2.19 ± 0.32	26 ± 58	2.47 ± 0.19	2.08	1.1 - 25.8	7.1/11 (0.80)

7.10.2 MONO AND STEREO SPECTRA WITH EBL ABSORPTION

It has been shown in sec. 7.5.2 how the curvature of the HESS-I spectra is most probably due to EBL absorption only. One can test if the HESS-II data can reveal an intrinsic curvature. Here, only the flaring and the low states are considered, the cumulative dataset is ignored due to the detected spectral variability. The results are summarized in Table 7.17 and 7.18. As for the HESS-I analysis, no significant intrinsic curvature can be detected in all four datasets. An EBL absorbed PL fits the data well in all cases. For the Stereo analyses, some curvature parameters are not consistent with zero, but the overall fits are not significantly better than the absorbed PL ($< 1.5\sigma$). The Mono and Stereo PL spectral indices of the flaring state are marginally compatible inside the $1\text{-}\sigma$ errorbars, but not their normalizations, which differ significantly. The same is valid for the low state, although the difference in the normalization is not so much pronounced. The comparison with the HESS-I results (Table 7.11) shows that the HESS-II intrinsic spectral indices are in general 0.3-0.4 harder. This is expected for the Stereo analysis, which already showed harder observed spectra with a stronger curvature. It is instead surprising for the Mono analysis, which yielded compatible observed spectra up to 5-6 TeV. This could hint towards a too large absorption, as discussed below.

The energy calibration issue mentioned in the previous section can affect the current analysis even more deeply than the previous one. One has to consider that the EBL absorption is energy dependent. If the energy scale is shifted, an incorrect value of the absorption will be used, either too large or too small depending on the direction of the shift, leading to harder or softer intrinsic spectra. In addition, the shape of the EBL density will not match its imprint on the observed absorbed spectra.

An attempt to derive the best EBL normalization as in sec. 7.6 has been carried out also with the HESS-II PL absorbed spectra. Although it is true that in the case of energy bias the results will not be reliable, these could hint towards an excess (or deficit) of absorption. The spectra of the low state have too low and flat TS distributions and are not constraining. The flaring state offers instead better indications, although the errors on the measures are quite large. For Stereo,

Table 7.18: Spectral results comprising EBL absorption for the 2014 dataset with Stereo *VeryLoose* cuts.

	Γ	β/E_{cut}	$d\Phi/dE$ (3.5 TeV) [$10^{-12} cm^{-2} s^{-1} TeV^{-1}$]	E_{dec} [TeV]	Energy range [TeV]	$\chi^2/d.o.f.$ (prob)
Flare state						
PL	1.73 ± 0.06		13.7 ± 0.4	3.92	1.5 - 26.8	11.1/10 (0.35)
CPL	1.63 ± 0.10	0.13 ± 0.09	14.2 ± 0.6	2.85	1.5 - 26.8	9.3/9 (0.41)
ECPL	1.57 ± 0.19	31 ± 34	14.0 ± 0.5	3.06	1.5 - 26.8	10.3/9 (0.33)
Low state						
PL	2.20 ± 0.08		2.66 ± 0.11	3.24	1.5 - 32.5	19.5/13 (0.11)
CPL	2.02 ± 0.15	0.21 ± 0.15	2.83 ± 0.16	2.55	1.5 - 32.5	17.3/12 (0.14)
ECPL	1.82 ± 0.30	11.3 ± 8.4	2.80 ± 0.15	2.72	1.5 - 32.5	17.5/12 (0.13)

one derives $\alpha_{Stereo} \sim 1.1 \pm 0.15$, for Mono $\alpha_{Mono} \sim 0.7 \pm 0.25$. Hence, the Stereo spectra yield a normalization compatible with the model of FR08, as also found with HESS-I, while the Mono spectra seem to indicate a too large absorption. This is in line with a larger bias found for the Mono analysis in sec. 8.2.1. A support to this hypothesis comes by running the test again using an EBL model scaled to higher energies by 18%¹⁰. Both TS distributions are slightly broader and are shifted to larger normalization values, but with similar TS maxima as for the non-scaled cases. They peak at $\alpha_{Stereo}^{shifted} \sim 1.6 \pm 0.2$ and $\alpha_{Mono}^{shifted} \sim 1.1 \pm 0.4$. Keeping the un-scaled FR08 model as the correct one (as suggested in sec. 7.6) the new Stereo result implies that the energy scale in the spectrum is correct, and hence that a 15-20% bias is accounted for in the spectral analysis. Again, the harder spectra with respect to HESS-I can be caused by the incorrect spectral tables. For the Mono case, the large statistical errors make the two results compatible, although the 0.4 shift of the peak. However, this trend and the larger bias for the Mono energies suggest that the latter is not completely taken into account in the Mono spectral analysis, leading to a harder intrinsic spectrum caused by a too large de-absorption.

7.11 LIGHTCURVE COMPARISON

In Fig. 7.30 the lightcurves from the three analyses are compared. Three time binnings are used: nightwise, runwise and 240 s slices (the last one for the flare night only). The lightcurves have been generated using the average ECPL spectrum derived in the spectral analysis. The HESS-I and Stereo points match fairly well at low fluxes, but show significant discrepancies at higher values. The Mono lightcurves systematically underestimate the emission, in most cases significantly. These differences are probably due to unknown systematics in the new HESS-II analysis and to the issues discussed above for the spectral reconstruction (energy bias and fixed look-up

¹⁰Being the HESS-II energies larger than the HESS-I energies, the absorption values ought to be shifted to higher energies, as well.

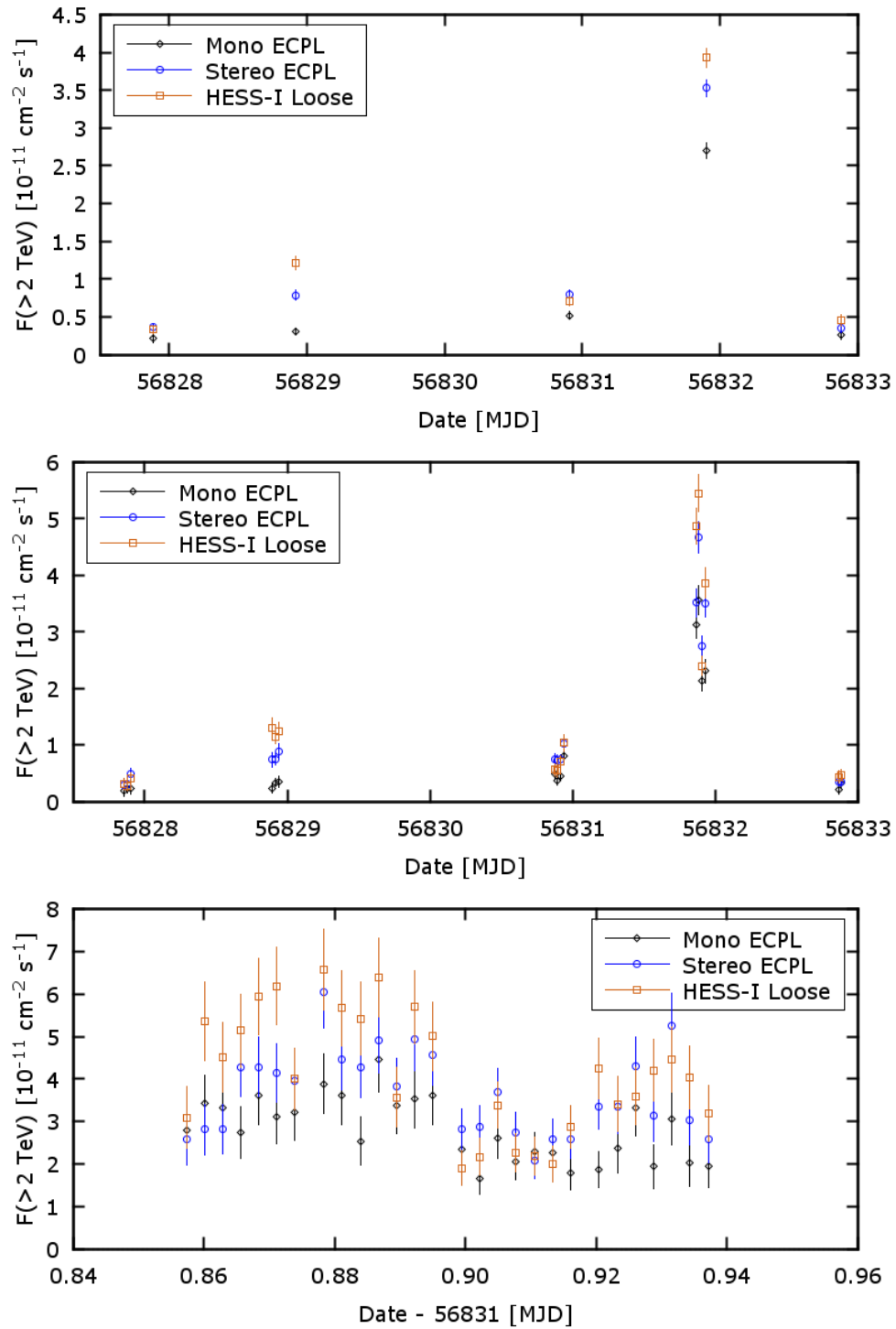


Figure 7.30: Comparison of the 2014 lightcurves for the Mono, Stereo and HESS-I analyses. *Top*nightwise; *middle*runwise; *bottom*zoom-in of the flaring state in slices of 240 s.

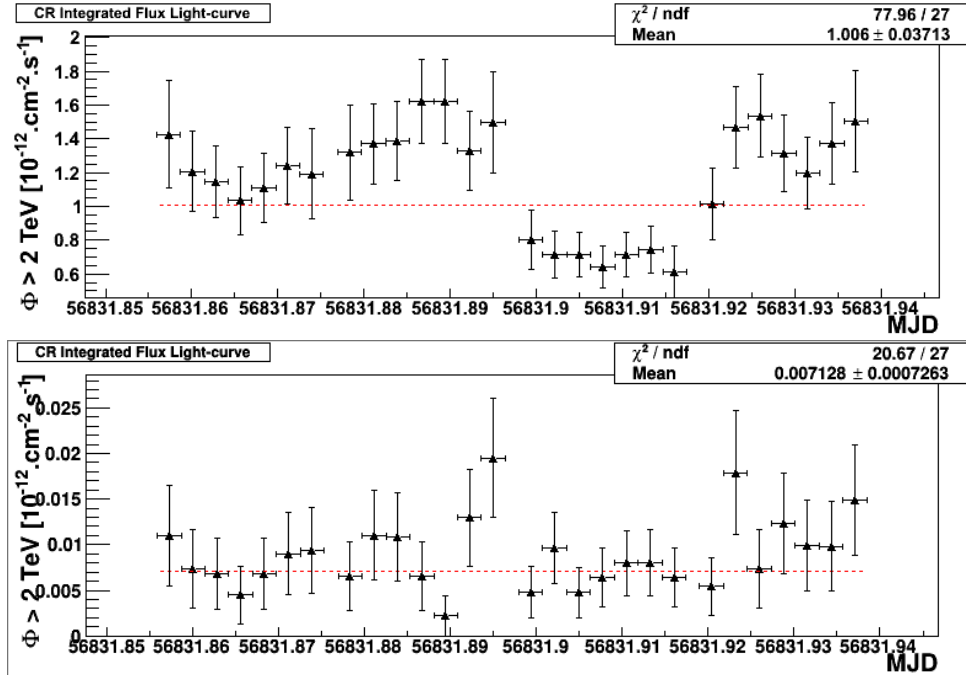


Figure 7.31: CR lightcurves for the 2014 flare in 240 s bins. *Top:* HESS-I, *bottom:* Stereo. The significantly different flux values are a byproduct of different background rejection efficiencies, different cuts, and the improper use of photon effective areas to calculate CR fluxes.

tables). Again, the HESS-II analysis does not seem reliable for the Mrk 501 data. However, the similar evolution of the lightcurves is reassuring and could indicate only a scaling problem. This is visible on a runwise basis and in some features of the 240 s bin lightcurve (middle and bottom panels of Fig. 7.30). An example in the short time binned lightcurve is the third run, between date 0.90 and 0.92: the flux is rather constant for all three sub-arrays, but all show a small increase in the third slice. The behavior seems to differ, instead, between the first two runs (date 0.86 to 0.90). Here, the very small number of OFF events in the HESS-II datasets could contribute to the difference because of statistical fluctuations.

The flux ratio between the reconstruction chains varies on a runwise basis. The HESS-II lightcurves show a less accentuated variability, as well. This can in principle shade some doubts on the accuracy of the results derived with HESS-I, which would have important consequences. For example, a less strong variability during the flare would lower the Quantum Gravity limits derived in sec. 7.8. Its absence would prevent their calculation at all.

The different flux ratios are most probably due to effective area corrections only. Calculating the mean effective areas for HESS-I from flux, excess and livetime of each run, one sees that their values vary as function of the Zenith angle, as expected. While the first, second and fourth runs have similar areas, the third's is 45% larger. The effect can be seen in the top panel of Fig. 7.31, where the HESS-I CR background lightcurve is shown. The CR flux is expected to be constant or to vary because of changing atmospheric conditions. A step like the one visible here could be caused only by a sudden appearance of thick clouds, but no clouds were present

during the observation. The same step is almost invisible in the Stereo CR 240 s bin lightcurve (Fig. 7.31, *bottom*¹¹), although, when plotted runwise a small step is visible as well. This suggests that the feature could be due to a possible too large effective area used. One has to note, however, that for the CR lightcurve the effective area of the third run is 60% larger than in the other runs, whereas the difference is 45% for the γ -ray lightcurve. Therefore, the step appears here more pronounced. In addition, there is a 35% increase also for the third run in both Stereo γ -ray and CR lightcurves. The actual difference in the increase of the average effective areas is of the order of 10% and cannot account for the flux differences of the γ -ray lightcurves.

The large jump in the values of the effective area as function of the Zenith angle is also due to the different positions of the OFF regions in the sky with respect to the ON region, as a consequence of the wobble observations. An example is shown in the top panel of Fig. 7.32 for the 2014 flare night. In the third run, all OFF regions lie above the source at smaller Zenith angles, which implies larger average effective areas. The mean Zenith angle of the observation is shown in the middle panel of Fig. 7.32, for the 240 s lightcurve. The three analysis chains are compared and agree very well. The flux differences are not explained by an incorrect determination of the Zenith angle.

For observations at large Zenith angles like for Mrk 501, small differences in the altitude lead to significant variations in the effective area. The Zenith angle must therefore be calculated properly for every ON and OFF region at every given time, i.e. practically on an event-by-event basis. This is done differently in the HESS-I and HESS-II analyses. One can check possible different dependencies on the Zenith angle position plotting the ratio of the Stereo and HESS-I fluxes as function of the distance in Zenith angle between the source and the mean Zenith angle of the observation. The result is shown in the bottom plot of Fig. 7.32 for the whole 2014 240 s lightcurve. No dependence can be seen.

¹¹Here, only the shape of the lightcurves is important. The significantly different flux values are a byproduct of different background rejection efficiencies, different cuts, and the improper use of photon effective areas to calculate CR fluxes.

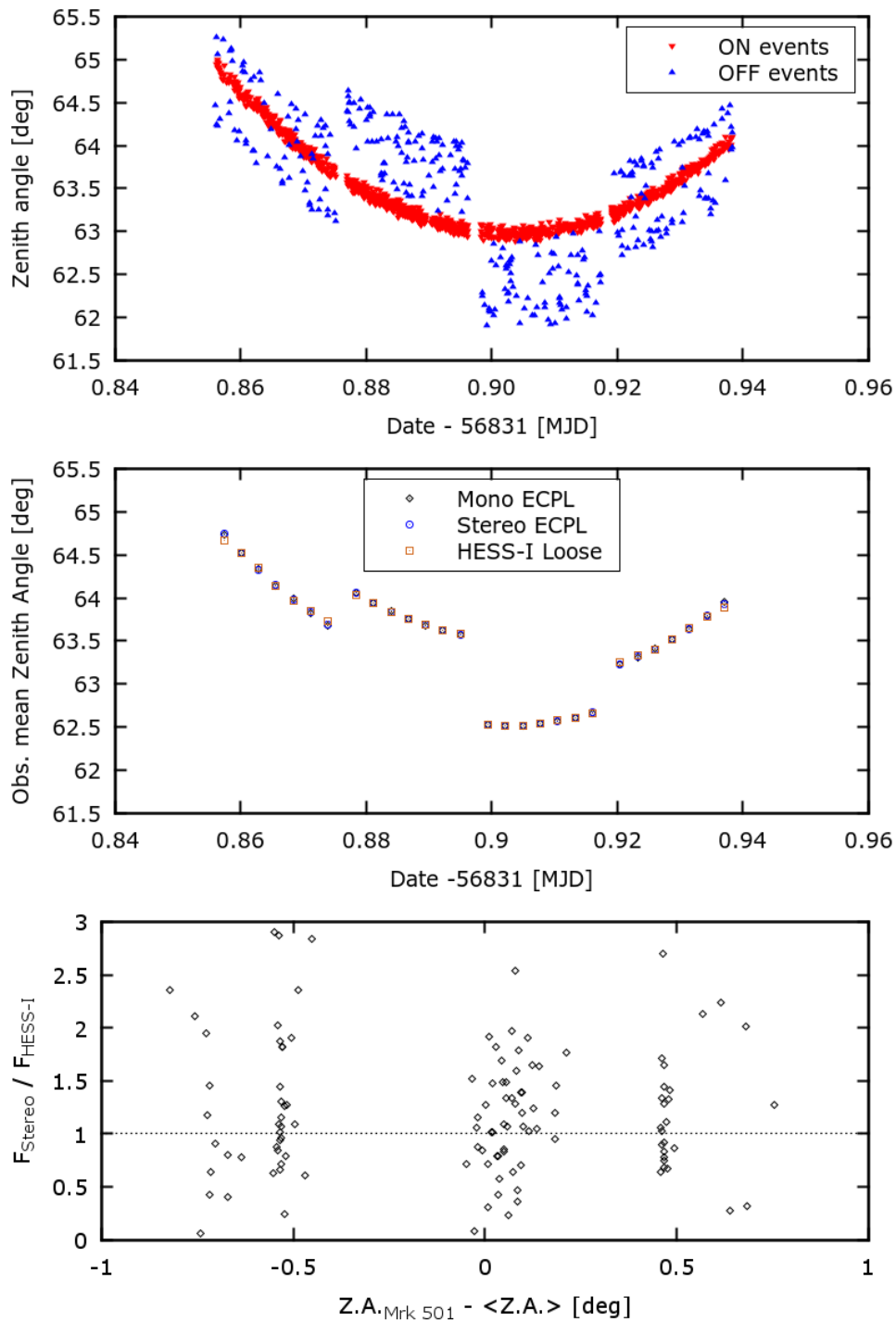


Figure 7.32: *Top:* Zenith angle distribution of the ON (red) and OFF (blues) events of the 2014 flare night for the HESS-I analysis. *Middle:* comparison of the mean Zenith angle of the FoV for the 2014 flare in 240 s slices. *Bottom:* ratio of the Stereo and HESS-I fluxes as function of the difference of the Zenith angle of Mrk 501 and the mean Zenith angle of the FoV.

7.12 CONCLUSIONS

In this chapter, H.E.S.S. observations of Mrk 501 between 2004 and 2014 have been presented in a MWL context. Flux and spectral variability have been detected in the X-ray and γ -ray bands. In particular, harder spectra are found in correspondence of high fluxes, confirming what has been reported in the literature. The novelty of this study resides in the combination of high energies and short timescales reached in the VHE observations.

A flaring state compatible with the 1997 historical maximum has been observed in June 2014. Rapid variability with flux doubling timescales as short as few minutes has been detected for the first time in the 2 - 20 TeV energy range. The fractional variability calculated on two energy subsets shows that Mrk 501 is more variable at high energies. This suggests that the electron distribution responsible for the γ -ray emission hardens during periods of high emission, increasing its maximal energy. From the doubling flux timescale one can derive constraints on the size of the emission region. Because of causality, it cannot be larger than the light crossing time. For $\Delta t = 10$ min and a Doppler factor $\delta = 10$ one derives $R = 1.8 \times 10^{14} (\Delta t/10 \text{ min})(\delta/10)$ cm. In the literature, values of a factor of a few larger are used for the SED modeling of high states.

The comparison of the VHE lightcurve with the X-ray and optical lightcurves show no direct relation. The different behavior at X-ray energies can in principle be explained by the time offset (typically 90 min) between the observations in the two bands. This would imply the capability of the source to increase its γ -ray flux of a factor of about four in this period. Instead, the optical emission clearly does not correlate with the VHE flux. The source is in optical low state in the strictly simultaneous observations during the 2014 flare, while its flux is significantly higher during the TeV low states in 2004 and 2006. This suggests the presence of at least two zones or mechanisms able to produce flaring events in this source. This hypothesis is supported by the discovery at radio wavelengths of off-axis jet components, one of which is clearly visible during the 2012 VHE high state.

The TeV spectra are hard during periods of high flux, and softer otherwise. The curvature in the observed spectra is due to EBL absorption only and the intrinsic spectra are well described by a simple PL. In particular, during the 2014 flare night the hard simple PL spectrum extends above 20 TeV, indicating the absence of Klein-Nishina suppression at these high energies. The treatment of the emission in the Thomson limit is unlikely. The emission is more easily explained in the Klein-Nishina limit. It is possible to determine the minimum value of $\gamma_{e,max}$ from the highest observed energy in the H.E.S.S. spectrum: $\gamma_{e,max} = 4 \times 10^6 (10/\delta)$. The absence of a detectable cut-off, however, implies that the underlying electron energy distribution must reach significantly larger γ_e . From the combination of the maximal synchrotron and IC energies, it is possible to constrain the magnetic field of the emission region: $B \sim 0.075 (\delta/10)(E_{syn}^{max}/200 \text{ keV})(20 \text{ TeV}/E_{IC}^{max})^2$ G. The values derived here are in the range of values used in the literature in more precise SED fitting.

Studies on the EBL intensity exclude the hypothesis of a non-existent EBL at the 9.6σ level. The normalization factors are derived from several datasets and are all consistent with the model of FR08: $\alpha_{all} = 0.99 \pm 0.15$, $\alpha_{2012+2014}^{flare} = 0.91_{-0.15}^{+0.16}$, $\alpha_{2014}^{flare} = 0.90_{-0.17}^{+0.20}$. The result supports a low EBL intensity between $2.4 \mu\text{m}$ and $30 \mu\text{m}$.

The exceptional flaring event permitted the derivation of limits on the QM scale. The quadratic limits of 1.15×10^{11} GeV are the best derived up to now from GRB and AGN observations.

For the technical results, it has been shown how the pointing model of the H.E.S.S. array is not precise at the large Zenith angles of Mrk 501. Its fitted position is 1 arcmin away from the nominal radio position. In addition, it has been shown how the Mono and Stereo analysis are currently not reliable for this study.

CHAPTER 8

SYSTEMATIC STUDIES: HESS-I VS HESS-II COMPARISON

The initial test analysis of the 2014 Mrk 501 observations yielded remarkable results. The spectra reached up to 30 TeV, which was unexpected due to the large EBL optical depth at those energies. The CT 5 Mono analysis showed spectra that reached the same energies as the HESS-I analysis, and actually seemed to outperform the small telescopes at the highest energies. This was completely unexpected for an instrument with a much smaller effective area and a lower sensitivity above a few TeV. The large Zenith angle of the observations was also considered critical, because the shower images are very elongated in this case. Since the FoV of the CT 5 camera is smaller than for HESS-I, a higher number of truncated (and therefore rejected) images was expected.

For the first time in Cherenkov astronomy, thanks to the different HESS sub-arrays, it was possible to cross check the results of the same observation using two facilities with independent calibrations. Therefore, it was decided to compare event by event the photon-lists reconstructed with the Mono and HESS-I analyses, in order to test if the respective energies are consistent within the uncertainties of the two instruments. In a second step, also the Stereo analysis was compared. The findings are described in this chapter.

8.1 COMPARISON WITH ORIGINAL DATA CALIBRATION AND CUTS

The first comparison has been made with a precedent DST production and software version for the HESS-II analysis than the one used in the previous chapters. Here, the Prod4 DSTs and paris-0-8-28 software have been used. Only the *Std* cuts were applied because at the time they were the only reliable ones for the HESS-II analysis.

In the whole chapter, the photon lists are obtained using the *Reflected Region Background* model (sec. 4.7.1). The photons falling in the ON-source region (ON region) will be called ON

photons (or events), those falling in an OFF-source region (OFF region) will be called OFF photons (or events). The size of the ON and OFF regions changes depending on the analysis, and all the regions are on a circle around the camera center. Therefore, the number of OFF regions varies with the analysis as well, and they cover different areas in the sky. For this reason, it is not possible to directly compare the number of OFF events of two different analyses.

When considering photons from the whole FoV, the ON events will remain the same, since the ON region is not modified. All other events will be OFF events. Also in this case, a direct comparison of the number of photons is not possible because of the different sizes of the FoV of the sub-arrays. However, the OFF regions of the *Reflected Region Background* model are obviously completely included.

8.1.1 MRK 501

First of all, the photon lists were retrieved from the Mono and HESS-I standard analyses of Mrk 501. Because of different selection criteria at the time of this study, the dataset passing the run selection for CT5 is smaller than the one of HESS-I. Specifically, the runs of the second low state night are discarded. The HESS-I photon list has been adjusted accordingly: it contains 1651 γ -like events, 1216 of which ON photons and 435 OFF photons. The Mono list contains 12243 events, 5156 ON and 7087 OFF. The photons in common between the two lists have been selected comparing their timestamps in MJD. These timestamps have a lower precision than the actual event-time, but are good enough for the sampling rates of the HESS-I and HESS-II cameras. Considering that the sampling rates differ by a factor of 10 and that most of the recorded events are hadron-like and are rejected by the cuts, the chance of comparing two different events because of a low timestamp resolution is estimated to be smaller than 1%.

Due to the much larger number of events in the Mono list, as a first order approximation one would expect that all HESS-I ON photons will be contained in it. However, the ON region is defined as the 68% containment radius, so that it is likely that some HESS-I ON events are spread outside the Mono ON region. In addition, one has to take into account the energy distribution of the events, since it is possible that the ensemble at high energies is smaller for Mono than for HESS-I.

The first most notable result of the comparison is that only around 40% of the HESS-I ON photons actually find a correspondence in the Mono sample. 60% are hence not recognized as γ -like events (Fig. 8.1). The second result is the discovery of a systematic shift in the energy reconstruction: the reconstructed Mono energies are on average more than 20% higher with respect to those of the same photons in HESS-I (Fig. 8.2, *left*). These discrepancies could have in principle a rather simple explanation: the observations were taken at Zenith angles that have never been tested before. Therefore, on the one hand, it would not be surprising if the PSF of CT5 would rapidly degrade, requiring a significantly larger extraction region to retrieve the missing photons. On the other hand, it could well be that the energy reconstruction worsens with the Zenith angle, as well, especially at higher energies. To test the first hypothesis, a Mono analysis with a larger ON region was carried out, while to test the second one, other two sources were analyzed at different Zenith angles: PKS 2155-304 and the Crab Nebula.

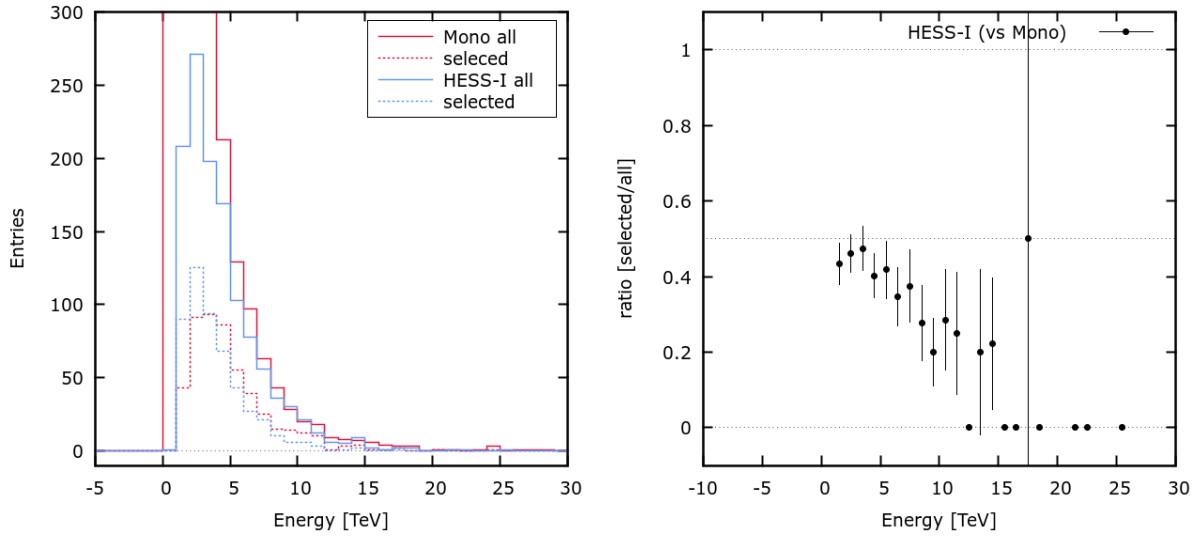


Figure 8.1: *Left:* Energy distributions of the total number of γ -like events (*all*) and the number of events in common between the two samples (*selected*) for the HESS-I and Mono analyses of Mrk 501. The distributions are derived from the comparison of the ON regions only. Comparing the two *all* histograms, one would expect a matching ratio close to 1, which is not the case. From the *selected* histograms it is apparent that the Mono dataset samples higher energies. *Right:* matching ratio as function of the energy. A clear decrease is apparent.

The increase of the ON region size of a factor of 3 (from 0.03 to 0.1 deg²) did not provide the missing photons as expected. Only 5% more photons are found, while 55% are still missing. One can then look for matches among the γ -like events in the whole Mono FoV. Again, just a bunch more HESS-I ON events find a counterpart, and, despite the HESS-I OFF regions being in this case fully contained in the Mono FoV, less than 10% of the OFF events are found in both samples. One can wonder if a large part of HESS-I photons are reconstructed as hadrons in the Mono analysis. This is the case only for less than 10% of the HESS-I ON photons. The same is valid the other way around: almost the same number of Mono ON photons are hadron-like for HESS-I. In some cases, one ON event correlates with one OFF event. Most of the time, the angular distance between them is significantly larger than expected from the angular resolution. Therefore, either these events are very poorly reconstructed, or they are two different events that share the same timestamp.

In total, we can account for about 50% of the HESS-I ON events being detected in Mono as well. The rest is possibly rejected by the different cuts of the Mono analysis at a much earlier stage, so that they do not even appear as hadron-like events. From the right plot of Fig. 8.1 it is also apparent that the ratio of the selected events is energy dependent. This is not completely unexpected, since at large Zenith angles higher energies imply larger and more elongated shower images. Since the CT5 camera has a smaller FoV than HESS-I, this leads to an higher fraction of truncated showers, which are then rejected or misreconstructed.

As it appears clear from the top-left plot in Fig. 8.2, there is a systematic bias between the

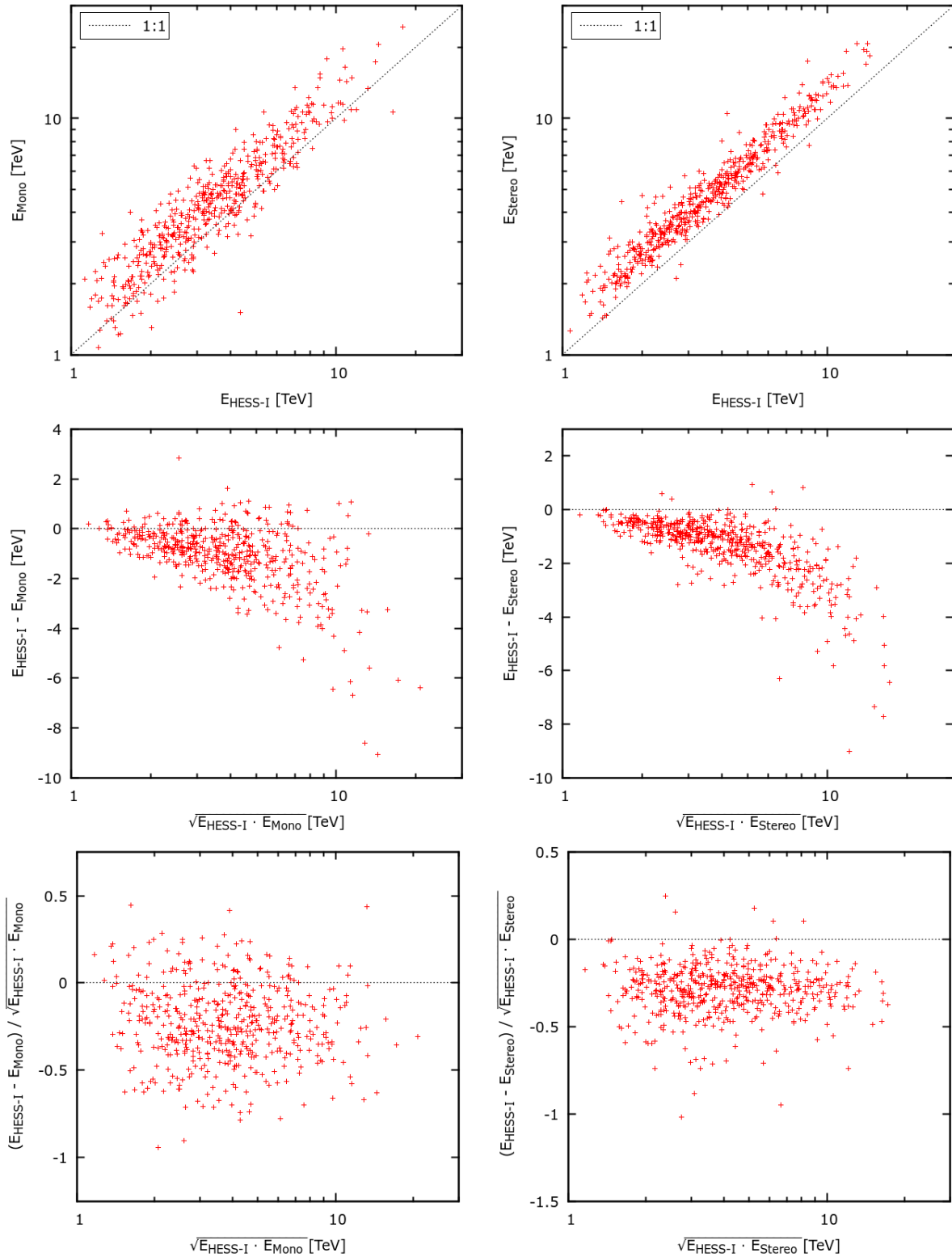


Figure 8.2: Comparisons of the common γ -like events of Mrk 501 between HESS-I and Mono (*left*) or Stereo (*right*). *Top:* energy comparison. A systematic shift towards higher Mono energies with mean value of $28 \pm 1\%$ is to be seen. The bias slightly decreases with increasing energy. The bias for the Stereo dataset is larger, with a median value of $33 \pm 1\%$. *Middle:* photon energy difference as function of the photons mean energy. The increase of the spread of the distribution with energy is expected, but it should be centered around zero. Here, the deviation from zero increases with increasing energy as well. *Bottom:* Same as above, but the energy difference is weighted by the mean photon energy. The distribution is flat, but centered around $-21 \pm 1\%$ (Mono) and $-28 \pm 1\%$ (Stereo). The Stereo distributions are more compact.

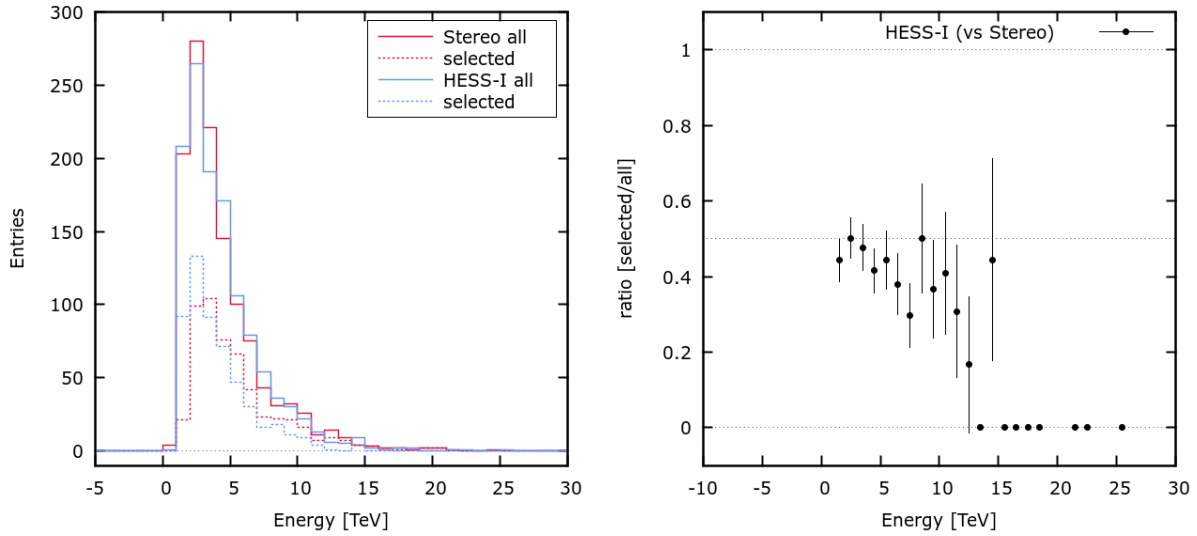


Figure 8.3: Same as in Fig. 8.1 but for the Stereo analysis. *Left:* comparing the two *all* histograms, a matching ratio of at least 0.8 is expected, which is not the case. From the *selected* histograms it is apparent that the Stereo dataset samples higher energies. *Right:* the matching ratio is flatter against energy than for Mono.

Mono and HESS-I energies. The bias has been estimated via linear fits of the $E_{\text{HESS-II}}$ vs $E_{\text{HESS-I}}$ plots (both linear- and log-scale) and calculating the mean values of the $E_{\text{HESS-II}}/E_{\text{HESS-I}}$ distributions. In addition, mean values have been calculated also for the distributions derived in six energy bins, which were determined dividing equally the total number of events. The linear parametrization has the form $y = a + bx$ for the linear-scale plots and $\log y = A + B \log x$ for the log-scale plots. For no bias, one expects $a = A = 0$ and $b = B = 1$. For a purely multiplicative bias¹, one expects $a = 0$, $b \neq 1$, corresponding to $A \neq 0$, $B = 1$.

The Mono energies are higher than the HESS-I energies by a mean value $E_{\text{Mono}}/E_{\text{HESS-I}} - 1 = 28 \pm 1\%$. The bias slightly decreases in bins with increasing energy (from $35 \pm 4\%$ to $21 \pm 3\%$). This is also seen in the fit of the E_{Mono} vs $E_{\text{HESS-I}}$ linear plot, for which a is significantly different from zero and the b is smaller than the mean value of the $E_{\text{Mono}}/E_{\text{HESS-I}}$ distribution (this corresponds to $B < 1$ for the fit of the log-log plot). Since no safe energy threshold has been considered in this study, it is possible that it could be responsible for the larger median value of the offset at low energies. The energy difference and scaled energy difference plots (Fig. 8.2, *middle-left* and *bottom-left*, respectively) show the same characteristics in a different representation: the distributions are not centered around zero as it is expected for no bias. In the middle-left plot, it is foreseen that the spread increases with energy because the energy resolution is a multiplicative factor. However, here the deviation from zero increases with energy, as well. The bottom-left plot shows a bias of $-21 \pm 1\%$ of the mean energy.

¹The bias is actually defined as a multiplicative factor, whereas the offset is an additive factor. In this chapter, these two terms are improperly used as synonyms because in general the energy difference cannot be described with only one of them, and to avoid too many repetition in the text.

In order to understand if the issues shown in the Mono results are due to the larger uncertainties deriving from the lack of stereoscopy and possibly to an analysis calibrated for low energies, the same comparison as above has been done for the Stereo analysis. It yields 1486 events, 1212 ON and 274 OFF. The number of common ON events between the Stereo and HESS-I analyses is 44% (Fig. 8.3), similar to the Mono case. In this case, the ON region size is the same for both analyses (0.01 deg^2). Because of the similar angular resolution and the involvement of the same telescopes, one does not expect a large fraction of γ -like events to fall outside the tested regions. 8% of the HESS-I ON events are found outside the Stereo ON region. Again, almost 50% of the photons are missing. They must therefore be ascribed either to the impossibility to reconstruct the same events, or to the different cuts used in the Stereo mode.

The issue with the energy bias is unsolved, as well. One can see on the right side of Fig. 8.2 that the energy distributions are more compact, but also that the bias is even larger than for the Mono analysis. The larger compactness is due to the better energy resolution achievable in Stereo mode. The mean offset is $E_{\text{Stereo}}/E_{\text{HESS-I}} - 1 = 33 \pm 1\%$ and the bias of the weighted energy difference is $-28 \pm 1\%$ of the mean energy.

8.1.2 CRAB NEBULA

As mentioned in the previous section, the Mrk 501 observations were taken at Zenith angles never tested before. There is therefore the question, whether or not large Zenith angles could be related to the energy bias or to the missing events. The Crab Nebula and PKS 2155-304 have been analyzed in order to test if the effects discovered for Mrk 501 still exist at lower Zenith angles in two complementary ranges.

The Crab Nebula runlist comprises 41 good quality runs collected between September 2013 and beginning of January 2014. Because of DST availability at the time of the analysis, only 33 of them were used.

As for Mrk 501, only 40% of the 4177 HESS-I ON events find a counterpart among the 12721 Mono ON photons, with a strong energy dependence (Fig. 8.4). The ratio increases to 49% when searching for matching photons in the whole Mono FoV. The fact that 9% of the events have a match outside the Mono ON region can be explained by the broad tail of the Mono PSF for this analysis (Fig. 8.5, *left*). Only 27% of the 1585 HESS-I OFF events are found in the Mono FoV. 6% of the HESS-I ON events were reconstructed as hadrons in Mono. We are facing a photon "loss" of around 50% also for the Crab Nebula.

Concerning the energy comparison (Fig. 8.6, *left*), the bias is reduced with respect to the one seen for Mrk 501. The mean value $E_{\text{Mono}}/E_{\text{HESS-I}} - 1 = 6 \pm 1\%$. Larger biases are to be seen at low energies ($10 \pm 2\%$), possibly because some events below the safe energy threshold of HESS-I are considered. The fit to the scaled energy difference has a negative slope, which indicates that the bias of the Mono energies increases with energy. This seems to be in agreement with a worsening of the accuracy of the Mono energy reconstruction at high energies and would support a Zenith angle dependence of the energy bias.

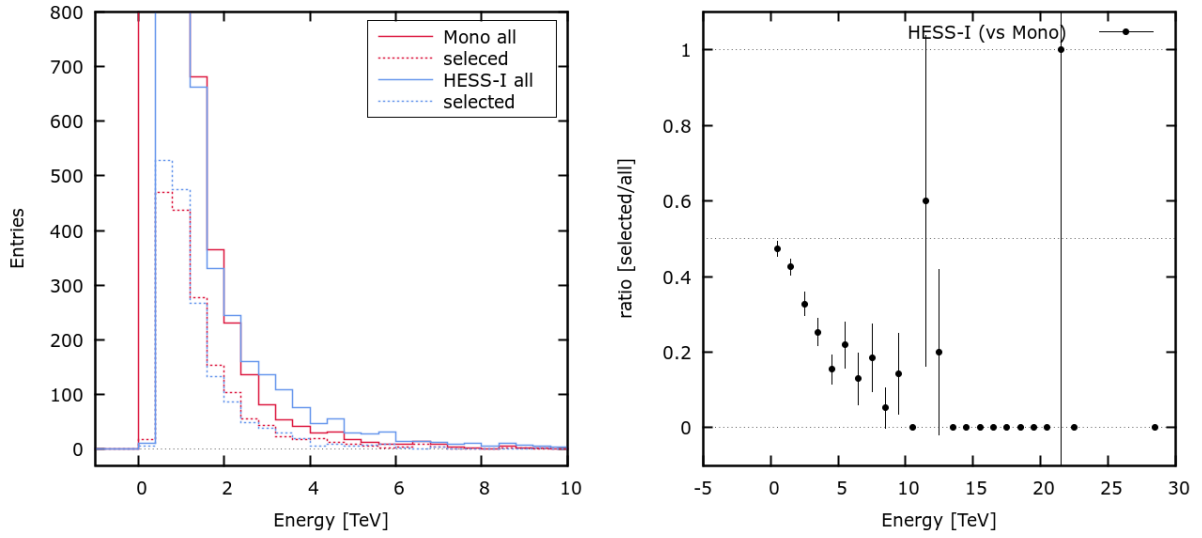


Figure 8.4: Same as in Fig. 8.1 but for the Crab Nebula. *Left:* comparing the two *all* histograms, a matching ratio of 0.5 also above 3 TeV is expected, which is not the case. From the *selected* histograms it is apparent that the Mono dataset samples higher energies. *Right:* the matching ratio rapidly decreases with energy.

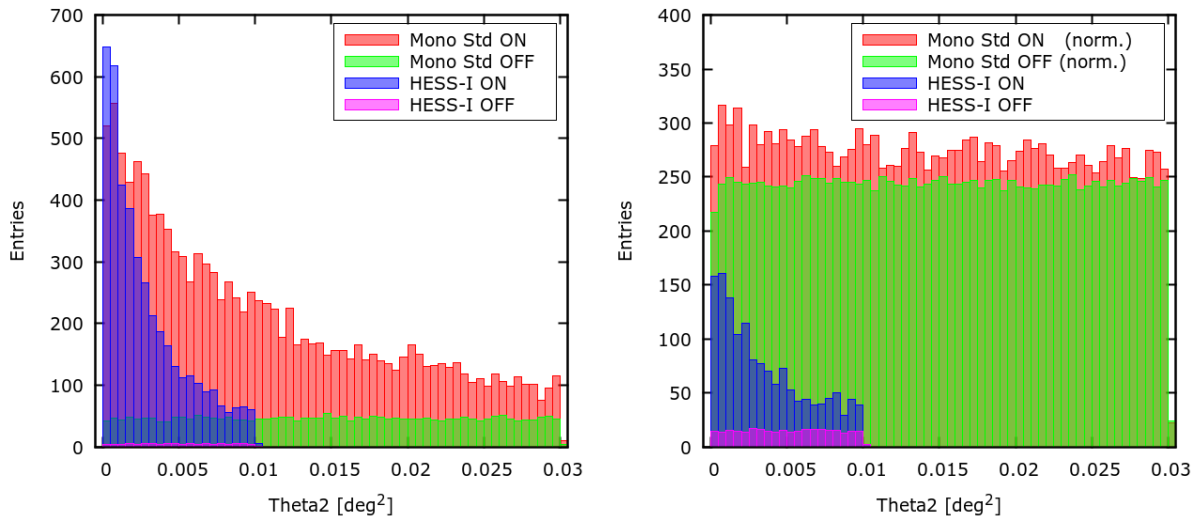


Figure 8.5: θ^2 distributions for the HESS-I and Mono analyses of the Crab Nebula (*left*) and PKS 2155-304 (*right*) inside of the respective ON regions. The Mono ON plots show broad tails compared to the HESS-I distributions. In the case of PKS 2155-304, the Mono data have been scaled for visualization purposes.

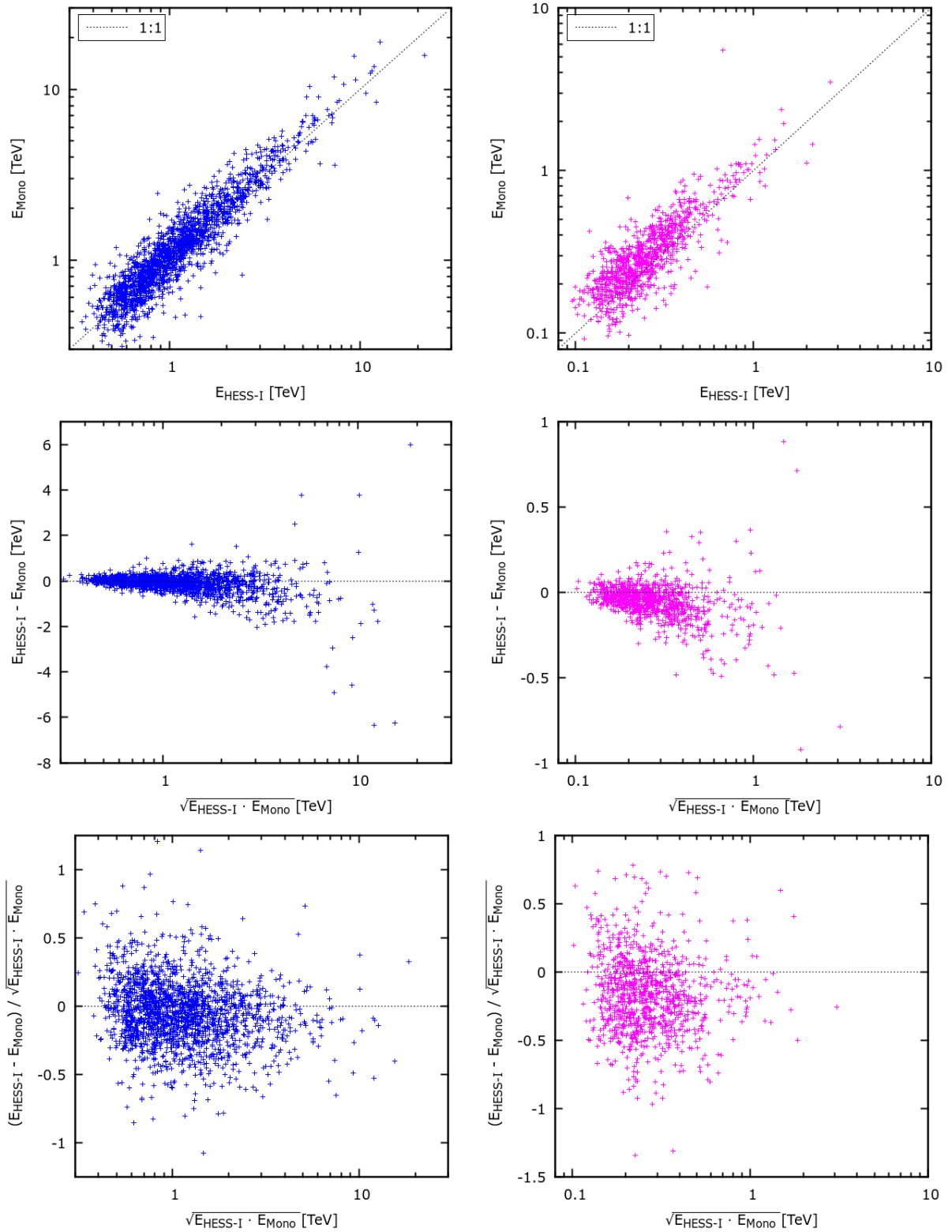


Figure 8.6: Same as in Fig. 8.2 but for the Crab Nebula (left) and PKS 2155-304 (right). For the Crab Nebula, the bias is smaller than in the case of Mrk 501. The mean value is $6 \pm 1\%$, but the mean energy difference tends to negative values with increasing energy, as well. For PKS 2155-304, the systematic shift towards higher Mono energies is $23 \pm 1\%$.

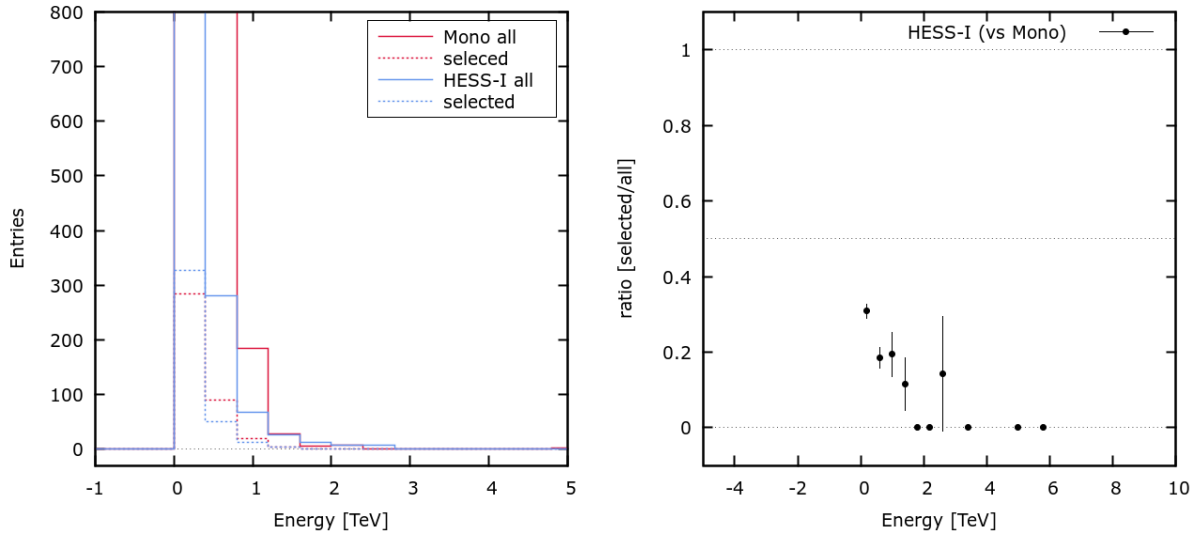


Figure 8.7: Same as in Fig. 8.1 but for PKS 2155-304. *Left:* comparing the two *all* histograms, a matching ratio for the ON events close to 1 is expected, which is not the case. From the *selected* histograms it is apparent that the Mono dataset samples higher energies. *Right:* the matching ratio rapidly decreases with energy.

8.1.3 PKS 2155-304

In order to test a Zenith angle range complementary to the two previous ones, an additional comparison has been carried out for PKS 2155-304 for Zenith angles below 30 deg. For the runlist, only 5 telescope observations between July and October 2013 were considered, for a total of 45 runs.

Only 27% of the 1462 HESS-I ON source γ -like events have a counterpart in the Mono ON region (45994 γ). Extending the research to the whole Mono FoV, the value increases to 42%. Of the 3595 HESS-I OFF events, only 31% find a match in the Mono FoV. As for the Crab Nebula, the broad tail of the θ^2 distribution (Fig. 8.5, *right*) can explain why so many matches are found outside the Mono ON region. 15% of HESS-I ON photons are Mono hadrons. Again, around 50% of the HESS-I γ -like events are missing, which is surprising, given the factor of at least 30 more photons in the Mono analysis (Fig. 8.7).

In contrast to the possible Zenith angle dependence hinted by the Crab Nebula results, the energy offset is here again larger (Fig. 8.6, *right*), with a mean value $E_{\text{Mono}}/E_{\text{HESS-I}} - 1 = 23 \pm 1\%$. The larger bias is at energies below 160 GeV ($39 \pm 3\%$), while above it, it ranges between 17 and 26%.

8.1.4 SUMMARY

In Fig. 8.8, the distributions for the three sources are compared. Despite covering different Zenith angle and energy ranges, they are rather consistent in their offsets. All three sources also show a

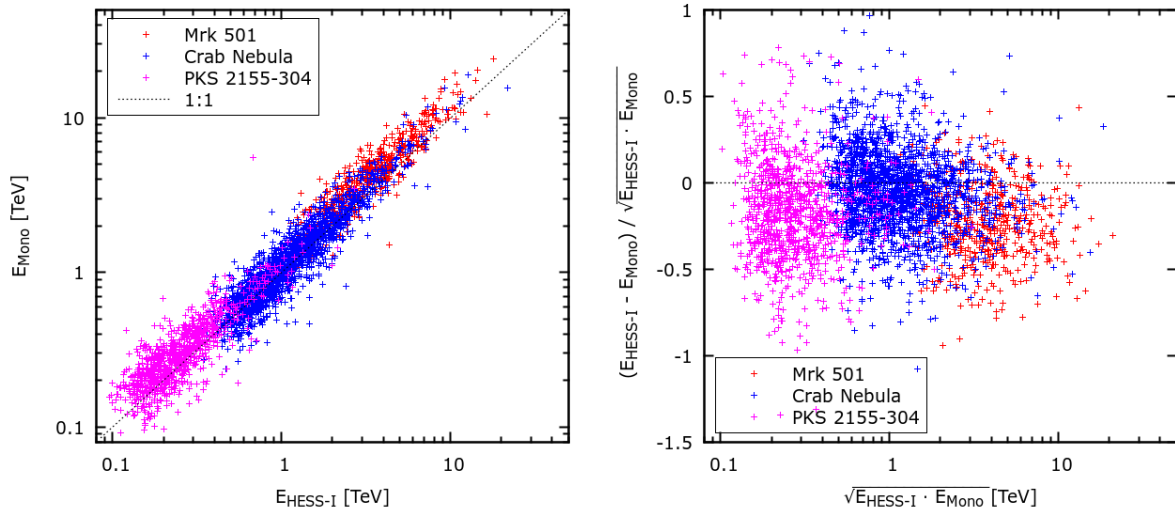


Figure 8.8: Comparison of the distributions of the three sources for the Mono analysis. An overall bias in the energy reconstruction is shown. The Crab Nebula data are less affected.

large percentage of missing HESS-I photons in the Mono (and Stereo, for the only source tested, Mrk 501) datasets. The matching exhibits also an energy dependence. Since energy bias and missing events are present for all sources, it is clear that they do not depend on the Zenith angle of the observation, but rather are intrinsic to the analysis of HESS-II data.

A further analysis using an updated data calibration and optimized cuts has been carried out and will be presented in the next section.

8.2 COMPARISON WITH UPDATED DATA CALIBRATION AND OPTIMIZED CUTS

Since data with an updated calibration have been available, and the cuts have been optimized, the study presented above was repeated using Prod6 DSTs and the software paris-0-8-30. This was also a way to test the efficacy of the new cuts. Here, the Mono and Stereo analyses have been repeated for the same three sources studied above. The HESS-I results, instead, are the same as in the previous sections.

The runlists are not exactly the same as before, because the quality criteria have been changed slightly and because the data were recalibrated, leading to some losses. For Mrk 501, the HESS-I runlist has been used, hence there are three runs more in the comparison. For the other two sources, some observations failed the broken pixel cuts. In the case of the Crab Nebula, an inspection showed that the dismissed runs failed the criteria for being just above the limits. Most of them were therefore still considered of good quality and only two were lost. For PKS 2155-304, 62% of the runlist is lost with the new quality selection. In order to keep the comparison as similar as possible, also in this case the observations just outside the limits were kept. Nonetheless, the runlist is reduced from 45 to 28 runs.

The optimized cuts to be used with the Prod6 DSTs are much tighter than for Prod4. It has to be noted that the cuts for the HESS-I and HESS-II analyses basically share only their names and are very different otherwise. Therefore, *Loose* cuts are used instead of *Std* cuts, in order to have HESS-II samples large enough to expect that all HESS-I events are included (e.g. see Table 7.14). The only exception is Mrk 501, for which *VeryLoose* cuts have been used in the Stereo analysis, in order to maximize the number of ON source events against a very low level of background. Due to some uncorrected bugs in the software, it was not possible to retrieve the γ -like and hadron-like events of the whole FoV, hence these comparisons were not possible.

8.2.1 MRK 501

Concerning Mrk 501, the comparison of the HESS-I events with the Mono ones yields results that in some aspects are worse than for Prod4. Only 26% of the 1368 HESS-I ON γ -like events find a match among the 2506 Mono ON events. The number of events in the Prod6 photon-list is 50% smaller than in the Prod4 one, despite the larger runlinst. This is due to the stronger cuts applied. Instead, the number of HESS-I photons has increased accordingly to the number of runs used. The combination of these two facts can explain the fewer matches obtained with Prod6 than with Prod4. A non-perfect event match is also expected by the fact that there are more HESS-I than Mono events in the ON region above 3 TeV, as can be seen in Fig. 8.9, *left*. The matching ratio as function of the energy is the same for the two DST productions above 8 TeV (Fig. 8.1 and 8.9, *right*). Below 8 TeV, the matching ratio is significantly lower for Prod6, but it is also flatter, whereas it significantly decreases in Prod4.

The mean energy bias is $E_{\text{Mono}}/E_{\text{HESS-I}} - 1 = 41 \pm 2\%$ (13% more than for Prod4), but with a narrower spread than for the previous comparison (Fig. 8.11, *top-left*). This additional shift in energy remains unsolved.

The Stereo ON sample (derived with a *VeryLoose* cuts analysis) contains 1988 γ -like events and is larger than the HESS-I sample. The energy distributions of the two sets (Fig. 8.10, *left*) suggest that all HESS-I events should find a Stereo counterpart. Instead, the matching ratio is 60%, which is however much better than for the same comparison with Prod4 data (44%). The ratio is also almost constant throughout the energy range (Fig. 8.10, *right*).

In contrast to the increased bias for the Mono results, the Stereo bias for Prod6 halves with respect to Prod4. Its mean value is $E_{\text{Stereo}}/E_{\text{HESS-I}} - 1 = 18 \pm 1\%$ (Fig. 8.11, *right*). The spread of the Stereo distributions is the same for the two DST productions.

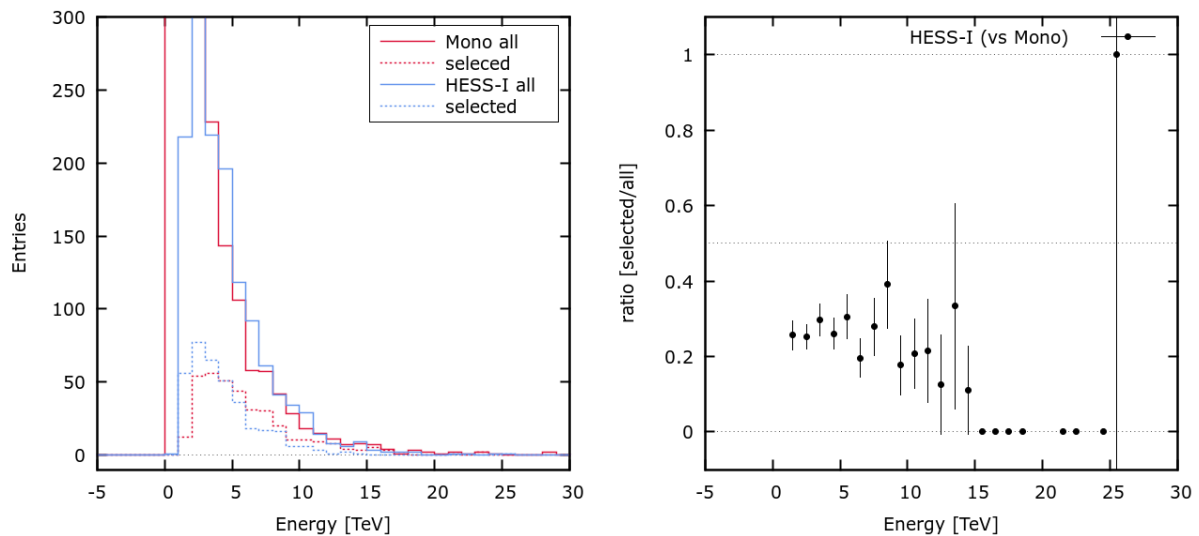


Figure 8.9: Mrk 501: same as in Fig. 8.1 but for Mono *Loose* cuts analysis with Prod6 DSTs. Comparing the two *all* histograms in the *left* plot, a matching ratio for the ON events close to 0.7 is expected. The actual value is only 26%, significantly less than for the Prod4 analysis, but more constant over the energy range (*right* plot). The two productions yield same ratios above 8 TeV.

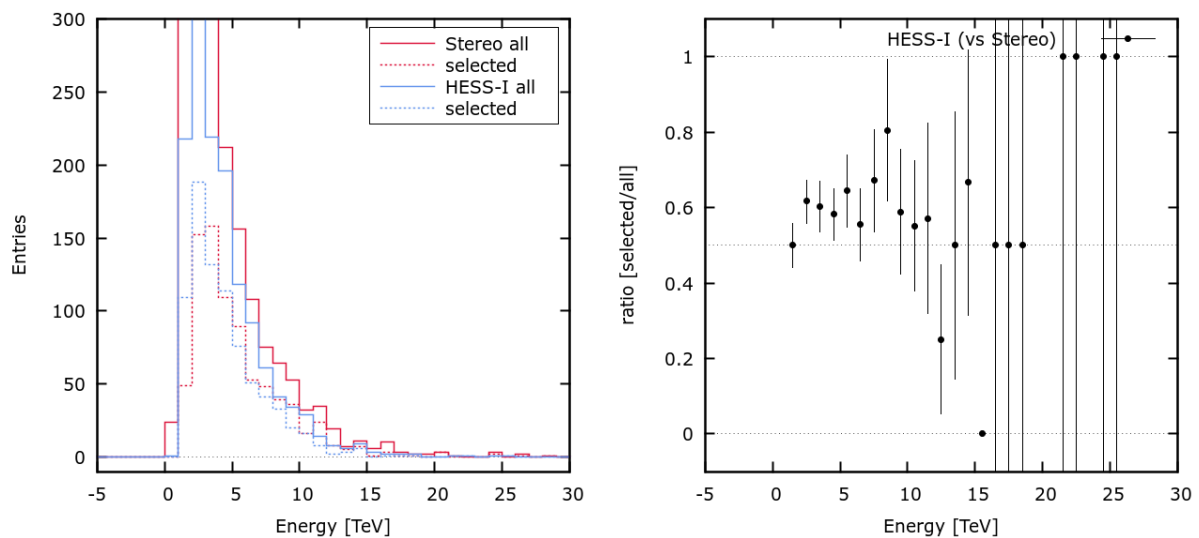


Figure 8.10: Mrk 501: same as in Fig. 8.1 but for Stereo *VeryLoose* cuts analysis with Prod6 DSTs. Comparing the two *all* histograms in the *left* plot, a matching ratio close to 1 is expected. The actual value is around 60%, a large improvement with respect to the 44% of the Prod4 analysis. The ratio is also more homogeneous over the energy range (*right* plot).

8.2. COMPARISON WITH UPDATED DATA CALIBRATION AND OPTIMIZED CUTS 201

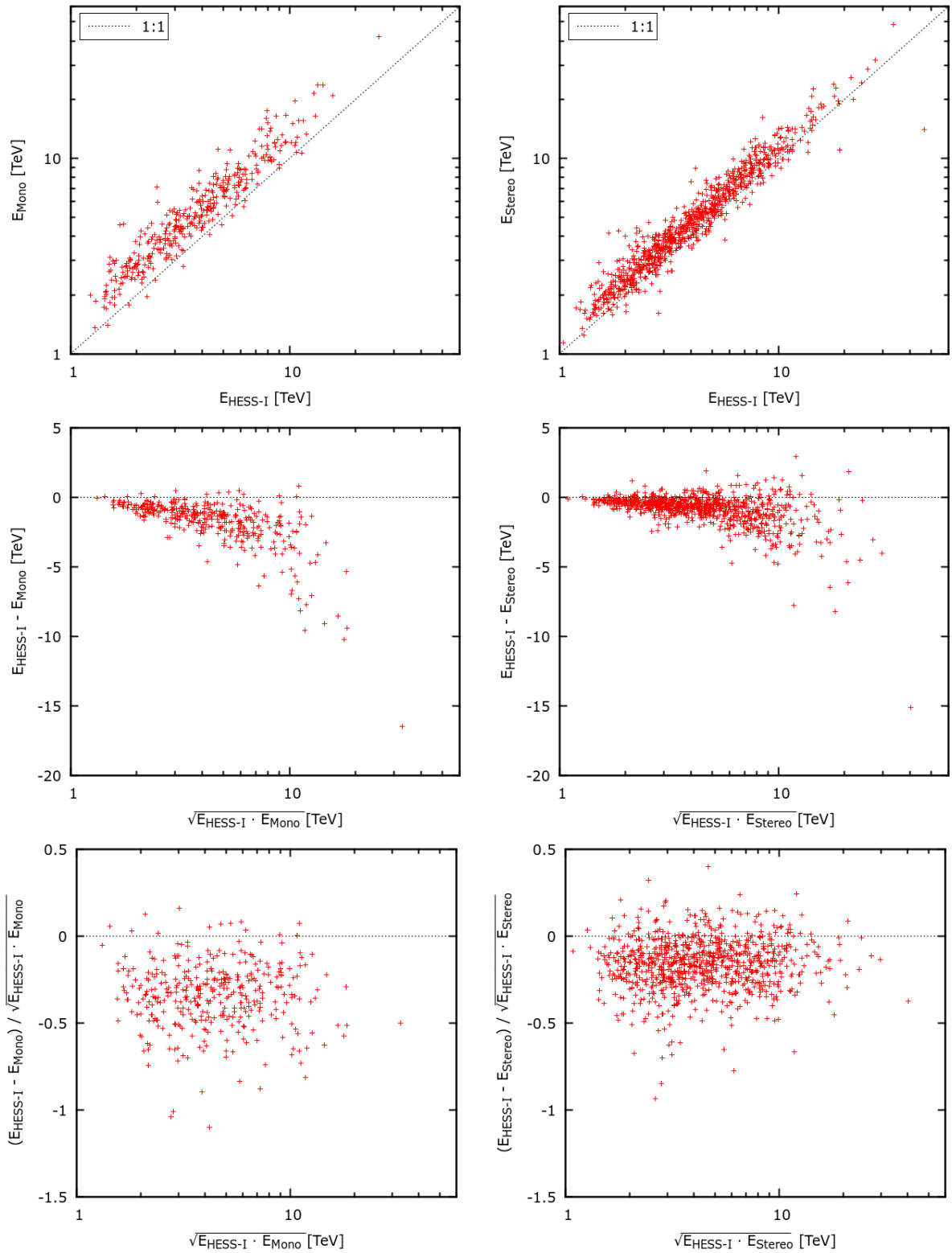


Figure 8.11: Mrk 501: same as in Fig. 8.2 but for Mono *Loose* (left) and Stereo *VeryLoose* cuts (right) analyses with Prod6 DSTs. For Mono, the systematic bias worsens with respect to Prod4 and is almost $41 \pm 2\%$, while it significantly improves for the Stereo analysis, almost halving its value and reducing it to $18 \pm 1\%$.

8.2.2 CRAB NEBULA

The analysis of the Crab Nebula data yields 3917 HESS-I and 7671 Mono ON events. The matching ratio is 38%, similar to the Prod4 case. A non-perfect match is expected from the two event distributions, which show higher number of HESS-I events above 1 TeV (Fig. 8.12, *left*). The ratio also decreases with energy (Fig. 8.12, *right*). As in the case of Mrk 501, the mean energy bias increases in comparison to the previous production, with the mean offset rising from $6 \pm 1\%$ to $19 \pm 1\%$ (Fig. 8.14, *left*).

The comparison with the 6469 Stereo ON photons yields a fraction of matching events of 68%. As for Mrk 501, the matching ratio as function of the energy is flatter than in the Mono case (Fig. 8.13, *right*). There is no energy bias ($E_{\text{Stereo}}/E_{\text{HESS-I}} - 1 = 0 \pm 1\%$) and the spread is narrow (Fig. 8.14, *right*). The narrow distributions centered on 0 or on the 1:1 relation look exactly how they should be in all cases.

8.2.3 PKS 2155-304

Similarly to the Mono analysis comparisons for Mrk 501 and the Crab Nebula, the PKS 2155-304 one shows a low matching ratio of only 27% and an increase of the mean energy bias from $23 \pm 1\%$ to more than $35 \pm 2\%$ (Fig. 8.17, *left*) from the Prod4 DSTs to the current one. The matching also decreases with energy in the same way as for Prod4 (Fig. 8.15, *right*). The Stereo analysis, instead, is much more in agreement with the HESS-I. 60% of the HESS-I γ -like events have a match (Fig. 8.16) and the mean energy bias is $7 \pm 1\%$ (Fig. 8.17, *right*). However, the bias significantly and monotonically reduces with energy from $14 \pm 1\%$ below 180 GeV to $2 \pm 1\%$ above 600 GeV.

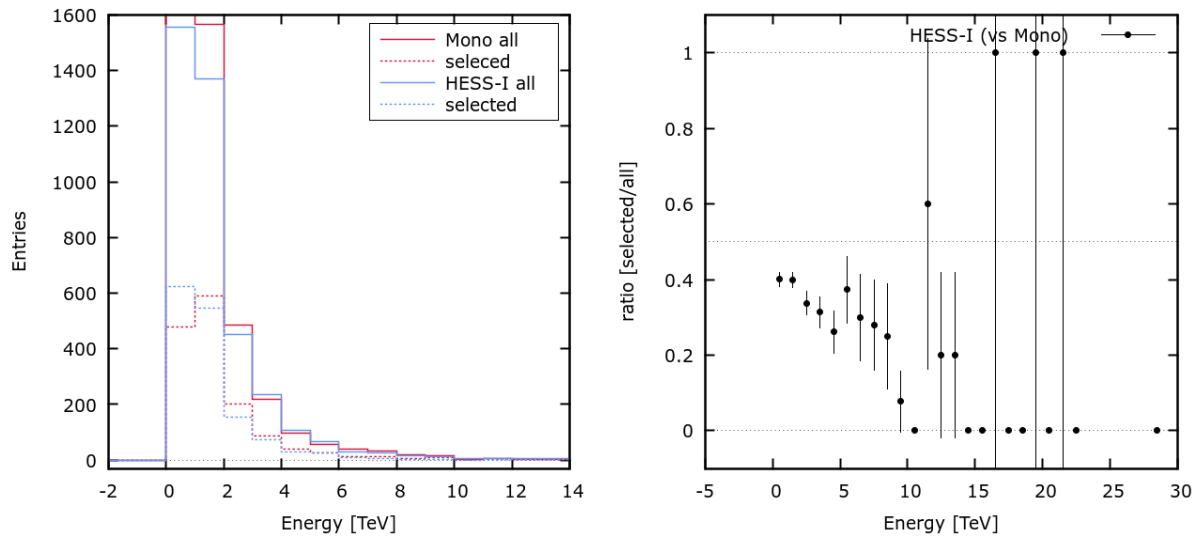


Figure 8.12: Crab Nebula: same as in Fig. 8.1 but for Mono *Loose* cuts analysis with Prod6 DSTs. Comparing the two *all* histograms in the *left* plot, a matching ratio for the ON events close to 0.8 is expected. The actual value is 38%, similar to Prod4, but in this case it is more constant over the energy range (*right* plot).

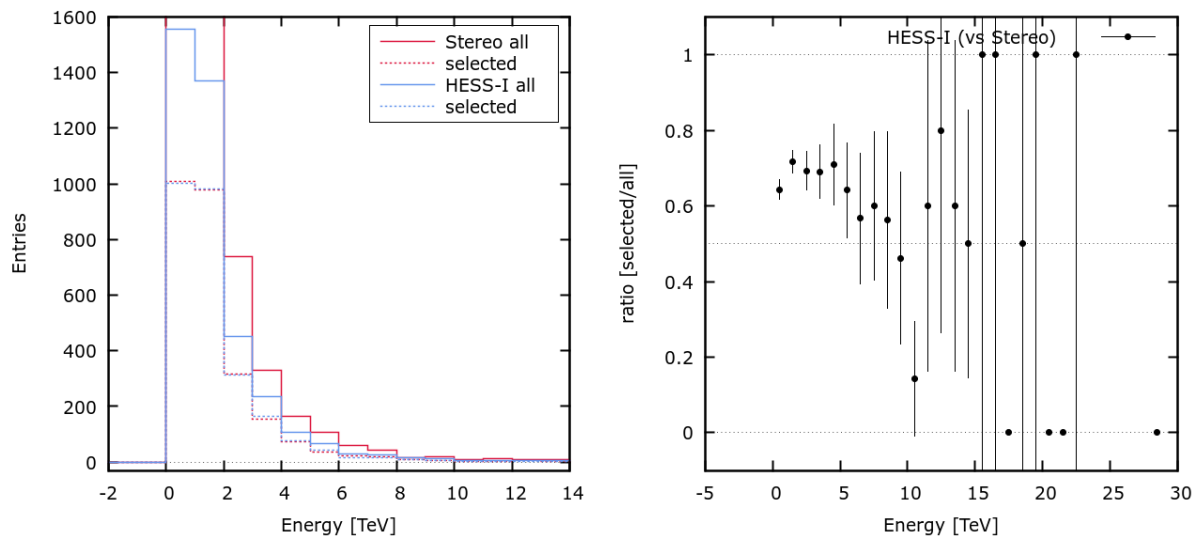


Figure 8.13: Crab Nebula: same as in Fig. 8.1 but for Stereo *Loose* cuts analysis with Prod6 DSTs. Comparing the two *all* histograms in the *left* plot, a matching ratio for the ON events close to 1 is expected. The actual value is 68%, relatively constant over the energy range (*right* plot).

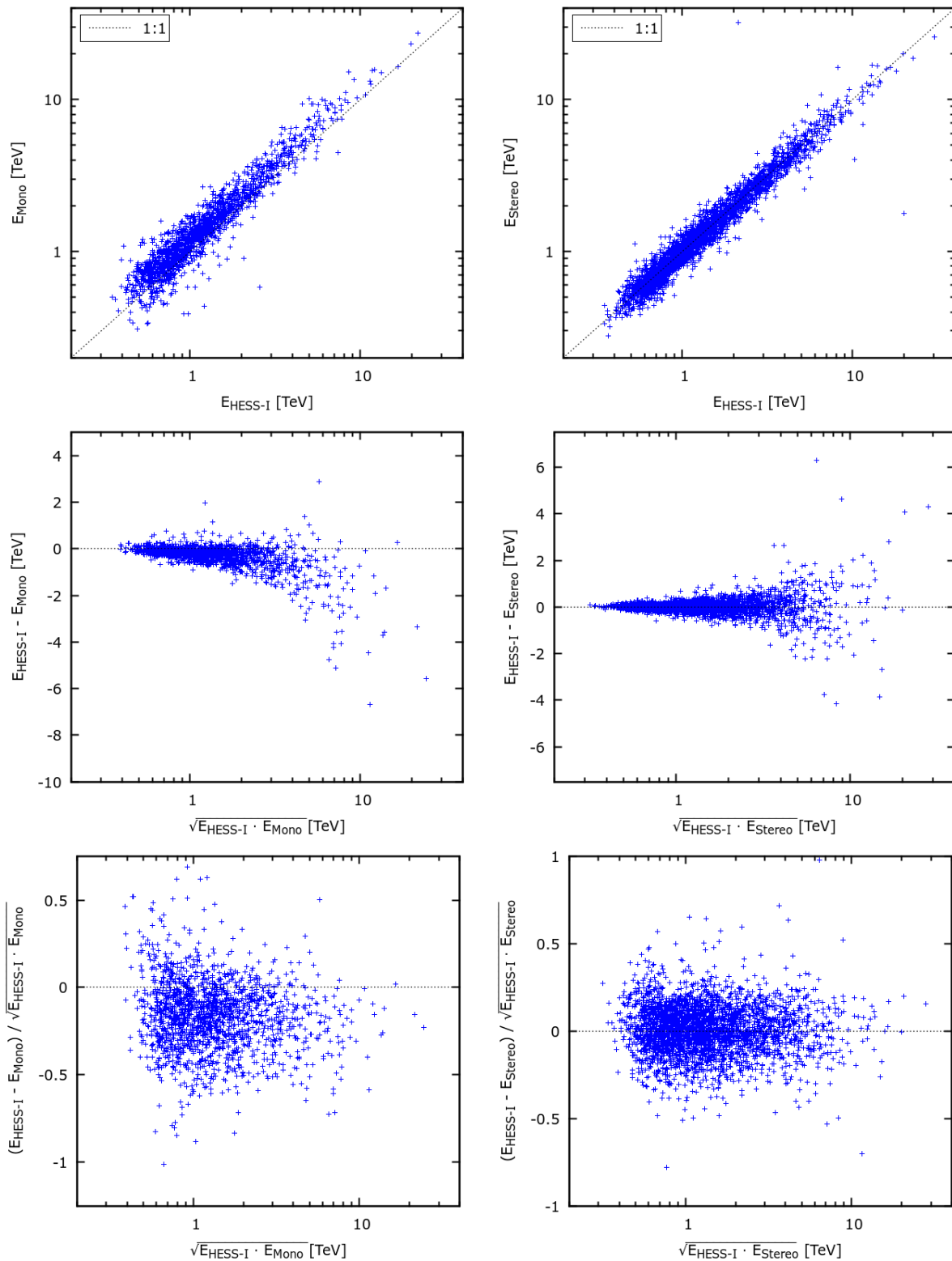


Figure 8.14: Crab Nebula: same as in Fig. 8.2 but for Mono (*left*) and Stereo (*right*) Loose cuts analyses with Prod6 DSTs. For Mono, the systematic bias is three times higher than for Prod4, reaching $19 \pm 1\%$. For Stereo, the energy bias disappears.

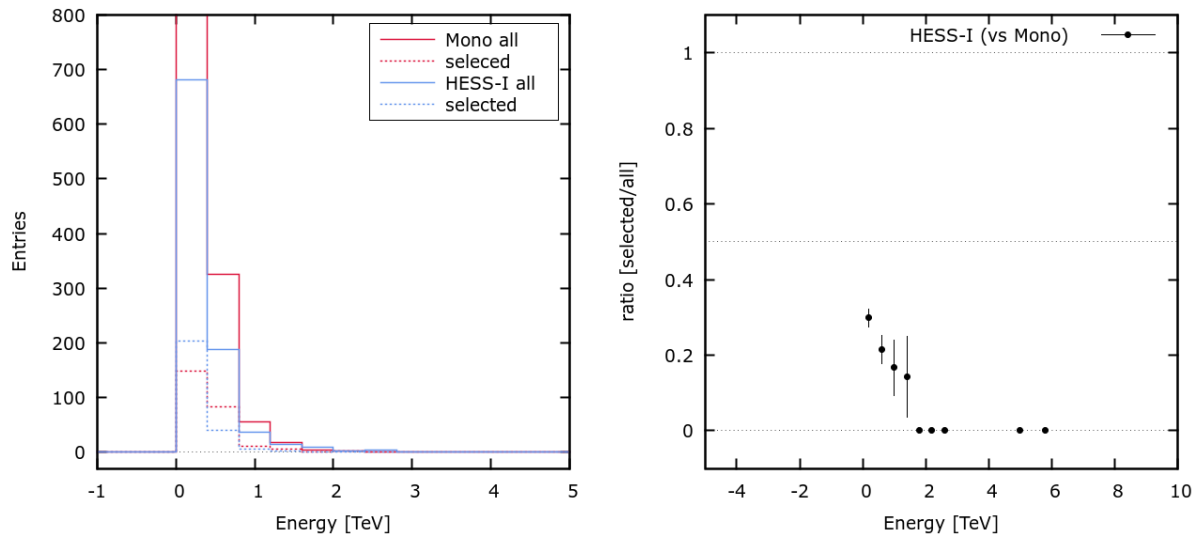


Figure 8.15: PKS 2155-304: same as in Fig. 8.1 but for Mono *Loose* cuts analysis with Prod6 DSTs. Comparing the two *all* histograms in the *left* plot, a matching ratio for the ON events close to 1 is expected. The actual value is only 27%, and strongly decreasing with energy (*right* plot). The results are very similar to the Prod4 ones.

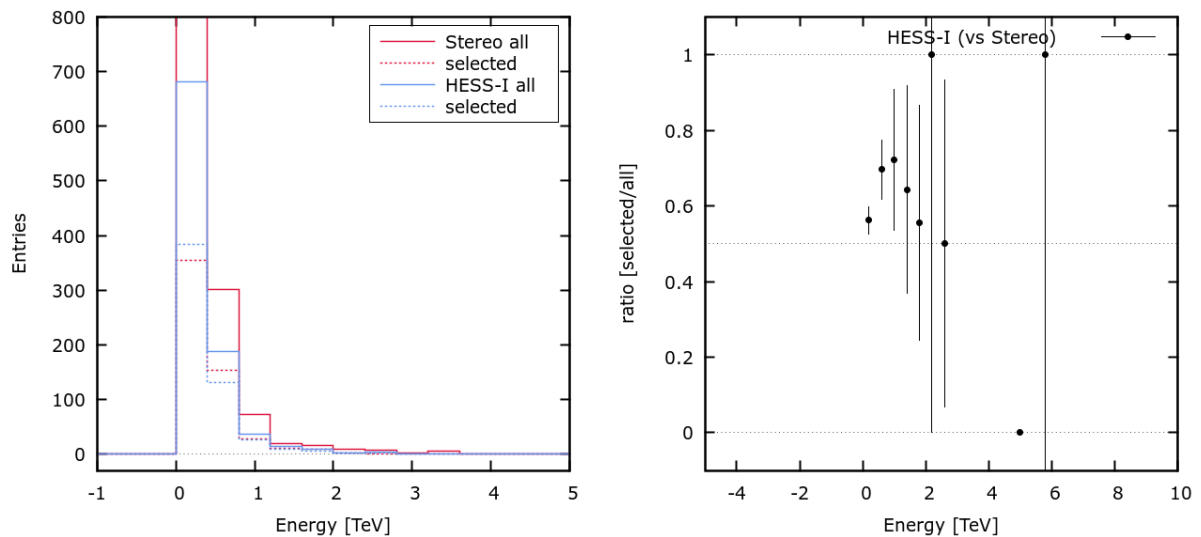


Figure 8.16: PKS 2155-304: same as in Fig. 8.1 but for Stereo *Loose* cuts analysis with Prod6 DSTs. Comparing the two *all* histograms in the *left* plot, a matching ratio for the ON events close to 1 is expected. The actual value is 60%, relatively constant with energy (*right* plot).

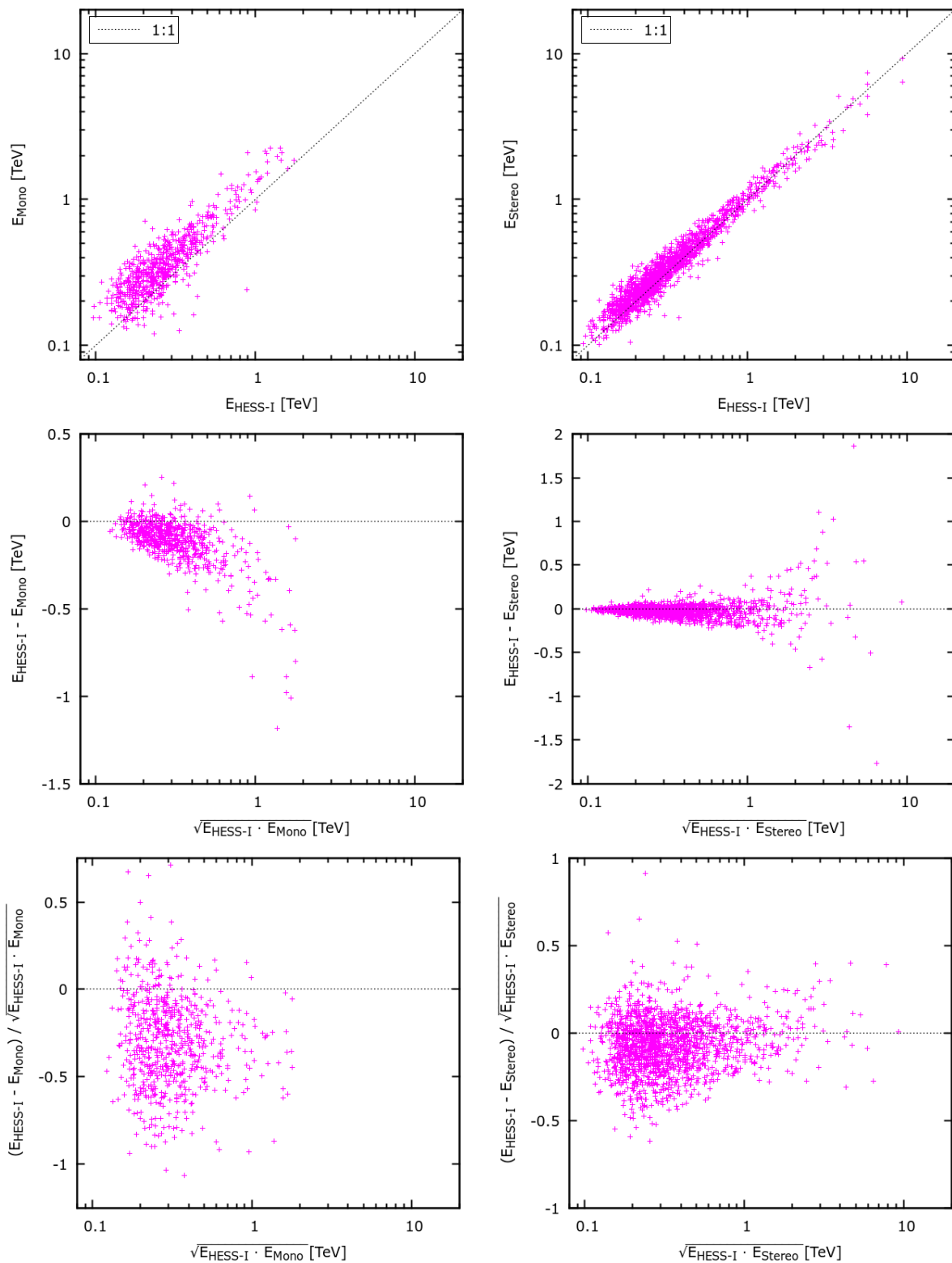


Figure 8.17: PKS 2155-304: same as in Fig. 8.2 but for Mono (*left*) and Stereo (*right*) Loose cuts analyses with Prod6 DSTs. For Mono, the systematic shift is 50% larger than for Prod4, reaching $35 \pm 2\%$. For Stereo, it is only $7 \pm 1\%$, and monotonically decreases with energy.

8.2.4 SUMMARY OF THE UPDATED ANALYSIS

In Fig. 8.18 the comparisons of the three sources are plotted together for the Mono (*left*) and Stereo (*right*) analyses, respectively. It can clearly be seen that the same trend is common to all sources for the two analyses.

In Table 8.1, the results of the comparisons for the analyses with both Prod4 and Prod6 DSTs (and respective cuts) are summarized. For the Mono analysis, there is a significant decrease in the matching ratio of the ON source photons from Prod4 to Prod6 for Mrk 501. This can be at least partly explained with the harder cuts used in the second case, which reject many more events. The energy bias significantly worsens, reaching a factor of 2 for the Crab Nebula.

For the Stereo analysis, comparisons can be made only for Mrk 501. Both the matching ratio and the energy bias improve with Prod6. In general, the matching ratio is fairly good above 60% for all three sources. The energy bias is significantly smaller than for Mono and absent in the case of the Crab Nebula.

The Crab Nebula is less affected by the energy bias and by the missing photons for all analyses in comparison to the other two sources. A possible explanation could be that, being the Crab Nebula a standard candle for the TeV astronomy, it is often used for tests and compared to Montecarlo simulations. Therefore, the analyses could be better tuned on this source.

Table 8.1: Summary of the comparisons of HESS-I ON-source γ -like events with Mono and Stereo events from analyses with Prod4 and Prod6 DSTs and respective cuts.

		Ratio ON events		Energy bias	
		Prod4	Prod6	Prod4	Prod6
Mrk 501	Mono	40%	26%	$28 \pm 1\%$	$41 \pm 2\%$
	Stereo	44%	60%	$33 \pm 1\%$	$18 \pm 1\%$
Crab Nebula	Mono	40%	38%	$6 \pm 1\%$	$19 \pm 1\%$
	Stereo	–	68%	–	$0 \pm 1\%$
PKS 2155-304	Mono	$27\%^\dagger$	27%	$23 \pm 1\%$	$35 \pm 2\%$
	Stereo	–	60%	–	$7 \pm 1\%$

\dagger This value increases up to 42% when considering the whole Mono FoV.

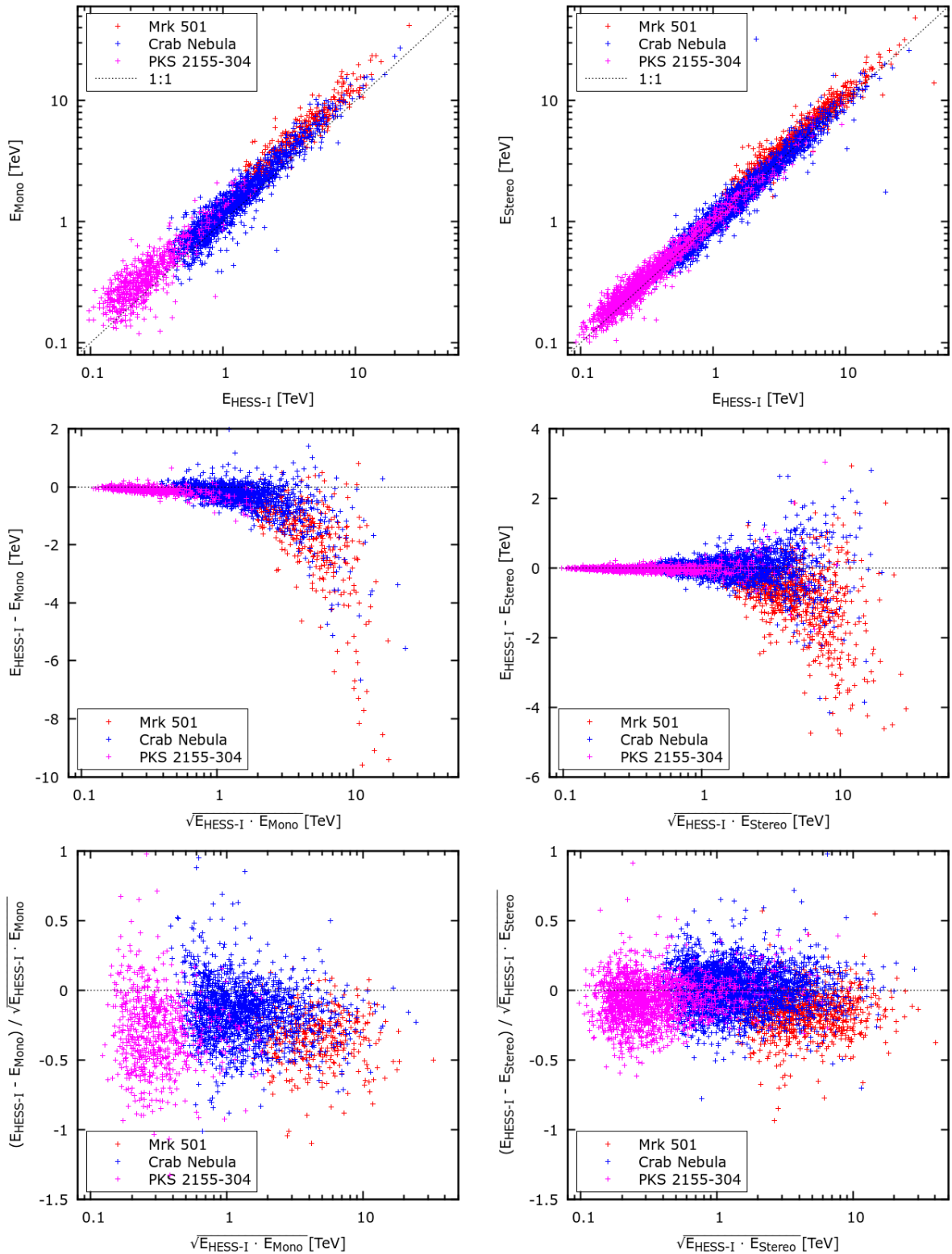


Figure 8.18: Same as in Fig. 8.8 but for Mono (*left*) and Stereo (*right*) *Loose* cuts analysis with Prod6 DSTs. For Mono, the bias is systematic for all three sources, with the same trend and similar offsets, although the Crab Nebula data seem less affected. There is a significant worsening in the agreement between the HESS-I and Mono energy reconstruction with respect to Prod4. For Stereo, the agreement with the HESS-I energy reconstruction is improved with respect to Prod4. For the Crab Nebula data, there is no bias.

8.3 EFFECTS OF THE CUTS

In order to test if the number of missing events in the Stereo analysis is due only to the different cuts used with respect to the HESS-I analysis, an additional test has been carried out for the Mrk 501 dataset. The HESS-I cuts were changed (when possible²) in order to match the Stereo ones. The ON region size was first left to the standard HESS-I value (0.01°) and then changed to the Stereo one (0.006°). The results of the new custom analyses were compared with both the HESS-I and Stereo ones. They showed that the new cuts sample a different ensemble of events.

Compared to the standard HESS-I analysis, the ensemble is larger for the same ON region size, smaller otherwise. In the first case, about 7% of the custom γ -like events are not found in the HESS-I sample. A matching ratio smaller than 1 is recovered also the other way around, although the number of standard HESS-I events is smaller. 7% of custom γ -like events miss a match also when comparing the smaller ON region. This suggests that the 7% difference is intrinsic to the choice of the cuts.

The comparisons with the Stereo events yields matching ratios around 60%, similar to the ones found in the study described in the previous paragraphs. Part of the deficit is ascribed to the remaining difference in the cuts. Although, it is more likely that the additional cuts on CT5 in the Stereo reconstruction play an important role in rejecting the missing events.

The issue of the overwhelming number of missing γ -like events in the Mono analysis was tested in a separate test set³. A new DST test production (Prod8_Test12) and a development software version (paris-0-8-32) were used on the Mrk 501 dataset. The new software allows for a direct comparison of the populations of events reconstructed and selected by two reconstruction methods. For instance, given an ensemble of γ -ray candidates in Stereo, it is possible to check how many of them are reconstructed in Mono and what are the given event classes. Here, the events accepted by a Combined *Std* cuts analysis were compared with the ones accepted by a Mono *Std* cuts analysis. A Combined analysis is a Stereo analysis which accepts Mono events when no information is available from the HESS-I telescopes.

It was found that 73% of the γ -like Stereo events are reconstructed as VHE events in Mono, but only 26% survive all the cuts and are classified as γ -like events. This value is in line with what has been found in sec. 8.2.1. In order to test where the events are lost, one cut at a time was switched off. A consistent part of the events (around 40% of those that survived up to that point) are rejected by the DirectionError cut. Looking at the DirectionError distribution plots (Fig. 8.19), this should not be the case. The cut ($\text{DirectionError} < 0.3^\circ$) should in fact reject only around 15% of the events. The reason is still unclear at the time of writing this report.

²Some cuts have been developed specifically for the HESS-II analysis and are not implemented in versions of the software older than paris-0-8-30.

³These results have been provided by Mathieu de Naurois, H.E.S.S. internal communication, <https://hess-confluence.desy.de/confluence/display/HESS/ParisAnalysis+Developments+-+Crossing+several+reconstructions>

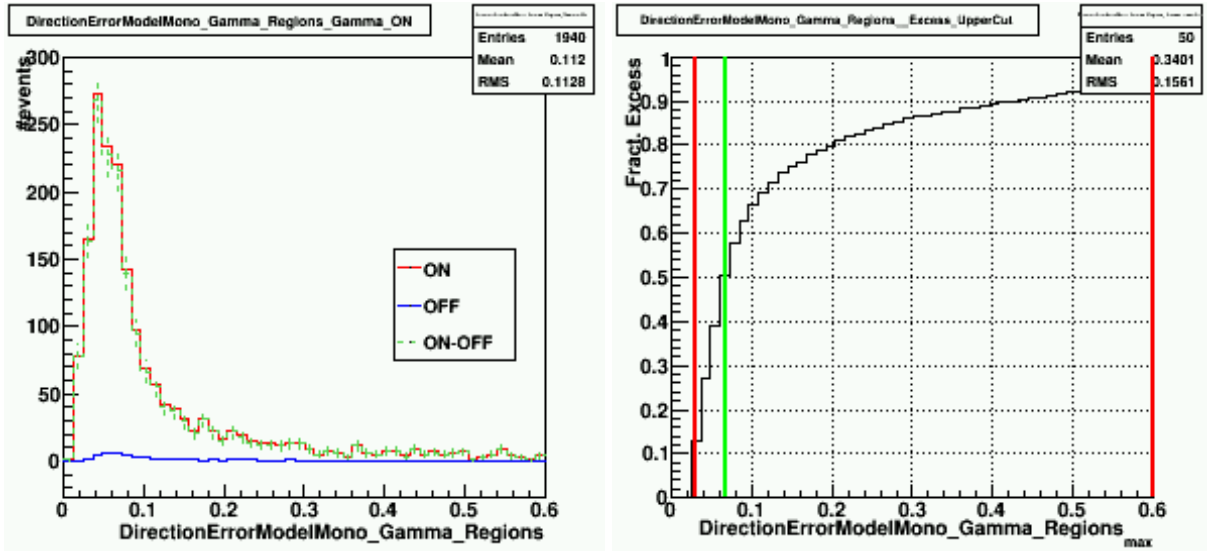


Figure 8.19: *Left:* Distribution of γ -like events as a function of the direction error for ON, OFF and excess events. *Right:* Fraction of excess as a function of the direction error. The green line at 0.06° corresponds to 50% of the excess. In this analysis, only 60% of the γ -like events are kept, corresponding to $\sim 0.09^\circ$, much less of the $< 0.3^\circ$ set by the cut. From Mathieu de Naurois, H.E.S.S. internal communication.

8.4 TEST WITH INDEPENDENT SOFTWARE AND DATA CALIBRATION

In order to see if the the energy bias affects only the software, the data and the reconstruction methods used in this work, the same study has been performed in a completely different environment. Here, a different software, data calibration chain and event reconstruction methods have been adopted⁴. The runlists used here are subsets of the runs used in sec. 8.1 that also pass the new independent quality selection. They comprise 17, 22 and 29 runs for Mrk 501, the Crab Nebula and PKS 2155-304, respectively. The analyses were run in the HAP framework with different γ -hadron separation techniques and *Std* cuts: Boosted Decision Tree (BDT, also known as TMVA, Ohm et al. 2009) for HESS-I, MonoReco (also based on TMVA, Murach et al. 2015) for Mono, and Hillas parameters (sec. 4.3, Aharonian et al. 2006a) for Stereo. Because of missing training at the very high Zenith angles of Mrk 501, TMVA could underperform in the HESS-I and Mono analyses of this source. Another source of imprecision could be the inhomogeneity of the γ -hadron separation methods. However, this should not affect the study significantly, since all three methods are based on the Hillas event reconstruction.

The results confirm what has been found in sec. 8.2, and the similarity of certain values is surprising. The Mono reconstruction shows mean energies $36 \pm 0.4\%$, $21 \pm 1\%$ and $22 \pm 3\%$ higher than HESS-I for Mrk 501, the Crab Nebula and PKS 2155-304, respectively (Fig. 8.20, *left*). For the Stereo analysis there is a bias, as well, but less pronounced. It is $9 \pm 1\%$, $8 \pm 1\%$ and $8 \pm 1\%$ for the three sources, respectively, unlike for Prod6 (Fig. 8.20, *right*).

⁴The analyses of the three sources were carried out by Alison Mitchell, who provided the photon-lists for the study.

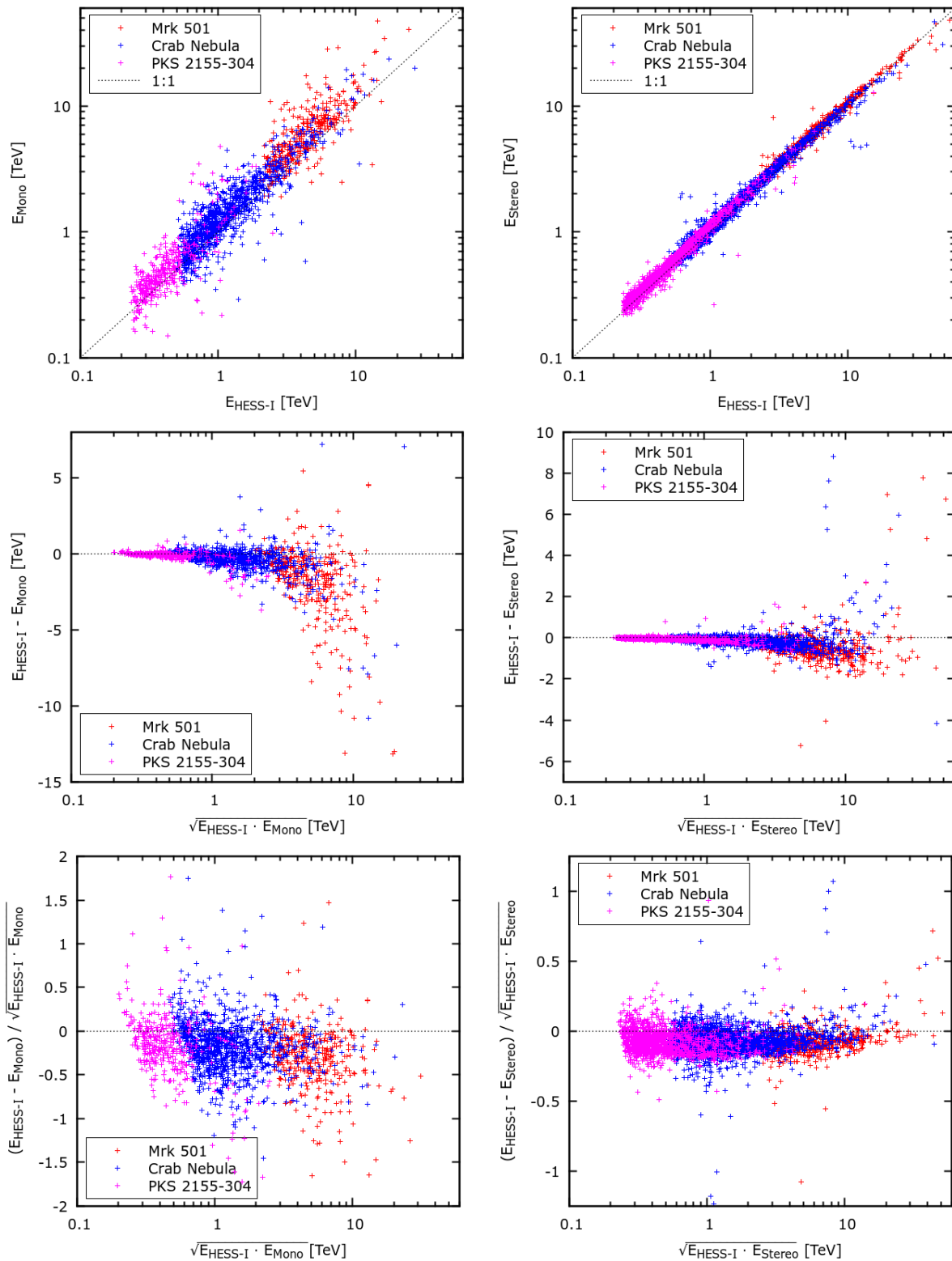


Figure 8.20: Same as in Fig. 8.8 but for Mono (*left*) and Stereo (*right*) *Std* cuts analysis in the HAP framework. For Mono, the bias is systematic for all three sources, with the same trend and similar offsets, although the Mrk 501 data are more affected. For Stereo, the agreement with the HESS-I energy reconstruction is the same for all three sources around 8-9%.

The matching ratio is lower for Mono than for Stereo. For Mrk 501, the Crab Nebula and PKS 2155-304 one has 0.42%, 0.36% and 0.28% for Mono and 0.54%, 0.77% and 0.80% for Stereo, respectively.

The similarity of the results suggests that these problems could be linked to the not fully correct understanding of the H.E.S.S. array or to some issues in the telescopes calibration.

8.5 CONCLUSIONS

In the analysis of HESS-II data, two problems have been discovered. The first one concerns the number of photons reconstructed for the different H.E.S.S. sub-arrays: a significant part of the HESS-I ON source photons are missing from the Mono and Stereo samples. The second one is the presence of an energy bias between the reconstructions. In general, one can expect a better agreement of HESS-I with Stereo than with Mono because HESS-I is a subarray of Stereo, while HESS-I and Mono are completely different instruments. However, the work presented in this chapter showed that it is not always the case.

In order to study these issues, a comparison of the photon-lists obtained for the three telescope subarrays has been done. Three sources have been tested, which cover complementary Zenith angles and energy ranges, together with two software versions that use different sets of cuts and data calibrations (DSTs Prod4 and Prod6).

The analyses of Prod4 data showed that between 56% and 73% of the HESS-I events in the ON region are not recognized as γ -like events by the Mono or Stereo analyses in their respective ON regions. The ratio of matching events strongly decreases with energy for Mono and is more constant for Stereo. The common events show an energy bias towards higher Mono or Stereo energies up to almost 30%. The fact that a strong bias is seen in both the Mrk 501 as well as in the PKS 2155-304 datasets, which cover completely different Zenith angles and energy ranges, rules out the hypothesis that the incongruencies are due to the unusual extreme Zenith angle of the Mrk 501 observations.

The analyses of the Prod6 data yielded different results for Mono and Stereo, with a worsening for the former and an improvement for the latter. The matching ratio for the Mono analysis is less than 30% for both Mrk 501 and PKS 2155-304. The energy bias is 10% higher for all three sources, reaching 40% for Mrk 501. On the other hand, matching ratios of 60% or more, rather constant over the energy range, are found for the Stereo analysis. The energy bias is smaller: it almost halves for Mrk 501 with respect to Prod4 and is zero for the Crab Nebula.

The results for the Crab Nebula are in general better than for the other sources. This could be due to the fact that this source is a standard candle for the TeV astronomy, and is often used for tests and comparisons with the Montecarlo simulations. Hence, the analyses could be better tuned on it.

Tests with modified cuts have shown how the cuts for the HESS-I and Stereo analyses effectively sample different events, and hence explain part of the matching deficit between the two reconstructions. The cuts on CT5 in the Stereo analysis, however, can play an important role in

rejecting the missing events. For the Mono analysis, it seems that a consistent part of the events are rejected by the DirectionError cut, which appears to discard significantly more events than it should for no clear reason.

Similar problems about missing events and energy bias for both Mono and Stereo analyses have been detected also using independent software and data calibration. This suggest a common origin of these problems, that could be linked to a not fully correct understanding of the H.E.S.S. array or to some issues in the telescopes calibration. Some level of energy bias is visible in the comparison of Montecarlo simulations with real data, as well. It is corrected for during the spectral analysis via the effective areas. However, this bias is of the order of 10%, which is much lower than the one found in this study in some cases. It also does not take into consideration that its value significantly changes depending on the source.

SUMMARY AND OUTLOOK

In my PhD thesis, I presented the results of the analysis of three point-like γ -ray emitters observed at VHE with H.E.S.S. . Two of them are the well known BL Lac objects 1ES 0229+200 and Mrk 501, the third one is HESS J1745-290, a compact source discovered in the direction of the Galactic Center during the H.E.S.S. Galactic Plane survey. I exploited multiwavelength observations in order to assess the physical properties of the three sources and of the ambient medium, both via spectral and variability studies and by comparison with models and predictions found in the literature. For the analysis of the two blazars, I used observations performed with both the HESS-I and the HESS-II arrays. I presented a systematic comparison of the γ -ray energies as they are reconstructed for different sub-arrays of the H.E.S.S. system. I also introduced the theoretical, phenomenological and technical bases needed for a better understanding of the whole work.

In chapter 5 I attempted to determine the nature of the Galactic source HESS J1745-290. The γ -ray emission is likely linked to Sgr A*, the black hole at the center of the Galaxy, but up to now it could not be associated definitively. I used H.E.S.S. VHE and *Chandra* X-ray data from the 2012 multiwavelength campaign in order to find correlated variability in simultaneous observations of X-ray flares. Only in two occasions both instruments observed simultaneously during a flare, preventing an in depth correlation study. Additionally, no significant variability was detected in the H.E.S.S. dataset. In conclusion, it was not possible to associate the γ -ray emission with the Galactic black hole Sgr A*.

In chapter 6, I presented the 2004-2013 long term monitoring of the BL Lac object 1ES 0229+200. This source shows significant monthly and yearly variability at VHE, as well as in the X-ray band. The correlation of the variability supports a synchrotron self Compton emission model. Together with a refined spectrum in the GeV band, it helps constraining the strength of the intergalactic magnetic field. Assuming that the emission at ~ 600 GeV consists of secondary photons, the IGMF can be estimated to be $B_{IGMF} \sim 5 \times 10^{-17}$ G. On the other hand, the detected variability above 1 TeV implies that the radiation of 1ES 0229+200 is dominated by primary γ -rays. Assuming “soft” and “hard” models as in Vovk et al. (2012), the IGMF strength can be estimated

to be $> 10^{-16}$ G and $\sim 3 \times 10^{-16}$ G, respectively. The existence of an effective plasma excitation cooling would prevent any estimation of the IGMF.

In chapter 7 I showed the analysis of the flaring state of the blazar Mrk 501. I found that the intrinsic spectrum is hard and shows a dependency on the flux state. I used the spectra of different flux states to constrain the EBL intensity at mid-infrared wavelengths and confirmed that the model of Franceschini et al. (2008) describes well the EBL density for the redshift of this source. Multiwavelength observations hint towards the necessity of at least two emission zones or mechanisms to explain the broadband emission of Mrk 501.

The hard multi-TeV spectra of Mrk 501 and 1ES 0229 indicate the absence of Klein-Nishina suppression. Since the treatment of the emission in the Thomson limit is unlikely at such high energies, this implies that either the minimum maximal energy of the electron distribution is very high (minimum $\gamma_{e,max} = 4 \times 10^6 (10/\delta)$ for Mrk 501), or that very large Doppler factors are involved in these sources.

Comparing the results of the analyses of both the HESS-I and the HESS-II arrays, I found that the analysis of HESS-II data proved not to be fully reliable yet, at least for the sources considered in this work. In chapter 8, I showed how the energy values of Mono and Stereo data are systematically biased with respect to those of the HESS-I analysis. Although at least part of this bias should be already corrected in the spectral analysis, I showed that significant systematics remain, which also seem to depend on the source considered.

However, many improvements are currently being done towards a better understanding of the hybrid H.E.S.S. system and of its data analysis, including a reduction of the systematics that affect the results. The new software and DST production, currently under development, seem to solve several issues, starting from the energy bias. The analysis of HESS-I data will be improved as well. This means that within a short amount of time the potential of the data of Mrk 501 and 1ES 0229 could be finally fully exploited. It will be possible to derive more accurate spectra extending to lower energies and likely showing more precise features, both intrinsic and due to EBL absorption. Spectral variability will likely be more easy to assess, as well. All this will allow for a better characterization of the intrinsic emission mechanism and of the EBL density. Improvements in the transition region between the H.E.S.S. and *Fermi* energy ranges, together with a better description of flux variability will allow for tighter constraints on the IGMF strength.

BIBLIOGRAPHY

- Abdo, A. A., Ackermann, M., Ajello, M., et al. 2010, *ApJ*, 723, 1082
- Abdo, A. A., Ackermann, M., Ajello, M., et al. 2011, *ApJ*, 727, 129
- Acciari, V. A., Arlen, T., Aune, T., et al. 2011, *ApJ*, 729, 2
- Acero, F., Ackermann, M., Ajello, M., et al. 2015, *ApJS*, 218, 23
- Ackermann, M., Ajello, M., Allafort, A., et al. 2013, *ApJS*, 209, 34
- Aharonian, F., Akhperjanian, A., Barrio, J., et al. 2001a, *ApJ*, 546, 898
- Aharonian, F., Akhperjanian, A., Beilicke, M., et al. 2004a, *A&A*, 421, 529
- Aharonian, F., Akhperjanian, A. G., Anton, G., et al. 2009a, *A&A*, 502, 749
- Aharonian, F., Akhperjanian, A. G., Anton, G., et al. 2009b, *A&A*, 503, 817
- Aharonian, F., Akhperjanian, A. G., Aye, K.-M., et al. 2005a, *A&A*, 437, 95
- Aharonian, F., Akhperjanian, A. G., Aye, K.-M., et al. 2004b, *A&A*, 425, L13
- Aharonian, F., Akhperjanian, A. G., Barres de Almeida, U., et al. 2008a, *A&A*, 492, L25
- Aharonian, F., Akhperjanian, A. G., Barres de Almeida, U., et al. 2007a, *A&A*, 475, L9
- Aharonian, F., Akhperjanian, A. G., Barres de Almeida, U., et al. 2008b, *A&A*, 478, 387
- Aharonian, F., Akhperjanian, A. G., Barrio, J. A., et al. 1997, *A&A*, 327, L5
- Aharonian, F., Akhperjanian, A. G., Barrio, J. A., et al. 1999a, *A&A*, 349, 29
- Aharonian, F., Akhperjanian, A. G., Bazer-Bachi, A. R., et al. 2007b, *ApJ*, 664, L71
- Aharonian, F., Akhperjanian, A. G., Bazer-Bachi, A. R., et al. 2006a, *A&A*, 457, 899
- Aharonian, F., Akhperjanian, A. G., Bazer-Bachi, A. R., et al. 2006b, *Phys. Rev. Lett.*, 97, 221102
- Aharonian, F., Akhperjanian, A. G., Bazer-Bachi, A. R., et al. 2006c, *Nature*, 440, 1018
- Aharonian, F., Akhperjanian, A. G., Bazer-Bachi, A. R., et al. 2006d, *ApJ*, 636, 777
- Aharonian, F., Akhperjanian, A. G., Bazer-Bachi, A. R., et al. 2005b, *A&A*, 441, 465
- Aharonian, F., Akhperjanian, A. G., Bazer-Bachi, A. R., et al. 2007c, *A&A*, 470, 475
- Aharonian, F. A., Akhperjanian, A. G., Barrio, J. A., et al. 2000, *A&A*, 353, 847
- Aharonian, F. A., Akhperjanian, A. G., Barrio, J. A., et al. 1999b, *A&A*, 349, 11

- Aharonian, F. A., Akhperjanian, A. G., Barrio, J. A., et al. 1999c, *A&A*, 342, 69
- Aharonian, F. A., Akhperjanian, A. G., Barrio, J. A., et al. 2001b, *A&A*, 366, 62
- Ahlers, M. 2011, *Phys. Rev. D*, 84, 063006
- Albert, J., Aliu, E., Anderhub, H., et al. 2007, *ApJ*, 669, 862
- Aleksić, J., Ansoldi, S., Antonelli, L. A., et al. 2015, *A&A*, 573, A50
- Aliu, E., Archambault, S., Arlen, T., et al. 2014, *ApJ*, 782, 13
- Amenomori, M., Ayabe, S., Cao, P. Y., et al. 2000, *ApJ*, 532, 302
- Anderhub, H., Antonelli, L. A., Antoranz, P., et al. 2009, *ApJ*, 705, 1624
- Anderhub, H., Backes, M., Biland, A., et al. 2013, *Journal of Instrumentation*, 8, 6008P
- APOD. 2015, <http://apod.nasa.gov/apod/>
- Arlen, T. C., Vassilev, V. V., Weisgarber, T., Wakely, S. P., & Yusef Shafi, S. 2014, *ApJ*, 796, 18
- Atkins, R., Benbow, W., Berley, D., et al. 1999, *ApJ*, 525, L25
- Baganoff et al. 2012, *Chandra* x-ray visionary project of Sgr A*, http://http://space.mit.edu/asc/SGRA/Project_Page.html
- Barbieri, G. & Romano, G. 1977, *Acta Astron.*, 27, 195
- Barrau, A., Bazer-Bachi, R., Beyer, E., et al. 1998, *Nuclear Instruments and Methods in Physics Research A*, 416, 278
- Bell, A. R. 1978, *Monthly Notices of the Royal Astronomical Society*, 182, 147
- Berge, D. 2006, PhD thesis, Ruprecht-Karls-Universität Heidelberg, Germany
- Berge, D., Funk, S., & Hinton, J. 2007, *A&A*, 466, 1219
- Bernlöhr, K. 2000, Monte Carlo images of air showers, <https://www.mpi-hd.mpg.de/hfm/~bernlohr/HESS/>
- Bernlöhr, K., Carrol, O., Cornils, R., et al. 2003, *Astroparticle Physics*, 20, 111
- Biteau, J. & Williams, D. A. 2015, *ApJ*, 812, 60
- Blandford, R. D. & Ostriker, J. P. 1978, *ApJ*, 221, L29
- Blumenthal, G. R. & Gould, R. J. 1970, *Reviews of Modern Physics*, 42, 237
- Borracci, F., Barres de Almeida, U., Paneque, D., Sitarek, J., & Perri, M. 2013, in *Proceedings of the 33rd ICRC, Rio de Janeiro, Brazil*
- Böttcher, M. 2007, *Ap&SS*, 309, 95
- Böttcher, M. 2012, ArXiv e-prints [arXiv:1205.0539]
- Böttcher, M. & Dermer, C. D. 2002, *ApJ*, 564, 86
- Bradbury, S. M., Deckers, T., Petry, D., et al. 1997, *A&A*, 320, L5
- Broderick, A. E., Chang, P., & Pfrommer, C. 2012, *ApJ*, 752, 22
- Carroll, B. W. & Ostlie, D. A. 1996, *An Introduction to Modern Astrophysics*
- Caswell, J. L. & Wills, D. 1967, *MNRAS*, 135, 231
- Catanese, M., Bradbury, S. M., Breslin, A. C., et al. 1997, *ApJ*, 487, L143
- Cawley, M. F., Fegan, D. J., Harris, K., et al. 1990, *Experimental Astronomy*, 1, 173
- Chakraborty, N., Cologna, G., Kastendieck, M. A., et al. 2015, ArXiv e-prints [arXiv:1509.04893]
- Chang, P., Broderick, A. E., Pfrommer, C., et al. 2014, *ApJ*, 797, 110

- Cologna, G., Chakraborty, N., Mohamed, M., et al. 2015a, ArXiv e-prints [arXiv:1509.04458]
- Cologna, G., Mohamed, M., Wagner, S. J., et al. 2015b, ArXiv e-prints [arXiv:1509.04470]
- Cornils, R., Gillessen, S., Jung, I., et al. 2003, *Astroparticle Physics*, 20, 129
- Crocker, R. M., Fatuzzo, M., Jokipii, J. R., Melia, F., & Volkas, R. R. 2005, *ApJ*, 622, 892
- Cusumano, G., La Parola, V., Maselli, A., & Segreto, A. 2013, The 66-month Palermo BAT Catalogue, http://bat.ifc.inaf.it/bat_catalog_web/66m_bat_catalog.html, accessed December 2015
- Cusumano, G., La Parola, V., Maselli, A., & Segreto, A. 2014, The 100-month Palermo BAT Catalogue, http://bat.ifc.inaf.it/100m_bat_catalog/100m_bat_catalog_v0.0.htm, accessed December 2015
- Daum, A., Hermann, G., Heß, M., et al. 1997, *Astroparticle Physics*, 8, 1
- Davies, J. & Cotton, E. 1957, *J. Solar Energy Sci. Eng.*, 1, 16
- de la Calle Pérez, I., Bond, I. H., Boyle, P. J., et al. 2003, *ApJ*, 599, 909
- De Naurois, M. 2012, Very High Energy astronomy from H.E.S.S. to CTA. Opening of a new astronomical window on the non-thermal Universe., Université Pierre et Marie Curie - Paris VI, 2012. <tel-00687872>
- de Naurois, M. & Rolland, L. 2009, *Astroparticle Physics*, 32, 231
- de Vaucouleurs, G., de Vaucouleurs, A., Corwin, Jr., H. G., et al. 1991, Third Reference Catalogue of Bright Galaxies. Volume I: Explanations and references. Volume II: Data for galaxies between 0^h and 12^h . Volume III: Data for galaxies between 12^h and 24^h .
- Dermer, C. D., Cavadini, M., Razzaque, S., et al. 2011, *ApJ*, 733, L21
- Djannati-Atai, A., Piron, F., Barrau, A., et al. 1999, *A&A*, 350, 17
- Dolag, K., Kachelriess, M., Ostapchenko, S., & Tomàs, R. 2011, *ApJ*, 727, L4
- Domínguez, A., Primack, J. R., Rosario, D. J., et al. 2011, *MNRAS*, 410, 2556
- Donato, D., Sambruna, R. M., & Gliozzi, M. 2005, *A&A*, 433, 1163
- Elvis, M., Plummer, D., Schachter, J., & Fabbiano, G. 1992, *ApJS*, 80, 257
- Essey, W., Ando, S., & Kusenko, A. 2011a, *Astroparticle Physics*, 35, 135
- Essey, W., Kalashev, O., Kusenko, A., & Beacom, J. F. 2011b, *ApJ*, 731, 51
- Essey, W., Kalashev, O. E., Kusenko, A., & Beacom, J. F. 2010, *Phys. Rev. Lett.*, 104, 141102
- Essey, W. & Kusenko, A. 2010, *Astroparticle Physics*, 33, 81
- Falomo, R. & Kotilainen, J. K. 1999, *A&A*, 352, 85
- Fermi, E. 1949, *Physical Review*, 75, 1169
- Finke, J. D., Razzaque, S., & Dermer, C. D. 2010, *ApJ*, 712, 238
- Forman, W., Jones, C., Cominsky, L., et al. 1978, *ApJS*, 38, 357
- Fossati, G., Maraschi, L., Celotti, A., Comastri, A., & Ghisellini, G. 1998, *MNRAS*, 299, 433
- Fouqué, P., de Lyon (France), O., & de Paris-Meudon, O. 1992, Catalogue of Optical Radial Velocities, Monographies de la base de données extragalactiques (Observatoire de Lyon)
- Franceschini, A., Rodighiero, G., & Vaccari, M. 2008, *A&A*, 487, 837
- Funk, S. 2005, PhD thesis, Ruprecht-Karls-Universität Heidelberg, Germany
- Funk, S., Hermann, G., Hinton, J., et al. 2004, *Astroparticle Physics*, 22, 285

- Ghez, A. M., Salim, S., Weinberg, N. N., et al. 2008, *ApJ*, 689, 1044
- Gillessen, S., Eisenhauer, F., Trippe, S., et al. 2009, *ApJ*, 692, 1075
- Gilmore, R. C., Prada, F., & Primack, J. 2010, *MNRAS*, 402, 565
- Gilmore, R. C., Somerville, R. S., Primack, J. R., & Domínguez, A. 2012, *MNRAS*, 422, 3189
- Giommi, P., Ansari, S. G., & Micol, A. 1995, *A&AS*, 109, 267
- Giroletti, M., Giovannini, G., Taylor, G. B., & Falomo, R. 2004, *ApJ*, 613, 752
- Giozzi, M., Sambruna, R. M., Jung, I., et al. 2006, *ApJ*, 646, 61
- Grazian, A., Cristiani, S., D'Odorico, V., Omizzolo, A., & Pizzella, A. 2000, *AJ*, 119, 2540
- H. E. S. S. Collaboration, Abramowski, A., Aharonian, F., et al. 2014, *A&A*, 562, A145
- Hauser, M., Möllenhoff, C., Pühlhofer, G., et al. 2004, *Astronomische Nachrichten*, 325, 659
- Hayashida, N., Hirasawa, H., Ishikawa, F., et al. 1998, *ApJ*, 504, L71
- Healey, S. E., Romani, R. W., Cotter, G., et al. 2008, *ApJS*, 175, 97
- Heitler, W. 1954, *Quantum theory of radiation* (Oxford University Press)
- H.E.S.S. Collaboration, Abramowski, A., Acero, F., et al. 2013, *A&A*, 550, A4
- H.E.S.S. Collaboration, Abramowski, A., Acero, F., et al. 2011, *Astroparticle Physics*, 34, 738
- Hickson, P., Auman, J. R., Ninkov, Z., et al. 1982, *ApJ*, 258, 53
- Hillas, A. M. 1985, *International Cosmic Ray Conference*, 3, 445
- Hinton, J. A. & the HESS Collaboration. 2004, *New A Rev.*, 48, 331
- Horan, D., Badran, H. M., Bond, I. H., et al. 2004, *ApJ*, 603, 51
- Huan, H., Weisgarber, T., Arlen, T., & Wakely, S. P. 2011, *ApJ*, 735, L28
- Hyvönen, T., Kotilainen, J. K., Falomo, R., Örndahl, E., & Pursimo, T. 2007, *A&A*, 476, 723
- Kalberla, P. M. W., Burton, W. B., Hartmann, D., et al. 2005, *A&A*, 440, 775
- Kataoka, J., Mattox, J. R., Quinn, J., et al. 1999, *ApJ*, 514, 138
- Kaufmann, S., Wagner, S. J., Tibolla, O., & Hauser, M. 2011, *A&A*, 534, A130
- Kneiske, T. M. & Dole, H. 2010, *A&A*, 515, A19
- Kondo, Y., Worrall, D. M., Mushotzky, R. F., et al. 1981, *ApJ*, 243, 690
- Kosack, K., Badran, H. M., Bond, I. H., et al. 2004, *ApJ*, 608, L97
- Koyama, S., Kino, M., Giroletti, M., et al. 2016, *A&A*, 586, A113
- Kubo, H., Asahara, A., Bicknell, G. V., et al. 2004, *New A Rev.*, 48, 323
- Lamer, G. & Wagner, S. J. 1998, *A&A*, 331, L13
- Lanyi, G. E., Boboltz, D. A., Charlott, P., et al. 2010, *AJ*, 139, 1695
- Le Bohec, S., Degrange, B., Punch, M., et al. 1998, *Nuclear Instruments and Methods in Physics Research A*, 416, 425
- Levinson, A. 2000, *Phys. Rev. Lett.*, 85, 912
- Li, T.-P. & Ma, Y.-Q. 1983, *ApJ*, 272, 317
- Liu, S., Melia, F., Petrosian, V., & Fatuzzo, M. 2006, *ApJ*, 647, 1099
- Longair, M. S. 1981, *High energy astrophysics* (Cambridge University Press)
- Lorenz, E. & The MAGIC Collaboration. 2004, *New A Rev.*, 48, 339
- MAGIC Collaboration, Albert, J., Aliu, E., et al. 2008, *Physics Letters B*, 668, 253
- Markarian, B. E. 1967, *Astrofizika*, 3, 24

- Markaryan, B. E. & Lipovetskii, V. A. 1972, *Astrophysics*, 8, 89
- Maza, J., Martin, P. G., & Angel, J. R. P. 1978, *ApJ*, 224, 368
- Mazin, D. & Raue, M. 2007, *A&A*, 471, 439
- Menzler, U. & Schlickeiser, R. 2015, *MNRAS*, 448, 3405
- Moles, M., Masegosa, J., & del Olmo, A. 1987, *AJ*, 94, 1143
- Mufson, S. L., Hutter, D. J., Hackney, K. R., et al. 1984, *ApJ*, 285, 571
- Murach, T., Gajdus, M., & Parsons, R. D. 2015, ArXiv e-prints [arXiv:1509.00794]
- Neilsen, J., Nowak, M. A., Gammie, C., et al. 2013, *ApJ*, 774, 42
- Neronov, A. & Semikoz, D. V. 2009, *Phys. Rev. D*, 80, 123012
- Neronov, A. & Vovk, I. 2010, *Science*, 328, 73
- Ohm, S., van Eldik, C., & Egberts, K. 2009, *Astroparticle Physics*, 31, 383
- Perley, R. A., Dreher, J. W., & Cowan, J. J. 1984, *ApJ*, 285, L35
- Perlman, E. S., Stocke, J. T., Schachter, J. F., et al. 1996, *ApJS*, 104, 251
- Petrosian, A., McLean, B., Allen, R. J., & MacKenty, J. W. 2007, *ApJS*, 170, 33
- Petry, D., Böttcher, M., Connaughton, V., et al. 2000, *ApJ*, 536, 742
- Pian, E., Vacanti, G., Tagliaferri, G., et al. 1998, *ApJ*, 492, L17
- Piron, F., Djannati-Atai, A., Punch, M., et al. 2001, *A&A*, 374, 895
- Pohl, M. 2002, *Einführung in die Hochenergieastrophysik* (Shaker-Verlag)
- Poutanen, J., Zdziarski, A. A., & Ibragimov, A. 2008, *MNRAS*, 389, 1427
- Primack, J. R., Bullock, J. S., & Somerville, R. S. 2005, in *American Institute of Physics Conference Series*, Vol. 745, *High Energy Gamma-Ray Astronomy*, ed. F. A. Aharonian, H. J. Völk, & D. Horns, 23–33
- Prosekin, A., Essey, W., Kusenko, A., & Aharonian, F. 2012, *ApJ*, 757, 183
- Punch, M., Akerlof, C. W., Cawley, M. F., et al. 1992, *Nature*, 358, 477
- Punch, M. & H.E.S.S. Collaboration. 2001, *International Cosmic Ray Conference*, 7, 2814
- Quinn, J., Akerlof, C. W., Biller, S., et al. 1996, *ApJ*, 456, L83
- Quinn, J., Bond, I. H., Boyle, P. J., et al. 1999, *ApJ*, 518, 693
- Rector, T. A., Gabuzda, D. C., & Stocke, J. T. 2003, *AJ*, 125, 1060
- Rivers, E., Markowitz, A., & Rothschild, R. 2013, *ApJ*, 772, 114
- Rügamer, S., Oya, I., Hayashida, M., et al. 2009, ArXiv e-prints [arXiv:0907.0551]
- Rybicki, G. B. & Lightman, A. P. 1979, *Radiative processes in astrophysics* (John Wiley and Sons)
- Sambruna, R. M., Aharonian, F. A., Krawczynski, H., et al. 2000, *ApJ*, 538, 127
- Samuelson, F. W., Biller, S. D., Bond, I. H., et al. 1998, *ApJ*, 501, L17
- Scarpa, R., Urry, C. M., Falomo, R., Pesce, J. E., & Treves, A. 2000a, *ApJ*, 532, 740
- Scarpa, R., Urry, C. M., Padovani, P., Calzetti, D., & O’Dowd, M. 2000b, *ApJ*, 544, 258
- Schachter, J. F., Stocke, J. T., Perlman, E., et al. 1993, *ApJ*, 412, 541
- Schlickeiser, R., Elyiv, A., Ibscher, D., & Miniati, F. 2012a, *ApJ*, 758, 101
- Schlickeiser, R., Ibscher, D., & Supsar, M. 2012b, *ApJ*, 758, 102
- Schlickeiser, R., Krakau, S., & Supsar, M. 2013, *ApJ*, 777, 49

- Schwartz, D. A., Griffiths, R. E., Gursky, H., et al. 1978, *ApJ*, 224, L103
- Snijders, M. A. J., Boksenberg, A., Barr, P., et al. 1979, *MNRAS*, 189, 873
- Stecker, F. W., de Jager, O. C., & Salamon, M. H. 1996, *ApJ*, 473, L75
- Stecker, F. W., Malkan, M. A., & Scully, S. T. 2006, *ApJ*, 648, 774
- Stickel, M., Fried, J. W., & Kuehr, H. 1993, *A&AS*, 98, 393
- Supsar, M. & Schlickeiser, R. 2014, *ApJ*, 783, 96
- Takahashi, K., Mori, M., Ichiki, K., & Inoue, S. 2012, *ApJ*, 744, L7
- Tavecchio, F., Ghisellini, G., Bonnoli, G., & Foschini, L. 2011, *MNRAS*, 414, 3566
- Tavecchio, F., Ghisellini, G., Foschini, L., et al. 2010, *MNRAS*, 406, L70
- Taylor, A. M. 2016, *Nature*, 531, 43, news & Views
- Taylor, A. M., Vovk, I., & Neronov, A. 2011, *A&A*, 529, A144
- The Fermi-LAT Collaboration. 2015, ArXiv e-prints [arXiv:1508.04449]
- Tsuchiya, K., Enomoto, R., Ksenofontov, L. T., et al. 2004, *ApJ*, 606, L115
- Ulrich, M.-H., Kinman, T. D., Lynds, C. R., Rieke, G. H., & Ekers, R. D. 1975, *ApJ*, 198, 261
- Urry, C. M. & Padovani, P. 1995, *PASP*, 107, 803
- Urry, C. M., Scarpa, R., O'Dowd, M., et al. 2000, *ApJ*, 532, 816
- van Breugel, W. & Schilizzi, R. 1986, *ApJ*, 301, 834
- van Eldik, C., Bolz, O., Braun, I., et al. 2008, *International Cosmic Ray Conference*, 2, 589
- Vasileiou, V., Jacholkowska, A., Piron, F., et al. 2013, *Phys. Rev. D*, 87, 122001
- Vaughan, S., Edelson, R., Warwick, R. S., & Uttley, P. 2003, *MNRAS*, 345, 1271
- Vorontsov-Vel'Yaminov, B. A. & Arkhipova, V. P. 1964, in *Morphological catalogue of galaxies.*, 2 (1964), 0
- Vovk, I., Taylor, A. M., Semikoz, D., & Neronov, A. 2012, *ApJ*, 747, L14
- Wang, Q. D., Lu, F. J., & Gotthelf, E. V. 2006, *MNRAS*, 367, 937
- Weekes, T. C., Badran, H., Biller, S. D., et al. 2002, *Astroparticle Physics*, 17, 221
- Weekes, T. C., Cawley, M. F., Fegan, D. J., et al. 1989, *ApJ*, 342, 379
- Welford, W. T. & Winston, R. 1989, *High collection nonimaging optics* (Academic Press)
- Wiedner, C.-A. 1998, *hESS internal notes*
- Wikipedia. 2016, Active galactic nucleus — Wikipedia, The Free Encyclopedia, [Online; accessed 15-February-2016]
- Williams, D. A. 2005, in *American Institute of Physics Conference Series*, Vol. 745, *High Energy Gamma-Ray Astronomy*, ed. F. A. Aharonian, H. J. Völk, & D. Horns, 499–504
- Woo, J.-H., Urry, C. M., van der Marel, R. P., Lira, P., & Maza, J. 2005, *ApJ*, 631, 762
- Zhang, Y. H., Celotti, A., Treves, A., et al. 1999, *ApJ*, 527, 719